TECHNISCHE UNIVERSITÄT MÜNCHEN

Lehrstuhl für Flugsystemdynamik

Nonlinear adaptive control of an endo-atmospheric dual-actuator interceptor

Ralf Lange

Vollständiger Abdruck der von der Fakultät für Maschinenwesen der Technischen Universität München zur Erlangung des akademischen Grades eines

Doktor-Ingenieurs

genehmigten Dissertation.

Vorsitzender:	Univ.-Prof. Dr.-Ing. Mirko Hornung
Prüfer der Dissertation:	1. Univ.-Prof. Dr.-Ing. Florian Holzapfel 2. Univ.-Prof. Dr.-Ing. Axel Schulte, Universität der Bundeswehr München

Die Dissertation wurde am 20.12.2011 bei der Technischen Universität München eingereicht und durch die Fakultät für Maschinenwesen am 13.09.2012 angenommen.

Zusammenfassung

Die vorliegende Dissertation entwickelt ein nichtlineares, adaptives Flugregelungssystem für einen endo-atmosphärischen Flugkörper, welcher sowohl über aerodynamische Steuerflächen wie auch Querschubdüsen verfügt. Auf Basis eines Simulationsmodells werden die Flugleistungen und die inhärente Dynamik des Flugkörpers analysiert. Die Regelungsmethodik Backstepping wird dargestellt und dahingehend weiterentwickelt, dass sie zur Regelung des Flugkörpers angewendet werden kann. Aufsetzend auf definierten Leistungsanforderungen wird das Flugregelungssystem entworfen und implementiert. Die Regelungsparameter werden unter Nutzung eines Optimierungsalgorithmus automatisiert ermittelt. Das Flugregelungssystem wird gegen die Leistungsanforderungen in mehreren Testfällen validiert.

Abstract

A nonlinear adaptive flight control system for an endo-atmospheric dual-actuator interceptor is developed in this thesis. First, the flight performance and the inherent dynamics of the interceptor are analyzed, based on a simulation model. Thereafter, the control methodology Backstepping is introduced and further developed to be utilized for the control of the interceptor. Starting from specific performance requirements, the interceptor flight control system is designed and implemented. The control parameters are derived by employing an optimization algorithm. Finally, the flight control system is evaluated against the performance requirements in various test cases.

Preface and acknowledgments

The interdisciplinary character of control engineering emphasizes its importance and constitutes the basis for the fascination of engineers, including myself, about this field of technology. Although a wide basis of control engineering theory exists, which is versatile usable, every class of real systems exhibits special characteristics a control engineer needs to consider. Aeronautical and astronautical control engineering regularly demands most of all from a control engineer due to high requirements in stability, robustness, performance, reliability, or redundancy.
During the last century, theory of linear systems and control of latter became completely developed and is part of education as well as engineering practice today. Advances in theory made it possible to design observers and controllers for linear systems with uncertain parameters. Adaptive controllers for linear systems are common. Additionally, nonlinear system theory unfolded during the last few decades. Nonlinear control methodologies evolved from this foundation. The theoretical fundament for the control of nonlinear systems with uncertain parameters exists. Literature contains multiple examples for nonlinear adaptive control of nonlinear systems. Apart from that, the continuous publishing of papers, containing the application of nonlinear adaptive control to exemplary systems under certain conditions and assumptions, shows that nonlinear adaptive control is not at the state of being used regularly in engineering practice. Considering the widely accepted phenomenon that evolved methodologies need a period of time before they reach practical use and become standard procedures later, one might say that nonlinear adaptive control is in the transition phase from theoretical development and research to application.
This thesis wants to support this transition process and tries to bridge the gap sometimes seeming to lie between research and engineering. It wants to illustrate that the available nonlinear adaptive control methodologies can be applied successfully to high agile systems, that these methodologies have the capability to overcome the constant and time-varying uncertainties existing in real systems, and that defined performance requirements can be fulfilled at the same time. Furthermore, this thesis might present some process steps necessary for the implementation of a nonlinear adaptive control methodology in a real system.
To reach this intention, a nonlinear control methodology is applied to a specified plant, which is neither ideal nor an analytic model, in a control design process. Thereafter, the result of the design process is evaluated under various conditions against defined performance requirements to assess its capabilities. All steps are presented in detail to achieve that, apart from this thesis, the demonstrated process can be reapplied to other plants with different parameters, e.g. mass or aerodynamics, in engineering practice.
Commemorating the stated aim, it is noteworthy that the latter is not freely chosen. It is a logical consequence of the constellation under which this doctoral thesis was conducted: a partnership between industry and a university. From this perspective, it becomes evident that all parts of the methodology used had to be reviewed, if they would allow an implementation in a real system, and real system behavior had to be accounted for in the overall process.
At this stage, it is a pleasure for me to thank all persons who supported this work. Since the list of persons who I owe an acknowledgement would fill a section easily, I will only mention

two persons by name. First, I want to thank Prof. Dr.-Ing. Florian Holzapfel, Head of the Institute for Flight System Dynamics TU München, for supervising this dissertation, inspiring my thoughts, and the fruitful discussions we had. Second, I am very thankful to Mr. Manfred Braitinger, former Senior Vice President Defence & Security IABG mbH, who admitted his support to initiate this doctoral thesis. I want to thank Diehl BGT Defence GmbH & Co. KG for providing me the opportunity and support to finalize this thesis. Finally, I thank my family, my dear friends and colleagues for the support.

Contents

List of Figures

Chapter 1

Introduction

1.1 Interceptor overview

Although the beginning of missile technology reaches back to the 13th century, the development of operational missile systems began in the last century. During World War II military system architects merged the available, theoretical knowledge in the field of engineering with the practical experience from simple, unguided rockets to design the first operational systems employing missiles as effectors. Afterwards, the capabilities and performance of such systems grew at an enormous speed, and they became a definite as well as valuable part of military inventories.
The design of missile systems for different applications in the past decades lead to multiple missile types which can be categorized by either their field of use or technical criteria. In the following, a few of these missile categorizations are introduced to establish a context in which the specific interceptor, used in this dissertation, can be seen. The categorizations are derived from [28], [59] and [105].
From an overarching perspective, missiles are divided into non-military and military utilized missiles. While the former are mostly used for scientific research, the latter typically carry a warhead and are launched to hit a specified target. The interceptor considered in this thesis belongs to the group of military missiles. Second, missiles are categorized into unguided and guided missiles. Guided missiles exhibit the capability to alter their flight path, based on externally received or internally generated commands. Unguided missile do not own this ability. The interceptor accounted for in this work is a guided missile. The third taxonomy to be introduced accounts for the location of the launch point of the missile and the target location. Differentiating between air, surface and subsurface for the launch as well as the target location, the missile types represented in Figure 1.1 are derived. With respect to the beforehand presented categorization, the interceptor considered herein constitutes a surface-to-air missile. Using the flight envelope as criteria, missiles are divided into endo- and exo-atmospheric missiles. The former type of missile does operate in altitudes where the atmosphere is being effective, only. The trajectory of exo-atmospheric missiles runs outside of the effective atmosphere or at least contains a certain time of flight outside the effective atmosphere. The flight envelope of the considered interceptor is located in the effective atmosphere completely. Hence, it is an endo-atmospheric missile. A further categorization to be mentioned is based on the trajectory. It differentiates between aerodynamically flying and ballistic missiles. The former type of missile generates an angle of attack between the surrounding airflow and their body or aerodynamically shaped wings to produce lift as well as to control the missile. This results in the capability to fly an arbitrary trajectory inside the effective physical constraints. The flight path of ballistic missiles is determined by gravity. After a first, propelled flight phase, ballistic missiles fly the

		Target location		
		Air	**Surface**	**Subsurface**
Launch location	**Air**	Air-to-air missile (A/AM)	Air-to-surface missile (A/SM)	Air-to-subsurface missile (A/SSM)
	Surface	Surface-to-air missile (S/AM)	Surface-to-surface missile (S/SM)	Surface-to-subsurface missile (S/SSM)
	Subsurface	Subsurface-to-air missile (SS/AM)	Subsurface-to-surface missile (SS/SM)	Subsurface-to-subsurface missile (SS/SSM)

Figure 1.1: Missile categorization

remainder of the flight time without propulsion. The flight path of these missiles exhibits a Kepler- Trajectory, caused by the gravitation acting on the missiles. The interceptor of this thesis is an aerodynamically flying missile. The last categorization to be introduced separates missiles into aerodynamically controlled and thrust controlled missiles. The fact that the interceptor comprises thrust actuators at the bow of its fuselage and aerodynamic actuators at the stern, which will be illustrated in detail in Chapter 2, no definite allocation with respect to this categorization is possible.
The variety of presented categorizations and the mapping of the considered interceptor to each of these indicates that the design of a missile flight control system is very specific task. Related to every missile type and sometimes every subversion of a type are tight specifications, which allow the missile to fulfill its mission. These specifications must be met by the missile flight control system. The combination of plant variety and tight specifications most often requires new designs for missile flight control systems or at least extensive redesigns of existing control systems. The process of defining specifications, designing a missile flight control systems, and verifying its performance against the specifications will be elaborated in this work starting with Chapter 2.

1.2 Nonlinear control methodologies

After the solution of comprehensive control problems for linear systems with unknown parameters during the early 1980's, also nonlinear system theory rapidly advanced. The embodied approach of feedback linearization made it possible to convert nonlinear problems into simpler, solvable ones for the first time. The shortfall of the feedback linearization methodology, the inability to handle unknown parameters, if utilized in its straight formulation without adaptive augmentations, lead to the constitution of nonlinear adaptive control methodologies. Sliding Mode Control, Lyapunov Redesign, Backstepping and Passivity-Based Control are a few of

these, which are connectedly presented in [66]. Details are available in [53], [54], [88], [106], [112], and [117].
While many of the mentioned nonlinear adaptive control methodologies are restricted to systems satisfying the matching condition or the extended matching condition, Backstepping is adequate for systems with more than one integration between the control input and the unknown parameters, too. It was first presented 1991 in [67], which based on [65]. [20], [37], [63], [68], [111], [126], and [134] served as foundation from which Backstepping was derived. Further development of the method was achieved in [60], [69], and [70]. Besides the evolution of the methodology itself, [84], [85], [86], and [87] constitute spin offs of Backstepping.
The successful application of the Backstepping methodology to a broad variety of exemplary systems has been shown in many texts. On the other hand, only a limited set of references elaborates on the application of this method to aerospace systems. [123], [124], [133], and [139] are recent references for the application of Backstepping to aircraft systems. The number of sources dealing with Backstepping-based flight control for high agile missiles is even more limited. Approaches to such systems are found in [91], [118], [131], [137], and [138]. Although latter sources contain very beneficial results, simplifications or open issues remain in each of these references. The flight control system design in [118], [131], [137], and [138] is limited to the missiles pitch plane. Additionally, the missile aerodynamics of the these references are stated as nonlinear analytic functions. This differs from the design of a flight control system for a real missile, where tabular aerodynamic data, gathered from computations or wind tunnel measurements, will usually be given. The aerodynamic data is afflicted with non-negligible uncertainties in this case. [91], [131], [137], and [138] consider a missile with aerodynamic actuators only. Flight control system implementation issues, e.g. information availability according to the internal measurement unit capabilities or signal discretization, are neglected partly in [131] and completely in [137] as well as [138].
From the perspective of this thesis, no missile flight control system design scheme, employing nonlinear adaptive control methodologies, considering all degrees of freedom of the vehicle, accounting for existing uncertainties, and being applicable for dual-actuator configurations, exists. Additionally, no missile related source offers a modular design process which provides the capability to reuse its embedded steps. Based on this conclusion, the following thesis tries to overcome the limitations of the beforehand mentioned references to reach a nonlinear adaptive missile flight control system that offers the potential of being implemented in an existing missile airframe or a missile under development.

1.3 Outline

This thesis is structured in seven chapters. Chapter 2 starts with a description of the basic properties of the endo-atmospheric dual-actuator interceptor. The derivation of the nonlinear rigid body equations of motion which govern the motion of the interceptor follows. The description of the modeling of the external efforts that are acting on the interceptor and the modeled interceptor subsystems follows. The chapter closes with an illustration of the modeling of considered parameter uncertainties, whereupon uncertain constant parameters and time-varying parameters are treated separately.
Chapter 3 lays out the analysis of the interceptor flight dynamics. It constitutes the foundation for the synthesis of the interceptor flight control system. First, the interceptor is trimmed at steady-state flight conditions. Based on trim results for the flight of the interceptor with a constant load factor, the maneuver capabilities of the interceptor are derived. The second section of Chapter 3 presents the linearization of the interceptor flight dynamics. Following the de-

tailed description of the linearization algorithm and its modular implementation, the linearized longitudinal as well as the linearized roll rate dynamics of the interceptor are analyzed. This analysis covers the uncontrolled interceptor flight dynamics and the response of the linearized interceptor dynamics to control inputs. The investigation of the change of the respective linearized interceptor dynamics with respect to the flight condition ceases this section. The last section of Chapter 3 describes the nonlinear simulation frame utilized for this work.
In Chapter 4 the nonlinear control methodology Backstepping is introduced. After providing a brief overview, basic stability theorems are stated, followed by the derivation of the recursive design procedures for scalar strict-feedback systems as well as strict-feedback systems composed of two nonlinear systems. Additionally, the control task of tracking is treated. The third section of Chapter 4 introduces adaptive Backstepping. Following the presentation for Backstepping without uncertainties, the recursive design procedures for scalar parametric strict-feedback systems is derived and its boundedness and stability properties are illustrated. The results for the control task of tracking augment the illustration. In the next step, the design procedures for unknown control coefficients are derived, whereupon the most general case which contains an unknown control coefficient in every system equation is considered. Finally, nonlinear damping which provides the capability to overcome bounded disturbances and guarantees global boundedness without adaptation is presented. The beforehand presented design procedures of Chapter 4 are augmented by nonlinear damping terms and the overall boundedness and stability properties of the combined designs are derived.
After the theoretical background has been illustrated in detail, the fifth chapter carries out the design of the interceptor flight control system. The chapter starts by stating the performance requirements which govern the design of the interceptor flight control system. As first step in the design process, the top level architecture of the fight control system is derived in Section 5.2, based on the performance requirements. The roll rate control system is designed in Section 5.3. Thereafter, the pitch and yaw acceleration control systems follow. In Section 5.6 the design of the control allocation which blends the roll commands of the respective control systems and allocates them to the two actuator sections of the interceptor is conducted. Besides the control allocation algorithm, the developed algorithms for searching and identifying the optimal reaction jet cartridges to realize a calculated command are presented. The last section of Chapter 5 deals with the optimization of the flight control system parameters. Additionally, the structure of modular tools developed during this work to carry out this task is presented.
Chapter 6 evaluates the performance of the designed interceptor flight control system. Initially, the nominal case without uncertainties is treated. The performance of the controlled interceptor is assessed with respect to the given performance requirements specified in Chapter 5. Two scenarios are considered regarding the interceptor absolute velocity. In the second step, uncertain constant parameters are introduced into the system. The cases of an uncertain interceptor mass and an uncertain reaction jet cartridge thrust are examined separately in Section 6.2, and are evaluated against the performance requirements for the two velocity scenarios. The third section of Chapter 6 treats the robustness of the designed interceptor flight control system in the case of time-varying parameters. Finally, Section 6.4 evaluates the performance of the controlled interceptor in the two scenarios under combined uncertainties, whereupon combined uncertainty denotes a situation in which uncertain constant parameters as well as time-varying parameters are existent simultaneously in the system. This situation constitutes the most difficult environment for the designed interceptor flight control system.
The thesis closes with Chapter 7. This chapter embraces a summary of the presented content in combination with conclusions that can be drawn from the work. Furthermore, possible perspectives for future research are provided.

Chapter 2

Interceptor model

2.1 Generic endo-atmospheric interceptor

The design and evaluation of the nonlinear adaptive flight control system in this thesis is conducted for a generic endo-atmospheric dual-actuator interceptor. The approach of using a generic interceptor allows to abstract from the specific designs of existing missiles. Different design elements of various missiles are combined in the generic interceptor to enhance the applicability of the flight control system to be designed. Second, the choice of a generic interceptor renders the overall work unclassified. As stated in [9], exact data of existing missiles exhibits very restricted access, and high classification of the respective data is common. Hence, the use of real data would be in conflict to the aims of this work, which incorporate the application of a nonlinear adaptive control methodology to a high agile missile and making the results accessible for further research.
To define a generic interceptor layout for this thesis, the designs of existing missiles, which belong to the appropriate category according to Section 1.1, are analyzed. A fielded and successful operated design is chosen and altered to reach the desired unclassified level. Necessary basic geometrical data for the design is taken from open information sources. All other data is calculated from the available basic data in combination with the altered design by using analytical equations or open software tools. The result of the beforehand stated layout process is presented in the following.
The basic geometrical concept of the interceptor is that of a cruciform missile. The X_B - Y_B and the X_B - Z_B plane with respect to the body fixed frame are planes of symmetry. The definition of the body fixed frame is given in Appendix B, and is in accordance with [16], [47], [55], as well as [56]. Figure 2.1 shows the shape of the interceptor and illustrates its size. The interceptor has a length of $l = 5.200\,[m]$, a fin span of $s = 0.450\,[m]$, and a fuselage diameter of $d = 0.250\,[m]$. The fuselage diameter of the interceptor is used as mean aerodynamic chord.

$$\bar{c} = 0.250\,[m] \tag{2.1}$$

The fuselage cross-sectional area which is defined as area of reference for this work is calculated from the mean aerodynamic chord.

$$S_{Ref} = \frac{\pi}{4}\bar{c}^2 = 0.049\,[m^2] \tag{2.2}$$

The internal structure of the interceptor is divided into six sections which carry the interceptor subsystems. The missile bow forms the seeker section. It consists of the radome, the seeker antenna and the active radar seeker. After the seeker section follows the guidance and control

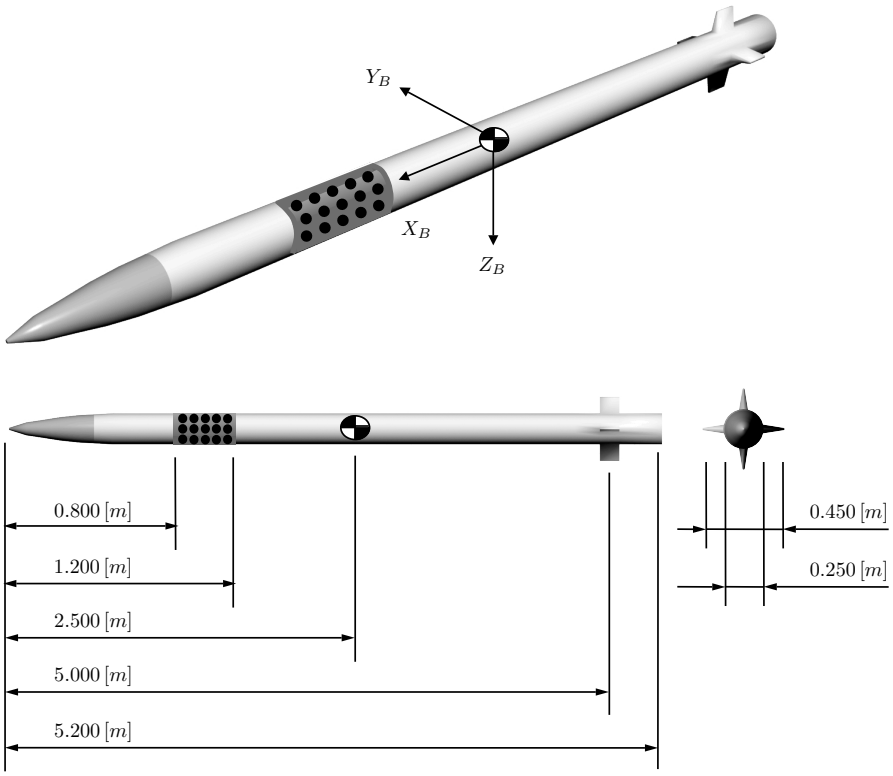

Figure 2.1: Generic endo-atmospheric dual-actuator interceptor

section, incorporating the guidance receiver for external guidance signals and the guidance processor, capable of calculating guidance commands for the interceptor based on external guidance signals as well as internal measurements by the active radar seeker. The third subsystem in the guidance and control section is the interceptor flight control system which is designed in the following chapters. The next section is the reaction jet actuator section. This section houses 180 single reaction jet cartridges which can be fired individually, once each. Five single cartridges form a reaction jet cartridge column along the X_B axis, as displayed in Figure 2.1. The position vectors of the individual cartridges in a reaction jet cartridge column, specified in the body fixed frame, are given by (2.3). The reaction jet cartridge columns are dispersed on the circumference of the interceptor fuselage in steps of $10\,[deg]$ starting in the direction of the negative Z_B axis and rotating according to a positive roll rate. This results in reaction jet cartridge attitudes, specified in the body fixed frame, according to (2.4).

$$\left(\vec{r}^{\,RJC}\right)_B = \begin{bmatrix} 1.700 & 1.600 & 1.500 & 1.400 & 1.300 \\ 0 & 0 & 0 & 0 & 0 \\ 0 & 0 & 0 & 0 & 0 \end{bmatrix}_B [m] \tag{2.3}$$

$$\left(\vec{\varphi}^{\,RJC}\right)_B = \begin{bmatrix} -180 & -170 & -160 & \cdots & 170 \end{bmatrix}_B^T [deg] \tag{2.4}$$

The reaction jet actuator section constitutes the first of the two actuator sections of the interceptor. The fourth section is the warhead section, followed by the propulsion section as the fifth section. The propulsion section is considered as a single stage, solid propellant rocket motor in this thesis. The sixth and last section of the interceptor is the aerodynamic actuator section. It comprises the actuator modules for the four rectangular shaped aerodynamic control surfaces,

which are arranged cruciform. The position vector of the aerodynamic actuator section, specified in the body fixed frame, is given by (2.5).

$$\left(\vec{r}^{\,Fin}\right)_B = \begin{bmatrix} -2.500 & 0 & 0 \end{bmatrix}_B^T \, [m] \tag{2.5}$$

A detailed description comprising the layout data and performance characteristics of the interceptor subsystems which are of importance for the design of the interceptor flight control system is given in the following sections.
Based on the considered internal structure, the sizes of the interceptor subsystems are derived. Latter are used to estimate the masses of the respective subsystems, whereupon the rocket motor is considered without the solid propellant. These results are utilized to estimate the center of gravity of the interceptor. In addition, the masses of the interceptor sections, the total interceptor mass, and inertia tensor with respect to the center of gravity of the interceptor are calculated from the interceptor subsystem mass estimates. The results for the total interceptor mass and the inertia tensor with respect to the center of gravity of the interceptor, specified in the body fixed frame, are given in (2.6) and (2.7).

$$m_{Empty} = 150.00\,[kg] \tag{2.6}$$

$$\left(I^G_{Empty}\right)_{BB} = \begin{bmatrix} 5.00 & 0 & 0 \\ 0 & 400.00 & 0 \\ 0 & 0 & 400.00 \end{bmatrix}_{BB} \quad [kgm^2] \tag{2.7}$$

2.2 Nonlinear rigid body equations of motion

In the following section the nonlinear rigid body differential equations which govern the motion of the interceptor are derived. These describe the changes of the rigid body states of the interceptor in a six degree of freedom representation. The total number of twelve nonlinear scalar differential equations can be divided into nonlinear differential equations specifying translation, rotation, attitude, and position. The dynamic behavior of the interceptor subsystems as well as the detailed modeling of the forces and moments acting on the interceptor are not accounted for at this point, but will be presented in the respective following sections. A further detailed derivation of the nonlinear rigid equations of motion is available in [11], [16], [45], [47], [110], and [130].

Translation
The basis for the derivation of the nonlinear rigid body equations of motion is Newton's second axiom. The axiom states that the rate of change of momentum of a body, measured with respect to an inertial reference frame, is proportional to the force imposed on the body. With the momentum of a rigid body given by (2.8), the second axiom is written as (2.9).

$$\vec{p}\,(t) = \int_m \vec{V}^I\left(\vec{x}^P, t\right) \, \mathrm{dm} \tag{2.8}$$

$$\sum \vec{F} = \left(\frac{\mathrm{d}}{\mathrm{dt}}\right)^I \vec{p}\,(t) = \left(\frac{\mathrm{d}}{\mathrm{dt}}\right)^I \int_m \vec{V}^I\left(\vec{x}^P, t\right) \, \mathrm{dm} \tag{2.9}$$

Under the assumption that the influence of the rate of change of the interceptor mass on the rate of change of the momentum is negligible, the mass is considered steady in (2.9). Expanding the right side of (2.9) for an arbitrary reference point R results in (2.10), whereupon the superscript

E denotes the Earth-Centered-Earth-Fixed frame and G represents the center of gravity of the interceptor.

$$\begin{aligned}\sum \vec{F} &= m \cdot \left\{ \left(\dot{\vec{V}}^R\right)^{EB} + \left(\vec{\omega}^{EB}\right) \times \left(\vec{V}^R\right)^E \right\} \\ &\quad + m \cdot \left\{ 2 \cdot \left(\vec{\omega}^{IE}\right) \times \left(\vec{V}^R\right)^E + \left(\vec{\omega}^{IE}\right) \times \left[\left(\vec{\omega}^{IE}\right) \times \left(\vec{r}^{RG}\right)\right] \right\} \\ &\quad + m \cdot \left\{ \left(\dot{\vec{\omega}}^{IB}\right)^B \times \left(\vec{r}^{RG}\right) + \left(\vec{\omega}^{IB}\right) \times \left[\left(\vec{\omega}^{IB}\right) \times \left(\vec{r}^{RG}\right)\right] \right\} \end{aligned} \tag{2.10}$$

By choosing the center of gravity of the interceptor as the reference point, the third term on the right hand side of (2.10) vanishes. Making the further assumptions, which are based on the capabilities and the flight envelope of typical missiles in the category of the interceptor, that the interceptor time of flight is significantly below one minute and the covered distance during the flight is small, the Coriolis force, the centrifugal force, and the geoid shape of the earth become negligible. Hence, a flat earth representation with an embedded, fixed coordinate frame is taken as inertial reference frame for the further derivation of the nonlinear rigid body equations of motion as well as the following work. This inertial reference frame is denoted by the index I. Incorporating the stated assumptions into Equation (2.10) leads to (2.11), which is specified in the body fixed frame. This differential equation describes the translation of the interceptor and constitutes the first nonlinear rigid body equation of motion in vector notation.

$$\left(\dot{\vec{V}}_K^G\right)_B^{IB} = \frac{1}{m} \sum \left(\vec{F}^G\right)_B - \left(\vec{\omega}_K^{0B}\right)_B \times \left(\vec{V}_K^G\right)_B^I \tag{2.11}$$

Equation (2.11) utilizes the kinematic velocity of the center of gravity of the interceptor, specified in the body fixed frame, $(\vec{V}_K^G)_B^I = \begin{bmatrix} u_K^G & v_K^G & w_K^G \end{bmatrix}_B^{I,T}$ as state vector to describe the translation of the interceptor. Another set of state variables to describe the translation consists of the absolute kinematic velocity $(V_{K,Abs}^G)_B^I$ of the center of gravity of the interceptor, the angle of attack $(\alpha_K^G)_B^I$, and the sideslip angle $(\beta_K^G)_B^I$. Wind is neglected in the calculation of $(V_{K,Abs}^G)_B^I$ herein. These alternate state variables are used occasionally in this work, too. Appendix B illustrates the relation between the two sets of state variables. The following equations provide the respective state transformation.

$$V_{K,Abs}^G = \sqrt{\left(u_K^G\right)^2 + \left(v_K^G\right)^2 + \left(w_K^G\right)^2} \tag{2.12}$$

$$\alpha_K^G = \arctan\left(\frac{w_K^G}{u_K^G}\right) \tag{2.13}$$

$$\beta_K^G = \arctan\left(\frac{v_K^G}{\sqrt{\left(u_K^G\right)^2 + \left(w_K^G\right)^2}}\right) \tag{2.14}$$

$$\dot{V}_{K,Abs}^G = \frac{u_K^G \dot{u}_K^G + v_K^G \dot{v}_K^G + w_K^G \dot{w}_K^G}{\sqrt{\left(u_K^G\right)^2 + \left(v_K^G\right)^2 + \left(w_K^G\right)^2}} \tag{2.15}$$

$$\dot{\alpha}_K^G = \frac{u_K^G \dot{w}_K^G - \dot{u}_K^G w_K^G}{\left(u_K^G\right)^2 + \left(w_K^G\right)^2} \tag{2.16}$$

$$\dot{\beta}_K^G = -\frac{\dot{u}_K^G u_K^G v_K^G - \left[\left(u_K^G\right)^2 + \left(w_K^G\right)^2\right] \dot{v}_K^G + v_K^G w_K^G \dot{w}_K^G}{\left[\left(u_K^G\right)^2 + \left(v_K^G\right)^2 + \left(w_K^G\right)^2\right] \sqrt{\left(u_K^G\right)^2 + \left(w_K^G\right)^2}} \tag{2.17}$$

Rotation

The derivation of the nonlinear differential equation describing rotation is also based on Newton's second axiom. In relation to (2.8), the angular momentum of a rigid body with respect to the center of the earth is written as (2.18). Employing Newton's axiom, while using the spin of the rigid body and the external moments acting on latter, results in (2.19).

$$\vec{H}^0(t) = \int_m \vec{r}^P\left(\vec{x}^P, t\right) \times \vec{V}^I\left(\vec{x}^P, t\right) \, \mathrm{dm} \tag{2.18}$$

$$\sum \vec{M}^0 = \left(\frac{\mathrm{d}}{\mathrm{dt}}\right)^I \vec{H}^0(t) = \left(\frac{\mathrm{d}}{\mathrm{dt}}\right)^I \int_m \vec{r}^P\left(\vec{x}^P, t\right) \times \vec{V}^I\left(\vec{x}^P, t\right) \, \mathrm{dm} \tag{2.19}$$

Implementing the assumption that the interceptor mass is steady, the right hand side of (2.19) is expanded to (2.20), whereupon an arbitrary reference point R is considered. I^R denotes the inertia tensor of the rigid body with respect to R.

$$\begin{aligned}\sum \vec{M}^0 \;=\;& I^R\left(\dot{\vec{\omega}}^{IB}\right)^B + \left(\vec{\omega}^{IB}\right) \times I^R\left(\vec{\omega}^{IB}\right) + \left(\vec{V}^R\right)^I \times \left(\vec{p}\right) + \left(\vec{r}^R\right) \times \left(\dot{\vec{p}}\right)^I \\ & + m\left(\dot{\vec{r}}^{RG}\right)^B \times \left(\vec{V}^R\right)^I + m\left(\vec{r}^{RG}\right) \times \left(\dot{\vec{V}}^R\right)^{IB} \\ & + m\left(\vec{\omega}^{IB}\right) \times \left[\left(\vec{r}^{RG}\right) \times \left(\vec{V}^R\right)^I\right]\end{aligned} \tag{2.20}$$

Choosing the center of gravity of the interceptor as reference point and taking the flat earth representation with the embedded, fixed coordinate frame as inertial reference frame, following the derivation for translation, (2.21) is derived. The latter is specified in the body fixed frame and describes the rotation of the interceptor with respect to the North-East-Down frame. (2.21) constitutes the second nonlinear rigid body equation of motion in vector notation.

$$\left(\dot{\vec{\omega}}_K^{0B}\right)_B^B = \left(I^G\right)_{BB}^{-1}\left[\sum\left(\vec{M}^G\right)_B - \left(\vec{\omega}_K^{0B}\right)_B \times \left(I^G\right)_{BB}\left(\vec{\omega}_K^{0B}\right)_B\right] \tag{2.21}$$

The rotation vector $\left(\vec{\omega}_K^{0B}\right)_B$ comprises the scalar states roll rate $\left(p_K^{0B}\right)_B$, pitch rate $\left(q_K^{0B}\right)_B$, and yaw rate $\left(r_K^{0B}\right)_B$.

Attitude

The attitude of the interceptor can be described by using Euler angles which express the angular displacement of the interceptor with respect to North-East-Down frame. The respective attitude vector comprises the roll angle Φ, the pitch angle Θ, and the heading angle Ψ. A visualization of the Euler angles is provided in Appendix B. Following [16], [46], and [148], the nonlinear differential equation describing the interceptor attitude, while Euler angles are employed, is given by (2.22).

$$\begin{bmatrix}\dot{\Phi}\\ \dot{\Theta}\\ \dot{\Psi}\end{bmatrix} = \begin{bmatrix}1 & \sin\Phi\tan\Theta & \cos\Phi\tan\Theta\\ 0 & \cos\Phi & -\sin\Phi\\ 0 & \frac{\sin\Phi}{\cos\Theta} & \frac{\cos\Phi}{\cos\Theta}\end{bmatrix}_B \cdot \begin{bmatrix}p_K^{0B}\\ q_K^{0B}\\ r_K^{0B}\end{bmatrix}_B \tag{2.22}$$

As it is seen from (2.22), the equation for $\dot{\Psi}$ contains a singularity for pitch angles of $\Theta = \pm 90\,[deg]$. Because the interceptor constitutes a high agile missile, the description of the interceptor attitude by Euler angles including the mentioned singularity is not appropriate for this work. The attitude description by Quaternions, which is free of singularities, instead constitutes a more appropriate method. Hence, Quaternions are chosen and employed throughout the following work. A complete introduction to Quaternion algebra and the derivation of the differential equation describing the attitude of the interceptor is found in [33], [130], and [148]. To stay inside the scope of the thesis, they are omitted here. The result of the derivation of the differential equation is given by (2.23). This equation describes the attitude of the interceptor with respect to the North-East-Down frame, specified in the body fixed frame, and constitutes the third rigid body equation of motion in vector notation.

$$\begin{bmatrix} \dot{q_0} \\ \dot{q_1} \\ \dot{q_2} \\ \dot{q_3} \end{bmatrix}_B = \frac{1}{2} \begin{bmatrix} 0 & -p_K^{0B} & -q_K^{0B} & -r_K^{0B} \\ p_K^{0B} & 0 & r_K^{0B} & -q_K^{0B} \\ q_K^{0B} & -r_K^{0B} & 0 & p_K^{0B} \\ r_K^{0B} & q_K^{0B} & -p_K^{0B} & 0 \end{bmatrix}_B \cdot \begin{bmatrix} q_0 \\ q_1 \\ q_2 \\ q_3 \end{bmatrix}_B + k\lambda \cdot \begin{bmatrix} q_0 \\ q_1 \\ q_2 \\ q_3 \end{bmatrix}_B \tag{2.23}$$

The second term on the right side of (2.23) is added based on [108] and [148] to diminish errors resulting from numerical integration schemes. The constant k is chosen as $k = 0.5$. The orthonormality error λ is calculated according to (2.24).

$$\lambda = 1 - \left(q_0^2 + q_1^2 + q_2^2 + q_3^2\right) \tag{2.24}$$

The transformations from Euler angles to Quaternions and vice versa, which are valuable for simulation initialization, output calculations, and the perceivability of results, are given by the following equations.

$$q_0 = \cos\left(\frac{\Psi}{2}\right)\cos\left(\frac{\Theta}{2}\right)\cos\left(\frac{\Phi}{2}\right) + \sin\left(\frac{\Psi}{2}\right)\sin\left(\frac{\Theta}{2}\right)\sin\left(\frac{\Phi}{2}\right) \tag{2.25}$$

$$q_1 = \cos\left(\frac{\Psi}{2}\right)\cos\left(\frac{\Theta}{2}\right)\sin\left(\frac{\Phi}{2}\right) - \sin\left(\frac{\Psi}{2}\right)\sin\left(\frac{\Theta}{2}\right)\cos\left(\frac{\Phi}{2}\right) \tag{2.26}$$

$$q_2 = \cos\left(\frac{\Psi}{2}\right)\sin\left(\frac{\Theta}{2}\right)\cos\left(\frac{\Phi}{2}\right) + \sin\left(\frac{\Psi}{2}\right)\cos\left(\frac{\Theta}{2}\right)\sin\left(\frac{\Phi}{2}\right) \tag{2.27}$$

$$q_3 = \sin\left(\frac{\Psi}{2}\right)\cos\left(\frac{\Theta}{2}\right)\cos\left(\frac{\Phi}{2}\right) - \cos\left(\frac{\Psi}{2}\right)\sin\left(\frac{\Theta}{2}\right)\sin\left(\frac{\Phi}{2}\right) \tag{2.28}$$

$$\tan\Psi = \frac{2\left(q_1 q_2 + q_0 q_3\right)}{q_0^2 + q_1^2 - q_2^2 - q_3^2} \tag{2.29}$$

$$\sin\Theta = -2\left(q_1 q_3 - q_0 q_2\right) \tag{2.30}$$

$$\tan\Phi = \frac{2\left(q_2 q_3 + q_0 q_1\right)}{q_0^2 - q_1^2 - q_2^2 + q_3^2} \tag{2.31}$$

Position

The nonlinear differential equation describing the interceptor position with respect to the inertial reference frame is derived from the relationship between the velocity vector, specified in the North-East-Down frame, and the position vector in the North-East-Down frame. Because the derivative of the latter is equal to the velocity vector, specified in the North-East-Down frame,

only a transformation for the velocity vector, specified in the body fixed frame, which is used in (2.11), is necessary to establish the respective nonlinear differential equation. By employing the transformation matrix from the body fixed frame to the North-East-Down frame, being found in [16] and provided by (2.32), Equation (2.33) is derived.

$$M_{0B} = \begin{bmatrix} \cos\Theta\cos\Psi & \sin\Phi\sin\Theta\cos\Psi - \cos\Phi\sin\Psi & \cos\Phi\sin\Theta\cos\Psi + \sin\Phi\sin\Psi \\ \cos\Theta\cos\Psi & \sin\Phi\sin\Theta\sin\Psi + \cos\Phi\cos\Psi & \cos\Phi\sin\Theta\sin\Psi - \sin\Phi\cos\Psi \\ -\sin\Theta & \sin\Phi\cos\Theta & \cos\Phi\cos\Theta \end{bmatrix} \tag{2.32}$$

$$\begin{bmatrix} \dot{x}^G \\ \dot{y}^G \\ \dot{z}^G \end{bmatrix}_0 = M_{0B} \cdot \begin{bmatrix} u_K^G \\ v_K^G \\ w_K^G \end{bmatrix}_B^I \tag{2.33}$$

To finally achieve the nonlinear differential equation for the position of the interceptor with respect to the inertial reference frame, a second transformation is employed. It transforms the position vector, specified in the North-East-Down frame, into the inertial reference frame. Considering that the inertial reference frame and the North-East-Down frame are oriented equally, besides the fact that the Z_0 and the Z_I axis point in opposite directions, the nonlinear differential equation is given by (2.34). This equation constitutes the fourth nonlinear rigid body equation of motion in vector notation.

$$\begin{bmatrix} \dot{x}^G \\ \dot{y}^G \\ \dot{z}^G \end{bmatrix}_I = \begin{bmatrix} 1 & 0 & 0 \\ 0 & 1 & 0 \\ 0 & 0 & -1 \end{bmatrix} \cdot M_{0B} \cdot \begin{bmatrix} u_K^G \\ v_K^G \\ w_K^G \end{bmatrix}_B^I \tag{2.34}$$

2.3 Modeling of external forces and moments

2.3.1 Gravity

Since the external efforts acting on the interceptor have been treated as a single vector in the derivation of the nonlinear rigid body equations of motion (2.11) and (2.21), these efforts are developed in detail now. According to their physical origin, the external forces and moments are divided into gravitation, aerodynamic forces and moments, propulsion forces, and reaction jet forces and moments. The modeling of the first is elaborated on in this section, while the other efforts are described in the following sections.

The interceptor is being subject to the gravitation of the earth, whereupon the gravitational force which actually acts on the interceptor varies, depending on the interceptor position and the interceptor altitude. Considering the assumption that the interceptor time of flight is significantly below one minute and the covered distance during the flight is small, which led to the implementation of a flat earth representation, the dependency of the gravitation from the interceptor position is neglected. Assuming that the interceptor operates in low to medium altitudes, gravity is implemented independent of the interceptor altitude. From the definition of the utilized coordinate frames according to Appendix B in conjunction with the used flat earth representation, it is evident that the gravitation vector is persistently oriented perpendicular to the surface of the flat earth representation and coincides with the Z_0 axis. Hence, gravity is specified in the North-East-Down frame and is transformed to the body fixed frame to enter (2.11). Equation (2.35) states the gravitational force acting on the center of gravity of the interceptor. The transformation matrix M_{B0} is equal to M_{0B}^T, which is provided in (2.32).

$$\left(\vec{F}_G^G\right)_B = \begin{bmatrix} F_{X,G}^G \\ F_{Y,G}^G \\ F_{Z,G}^G \end{bmatrix}_B = M_{B0} \cdot \begin{bmatrix} 0 \\ 0 \\ mg \end{bmatrix}_0 \tag{2.35}$$

2.3.2 Aerodynamic forces and moments

The aerodynamic forces and moments acting on the interceptor arise from the airflow streaming over the interceptor fuselage and aerodynamic control surfaces at the stern of the interceptor. The unique shape of a body, in this case the interceptor, results in specific aerodynamic forces and moments that arise. Hence, the latter are a unique characteristic of the body interacting with the airflow. This implies that the aerodynamic forces and moments must be calculated, analyzed, and accurately be taken into account for every configuration. The complex aerodynamic force and moment characteristics for a body are stored in dimensionless aerodynamic coefficients.
Calculation of the aerodynamic forces acting on the center of gravity of the interceptor, specified in the body fixed frame, is done by (2.36). The aerodynamic moments with respect to the center of gravity of the interceptor, specified in the body fixed frame, are calculated via (2.37). The dynamic pressure $\bar{q}$ is given by (2.38). As introduced earlier, wind is neglected in $(V^G_{K,Abs})^I_B$.

$$\left(\vec{F}^G_A\right)_B = \begin{bmatrix} F^G_{X,A} \\ F^G_{Y,A} \\ F^G_{Z,A} \end{bmatrix}_B = \begin{bmatrix} C_X \bar{q} S_{Ref} \\ C_Y \bar{q} S_{Ref} \\ C_Z \bar{q} S_{Ref} \end{bmatrix}_B \tag{2.36}$$

$$\left(\vec{M}^G_A\right)_B = \begin{bmatrix} M^G_{L,A} \\ M^G_{M,A} \\ M^G_{N,A} \end{bmatrix}_B = \begin{bmatrix} C_L \bar{q} S_{Ref} \bar{c} \\ C_M \bar{q} S_{Ref} \bar{c} \\ C_N \bar{q} S_{Ref} \bar{c} \end{bmatrix}_B \tag{2.37}$$

$$\bar{q} = \frac{\rho_{Air}}{2} \left[\left(V^G_{K,Abs}\right)^I_B \right]^2 \tag{2.38}$$

Following [148], the dimensionless aerodynamic coefficients C_i in (2.36) and (2.37) are nonlinear functions of the state variables, their time derivatives, and the control surface deflections, as indicated in Equation (2.39). The variables δ_L, δ_M, and δ_N denote the roll, pitch, and yaw control deflection of the interceptor. The analytic function which describes the relationship is unknown.

$$C_i = f\left\{ \left(u^G_K\right)^I_B, \left(v^G_K\right)^I_B, \left(w^G_K\right)^I_B, \left(p^{0B}_K\right)_B, \left(q^{0B}_K\right)_B, \left(r^{0B}_K\right)_B, \ldots, \delta_L, \delta_M, \delta_N \right\} \tag{2.39}$$

Under the assumption that the partial derivatives of the aerodynamic function are continuous and the disturbance values are small, (2.39) is expanded into a Taylor series in terms of the state variables and the control surface deflections. This approach is in line with [148]. The partial derivatives of the Taylor series represent specific aerodynamic effects and can be measured in wind tunnel tests or calculated, utilizing different methods, for a set of flight conditions which is representative for the flight envelope of the interceptor. Details on specific aerodynamic effects as well as their calculation are available in the seminal sources [114] and [115]. [59] and [105] provide an overview. The aerodynamic data set which is resulting from measurement or calculation consists of aerodynamic lookup tables for the respective aerodynamic derivatives, whose dimensions are determined by the number of independent variables considered during aerodynamic lookup table generation. The aerodynamic lookup tables are arranged in application rules, describing the build-up of the aerodynamic coefficients, and finally utilized in (2.36) and (2.37) to calculate the aerodynamic forces and moments acting on the interceptor.
The aerodynamic data set for the interceptor is generated by using the Missile DATCOM aerodynamic prediction tool which employs semi empiric formulas, following [8]. Thereafter, the generated results are post-processed to create a uniform structure of the application rules for

the aerodynamic derivatives. This leads to (2.40) and (2.41). All variables are specified in the body fixed frame.

$$\begin{aligned} C_X &= C_{X,0}\left(\alpha_K^G, \beta_K^G, M\right) + C_{X,Alt}\left(\alpha_K^G, \left(z^G\right)_I, M\right) \\ &\quad + C_{X,Base}\left(\alpha_K^G, \beta_K^G, M\right) \cdot k_{Prop} + C_{X,\delta_{Total}}\left(\alpha_K^G, \delta_{Total}, M\right) \cdot \delta_{Total} \\ &\quad + C_{X,p}\left(\alpha_K^G, \beta_K^G, M\right) \cdot p_K^{0B,*} + C_{X,q}\left(\alpha_K^G, \beta_K^G, M\right) \cdot q_K^{0B,*} + C_{X,r}\left(\alpha_K^G, \beta_K^G, M\right) \cdot r_K^{0B,*} \end{aligned} \tag{2.40}$$

$$\begin{aligned} C_i &= C_{i,0}\left(\alpha_K^G, \beta_K^G, M\right) \\ &\quad + C_{i,\delta_L}\left(\alpha_K^G, \beta_K^G, M\right) \cdot \delta_L + C_{i,\delta_M}\left(\alpha_K^G, \beta_K^G, M\right) \cdot \delta_M + C_{i,\delta_N}\left(\alpha_K^G, \beta_K^G, M\right) \cdot \delta_N \\ &\quad + C_{i,p}\left(\alpha_K^G, \beta_K^G, M\right) \cdot p_K^{0B,*} + C_{i,q}\left(\alpha_K^G, \beta_K^G, M\right) \cdot q_K^{0B,*} + C_{i,r}\left(\alpha_K^G, \beta_K^G, M\right) \cdot r_K^{0B,*} \end{aligned}$$

$$i = Y, Z, L, M, N \tag{2.41}$$

M denotes the Mach number. The aerodynamic derivative $C_{X,Base}\left(\alpha_K^G, \beta_K^G, M\right)$ represents the aerodynamic drag induced by propulsion. The factor k_{Prop} indicates the status of the single stage, solid propellant rocket motor of the interceptor. k_{Prop} is identical to either zero or one, whereupon $k_{Prop} = 1$ represents a burning rocket motor. The aerodynamic derivative $C_{X,\delta_{Total}}\left(\alpha_K^G, \delta_{Total}, M\right)$ is the aerodynamic drag resulting from the total control surface deflection δ_{Total}. δ_{Total} is calculated according to (2.42). Equation (2.43) states the formula for the respective total angle of attack α_{Total}. The normalized roll rate $p_K^{0B,*}$, the normalized pitch rate $q_K^{0B,*}$, and the normalized yaw rate $r_K^{0B,*}$ are given by (2.44) to (2.46).

$$\delta_{Total} = \sqrt{2} \cdot \left(\delta_M \frac{\left| \left(\alpha_K^G\right)_B^I \right|}{\alpha_{Total}} - \delta_N \frac{\left| \left(\beta_K^G\right)_B^I \right|}{\alpha_{Total}} \right) \tag{2.42}$$

$$\alpha_{Total} = \arccos\left(\frac{\left(u_K^G\right)_B^I}{\left(V_{K,Abs}^G\right)_B^I} \right) \tag{2.43}$$

$$p_K^{0B,*} = \frac{\left(p_K^{0B}\right)_B \bar{c}}{2\left(V_{K,Abs}^G\right)_B^I} \tag{2.44}$$

$$q_K^{0B,*} = \frac{\left(q_K^{0B}\right)_B \bar{c}}{2\left(V_{K,Abs}^G\right)_B^I} \tag{2.45}$$

$$r_K^{0B,*} = \frac{\left(r_K^{0B}\right)_B \bar{c}}{2\left(V_{K,Abs}^G\right)_B^I} \tag{2.46}$$

To further enhance the quality of the generated aerodynamic data, a modular set of aerodynamic data correction routines is applied. This modular set of routines has been developed during this work and employs a five step approach to derive a high quality set of aerodynamic data for a cruciform missile. The first step annihilates known deficits of Missile DATCOM. Based on the results presented in [1], the aerodynamic lookup tables $C_{X,0}\left(\alpha_K^G, \beta_K^G, M\right)$ are corrected. The following steps of the modular set factors in the symmetry of a cruciform missile. Following [148], a significant number of aerodynamic derivatives vanishes, because the X_B - Y_B and the X_B - Z_B

plane with respect to the body fixed frame constitute planes of symmetry. Hence, the second step erases all vanishing aerodynamic derivatives from the aerodynamic data set. The third step eliminates aerodynamic lookup table offsets. The zero crossing is enforced for all aerodynamic lookup tables which must exhibit the former for respective independent variables identical to zero. Thereafter, the symmetry of aerodynamic lookup tables is implemented in step four. The symmetry of a cruciform missile implies that a significant number of aerodynamic lookup tables must feature symmetry as well. $C_{Z,0}\left(\alpha_K^G, \beta_K^G, M\right)$, for example, is axially symmetric with respect to $\left(\beta_K^G\right)_B^I = 0\,[deg]$. The fifth and final step considers relationships between aerodynamic lookup tables which are based on the symmetry of a cruciform missile, e.g. $C_{Z,0}\left(\alpha_K^G, \beta_K^G, M\right) = C_{Y,0}^T\left(\alpha_K^G, \beta_K^G, M\right)$, and implements these relationships in the aerodynamic data set.
The application of the developed modular set of aerodynamic data correction routines to the aerodynamic data set of the interceptor leads to the application rules (2.47) to (2.52). These are specified in the body fixed frame.

$$\begin{aligned}
C_X &= C_{X,0}\left(\alpha_K^G, \beta_K^G, M\right) + C_{X,Alt}\left(\alpha_K^G, \left(z^G\right)_I, M\right) \\
&\quad + C_{X,Base}\left(\alpha_K^G, \beta_K^G, M\right) \cdot k_{Prop} + C_{X,\delta_{Total}}\left(\alpha_K^G, \delta_{Total}, M\right) \cdot \delta_{Total} && (2.47)\\
C_Y &= C_{Y,0}\left(\alpha_K^G, \beta_K^G, M\right) + C_{Y,r}\left(\alpha_K^G, \beta_K^G, M\right) \cdot r_K^{OB,*} + C_{Y,\delta_N}\left(\alpha_K^G, \beta_K^G, M\right) \cdot \delta_N && (2.48)\\
C_Z &= C_{Z,0}\left(\alpha_K^G, \beta_K^G, M\right) + C_{Z,q}\left(\alpha_K^G, \beta_K^G, M\right) \cdot q_K^{OB,*} + C_{Z,\delta_M}\left(\alpha_K^G, \beta_K^G, M\right) \cdot \delta_M && (2.49)\\
C_L &= C_{L,0}\left(\alpha_K^G, \beta_K^G, M\right) + C_{L,p}\left(\alpha_K^G, \beta_K^G, M\right) \cdot p_K^{OB,*} + C_{L,\delta_L}\left(\alpha_K^G, \beta_K^G, M\right) \cdot \delta_L && (2.50)\\
C_M &= C_{M,0}\left(\alpha_K^G, \beta_K^G, M\right) + C_{M,q}\left(\alpha_K^G, \beta_K^G, M\right) \cdot q_K^{OB,*} + C_{M,\delta_M}\left(\alpha_K^G, \beta_K^G, M\right) \cdot \delta_M && (2.51)\\
C_N &= C_{N,0}\left(\alpha_K^G, \beta_K^G, M\right) + C_{N,r}\left(\alpha_K^G, \beta_K^G, M\right) \cdot r_K^{OB,*} + C_{N,\delta_N}\left(\alpha_K^G, \beta_K^G, M\right) \cdot \delta_N && (2.52)
\end{aligned}$$

The derived high quality aerodynamic data set described by the beforehand provided equations constitutes the foundation for the development of the interceptor flight control system. Appendix C illustrates the content of this aerodynamic data set for the interceptor flight condition $\left(V_{K,Abs}^G\right)_B^I = 600\,[m/s]$ and $\left(z^G\right)_I = 10000\,[m]$. Later, this high quality aerodynamic data set is charged with specified uncertainties to test and evaluate the designed interceptor flight control system.

2.3.3 Propulsion

As introduced in Section 2.1, the interceptor is propelled by a single stage, solid propellant rocket motor. It is assumed that the rocket motor is aligned with the X_B axis of the body fixed frame. This implies that the thrust force acting on the center of gravity of the interceptor which is generated by the single stage, solid propellant rocket motor points in the direction of the positive X_B axis. Neither thrust forces in the direction of the remaining axis of the body fixed frame nor moments with respect to the center of gravity of the interceptor arising from propulsion are considered. Hence, the propulsion force acting on the center of gravity of the interceptor is given by (2.53).

$$\left(\vec{F}_P^G\right)_B = \begin{bmatrix} F_{X,P}^G \\ F_{Y,P}^G \\ F_{Z,P}^G \end{bmatrix}_B = \begin{bmatrix} F_{Thrust,Abs} \\ 0 \\ 0 \end{bmatrix}_B \qquad (2.53)$$

The modeling of the single stage, solid propellant rocket motor in this thesis allows the implementation of a thrust profile for the generated thrust force $F_{Thrust,Abs}$. Considering standard single stage, solid propellant rocket motors, a thrust profile exhibits an ignition phase, a boost

phase with highly increasing thrust, a burn phase with approximately constant thrust, and a burnout phase with constantly decreasing thrust. Additionally, constant $F_{Thrust,Abs}$, including zero, are available in the simulation. This provides the capability to examine dedicated flight conditions, including the situation after burnout of the single stage, solid propellant rocket motor.

2.3.4 Reaction jet forces and moments

The fourth external effort acting on the interceptor is the force generated by the reaction jet actuator section. The contained reaction jet cartridges each constitute a small, solid propellant rocket motor which generates a thrust force while burning. Based on the fact that the reaction jet actuator section is located ahead of the center of gravity of the interceptor, a lever arm between the individually generated thrust force of the reaction jet cartridges and the center of gravity of the interceptor exists. Hence, the reaction jet cartridges give rise to moments with respect to the center of gravity of the interceptor.
Considering the interceptor geometry according to Section 2.1, it is assumed that the reaction jet cartridges are mounted perpendicular to the X_B axis. Denoting the thrust force of an individual reaction jet cartridge as $F_{RJC,Abs}$, the force of the reaction jet actuator section acting on the center of gravity of the interceptor, specified in the body fixed frame, is given by (2.54).

$$\left(\vec{F}^{G}_{RJC}\right)_B = \begin{bmatrix} F^{G}_{X,RJC} \\ F^{G}_{Y,RJC} \\ F^{G}_{Z,RJC} \end{bmatrix}_B = \begin{bmatrix} 0 \\ \sum\limits_{i=1}^{36}\sum\limits_{j=1}^{5} \left\{ F_{RJC,Abs,ij} \sin\left(\varphi_i^{RJC}\right) \delta_{RJC,ij} \right\} \\ \sum\limits_{i=1}^{36}\sum\limits_{j=1}^{5} \left\{ -F_{RJC,Abs,ij} \cos\left(\varphi_i^{RJC}\right) \delta_{RJC,ij} \right\} \end{bmatrix}_B \tag{2.54}$$

The indices i and j in (2.54) identify the individual reaction jet cartridges. The index i represents the reaction jet cartridge attitude according to (2.4) and is identical to the index of the respective vector element. The index j reflects the number of an individual cartridge in a reaction jet cartridge column and is identical to the column index of the reaction jet cartridge position matrix (2.3). The reaction jet cartridge deflection operator δ_{RJC} represents the status of an individual cartridge.
Assuming that the individual reaction jet cartridge thrust vectors intersect with the X_B axis, which implies that the reaction jet actuator section does not generate a roll moment, the moment with respect to the center of gravity of the interceptor, specified in the body fixed frame, is calculated according to (2.55).

$$\left(\vec{M}^{G}_{RJC}\right)_B = \begin{bmatrix} M^{G}_{L,RJC} \\ M^{G}_{M,RJC} \\ M^{G}_{N,RJC} \end{bmatrix}_B = \begin{bmatrix} 0 \\ \sum\limits_{i=1}^{36}\sum\limits_{j=1}^{5} \left\{ F_{RJC,Abs,ij} \cos\left(\varphi_i^{RJC}\right) \left(x_j^{RJC} - x^{G}\right) \delta_{RJC,ij} \right\} \\ \sum\limits_{i=1}^{36}\sum\limits_{j=1}^{5} \left\{ F_{RJC,Abs,ij} \sin\left(\varphi_i^{RJC}\right) \left(x_j^{RJC} - x^{G}\right) \delta_{RJC,ij} \right\} \end{bmatrix}_B \tag{2.55}$$

2.4 Interceptor subsystems

2.4.1 Aerodynamic actuator

While the preceding section illustrated the calculation of the external efforts acting on the interceptor for the nonlinear rigid body equation of motions, the following section concentrates

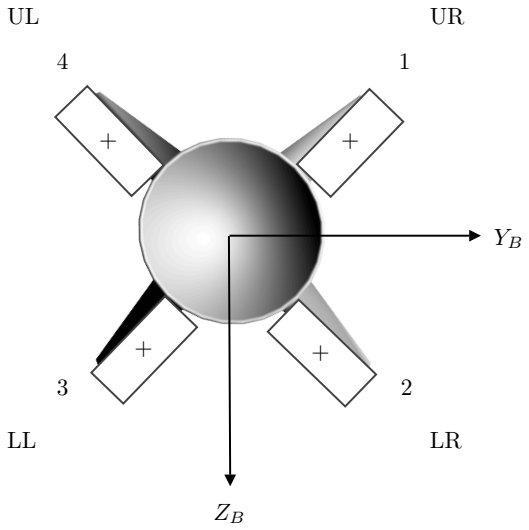

Figure 2.2: Aerodynamic control surface arrangement, denotation, and deflection convention

on the interceptor subsystems modeled in this work. The properties and capabilities of the modeled interceptor subsystems, which in the last resort influence the external efforts acting on the interceptor, are presented. The aerodynamic actuator, the reaction jet actuator, and the internal sensor system are considered. All other subsystems of the interceptor, being an integral part of the latter according to Section 2.1, are neglected herein.
The aerodynamic actuator of the interceptor is comprised of four rectangular shaped aerodynamic control surfaces. These are arranged in a cruciform configuration. Figure 2.2 utilizes an interceptor rear view to illustrate the control surface arrangement as well as the control surface denotation and deflection convention which is used in this work.
Based on the fact that the interceptor exhibits three rotational degrees of freedom, addressed by the interceptor flight control system via the roll deflection command $\delta_{L,Cmd}$, the pitch deflection command $\delta_{M,Cmd}$, and the yaw deflection command $\delta_{N,Cmd}$, but four control surfaces exist, a mapping from the deflection commands to the specific control surface deflection commands is necessary. This mapping blends $\delta_{L,Cmd}$, $\delta_{M,Cmd}$, and $\delta_{N,Cmd}$ into individual control surface deflection commands. In accordance with [148], this mapping is given by (2.56).

$$\begin{bmatrix} \delta_{UR,Cmd} \\ \delta_{LR,Cmd} \\ \delta_{LL,Cmd} \\ \delta_{UL,Cmd} \end{bmatrix} = \begin{bmatrix} -1 & 1 & -1 \\ -1 & 1 & 1 \\ 1 & 1 & -1 \\ 1 & 1 & 1 \end{bmatrix} \cdot \begin{bmatrix} \delta_{L,Cmd} \\ \delta_{M,Cmd} \\ \delta_{N,Cmd} \end{bmatrix} \tag{2.56}$$

The calculated individual control surface deflection commands are forwarded to the actuator modules. The dynamics of the individual control surface actuator modules are modeled as second order, linear time invariant systems. To further enhance the representation the dynamics of the actuator modules, the second order, linear time invariant systems are augmented by two memoryless nonlinearities. Details on such nonlinearities are available in [66] and [122]. The integration of the individual control surface velocity $\dot{\delta}_i$ is limited according to (2.57). The integrators for the control surface positions δ_i in the actuator modules are also confined. (2.58)

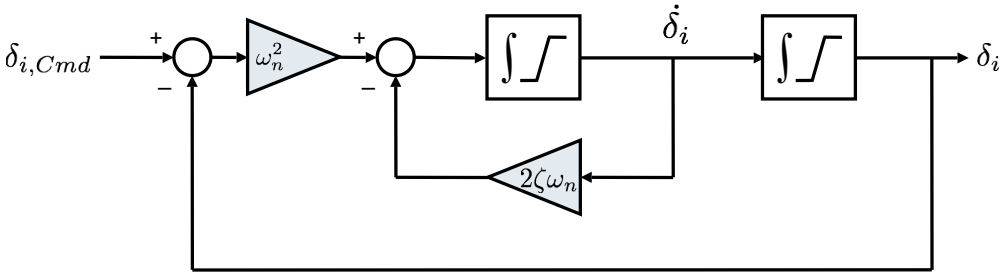

Figure 2.3: Actuator module block diagram

provides the respective bound.

$$\left|\dot{\delta}_i\right| \leq 360\,[deg/s] \tag{2.57}$$

$$|\delta_i| \leq 45\,[deg] \tag{2.58}$$

$$i = UR, LR, LL, UL$$

Figure 2.3 displays the block diagram of the individually implemented control surface actuator modules. The natural frequency ω_n of the four actuator modules is chosen as $\omega_n = 20\,[rad/s]$. The damping coefficient of the actuator modules is set to $\zeta = 1$.
The particular control surface deflections δ_i which constitute the outputs of the actuator modules are composed to the three control surface deflections δ_L, δ_M, and δ_N afterwards. δ_L, δ_M, and δ_N are inputs for the application rules (2.47) to (2.52). The composition is available from [148] and stated in (2.59).

$$\begin{bmatrix}\delta_L\\ \delta_M\\ \delta_N\end{bmatrix} = 0.25 \begin{bmatrix}-1 & -1 & 1 & 1\\ 1 & 1 & 1 & 1\\ -1 & 1 & -1 & 1\end{bmatrix} \cdot \begin{bmatrix}\delta_{UR}\\ \delta_{LR}\\ \delta_{LL}\\ \delta_{UL}\end{bmatrix} \tag{2.59}$$

2.4.2 Reaction jet actuator

The reaction jet actuator houses 180 reaction jet cartridges. They are geometrically composed according to Section 2.1. Each reaction jet cartridge constitutes a small, solid propellant rocket motor which can be utilized once during the flight of the interceptor. The firing of individual reaction jet cartridges as well as the simultaneous use of multiple reaction jet cartridges is possible. The maximum number of reaction jet cartridges available for simultaneous firing is limited according to (2.60).

$$\delta_{RJC} \leq 3 \tag{2.60}$$

Besides their position in the interceptor fuselage and their attitude, all 180 reaction jet cartridges exhibit identical properties. The main characteristic of the reaction jet cartridges is the reaction jet cartridge thrust profile. It describes the development of the thrust force $F_{RJC,Abs}$ which is generated by an individual reaction jet cartridge over the cartridge burn time $t_{RJC,Burn}$. Performance details, like the reaction jet cartridge fuze delay or the maximum reaction jet cartridge thrust force, can be identified in the reaction jet cartridge thrust profile. A generic reaction jet cartridge thrust profile is developed for this thesis. Figure 2.4 shows this reaction jet cartridge thrust profile.
All reaction jet cartridges are implemented separately in the interceptor model, whereupon the

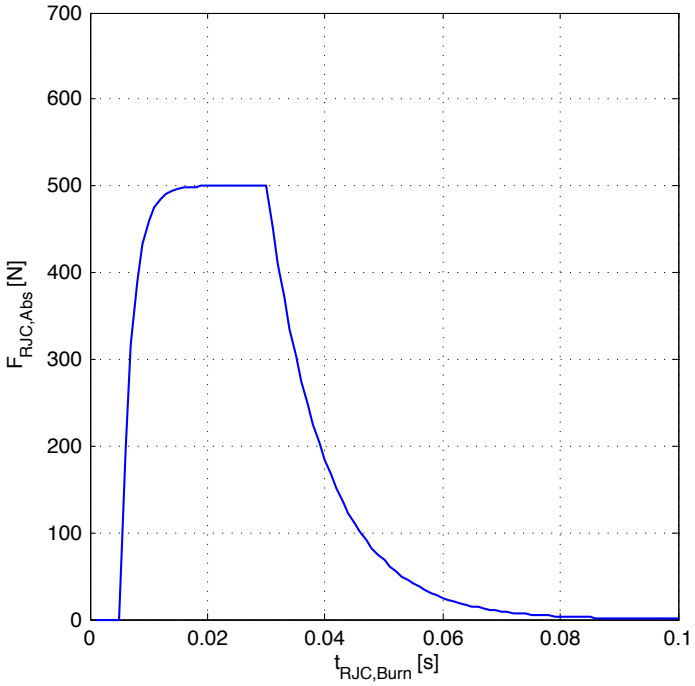

Figure 2.4: Reaction jet cartridge thrust profile

respective positions, attitudes, and the reaction jet cartridge thrust profile are considered. The individual reaction jet cartridge subsystems are triggered by a reaction jet cartridge deflection operator δ_{RJC}, being either identical to 0 or 1. Prior to firing, $\delta_{RJC} = 0$ for the respective reaction jet cartridges. Hence, the latter do not contribute to the forces and moments calculation in (2.54) and (2.55). By setting $\delta_{RJC} = 1$ for particular reaction jet cartridges, these subsystems generate the reaction jet cartridge thrust profile displayed in Figure 2.4. The profile itself is stored in a lookup table, using $t_{RJC,Burn}$ as input and providing $F_{RJC,Abs}$ as output. External efforts acting on the interceptor result. After $t_{RJC,Burn}$ is elapsed, the thrust force of the particular reaction jet cartridges is set to $F_{RJC,Abs} = 0$. The contribution to (2.54) and (2.55) is annihilated. At the same time, the remaining, unchanged reaction jet cartridge deflection operators $\delta_{RJC} = 1$ indicate which particular cartridges are already consumed.

2.4.3 Internal sensor system

The third interceptor subsystem which is considered, modeled, and presented in this work is the internal sensor system. It consists of an inertial measurement unit and additional sensors. The inertial measurement unit measures a part of the state vector of the interceptor. The additional sensors provide signals that are not part of the state vector. All measurements are forwarded to the interceptor flight control system. This functionality is not especially related to the interceptor or the internal sensor system. It constitutes the reason for an internal sensor system being an integral part of every aerospace system. Hence, an internal sensor system is accounted for. The study of [7], [9], [15], [22], [141], and [148] in conjunction with [89] and [129] leads to the following two conclusions concerning the measurement of signals in aerospace systems. An internal sensor system constitutes a complex system, which requires a detailed modeling, if all contained subsystems are considered adequately. Vice versa, all measured signals, including that of an internal sensor system, are affected by common measurement effects. These effects are mea-

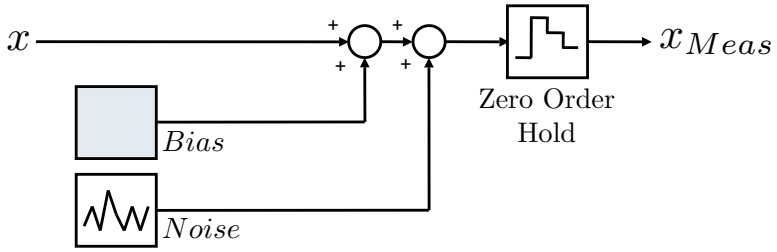

Figure 2.5: Measurement effect implementation

surement bias, measurement noise, and discretization. Measurement bias denotes a systematic displacement of the measured signal from the real signal. With respect to an internal sensor system, measurement bias could arise from an angular displacement of the inertial measurement unit axis from the body fixed frame of the vehicle. Measurement noise is caused by the random noise omnipresent in all signals. Hence, it exists in an internal sensor system. Discretization describes the effect that signals are measurable at distinct time instances only. Although the time between two measurement instances can be very small, measured signals are affected by discretization. Envisioning the two described conclusions and focussing on the main topic of this work, the design of the interceptor flight control system, it is decided not to model the internal sensor system, but to account for the three measurement effects.
Proceeding from the beforehand decision, it is assumed that the inertial measurement unit is located at the center of gravity of the interceptor, implying that no effects originating from a displacement of the inertial measurement unit, illustrated in [9], are considered. Furthermore, it is presumed that the inertial measurement unit is capable to measure the inertial accelerations of the center of gravity of the interceptor, specified in the body fixed frame, $\left(\vec{a}^{\,G}\right)_B^{II}$ and the rotation vector with respect to the body fixed frame, specified in the body fixed frame, $\left(\vec{\omega}_K^{0B}\right)_B$. $\left(\vec{\omega}_K^{0B}\right)_B$ is considered to be integrated inside the inertial measurement unit to derive the Euler angles. The Euler angles are supposed to be utilized to calculate the inertial accelerations of the center of gravity of the interceptor, specified in the body fixed frame, without gravity $\left(\vec{a}^{\,G}\right)_{B,woG}^{II}$, which are provided to the interceptor flight control system. The individual aerodynamic control surface deflections δ_i, the individual aerodynamic control surface velocities $\dot{\delta}_i$, and the statuses of the particular reaction jet cartridges are assumed to be measured by additional sensors.
To factor in the common measurement effects, a subsystem which implements latter is employed for each measured signal. This subsystem adds a measurement bias and measurement noise to the signals, whereupon the measurement bias, the measurement noise power, and the measurement noise sampling rate are configurable. Afterwards, the signals are digitized with an adjustable sampling rate. The output of the discretization constitutes the measured signal which is forwarded to the interceptor flight control system. Figure 2.5 shows the block diagram of the measurement effect implementation subsystem.

2.5 Modeling of parameter uncertainties

2.5.1 Uncertain constant parameters

The beforehand presented sections of Chapter 2 illustrated the interceptor layout and introduced the properties of the interceptor. Thereafter, the nonlinear rigid body equations of motion have been affiliated. The presentation of the modeling of the external efforts acting on the interceptor followed. Finally, the interceptor subsystems which are considered in this work

have been illustrated, including their respective properties. Although the derivations and the modeling consider a significant level of detail, the dynamics of the interceptor simulation model differ from the dynamics a real interceptor system. There are five reasons for this difference in the dynamical behavior.

The first reason for differences in the dynamics of the interceptor simulation model and that of a real interceptor system are simplifications. These have been introduced at dedicated points of the modeling process and allow to simplify the structure of the interceptor simulation model and to concentrate on the focus of this work. The consideration of a flat earth representation with an embedded, fixed coordinate frame as inertial reference frame constitutes a simplification. All introduced simplifications are explicitly stated in this work.

Second reason for a different dynamical behavior between the interceptor simulation model and a real interceptor system are unknown or not modeled dynamics. The interceptor, like any dynamical system, exhibits dynamics which are either unknown or feature a level of complexity that makes modeling impossible or at least significantly increases the required modeling effort. Structural modes are an example for this type of dynamics. Although structural modes of the interceptor as well as of its subsystems exist, they are not accounted for in this thesis, because their properties can not be determined terminatory.

Model uncertainties constitute the third reason for behavioral differences between the interceptor simulation model and a real interceptor system. Model uncertainties comprise effects which are reflected in the simulation model, but the dynamic order of the representation in the simulation model is not in line with the dynamic order of the real system. The size and the amount of the model uncertainties constitute an important factor for the behavioral difference between a simulation model and the respective real system. The aerodynamic control surface actuator modules are an example for model uncertainties in this work . These modules are considered as second order, linear systems, whereas real aerodynamic control surface actuator modules are systems of higher order.

The fourth and the fifth reason, which generate differences in the dynamics of the the interceptor simulation model and that of a real interceptor system, are uncertain constant parameters and time-varying parameters. These types of uncertainties are explicitly implemented in the interceptor simulation model, and are treated in detail in the following.

Uncertain constant parameters are properties of the interceptor which are represented correctly in the interceptor simulation model concerning their physical impact. On the other hand, the values of these properties which are used in the interceptor simulation model are not correct, because the true values are either unknown or not measurable during the flight of the interceptor. As the denotation uncertain constant parameters indicates, these properties are constant or at least vary so slow with time, compared to the states of the interceptor, that they are treated as quasi constant. Usually, there exists a value or a function which defines the nominal behavior for each uncertain constant parameter. The difference between the nominal behavior and the real behavior constitutes the uncertainty for the respective property.

The total interceptor mass m_{Empty} and the inertia tensor with respect to the center of gravity of the interceptor $(I^G_{Empty})_{BB}$ are considered as uncertain constant parameters in this thesis. (2.61) is utilized to implement uncertainty for m_{Empty} and $(I^G_{Empty})_{BB}$ in the interceptor simulation model before the beginning of the simulation. r is a random number in the interval $r \in (0; 1)$. Δp specifies the level of uncertainty that is taken into account for the respective property, expressed as a percentage. After the implementation of the uncertainty, the values of the properties are held constant during the simulated flight of the interceptor.

$$p_{Uncertain} = (2\,(r - 0.5)\,\Delta p + 1)\,p_{Nominal} \tag{2.61}$$

The implementation via (2.61) allows to examine the interceptor flight control system performance under various uncertain constant parameter conditions.

2.5.2 Time-varying parameters

The second type of uncertainty which is explicitly incorporated in this work and implemented in the interceptor simulation model are time-varying parameters. Time-varying parameters also constitute properties of the interceptor that are represented correctly in the interceptor simulation model concerning their physical impact. Unlike uncertain constant parameters, these properties are subject to permanent change. Although nominal values for the time-varying parameters exist, the determination of the exact, current values of these properties during system operation is impossible.
The aerodynamic derivatives, given by the application rules (2.47) to (2.52), are considered as time-varying parameters in this thesis. This is based on the understanding of wind and turbulence as stochastic processes which distract the aerodynamic derivatives from their nominal values permanently. The implementation of the aerodynamic derivatives as time-varying parameters is done via (2.62). $C_{i,Nominal}$ constitutes the nominal value of the aerodynamic derivative which is derived from the implemented lookup table. ΔC_i specifies the level of uncertainty for the aerodynamic derivative percentage-wise. n denotes a random noise with a mean identical to zero and a variance equal to one. The sample rate of the random noise is configurable to account for different frequencies of parameter changes. In contrast to the implementation of the uncertain constant parameters, (2.62) is employed permanently during the simulated flight of the interceptor. Hence, the aerodynamic derivatives of the interceptor change at the predefined sample rate, if $\Delta C_i \neq 0$.

$$C_{i,Uncertain} = (n\Delta C_i + 1)\, C_{i,Nominal} \tag{2.62}$$

Like (2.61), Equation (2.62) provides the capability to examine the interceptor flight control system under arbitrary parameter conditions.

Chapter 3

Analysis of interceptor flight dynamics

3.1 Trim

The developed simulation model of the endo-atmospheric dual-actuator interceptor constitutes the basis for the following analysis, design, and validation. Induced by the complexity of the interceptor simulation model, numerical methods are utilized for these steps. These methods allow the use of computer systems to find appropriate solutions. Effectivity and efficiency for the analysis, design, and validation is achieved, if the routines which are employed on the computer systems feature a high degree of automation and provide a high degree of reusability. Hence, the latter two characteristics become secondary aims of this work. They are accounted for starting with this chapter.
Before the interceptor flight control system is designed, the flight dynamics of the interceptor are analyzed in detail. The achieved results support the design of the interceptor flight control system. The analysis of the interceptor flight dynamics is carried out in two steps. First, trim calculations are conducted. They provide insight into the interceptor flight performance capabilities. The trim results for steady-state flight conditions are linearized in the second step to investigate the uncontrolled as well as the controlled interceptor dynamics, and derive an assessment about the stability properties of the interceptor. Thereafter, the nonlinear simulation framework which is employed is introduced at the end of Chapter 3. These process steps follow the illustration in [46].
As first step in the analysis of the interceptor flight dynamics, steady-state flight conditions of the interceptor are determined by trim calculations. Although multiple steady-state as well as quasi steady-state flight conditions exist, which are treated in [17] and [48] in detail, only the steady-state horizontal flight of the interceptor is considered, because all other flight conditions are not of importance for this work. The calculated conditions for steady-state horizontal flight of the interceptor are used to explore the interceptor flight envelope. Additionally, these conditions are the input for the linearization afterwards. According to linear system theory, available in [81], the results of a linearization are only valid, if the considered system operates at a steady-state reference point. The flight of the interceptor with a constant load factor is also treated herein, because it is accessible via trim calculations and allows to derive the interceptor maneuver capabilities. This flight condition is not used for linearization afterwards, because the rate of change of the states of the interceptor is to high. The flight of the interceptor with a constant load factor neither constitutes a steady-state nor quasi steady-state flight condition. To conduct the trim calculations for the steady-state horizontal flight of the interceptor and the

flight of the interceptor with a constant load factor a methodology based on [48] is introduced and employed in the following.

Trim calculation methodology
Steady-state flight conditions of the interceptor are characterized by a unique set of values for the state variables and the control inputs of the interceptor. Hence, the trim calculations need to determine the state vector $\vec{x}$ and control input vector $\vec{u}$ of the interceptor which result in the desired steady-state flight condition. Understanding the desired steady-state flight condition as a set of conditions for the derivatives of the state variables, (3.1) needs to be solved for $\vec{x}$ and $\vec{u}$ to find the appropriate solution.

$$\dot{\vec{x}}_{Desired} = f\left(\vec{x}, \vec{u}\right) \tag{3.1}$$

The problem of finding the correct combination of state and input variable values for the desired steady-state flight condition of the interceptor is formulated as a system of nonlinear equations. This system of nonlinear equations is generated by defining the difference between the derivative of the state vector and the conditions for the desired steady-state flight condition as residual vector $\vec{r}$. (3.2) states the respective relationship. By solving the system of nonlinear equations, meaning $\vec{x}$ and $\vec{u}$ are determined in a way that $\vec{r}$ is identical to zero, the solution to the trim calculation is derived.

$$\begin{aligned} \vec{r} &= \dot{\vec{x}} - \dot{\vec{x}}_{Desired} \\ &= f\left(\vec{x}, \vec{u}\right) - \dot{\vec{x}}_{Desired} = 0 \end{aligned} \tag{3.2}$$

Due to the fact that the some of the states of the interceptor are not of concern for a desired steady-state flight condition and can take arbitrary values, no unique solution for (3.2) exists. This problem is overcome by mapping $\vec{x}$ and $\vec{u}$ of the interceptor into a flight condition parameter vector $\vec{p}$ and a solver parameter vector $\vec{x}_S$ for the trim calculation. $\vec{p}$ contains constant parameters which unambiguously determine the desired steady-state flight condition. On the other hand, the elements of $\vec{x}_S$ are calculated in a way that $\vec{r}$ is identical to zero. A numeric solver routine is employed for this calculation. By ensuring (3.3), a unique solution of (3.2) is guaranteed. The mapping also allows to implement parts of the solution of the trim problem which are available analytically.

$$\dim \vec{x}_S = \dim \vec{r} \tag{3.3}$$

Following the denotation in [46], the mapping of $\vec{x}$ and $\vec{u}$ into $\vec{p}$ and $\vec{x}_S$ is called trim template. Implementing the trim template into (3.2) leads to (3.4).

$$\vec{r} = f\left(\vec{p}, \vec{x}_S\right) = 0 \tag{3.4}$$

The trim calculation architecture resulting from the introduction of the trim template is illustrated in Figure 3.1. It displays the relationship between the $\vec{p}$, $\vec{x}_S$, $\vec{x}$, $\vec{u}$, and $\vec{r}$. As one might anticipate from Figure 3.1, this trim calculation architecture, which is integral part of the chosen trim calculation methodology, provides a high degree of reusability. The trim routine is applicable to all trim calculations. Only the trim templates are designed for the individual considered flight conditions. Therefore, two trim templates are necessary in this thesis to cover the steady-state horizontal flight of the interceptor and the flight of the interceptor with a constant load factor.
A detailed treatment of the utilized trim calculation methodology and the derivation of the trim template is available in [49], [50], and [51].

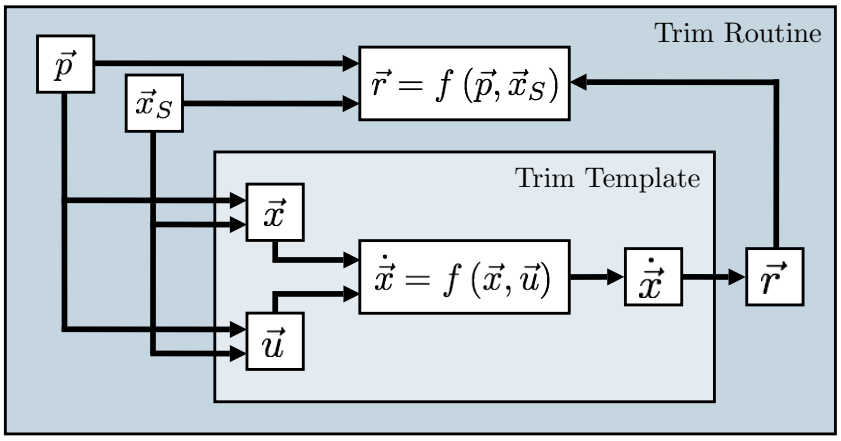

Figure 3.1: Trim calculation architecture

Steady-state horizontal flight

The trim calculation for the steady-state horizontal flight of the interceptor is treated in detail in the following. First, the trim template is derived. Afterwards, results of the trim calculation are presented.

Considering the nonlinear rigid body equations of motion, while at the same time neglecting the dynamics of the aerodynamic control surface actuator modules, $\vec{x}$ comprises twelve states. Accounting for δ_L, δ_M, and δ_N as well as the individual reaction jet cartridges, the interceptor exhibits 183 inputs. Envisioning that the individual cartridges of the reaction jet actuator section can only be used once during the flight of the interceptor, it is presumed that the latter section is not employed during steady-state flight conditions. Hence, $\vec{u}$ contains three inputs, leading to a sum of state variables and inputs equal to 15. On the other hand, the steady-state horizontal flight of the interceptor is defined by nine conditions. These conditions are given by (3.5) to (3.8), whereupon they are grouped following the derivation of the nonlinear rigid body equations of motion in Chapter 2.

$$\left(\dot{v}_K^G\right)_B^{IB} = \left(\dot{w}_K^G\right)_B^{IB} = 0 \tag{3.5}$$

$$\left(\dot{p}_K^{0B}\right)_B^B = \left(\dot{q}_K^{0B}\right)_B^B = \left(\dot{r}_K^{0B}\right)_B^B = 0 \tag{3.6}$$

$$\dot{\Phi} = \dot{\Theta} = \dot{\Psi} = 0 \tag{3.7}$$

$$\left(\dot{z}^G\right)_I = 0 \tag{3.8}$$

The number of conditions defining the steady-state horizontal flight of the interceptor implies that six variables out of $\vec{x}$ and $\vec{u}$ are treated as flight condition parameters, to guarantee a unique solution of (3.2). Because $\left(x^G\right)_I$ and $\left(y^G\right)_I$ have no influence on the steady-state horizontal flight of the interceptor, both states are defined identical to zero. Additionally, the heading angle Ψ has no influence on the steady-state horizontal flight. By setting $\Psi = 0\,[deg]$, the number of flight condition parameters reduces to three. The velocity of the center of gravity of the interceptor in the direction of the X_B axis $\left(u_K^G\right)_B^I$, the altitude of the center of gravity of the interceptor $\left(z^G\right)_I$, and the roll angle of the interceptor Φ are chosen as elements of $\vec{p}$. This choice leads to $\vec{x}_S$ according to (3.9).

$$\vec{x}_S = \begin{bmatrix} \left(v_K^G\right)_B^I & \left(w_K^G\right)_B^I & \left(p_K^{0B}\right)_B & \left(q_K^{0B}\right)_B & \left(r_K^{0B}\right)_B & \Theta & \delta_L & \delta_M & \delta_N \end{bmatrix}^T \tag{3.9}$$

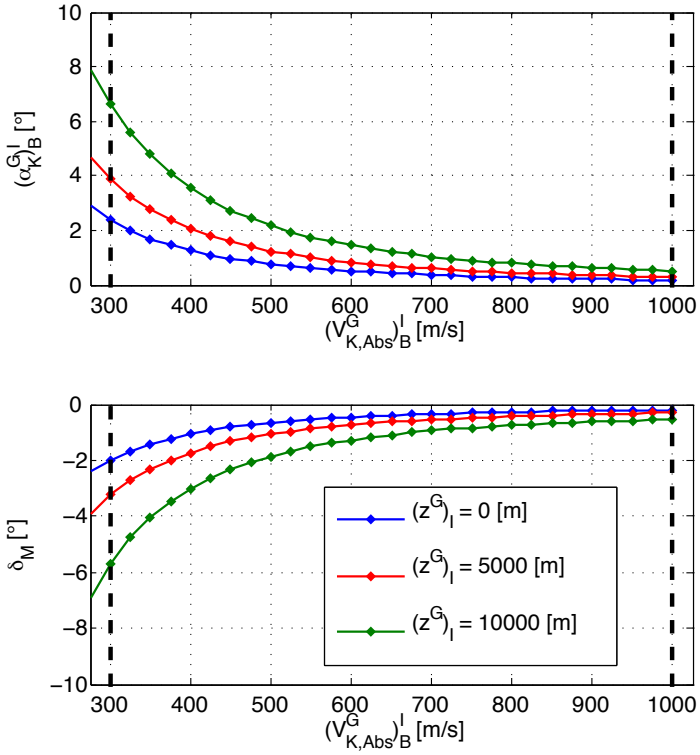

Figure 3.2: Trim calculation result steady-state horizontal flight

Although the choice of the elements of $\vec{p}$ in combination with (3.9) already constitutes the trim template for the steady-state horizontal flight of the interceptor, the system of nonlinear equations is further simplified. Noticing that during steady-state horizontal flight $\left(p_K^{0B}\right)_B$, $\left(q_K^{0B}\right)_B$, and $\left(r_K^{0B}\right)_B$ are identical to zero and considering (2.22), it is evident that the conditions (3.7) are satisfied automatically and need not to be solved. The number of elements in $\vec{x}_S$ and $\vec{r}$ reduces to six and the final trim template for this flight condition of the interceptor is established.
Based on the derived trim template, (3.2) is solved numerically by employing a fixed step gradient method in the trim routine. This method demonstrates an appropriate performance and robustness for the trim calculations in this work. The result of the trim calculation for the steady-state horizontal flight of the interceptor is displayed in Figure 3.2, whereupon three exemplarily values for $\left(z^G\right)_I$ are illustrated. The blue line visualizes the trim calculation result for $\left(z^G\right)_I = 0\,[m]$, the red line represents $\left(z^G\right)_I = 5000\,[m]$, and the green line shows the result for $\left(z^G\right)_I = 10000\,[m]$. Absolute kinematic velocities of the interceptor below and above the indicated $(V^G_{K,Abs})^I_B$ are considered of no operational relevance with respect to the steady-state flight condition herein.
Besides the illustration of the trim calculation result according to Figure 3.2, the result for the steady-state horizontal flight of the interceptor is utilized to derive the interceptor flight envelope. The display of the latter is omitted at this point, because it is contained in the following presentation.

Flight with constant load factor
Following the scheme presented for the trim calculation of the steady-state horizontal flight, a trim template for the flight of the interceptor with a constant load factor is derived. This

derivation is presented in an abbreviated manner herein, to stay inside the scope of this thesis; details are available in [48]. The trim template and the trim routine are utilized to conduct trim calculations for the flight of the interceptor with a constant load factor. The result of this calculation allows to determine the interceptor flight envelope as well as the maneuver capabilities of the interceptor.
Starting from the nonlinear rigid body equations of motion and using the identical assumptions as during the derivation of the trim template for steady-state horizontal flight, the interceptor exhibits 15 states and inputs. The flight of the interceptor with a constant load factor, in this case meaning a steady-state pull-up maneuver, is described by the seven conditions (3.10) to (3.12).

$$\left(\dot{\alpha}_K^G\right)_B^{IB} = \left(\dot{\beta}_K^G\right)_B^{IB} = 0 \tag{3.10}$$

$$\left(\dot{p}_K^{0B}\right)_B^B = \left(\dot{q}_K^{0B}\right)_B^B = \left(\dot{r}_K^{0B}\right)_B^B = 0 \tag{3.11}$$

$$\dot{\Phi} = \dot{\Psi} = 0 \tag{3.12}$$

This number of conditions implies that eight elements out of $\vec{x}$ and $\vec{u}$ need to be considered as flight condition parameters in this case. As for the steady-state horizontal flight, $\left(x^G\right)_I$, $\left(y^G\right)_I$, and Ψ have no influence on the steady-state flight condition. Therefore, they are set to zero and the number of flight condition parameters decreases to five. Now, the scope is limited to symmetrical steady-state pull-up maneuvers, where $\Phi = 0\,[deg]$ holds; four flight condition parameters in $\vec{p}$ remain. The latter are $(V_{K,Abs}^G)_B^I$, $\left(z^G\right)_I$, $\left(q_K^{0B}\right)_B$, and the flight path angle of the interceptor γ. Using the presumption $\Phi = 0\,[deg]$ in conjunction with the fact that $\left(p_K^{0B}\right)_B$ and $\left(r_K^{0B}\right)_B$ are identical to zero during such maneuver in (2.22), it is obvious that (3.12) is fulfilled automatically. $\left(q_K^{0B}\right)_B$ is derived according to (3.13).

$$\left(q_K^{0B}\right)_B = \dot{\Theta} \tag{3.13}$$

This result leaves (3.14) as the final $\vec{x}_S$ for the steady-state pull-up maneuver of the interceptor. Based on (3.13), $\left(q_K^{0B}\right)_B$ is replaced by $\dot{\Theta}$ in $\vec{p}$.

$$\vec{x}_S = \begin{bmatrix} \left(\alpha_K^G\right)_B^I & \left(\beta_K^G\right)_B^I & \delta_L & \delta_M & \delta_N \end{bmatrix}^T \tag{3.14}$$

Because the appearance of $\dot{\Theta}$ in $\vec{p}$ is undesirable, a descriptive way to specify the flight condition of the interceptor is developed. Following [48], the lift L of the interceptor during the steady-state pull-up maneuver is given by (3.15).

$$L = m\left(V_{K,Abs}^G\right)_B^I \dot{\gamma} + mg\cos\gamma \tag{3.15}$$

By using the definition of n_Z, stated in (3.16), (3.15) is solved for $\dot{\gamma}$ as (3.17).

$$n_Z = \frac{L}{mg} \tag{3.16}$$

$$\dot{\gamma} = \frac{g}{\left(V_{K,Abs}^G\right)_B^I}\left[n_Z - \cos\gamma\right] \tag{3.17}$$

The derivative of the approximation (3.18), which is developed in [48] and is valid for $\Phi = 0\,[deg]$ and small $(\beta_K^G)_B^I$, both given in the assumed maneuver, is built as (3.19). (3.10) is used in this step.

$$\Theta = \gamma + \left(\alpha_K^G\right)_B^I \tag{3.18}$$

$$\dot{\Theta} = \dot{\gamma} \tag{3.19}$$

This achieved, (3.13), (3.17), and (3.19) are combined and $\left(q_K^{0B}\right)_B$ is replaced by the right hand side of (3.17) in $\vec{p}$. The steady-state pull-up maneuver of the interceptor is described by the flight condition parameters $(V_{K,Abs}^G)_B^I$, $\left(z^G\right)_I$, n_Z, and γ. $\vec{x}_S$ is given in (3.14).
The interceptor flight envelope is determined by validating the trim calculation result for the flight of the interceptor with a constant load factor against the aerodynamic control surface position limit defined in (2.58). Therefore, the individual results which are comprised in the trim calculation result for a range of $(V_{K,Abs}^G)_B^I$ and $\left(z^G\right)_I$ are validated against (2.58). If the calculated δ_i of a particular trim calculation result are below the aerodynamic control surface position limit, the interceptor is able to realize the particular $(V_{K,Abs}^G)_B^I$ and $\left(z^G\right)_I$. The continuum of all realizable $(V_{K,Abs}^G)_B^I$ and $\left(z^G\right)_I$ constitutes the interceptor flight envelope with respect to the boundary (2.58). By limiting the maneuvers of the interceptor to the X_B - Z_B plane, defining $\gamma = 0\,[deg]$, and considering $n_Z = 1\,[g]$, the interceptor flight envelope for steady-state horizontal flight is achieved again.
The employment the beforehand described method for different load factors n_z, including the limitation of the maneuvers of the interceptor to the X_B - Z_B plane and the consideration of $\gamma = 0\,[deg]$, leads to the maneuver capabilities of the interceptor. The continuum of all $(V_{K,Abs}^G)_B^I$ and $\left(z^G\right)_I$ which is realizable by the interceptor under consideration of (2.58) and a specific n_Z describes the flight envelope in which the interceptor is capable to conduct maneuvers up to the respective n_Z.
Figure 3.3 illustrates the interceptor flight envelope and the maneuver capabilities of the interceptor for a set of n_Z. It is evident from Figure 3.3 that the interceptor exhibits an enormous flight envelope regarding the boundary given by (2.58). The interceptor flight envelope ranges from $(V_{K,Abs}^G)_B^I = 100\,[m/s]$ to $(V_{K,Abs}^G)_B^I = 1000\,[m/s]$, being the maximum $(V_{K,Abs}^G)_B^I$ considered in this thesis. Above $(V_{K,Abs}^G)_B^I = 300\,[m/s]$, the interceptor flight envelope is limited by the maximum considered $\left(z^G\right)_I = 20000\,[m]$. Furthermore, it is obvious that the interceptor is capable to maneuver at considerable n_Z without reaching the aerodynamic control surface position limit.

3.2 Linearization

3.2.1 Linearization algorithm and implementation

Although intense research on nonlinear systems was conducted in the recent past, only a limited number of methodologies for the analysis and especially the prediction of the behavior of nonlinear systems exists. Furthermore, as it is stated in [46] based on [41], [66], [73], [76], [122], [125], and [142], no deterministic standard approach to derive the stability properties of nonlinear systems is available.
In contrast, a wide spectrum of methodologies for the analysis of linear systems exists. These rest on a wide theoretical foundation and their systematic application allows the determination of the stability properties of linear systems. [39], [61], [80], [81], [119], [135], and [136] provide an overview of latter methodologies.
Following [66] and [125], the approximation of a nonlinear system by its linearization is possible in a small neighborhood of a stationary operating point. Additionally, it is allowed to draw conclusions about the stability of the stationary operating point of the nonlinear system from the stability of the stationary operating point of the linear system, if dedicated conditions apply. Hence, the nonlinear dynamics of the interceptor are linearized at stationary operating points and analyzed with the available methodologies for linear systems afterwards. The linear longi-

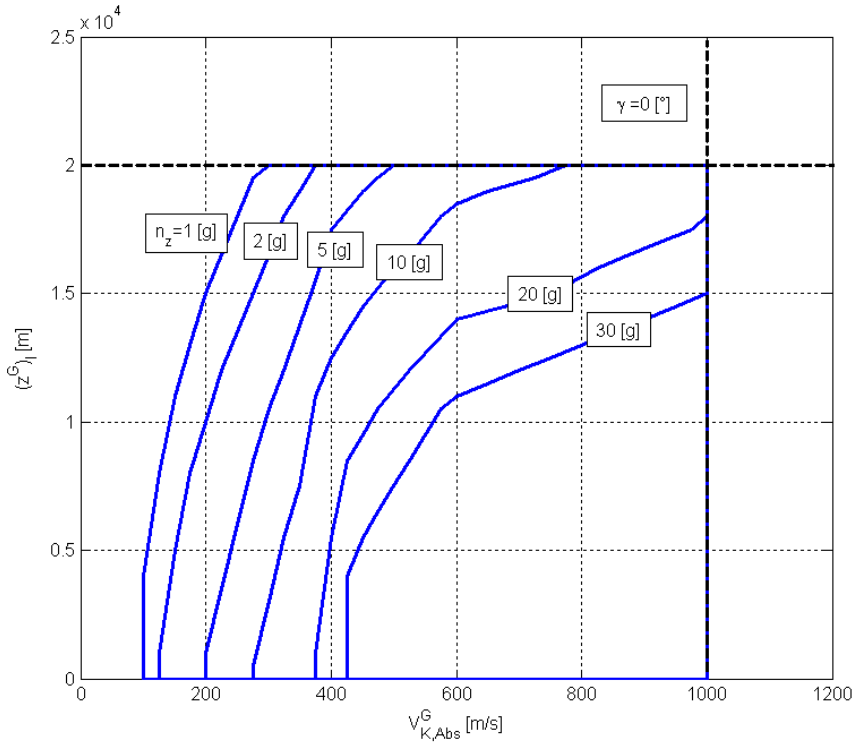

Figure 3.3: Interceptor flight envelope and maneuver capabilities

tudinal dynamics and the linear roll rate dynamics of the interceptor are analyzed separately. The results of this analysis support the design of the interceptor flight control system.
The abstract linearization algorithm which is employed origins from the presentation in [46] and [47]. [9] and [148], based on [36], provide an illustration explicitly related to nonlinear aerospace systems. These approaches are refused herein in favor for the more abstract algorithm. This allows the developed routines to be used again for other problems, while not being confined to aerospace applications. The stated aim of reusability of the products generated in the framework of this thesis is supported.
The nonlinear system considered for the linearization is given as a nonlinear, implicit differential equation and a nonlinear algebraic equation according to (3.20) and (3.21). The nonlinear, implicit differential equation contains the state equations, and the nonlinear algebraic equation comprises the output equations.

$$f\left(\dot{\vec{x}}, \vec{x}, \vec{u}\right) = 0 \tag{3.20}$$

$$y = h\left(\dot{\vec{x}}, \vec{x}, \vec{u}\right) \tag{3.21}$$

The nonlinear system exhibits n states, m inputs, and r outputs. Following [46], the linearization is carried out with respect to an operating point 0 which fulfills the nonlinear, implicit differential equation. Hence, (3.22) holds.

$$f\left(\dot{\vec{x}}_0, \vec{x}_0, \vec{u}_0\right) = 0 \tag{3.22}$$

First, the nonlinear system is developed into a Taylor series around 0. Denoting the perturbations from 0 according to (3.23) and the Jacobi-Matrices following the scheme of (3.24), the

nonlinear system is written as (3.25) and (3.26), whereupon the abbreviation $H.O.T.$ represents higher order terms.

$$\delta\dot{\vec{x}} = \dot{\vec{x}} - \dot{\vec{x}}_0 \qquad \delta\vec{x} = \vec{x} - \vec{x}_0 \qquad \delta\vec{u} = \vec{u} - \vec{u}_0 \qquad \delta\vec{y} = \vec{y} - \vec{y}_0 \tag{3.23}$$

$$\nabla_{\vec{x}} f\left(\dot{\vec{x}}, \vec{x}, \vec{u}\right) = \begin{bmatrix} \frac{\partial f_1}{\partial x_1} & \cdots & \frac{\partial f_1}{\partial x_n} \\ \vdots & \ddots & \vdots \\ \frac{\partial f_n}{\partial x_1} & \cdots & \frac{\partial f_n}{\partial x_n} \end{bmatrix}_{(\vec{x}=\vec{x}_0)} \tag{3.24}$$

$$f\left(\dot{\vec{x}}_0, \vec{x}_0, \vec{u}_0\right) + \nabla_{\dot{\vec{x}}} f\left(\dot{\vec{x}}, \vec{x}, \vec{u}\right) \delta\dot{\vec{x}} + \nabla_{\vec{x}} f\left(\dot{\vec{x}}, \vec{x}, \vec{u}\right) \delta\vec{x} + \nabla_{\vec{u}} f\left(\dot{\vec{x}}, \vec{x}, \vec{u}\right) \delta\vec{u} + H.O.T. = 0 \tag{3.25}$$

$$\vec{y}_0 + \delta\vec{y} = h\left(\dot{\vec{x}}_0, \vec{x}_0, \vec{u}_0\right) + \nabla_{\dot{\vec{x}}} h\left(\dot{\vec{x}}, \vec{x}, \vec{u}\right) \delta\dot{\vec{x}} + \nabla_{\vec{x}} h\left(\dot{\vec{x}}, \vec{x}, \vec{u}\right) \delta\vec{x} + \nabla_{\vec{u}} h\left(\dot{\vec{x}}, \vec{x}, \vec{u}\right) \delta\vec{u} + H.O.T. \tag{3.26}$$

The implementation of (3.22), the negligence of the higher order terms, and the rearrangement of the remaining terms lead to (3.27) and (3.28).

$$-\nabla_{\dot{\vec{x}}} f\left(\dot{\vec{x}}, \vec{x}, \vec{u}\right) \delta\dot{\vec{x}} = \nabla_{\vec{x}} f\left(\dot{\vec{x}}, \vec{x}, \vec{u}\right) \delta\vec{x} + \nabla_{\vec{u}} f\left(\dot{\vec{x}}, \vec{x}, \vec{u}\right) \delta\vec{u} \tag{3.27}$$

$$\delta\vec{y} = \nabla_{\dot{\vec{x}}} h\left(\dot{\vec{x}}, \vec{x}, \vec{u}\right) \delta\dot{\vec{x}} + \nabla_{\vec{x}} h\left(\dot{\vec{x}}, \vec{x}, \vec{u}\right) \delta\vec{x} + \nabla_{\vec{u}} h\left(\dot{\vec{x}}, \vec{x}, \vec{u}\right) \delta\vec{u} \tag{3.28}$$

Now, the Jacobi-Matrices in (3.27) and (3.28) are substituted according to (3.29). Solving the equations for $\delta\dot{\vec{x}}$ and $\delta\vec{y}$ leads to (3.30) and (3.31).

$$\begin{array}{lll} \tilde{E} = -\nabla_{\dot{\vec{x}}} f\left(\dot{\vec{x}}, \vec{x}, \vec{u}\right) & \tilde{A} = \nabla_{\vec{x}} f\left(\dot{\vec{x}}, \vec{x}, \vec{u}\right) & \tilde{B} = \nabla_{\vec{u}} f\left(\dot{\vec{x}}, \vec{x}, \vec{u}\right) \\ \tilde{H} = \nabla_{\dot{\vec{x}}} h\left(\dot{\vec{x}}, \vec{x}, \vec{u}\right) & \tilde{C} = \nabla_{\vec{x}} h\left(\dot{\vec{x}}, \vec{x}, \vec{u}\right) & \tilde{D} = \nabla_{\vec{u}} h\left(\dot{\vec{x}}, \vec{x}, \vec{u}\right) \end{array} \tag{3.29}$$

$$\delta\dot{\vec{x}} = \tilde{E}^{-1}\tilde{A}\delta\vec{x} + \tilde{E}^{-1}\tilde{B}\delta\vec{u} \tag{3.30}$$

$$\delta\vec{y} = \left[\tilde{H}\left(\tilde{E}^{-1}\tilde{A}\right) + \tilde{C}\right]\delta\vec{x} + \left[\tilde{H}\left(\tilde{E}^{-1}\tilde{B}\right) + \tilde{D}\right]\delta\vec{u} \tag{3.31}$$

Renaming the matrices in this equations according to the convention in (3.32) brings up the linear state space model given in (3.33) and (3.34). The linear state space model in vector notation is provided in (3.35). The vectors $\delta\dot{\vec{x}}$ and $\delta\vec{x}$ are of dimension $(n \times 1)$, $\delta\vec{u}$ is of dimension $(m \times 1)$, and $\delta\vec{y}$ is of dimension $(r \times 1)$. The matrix A exhibits the dimension $(n \times n)$, B $(n \times m)$, C $(r \times n)$, and D is of dimension $(r \times m)$.

$$\begin{array}{ll} A = \tilde{E}^{-1}\tilde{A} & B = \tilde{E}^{-1}\tilde{B} \\ C = \tilde{H}\left(\tilde{E}^{-1}\tilde{A}\right) + \tilde{C} & D = \tilde{H}\left(\tilde{E}^{-1}\tilde{B}\right) + \tilde{D} \end{array} \tag{3.32}$$

$$\delta\dot{\vec{x}} = A\delta\vec{x} + B\delta\vec{u} \tag{3.33}$$

$$\delta\vec{y} = C\delta\vec{x} + D\delta\vec{u} \tag{3.34}$$

$$\begin{bmatrix} \delta\dot{\vec{x}} \\ \delta\vec{y} \end{bmatrix} = \begin{bmatrix} A & B \\ C & D \end{bmatrix} \cdot \begin{bmatrix} \delta\vec{x} \\ \delta\vec{u} \end{bmatrix} \tag{3.35}$$

The presented abstract linearization algorithm is realized as a linearization routine which utilizes the trim calculation result for the steady-state horizontal flight of the interceptor as well as the interceptor simulation model itself to derive the linear state space model. In analogy to the trim

calculation, the linearization routine accounts for the nonlinear rigid body equations of motion. For this reason, the state vector of the linear state space model is given by (3.36) and the input vector is according to (3.37). The outputs of the linear state space model are in accordance with the measurements available from the internal sensor system. Additionally, the elements of $\vec{x}$ are available as outputs.

$$\vec{x} = \begin{bmatrix} \left(u_K^G\right)_B^I & \left(v_K^G\right)_B^I & \left(w_K^G\right)_B^I & \dots \\ \left(p_K^{0B}\right)_B & \left(q_K^{0B}\right)_B & \left(r_K^{0B}\right)_B & \dots \\ \left(x^G\right)_I & \left(y^G\right)_I & \left(z^G\right)_I & \dots \\ \Phi & \Theta & \Psi & \end{bmatrix}^T \tag{3.36}$$

$$\vec{u} = \begin{bmatrix} \delta_L & \delta_M & \delta_N \end{bmatrix}^T \tag{3.37}$$

The linearization routine employs numerical differentiation to calculate the Jacobi-Matrices in (3.29) and generate the linear state space model. A fixed differentiation step size is implemented to achieve a high performance of the linearization routine in terms of calculation velocity. Following [46], more capable numerical differentiation algorithms are necessary, if problems related to differentiation step size appear. Such algorithms are available from [45], [49], [50], and [51]. The architecture of the linearization routine is similar to the trim calculation architecture displayed in Figure 3.1. The modular approach supports the linearization of an entire trim calculation result. If this is conducted, an array of linear state space models results, whereupon the individual linear state space models relate to the particular trim conditions. In addition, the linearization routine is usable with the translation states according to (2.11) or the alternate states $(V_{K,Abs}^G)_B^I$, $(\alpha_K^G)_B^I$, and $(\beta_K^G)_B^I$.

3.2.2 Longitudinal interceptor dynamics

The dynamics of the uncontrolled interceptor are analyzed in the following, where the linearized longitudinal interceptor dynamics and the linearized roll rate interceptor dynamics are treated separately. Originating from the cruciform configuration, the linearized longitudinal and the linearized lateral interceptor dynamics coincide, if short time frames are taken into account. Hence, the linearized lateral interceptor dynamics are not considered, but the coincidence of the linearized longitudinal and the linearized lateral interceptor dynamics is proven. This approach follows [9] and [59]. The analysis is based on results derived with the beforehand presented linearization routine.

Coincidence of linearized longitudinal and linearized lateral interceptor dynamics
The linearization routine employed in this thesis calculates the matrices A, B, C, and D of the linear state space model given in (3.35). Following the derivation of the nonlinear rigid body equations of motion in Chapter 2, the state vector $\vec{x}$ in (3.35) is given by (3.36), whereupon the Euler angles substitute the Quaternions, because the former are more descriptive. The elements in A, B, C, and D are arranged in accordance with the states in $\vec{x}$.
To resolve this intricate description of the dynamics as well as to reach a comparability between the linearized longitudinal and the linearized lateral interceptor dynamics, the states in $\vec{x}$ are regrouped. (3.38) and (3.39) constitute $\vec{x}$ after regrouping, depending on the state variables

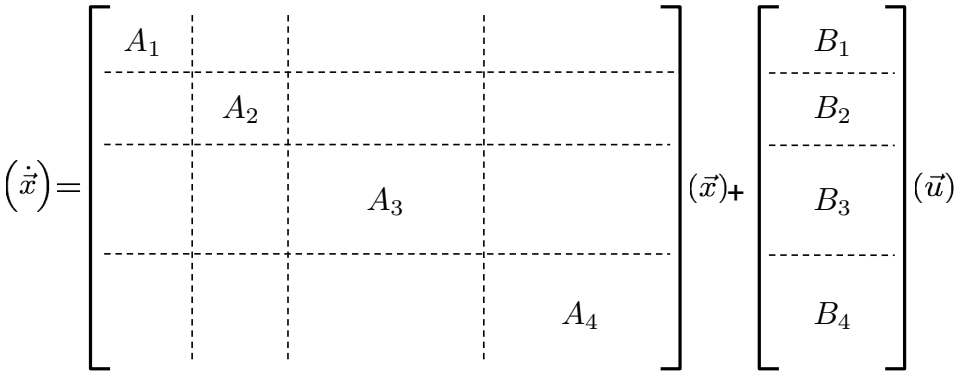

Figure 3.4: Transformed linear state equation

which are utilized to describe the translation of the interceptor.

$$\vec{x} = \begin{bmatrix} \left(x^G\right)_I & \left(u_K^G\right)_B^I & \Phi & \left(p_K^{0B}\right)_B & \dots \\ \left(z^G\right)_I & \Theta & \left(w_K^G\right)_B^I & \left(q_K^{0B}\right)_B & \dots \\ \left(y^G\right)_I & \Psi & \left(v_K^G\right)_B^I & \left(r_K^{0B}\right)_B & \end{bmatrix}^T \tag{3.38}$$

$$\vec{x} = \begin{bmatrix} \left(x^G\right)_I & \left(V_{K,Abs}^G\right)_B^I & \Phi & \left(p_K^{0B}\right)_B & \dots \\ \left(z^G\right)_I & \Theta & \left(\alpha_K^G\right)_B^I & \left(q_K^{0B}\right)_B & \dots \\ \left(y^G\right)_I & \Psi & \left(\beta_K^G\right)_B^I & \left(r_K^{0B}\right)_B & \end{bmatrix}^T \tag{3.39}$$

By employing an appropriate transformation matrix T and (3.40) to (3.43), the elements in A, B, C, and D are rearranged equivalently.

$$\tilde{A} = TAT^{-1} \tag{3.40}$$

$$\tilde{B} = TB \tag{3.41}$$

$$\tilde{C} = CT^{-1} \tag{3.42}$$

$$\tilde{D} = D \tag{3.43}$$

The result of this process is a transformed form of (3.35) which clearly displays the individual linearized interceptor dynamics. Furthermore, it provides the capability to compare, extract, and analyze the particular linearized interceptor dynamics straightforward. In this transformed form, A contains the matrices A_1 to A_4 along its main diagonal. Because A_3 contains the system matrix elements of those states which are exclusively involved in the linearized longitudinal interceptor dynamics, given by the elements five to eight in (3.38) and (3.39), and A_4 comprises the elements of A of states only related to the linearized lateral interceptor dynamics, the two dynamics become easily comparable. B is vertically separated into the matrices B_1 to B_4 by the transformation. Figure 3.4 illustrates the result of the transformation on the state equation of (3.35). The output equation is modified similarly by this transformation.
The matrices A_3, B_3, C_3, and D_3 are compared with the respective matrices of the index 4 inside the entire interceptor flight envelope. Except terms which are influenced by gravity, the matrices coincide at every considered flight condition, as expressed in (3.44) to (3.47). For example, at

the flight condition $(V_{K,Abs}^{G})_{B}^{I} = 600\,[m/s]$ and $\left(z^{G}\right)_{I} = 10000\,[m]$, the respective individual elements of the matrices show a deviation significantly below 1 [%]. Hence, the linearized lateral interceptor dynamics is not considered in the further analysis.

$$A_3 = A_4 \tag{3.44}$$
$$B_3 = B_4 \tag{3.45}$$
$$C_3 = C_4 \tag{3.46}$$
$$D_3 = D_4 \tag{3.47}$$

Linearized longitudinal interceptor dynamics

The extraction of the linearized longitudinal interceptor dynamics from the transformed form of (3.35) leads to (3.48). The state vector $\vec{x}$ for this reduced system is given by either (3.49) or (3.50). Based on (3.37), δ_M constitutes the input u.

$$\dot{\vec{x}} = A_{Pitch}\vec{x} + B_{Pitch}u \tag{3.48}$$

$$\vec{x} = \begin{bmatrix} \left(u_K^G\right)_B^I & \Theta & \left(w_K^G\right)_B^I & \left(q_K^{0B}\right)_B \end{bmatrix}^T \tag{3.49}$$

$$\vec{x} = \begin{bmatrix} \left(V_{K,Abs}^G\right)_B^I & \Theta & \left(\alpha_K^G\right)_B^I & \left(q_K^{0B}\right)_B \end{bmatrix}^T \tag{3.50}$$

This linearized longitudinal interceptor dynamics (3.48) exhibits four eigenvalues. These eigenvalues are separated into two pairs of complex eigenvalues describing two oscillatory motions.
The slower, lightly damped oscillatory motion, which following [16] is called Phugoid, describes an energy exchange between $(V_{K,Abs}^{G})_{B}^{I}$ and $\left(z^{G}\right)_{I}$. This oscillatory motion affects mainly steady-state flight conditions. A derivation and an analysis of the Phugoid is available in [9] and [47]. Considering the assumption that the interceptor time of flight is significantly below one minute, while at the same time anticipating frequent interceptor maneuvers to reach a desired target, the Phugoid is neglected.
The faster, heavy damped oscillatory motion constitutes an oscillation of $\left(q_K^{0B}\right)_B$ and $\left(\alpha_K^G\right)_B^I$. According to [16], this oscillatory motion is called Short Period. The interceptor states involved in the Short Period move the latter in the focus of the analysis of the linearized longitudinal interceptor dynamics. As illustrated in the signal flow diagrams in [16] and [47], δ_M generates $\left(q_K^{0B}\right)_B$, which in turn gives rise to $\left(\alpha_K^G\right)_B^I$. The presence of $\left(\alpha_K^G\right)_B^I$ leads to longitudinal acceleration $\left(a_Z^G\right)_B^{II}$ of the interceptor. Because $\left(a_Z^G\right)_B^{II}$ is of greatest importance for the interceptor to reach the desired target, a detailed analysis of the Short Period is inevitable.
Following the nomenclature in [16], [46], [90], and [130], the linearized state equation of the Short Period is written as (3.51). (3.51) constitutes a subset of (3.48).

$$\begin{bmatrix} \left(\dot{\alpha}_K^G\right)_B^{IB} \\ \left(\dot{q}_K^{0B}\right)_B^B \end{bmatrix} = \begin{bmatrix} Z_\alpha & Z_q \\ M_\alpha & M_q \end{bmatrix} \cdot \begin{bmatrix} \left(\alpha_K^G\right)_B^I \\ \left(q_K^{0B}\right)_B \end{bmatrix} + \begin{bmatrix} Z_{\delta_M} \\ M_{\delta_M} \end{bmatrix} \cdot \delta_M \tag{3.51}$$

The investigation of (3.51) for the interceptor for the flight condition $(V_{K,Abs}^{G})_{B}^{I} = 600\,[m/s]$ and $\left(z^{G}\right)_{I} = 10000\,[m]$ shows that the eigenvalues of the Short Period are $-5.69 \pm 6.76i$. This implies a natural frequency of $\omega_n = 8.83\,[rad/s]$ and a damping ratio of $\zeta = 0.64$. The latter is lower than the optimal damping ratio for a second order, time invariant system of $\zeta_{Opt} = \frac{1}{2}\sqrt{2}$ which is stated in the control literature, e.g. [81]. On the other hand, the comparison of ω_n and

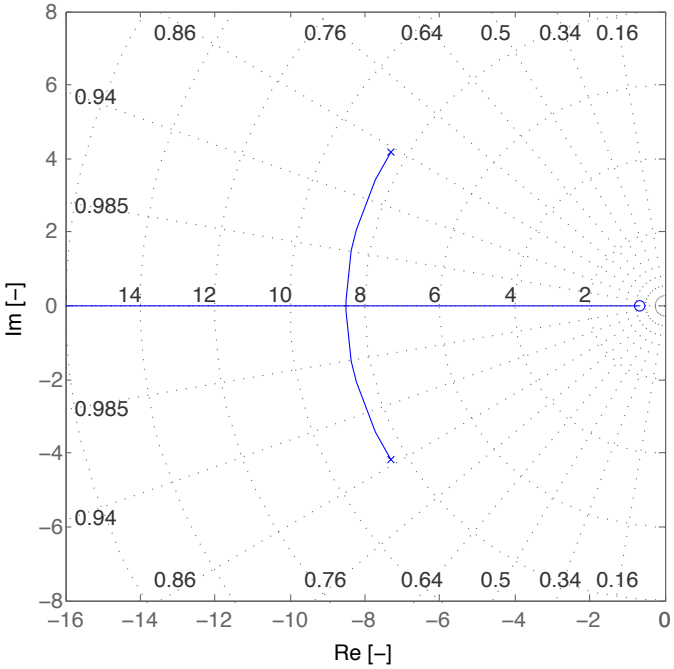

Figure 3.5: Root locus of $H_{\left(q_K^{0B}\right)_B \delta_M}(s)$ at $(V_{K,Abs}^G)_B^I = 600\,[m/s]$ and $\left(z^G\right)_I = 10000\,[m]$ for the Short Period

ζ of the interceptor with the values provided in [9] and [59] shows that the Short Period of the interceptor exhibits a similar dynamical behavior as other missiles in this category.
After analyzing the uncontrolled, linearized longitudinal interceptor dynamics, the response of the linearized longitudinal interceptor dynamics to control inputs is examined. Classical methodologies in the frequency domain, in this case the transfer function, or graphical methods, like the pole-zero plot, the root locus or the Bode plot, are utilized for this analysis.
Considering δ_M as the input of an interceptor flight control system loop for $\left(q_K^{0B}\right)_B$, the beforehand stated methodologies are employed for the flight condition $(V_{K,Abs}^G)_B^I = 600\,[m/s]$ and $\left(z^G\right)_I = 10000\,[m]$. The transfer function from δ_M to $\left(q_K^{0B}\right)_B$ is given by (3.52). Figure 3.5 illustrates the root locus and Figure 3.6 displays the Bode plot.

$$H_{\left(q_K^{0B}\right)_B \delta_M}(s) = \frac{-70.50 \cdot (s + 0.42)}{s^2 + 11.38s + 78.02} \tag{3.52}$$

It is obvious from Figure 3.5 that a feedback of $\left(q_K^{0B}\right)_B$ allows to increase ζ while at the same time keeping ω_n nearly constant.
Accounting for δ_M as the input and $\left(a_Z^G\right)_B^{II}$ as the output, the transfer function for the flight condition $(V_{K,Abs}^G)_B^I = 600\,[m/s]$ and $\left(z^G\right)_I = 10000\,[m]$ is given by (3.53). The pole-zero plot is shown in Figure 3.7.

$$H_{\left(a_Z^G\right)_B^{II} \delta_M}(s) = \frac{-33.37 \cdot (s - 43.94) \cdot (s + 19.87)}{s^2 + 11.38s + 78.02} \tag{3.53}$$

As displayed in Figure 3.7, the considered dynamics exhibits a zero in the right half plane, meaning it is non-minimum phase. Based on the fact that the aerodynamic control surfaces are located behind the center of gravity of the interceptor, the former generate a force acting

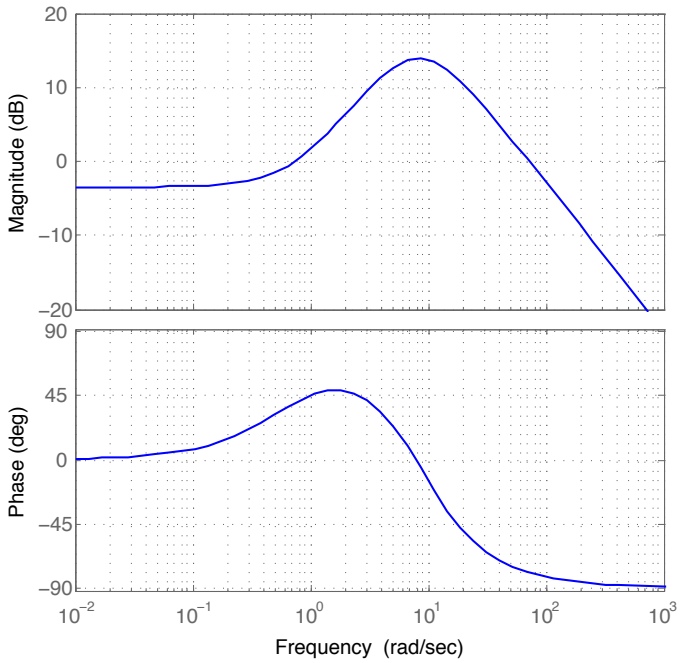

Figure 3.6: Bode plot of $H_{\left(q_K^{0B}\right)_B \delta_M}(s)$ at $(V_{K,Abs}^G)_B^I = 600\,[m/s]$ and $\left(z^G\right)_I = 10000\,[m]$ for the Short Period

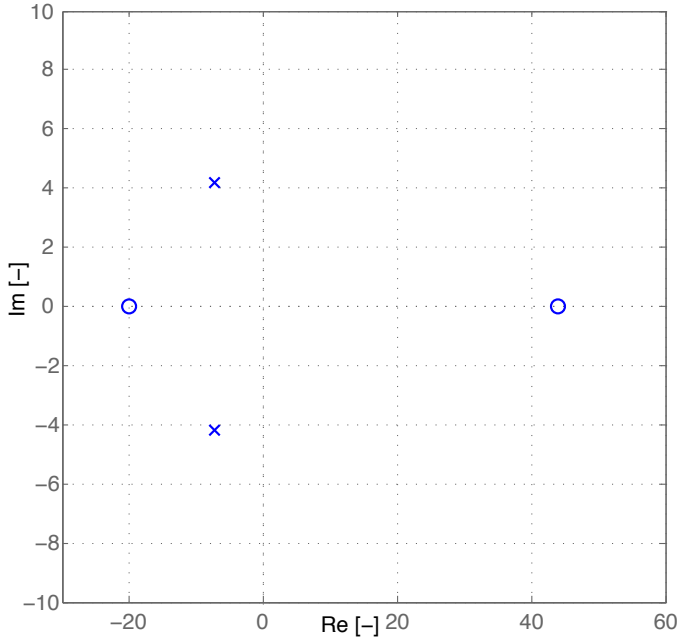

Figure 3.7: Pole-zero plot of $H_{\left(a_Z^G\right)_B^{II} \delta_M}(s)$ at $(V_{K,Abs}^G)_B^I = 600\,[m/s]$ and $\left(z^G\right)_I = 10000\,[m]$ for the Short Period

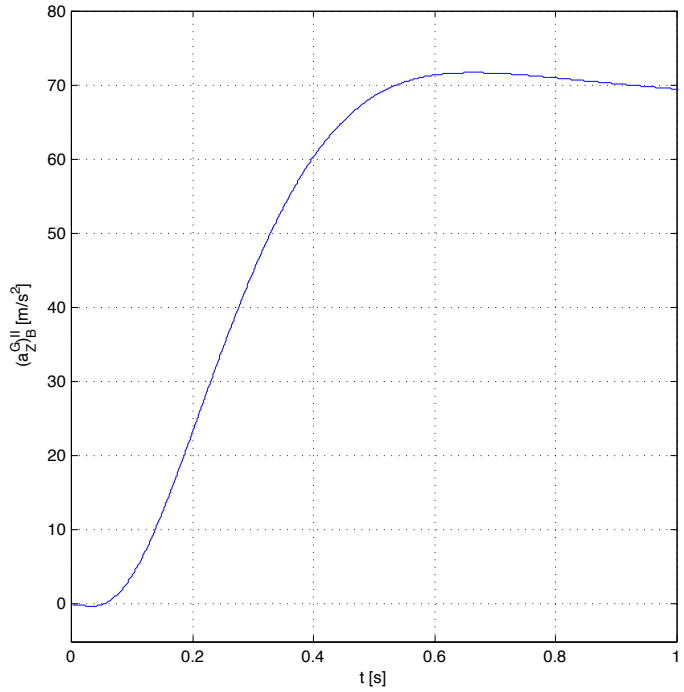

Figure 3.8: Initial $\left(a_Z^G\right)_B^{II}$ for $\delta_M = 10\,[deg]$ at $(V_{K,Abs}^G)_B^I = 600\,[m/s]$ and $\left(z^G\right)_I = 10000\,[m]$

on the interceptor which points in the opposite direction of the given command, once they are deflected. This implies that the center of gravity of the interceptor accelerates in the opposite direction of the command initially. After rotation of the interceptor and the establishment of an angle of attack between the interceptor fuselage and the surrounding airstream, the lift force generated by the fuselage exceeds the force originating from the aerodynamic control surfaces. Therefore, the center of gravity of the interceptor is accelerated in the direction of the command finally.
The non-minimum phaseness is also recognizable from (2.49). As Appendix C illustrates for $(V_{K,Abs}^G)_B^I = 600\,[m/s]$ and $\left(z^G\right)_I = 10000\,[m]$, $C_{Z,\delta_M}\left(\alpha_K^G, \beta_K^G, M\right)$ is negative inside the interceptor flight envelope. In combination with δ_M, the respective term always generates a force component which opposes the remaining terms of (2.49).
To underline that these effects, which have been found by establishing (3.53), are not confined to the linearized longitudinal interceptor dynamics, but instead originate from the interceptor configuration, an example employing the endo-atmospheric dual-actuator interceptor is presented. In this example, the interceptor is flying at $(V_{K,Abs}^G)_B^I = 600\,[m/s]$ and $\left(z^G\right)_I = 10000\,[m]$ in steady-state horizontal flight. $\delta_M = 10\,[deg]$ is applied at the beginning of the simulation. The resulting $\left(a_Z^G\right)_B^{II}$ is plotted in Figure 3.8, whereupon the time scale on the abscissa is chosen adequately. It is clearly visible that $\left(a_Z^G\right)_B^{II} < 0$ initially, meaning that the interceptor accelerates upwards, before it reaches the desired $\left(a_Z^G\right)_B^{II} > 0$ region, underpinning the beforehand considerations.

Influence of the flight condition on the linearized longitudinal interceptor dynamics
The paragraphs above analyzed the linearized longitudinal interceptor dynamics at distinct flight conditions inside the interceptor flight envelope. Because the aerodynamic forces and moments acting on the interceptor are dependent on the flight condition, which is evident from the appli-

cation rules (2.47) to (2.52), an influence of the flight condition on the linearized longitudinal interceptor dynamics exists. Hence, the change of the linearized longitudinal interceptor dynamics inside the interceptor flight envelope is examined now.
Following Section 3.1, the interceptor flight envelope for this analysis is bounded by (3.54) and (3.55). Variations of $(V^G_{K,Abs})^I_B$ and $\left(z^G\right)_I$ are considered separately to investigate the particular influence of the respective variables. The poles of the Short Period, as given in (3.51), are determined inside the interceptor flight envelope. The influence of $(V^G_{K,Abs})^I_B$ and $\left(z^G\right)_I$ on the linearized longitudinal interceptor dynamics is derived by plotting the poles of the Short Period for a set of flight conditions. Figure 3.9 illustrates the migration of the poles of the Short Period for a variation of $(V^G_{K,Abs})^I_B$ and $\left(z^G\right)_I$.

$$100\,[m/s] \leq \left(V^G_{K,Abs}\right)^I_B \leq 1000\,[m/s] \tag{3.54}$$

$$0\,[m] \leq \left(z^G\right)_I \leq 20000\,[m] \tag{3.55}$$

$(V^G_{K,Abs})^I_B$ is varied according to (3.54) in the upper diagram of Figure 3.9, whereupon $\left(z^G\right)_I = 10000\,[m]$. The increase of $(V^G_{K,Abs})^I_B$ leads to a rise of the natural frequency of the Short Period from $\omega_{n,Min} = 3.81\,[rad/s]$ to $\omega_{n,Max} = 13.59\,[rad/s]$. The respective damping ratio of the Short Period lies in the interval $\zeta_{Min} = 0.56$ to $\zeta_{Max} = 0.58$. The increase of ω_n with $(V^G_{K,Abs})^I_B$ is based on the increase of the aerodynamic moments acting on the interceptor. The latter rise due to the greater $\bar{q}$ at higher $(V^G_{K,Abs})^I_B$, generating an increased stabilization of the interceptor. The derivation of this relationship is available in [46].
The lower diagram of Figure 3.9 shows the migration of the poles of the Short Period for a change of $\left(z^G\right)_I$. The variation of $\left(z^G\right)_I$ is according to (3.55); $(V^G_{K,Abs})^I_B = 600\,[m/s]$. Induced by the change of $\left(z^G\right)_I$, the natural frequency of the Short Period changes from $\omega_{n,Max} = 10.89\,[rad/s]$ at $\left(z^G\right)_I = 0\,[m]$ to $\omega_{n,Min} = 2.84\,[rad/s]$ at $\left(z^G\right)_I = 20000\,[m]$, whereupon the damping ratio of the Short Period varies inside the interval $\zeta_{Max} = 0.98$ to $\zeta_{Min} = 0.47$. The reduction of ω_n with increasing $\left(z^G\right)_I$ originates from the decrease of ρ. This relationship is derived in the following.
The characteristic equation of the system matrix of (3.51) is written on the left hand side of (3.56). By understanding the left hand side as the general description of a second order, time invariant system in the frequency domain, as indicated in (3.56), the respective ω_n and ζ are calculated. ω_n and ζ are provided in (3.57) and (3.58).

$$s^2 - (Z_\alpha + M_q)\,s + Z_\alpha M_q - M_\alpha Z_q = s^2 + 2\zeta\omega_n s + \omega_n^2 = 0 \tag{3.56}$$

$$\omega_n = \sqrt{Z_\alpha M_q - M_\alpha Z_q} \tag{3.57}$$

$$\zeta = -\frac{Z_\alpha + M_q}{2\sqrt{Z_\alpha M_q - M_\alpha Z_q}} \tag{3.58}$$

The approximation of ω_n according to (3.59), whereupon (2.21) and (2.37) are used, results in calculation of the ratio of the natural frequencies of the Short Period for $\left(z^G\right)_I = 20000\,[m]$ and $\left(z^G\right)_I = 0\,[m]$ as stated in (3.59). The calculated ratio according to (3.60) is close the ratio $\omega_{n,Min}$ divided by $\omega_{n,Max}$. Hence, the presented approximation is feasible.

$$\omega_n \approx \sqrt{-M_\alpha} = \sqrt{-\frac{C_M \bar{q} S_{Ref} \bar{c}}{\left(I^G_{YY}\right)_{BB}}} \tag{3.59}$$

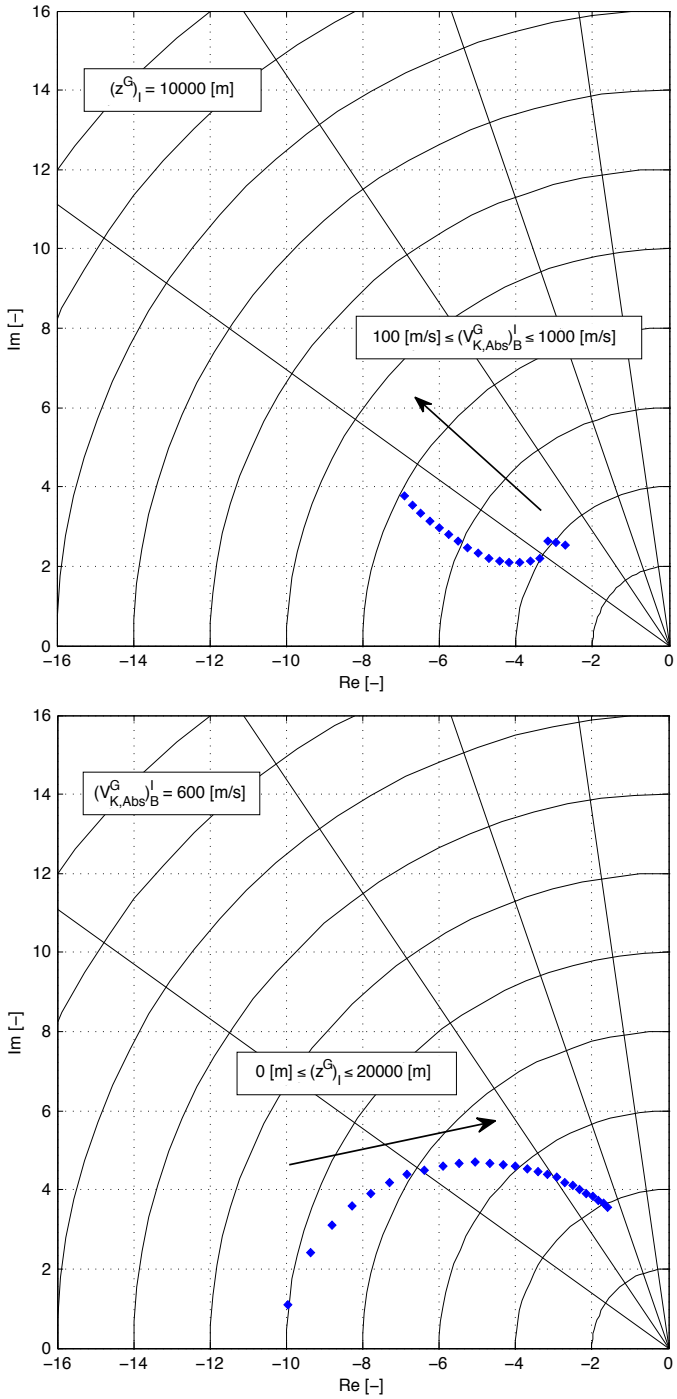

Figure 3.9: Migration of the poles of the Short Period at variation of $(V^G_{K,Abs})^I_B$ and $\left(z^G\right)_I$

$$\frac{\omega_{n,(z^G)_{I,Max}}}{\omega_{n,(z^G)_{I,Min}}} \approx \sqrt{\frac{\rho_{(z^G)_{I,Max}}}{\rho_{(z^G)_{I,Min}}}} \approx \sqrt{\frac{0.088}{1.225}} = 0.27 \tag{3.60}$$

A similar analysis is conducted for ζ. Approximating the latter as stated in (3.61) with the use of (2.21), (2.37), and (2.38) allows the calculation of the ratio of the damping of the Short Period for $\left(z^G\right)_I = 20000\,[m]$ and $\left(z^G\right)_I = 0\,[m]$. The comparison of the result in (3.62) with the ratio ζ_{Min} divided by ζ_{Max} shows that this approximation is not as good as the approximation for ω_n.

$$\zeta \approx \frac{-M_q}{2\sqrt{-M_\alpha}} = \frac{-\frac{C_{M,q}\rho\left(V^G_{K,Abs}\right)^I_B S_{Ref}\bar{c}^2}{4\left(I^G_{YY}\right)_{BB}}}{2\sqrt{-\frac{C_M\rho\left[\left(V^G_{K,Abs}\right)^I_B\right]^2 S_{Ref}\bar{c}}{2\left(I^G_{YY}\right)_{BB}}}} \tag{3.61}$$

$$\frac{\zeta_{(z^G)_{I,Max}}}{\zeta_{(z^G)_{I,Min}}} \approx \sqrt{\frac{\rho_{(z^G)_{I,Max}}}{\rho_{(z^G)_{I,Min}}}} \approx \sqrt{\frac{0.088}{1.225}} = 0.27 \tag{3.62}$$

The variation of ω_n and ζ of the Short Period inside the interceptor flight envelope, which is identical for the linearized lateral interceptor dynamics due to the coincidence of the respective dynamics, constitutes an important insight valuable for the design of the interceptor flight control system.

Besides the migration of the poles of the Short Period, the change of the non-minimum phase property, which has been found by considering the transfer function from the input δ_M to the output $\left(a^G_Z\right)^{II}_B$, inside the interceptor flight envelope is examined. The rational behind this investigation is to derive, if this main characteristic of the interceptor, originating from its configuration, varies with respect to its size.

Presuming that the interceptor is at steady-state horizontal flight, condition (3.63) holds. The aerodynamic forces in the X_B - Z_B plane are originating from the first and the last term in (2.49). $(\alpha^G_K)^I_B$, $(\beta^G_K)^I_B$, and M are identical for these two terms. The ratio of the third and the first term expresses how much of the aerodynamic forces is generated by the aerodynamic control surfaces in relationship to the lift generated by the interceptor fuselage. It indicates the size of the non-minimum phase behavior to be expected in case of maneuvers.

$$\left(F^G_{Z,A}\right)_B = \left(F^G_{Z,G}\right)_B \tag{3.63}$$

If the second term in (2.49) is neglected, $(\alpha^G_K)^I_B$, $(\beta^G_K)^I_B$, and δ_M are defined, and M is varied, the change of the non-minimum phaseness over the interceptor flight envelope becomes seizable by calculating the beforehand derived ratio. The δ_M to be chosen is a representation for the maneuver initialized by deflecting the aerodynamic control surfaces. Figure 3.10 displays the ratio for $(\alpha^G_K)^I_B = 2.5\,[deg]$, $(\beta^G_K)^I_B = 0\,[deg]$ and different δ_M over the range of M that is operationally relevant for the interceptor.

Figure 3.10 illustrates that the non-minimum phaseness generally decreases with increasing M. It is obvious that greater δ_M lead to an increased non-minimum phase behavior. This effect is logical, because an increased δ_M, meaning greater aerodynamic control surface deflections, gives rise to an increased aerodynamic force acting in the opposite direction of the command. On the other hand, the added non-minimum phaseness resulting from an increased δ_M is much smaller at higher M. Therefore, the aerodynamic control surfaces influence the interceptor dynamics to a much higher extend at low M.

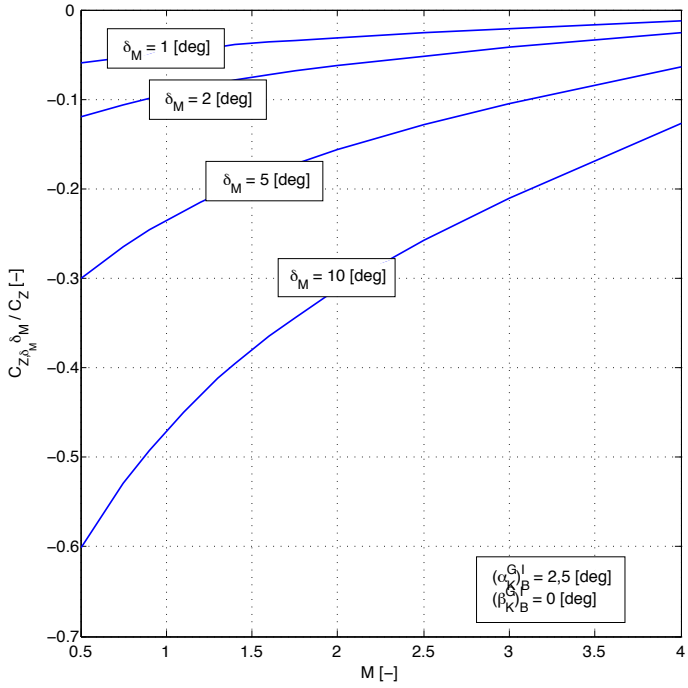

Figure 3.10: Change of the interceptor non-minimum phase behavior

Reaction jet cartridge effectivity

The last part of the uncontrolled longitudinal interceptor dynamics to be considered herein is the reaction jet cartridge effectivity. Due to the fact that the individual reaction jet cartridges can only be fired once and exhibit a fixed thrust profile, they are not adequate to reach and sustain a steady-state flight condition. Hence, neither trim calculations are conducted nor the linearized longitudinal interceptor dynamics is analyzed with this actuator section employed. In contrast, the effectivity of the reaction jet cartridges is of greatest interest for the design of the control allocation of the interceptor flight control system.

According to (2.3) and (2.4), the reaction jet cartridges differ regarding their attitude and lever arm to the center of gravity of the interceptor. Assuming that an appropriate element of $\left(\vec{\varphi}^{RJC}\right)_B$ for the implementation of a command is determined by the control allocation, only the different lever arms with respect to the center of gravity of the interceptor influence the reaction jet cartridge effectivity at this point. To assess this effectivity, the endo-atmospheric dual-actuator interceptor is employed, the reaction jet cartridges pointing in the direction of the Z_B axis are fired individually, and the variables $(\alpha_K^G)_B^I$, $\left(q_K^{0B}\right)_B$, and $\left(a_Z^G\right)_B^{II}$ are analyzed. Figure 3.11 shows the respective results.

It is evident from Figure 3.11 that a single reaction jet cartridge, acting in the optimal attitude concerning the command, is able to generate a maximum $(\alpha_K^G)_B^I$ of $0.28\,[deg]$ to $0.32\,[deg]$ and a maximum pitch rate of $2.2\,[deg/s] \leq \left(q_K^{0B}\right)_B \leq 3\,[deg/s]$. The $\left(a_Z^G\right)_B^{II}$ achieved by an individual reaction jet cartridge varies in the interval $4\,[m/s^2] \leq \left(a_Z^G\right)_B^{II} \leq 4.5\,[m/s^2]$.

Depending on the control variable to be chosen, these important results allow to design the control allocation in accordance with the effectivity of the different actuator sections of the interceptor. With this knowledge achieved, the analysis of the longitudinal interceptor dynamics is concluded in this work.

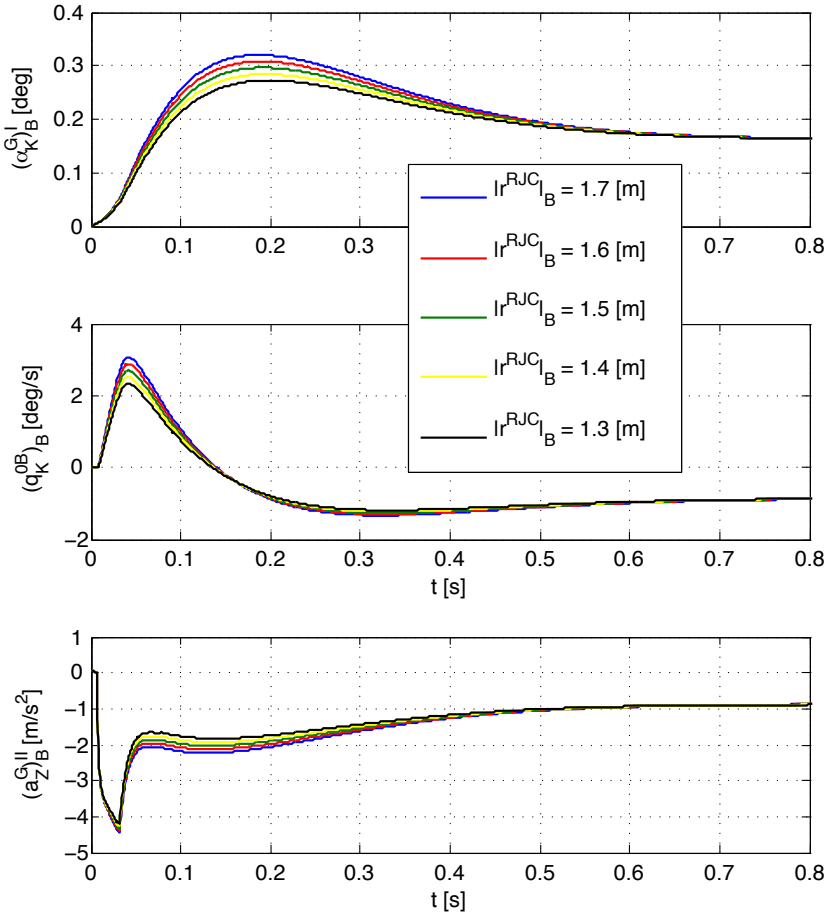

Figure 3.11: Reaction jet cartridge effectivity

3.2.3 Roll rate dynamics

After the linearized longitudinal interceptor dynamics have been examined in detail, the linearized roll rate interceptor dynamics are analyzed. Following the methodology in Section 3.2.2, the uncontrolled, linearized roll rate interceptor dynamics, the response of the linearized roll rate dynamics to control inputs, and the change of latter inside the interceptor flight envelope are taken into account.
The extraction of the linearized roll rate interceptor dynamics from the transformed form of (3.35) results in (3.64). The state vector $\vec{x}$ of the reduced system comprises $\left(p_K^{0B}\right)_B$ and Φ. The input u is given by δ_L.

$$\dot{\vec{x}} = A_{Roll}\vec{x} + B_{Roll}u \tag{3.64}$$

Based on the fact that the reaction jet cartridges, which are dispersed on the circumference of the interceptor fuselage, can only be used once, it is presumed that the interceptor flight control system controls $\left(p_K^{0B}\right)_B$ to a specified value to ensure permanent availability of the reaction jet actuator section during the flight. Hence, the linear differential equation which describes the dynamics of Φ is neglected. The remainder of (3.64) is written as (3.65), whereupon the denotation according [16], [46], [90], and [130] is employed.

$$\left(\dot{p}_K^{0B}\right)_B^B = L_p \cdot \left(p_K^{0B}\right)_B + L_{\delta_L} \cdot \delta_L \tag{3.65}$$

The analysis of (3.65) at the flight condition $(V_{K,Abs}^G)_B^I = 600\,[m/s]$ and $\left(z^G\right)_I = 10000\,[m]$ shows a real eigenvalue located at -14.72.
Regarding δ_L as the input of an interceptor flight control system loop for $\left(p_K^{0B}\right)_B$, the response of the linearized roll rate interceptor dynamics to control inputs is analyzed. The resulting transfer function from δ_L to $\left(p_K^{0B}\right)_B$ for the flight condition $(V_{K,Abs}^G)_B^I = 600\,[m/s]$ and $\left(z^G\right)_I = 10000\,[m]$ is given by (3.66). The root locus is shown in Figure 3.12. Figure 3.13 displays the Bode plot.

$$H_{\left(p_K^{0B}\right)_B \delta_L}(s) = \frac{-935.80}{s + 14.72} \tag{3.66}$$

Influence of the flight condition on the linearized roll rate interceptor dynamics
The beforehand presented analysis investigated the linearized roll rate interceptor dynamics at a distinct flight condition. Following the methodology in Section 3.2.2, the change of the linearized roll rate interceptor dynamics inside the interceptor flight envelope is examined in the following. To affiliate the influence of the flight condition on the linearized roll rate interceptor dynamics, variations of $(V_{K,Abs}^G)_B^I$ and $\left(z^G\right)_I$ are considered. The interceptor flight envelope is bounded according to (3.54) and (3.55). The migration of the pole of the linearized roll rate interceptor dynamics for variations of $(V_{K,Abs}^G)_B^I$ and $\left(z^G\right)_I$ provides insight into the influence of these variables. Figure 3.14 shows the migration of the pole of the linearized roll rate interceptor dynamics for variation of $(V_{K,Abs}^G)_B^I$ and $\left(z^G\right)_I$.
The upper diagram of Figure 3.14 displays the migration of the pole of the linearized roll rate interceptor dynamics for the variation of $(V_{K,Abs}^G)_B^I$ according to (3.54), whereupon $\left(z^G\right)_I = 10000\,[m]$. As indicated in the diagram, the pole of the linearized roll rate interceptor dynamics changes from $\omega_{n,Min} = 3.83\,[rad/s]$ to $\omega_{n,Max} = 24.59\,[rad/s]$ with the increase of $(V_{K,Abs}^G)_B^I$. The rise of ω_n is based on the increase of L_p in (3.65). Considering (2.21) and (2.37), L_p is written as (3.67). It shows the dependency of L_p on $(V_{K,Abs}^G)_B^I$.

$$L_p = \frac{C_{L,p}\rho\left(V_{K,Abs}^G\right)_B^I S_{Ref}\bar{c}^2}{4\left(I_{XX}^G\right)_{BB}} \tag{3.67}$$

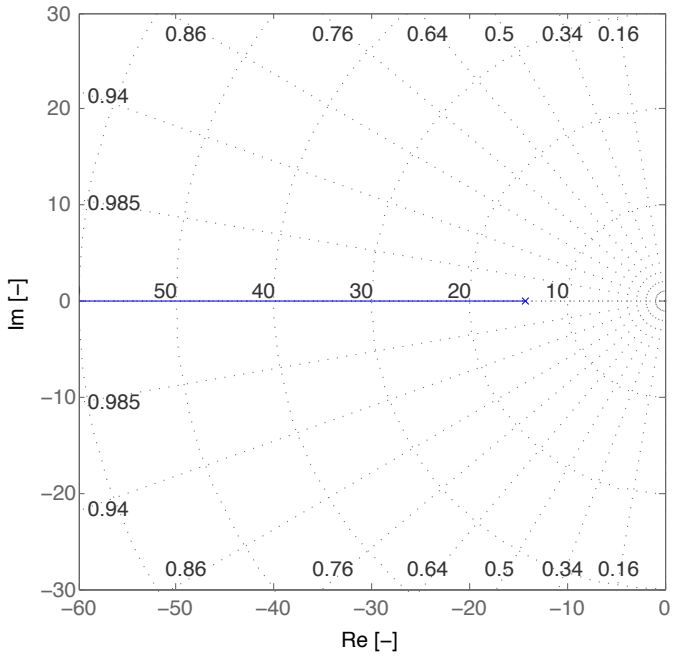

Figure 3.12: Root locus of $H_{\left(p_K^{0B}\right)_B \delta_L}(s)$ at $(V_{K,Abs}^G)_B^I = 600\,[m/s]$ and $\left(z^G\right)_I = 10000\,[m]$

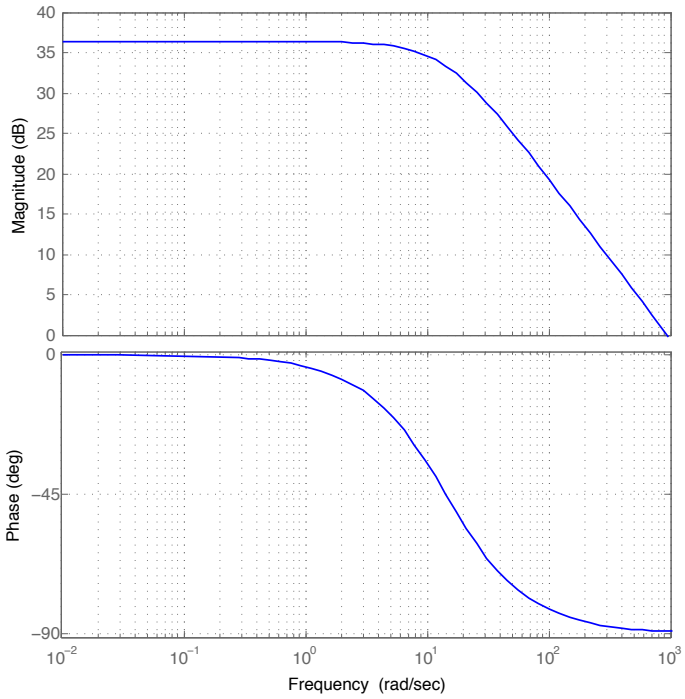

Figure 3.13: Bode plot of $H_{\left(p_K^{0B}\right)_B \delta_L}(s)$ at $(V_{K,Abs}^G)_B^I = 600\,[m/s]$ and $\left(z^G\right)_I = 10000\,[m]$

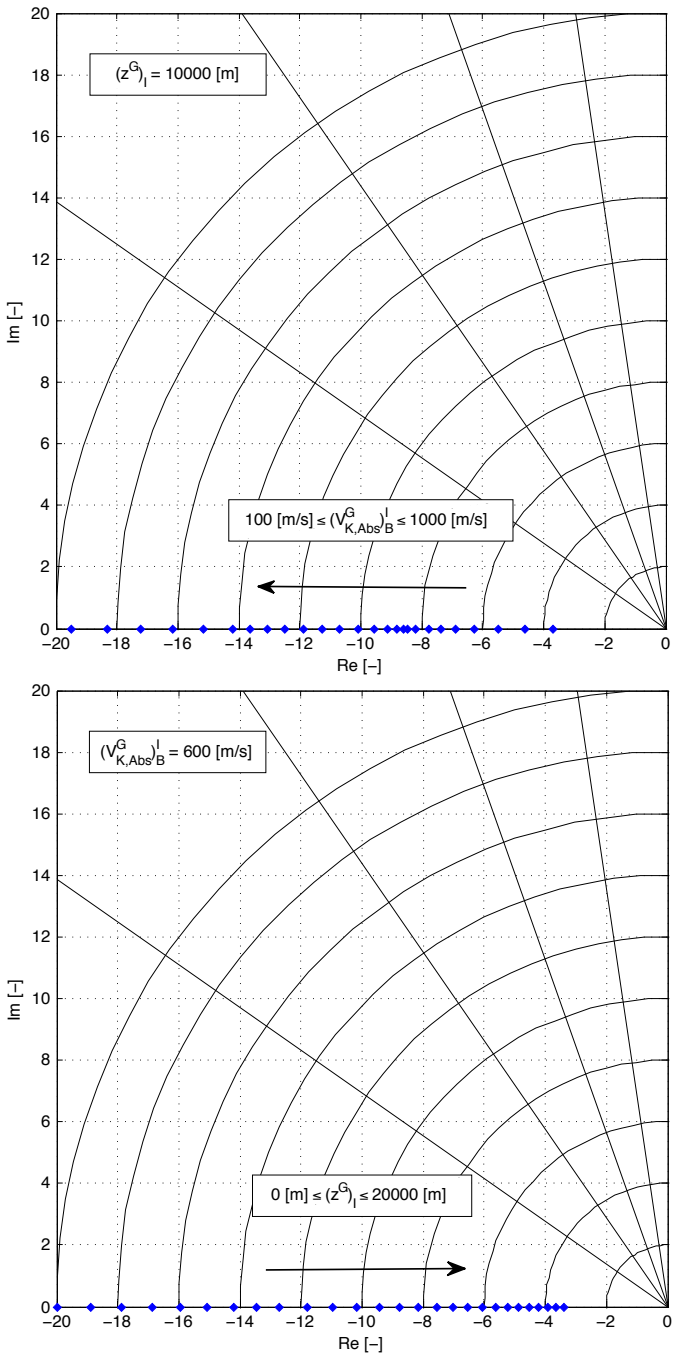

Figure 3.14: Migration of the pole of the linearized roll rate interceptor dynamics at variation of $(V^G_{K,Abs})^I_B$ and $\left(z^G\right)_I$

$\left(z^G\right)_I$ changes according to (3.55) in the lower diagram of Figure 3.14. The absolute kinematic velocity of the interceptor is chosen as $(V^G_{K,Abs})^I_B = 600\,[m/s]$. Based on the variation of $\left(z^G\right)_I$, the pole of the linearized roll rate interceptor dynamics changes from $\omega_{n,Max} = 34.39\,[rad/s]$ at $\left(z^G\right)_I = 0\,[m]$ to $\omega_{n,Min} = 3.42\,[rad/s]$ at $\left(z^G\right)_I = 20000\,[m]$. The reduction of ω_n is induced by the decrease of ρ with increasing $\left(z^G\right)_I$. (3.67) shows that, if ρ decreases, resulting from an increasing $\left(z^G\right)_I$, while $(V^G_{K,Abs})^I_B$ is kept constant and a dependency of $C_{L,p}$ on $\left(z^G\right)_I$ is neglected, L_p decreases, which results in a decrease of ω_n.
Like the results presented in Section 3.2.2, the variation of ω_n inside the interceptor flight envelope is also an important result for this work.

3.3 Nonlinear simulation

The beforehand presented results provide valuable insights into the flight dynamics of the interceptor. Vice versa, these results are augmented by nonlinear simulation to overcome the shortfalls related to linearization.
The linearization which is utilized by the classical methodologies in the frequency domain does not contain all characteristics of the nonlinear dynamics of the interceptor. Memoryless nonlinearities for example, as given in (2.57) and (2.58), are not represented therein. Hence, the presented results do not describe the interceptor dynamics to the full extent. Furthermore, the linearization is founded on steady-state flight conditions of the interceptor. The resulting linearized interceptor dynamics are valid for a small neighborhood of the particular steady-state flight condition only. This implies that the presented results neither describe the interceptor dynamics at larger neighborhoods of the steady-state flight conditions nor at non-steady-state flight conditions.
Nonlinear simulation constitutes a virtual flight of the interceptor. It considers all properties of the interceptor and its subsystems, as introduced in Chapter 2, and it is appropriate for all flight conditions. In this thesis, nonlinear simulation is utilized for design, testing, and performance evaluation of the interceptor flight control system.

Nonlinear simulation framework
As introduced in [46], a nonlinear simulation solves the nonlinear state equations of a system numerically. The states at the next time instant $\vec{x}\,(t + \Delta t)$ are calculated as a function of the actual states $\vec{x}\,(t)$, the derivatives of the actual states $\dot{\vec{x}}\,(t)$, the inputs $\vec{u}\,(t)$, and the simulation time step Δt. This procedure approximates the solution of the nonlinear state equations iteratively, although an error remains due to the discrete treatment of time.
The architecture of a nonlinear simulation is shown in Figure 3.15, which is based on the illustration in [46]. The nonlinear simulation of the interceptor exhibits the identical architecture. In this architecture, the interceptor including all subsystems as well as the interceptor flight control system is treated as a connected, quasi continuous system, based on Δt. The different parts of the interceptor are not separated and treated individually for integration. This methodology allows to employ any numerical integration method offered by the software which is utilized for implementation of the nonlinear simulation.
MATLAB® *Simulink*, which is used for the nonlinear simulation in this work, offers numerical integration methods with variable and with fixed step sizes. Given the explanations in [46], [104], and [130] the fourth order Runge-Kutta method is chosen as numerical integration method to solve the nonlinear state equations. This fixed step size numerical integration method marks a compromise between numerical accuracy which is necessary to achieve reliability of the

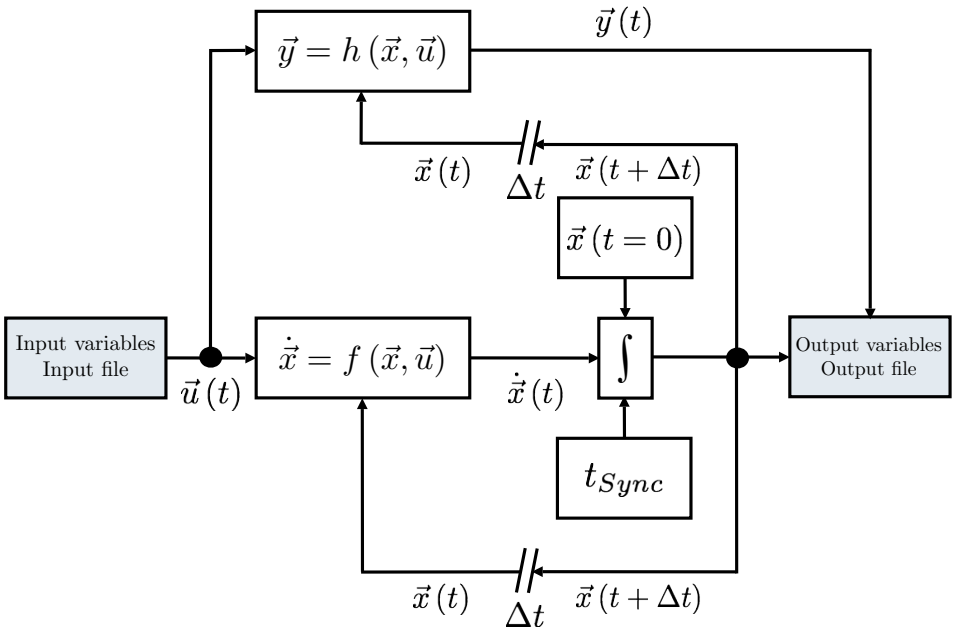

Figure 3.15: Nonlinear simulation architecture

nonlinear simulation results and performance in terms of nonlinear simulation velocity. (3.68) to (3.72), which are derived from [104], are used in the fourth order Runge-Kutta method to calculate $\vec{x}(t + \Delta t)$. As (3.68) to (3.71) indicate, the nonlinear state equations are evaluated four times in every simulation step of the nonlinear simulation.

$$\vec{k}_1 = \Delta t \cdot f(\vec{x}, t) \tag{3.68}$$

$$\vec{k}_2 = \Delta t \cdot f\left(\left(\vec{x} + \frac{1}{2}\vec{k}_1\right), \left(t + \frac{1}{2}\Delta t\right)\right) \tag{3.69}$$

$$\vec{k}_3 = \Delta t \cdot f\left(\left(\vec{x} + \frac{1}{2}\vec{k}_2\right), \left(t + \frac{1}{2}\Delta t\right)\right) \tag{3.70}$$

$$\vec{k}_4 = \Delta t \cdot f\left(\left(\vec{x} + \vec{k}_3\right), (t + \Delta t)\right) \tag{3.71}$$

$$\vec{x}(t + \Delta t) = \vec{x}(t) + \frac{1}{6}\vec{k}_1 + \frac{1}{3}\vec{k}_2 + \frac{1}{3}\vec{k}_3 + \frac{1}{6}\vec{k}_4 \tag{3.72}$$

To achieve usable nonlinear simulation results, Δt must be chosen significantly smaller than the smallest time constant of any system of the interceptor. Such choice ensures that even the fastest systems of the interceptor are considered adequately. Considering the reaction jet cartridge fuze delay, which is illustrated in Figure 2.4 and understood as the time constant of the respective systems, the simulation time step is defined as $\Delta t = 0.001\,[s]$.
Besides the necessity to chose Δt appropriately to achieve adequate nonlinear simulation results, Δt is a measure to influence the performance of the nonlinear simulation in terms of simulation velocity. The smaller Δt is defined, the more evaluations of the nonlinear state equations are necessary for a specified simulation time. A reduction of Δt leads to an increased time which is required by the nonlinear simulation to conduct the simulation. Empiric analysis shows that the interceptor nonlinear simulation operates at a quarter of real time on a workstation PC at $\Delta t = 0.001\,[s]$, whereupon the simulation framework of MATLAB® *Simulink* including

graphical output operates at the same time. Accounting for the interceptor time of flight, this nonlinear simulation velocity is acceptable for individual simulations. In addition, the empiric analysis shows that a further reduction of Δt results in a considerable loss of nonlinear simulation velocity, while at the same time the quality of the nonlinear simulation results does not enhance significantly. For this reason, Δt is not reduced further.
The observed nonlinear simulation velocity of a quarter of real time is adequate for individual simulations. Vice versa, this velocity is inappropriate for testing and evaluation of the interceptor flight control system. To achieve a higher nonlinear simulation velocity, additional programs accessing the interceptor without the graphical representation of the MATLAB® *Simulink* simulation model are developed. A nonlinear simulation velocity of approximately a third of real time is achieved at $\Delta t = 0.001\,[s]$. Additionally, the interceptor is build as code in C utilizing the *Real Time Workshop* component of the simulation framework. Employing the code instead of the interceptor provides the capability to operate the nonlinear simulation faster than real time. This nonlinear simulation velocity allows to conduct multiple, automatically initiated, and evaluated simulations. These are used for testing, optimization, and evaluation of the interceptor flight control system.

Chapter 4

Backstepping methodology

4.1 Overview

After major advances in differential-geometric theory of nonlinear feedback control and the thorough establishment of the feedback linearization methodology, which are presented in [24], [52], [53], [54], [58], [82], and [83], it became evident that other nonlinear control methodologies were necessary. The reasons behind this necessity were the wish to handle uncertainties present in the systems to be controlled and thereafter the desire to overcome the matching as well as the extended matching condition, meaning the ability to control systems with one or more integrators between the input and the unknown parameters. In addition, structured design procedures which allowed a systematic determination of an appropriate control law were missing.
The first approaches to nonlinear, adaptive control methodologies, illustrated in [23], relied on technically utmost difficult measurements, like the measurement of accelerations at joints of robot arms. This problematic aspect was removed by the work presented in [93], [98], [120], and [121]. In [132] a more general scheme of adaptive nonlinear regulation under the matching condition is shown. The matching condition, denoting the situation when the control and the parameter uncertainty appear in the same equation, was first relaxed to the extended matching condition around 1990, which is recognizable from the results in [4], [5], and [64]. The achievement presented in [65] and [63], being reviewed in [67], established the recursive design procedure denoted by adaptive Backstepping. It is not confined to the extended matching condition.
Besides other classes of systems, which are not considered herein, adaptive Backstepping is applicable to strict-feedback systems. These systems exhibit a triangular structure. In the scalar case, the first differential equation contains only the respective state and the state of the second equation. The second differential equation comprises the state of the first and second equation as well as the state of the third differential equation. This scheme leads to the mentioned triangular structure, if multiple equations are considered and they are written below each other. Only the last equation contains the input of the system.
The basic principle of the procedure is to consider the state of the second differential equation as input in the first equation and design an appropriate control law for the first equation under this assumption by using a Lyapunov function. By stepping back through the integrator to the second differential equation, meaning towards the input of the system, and accounting the state of the third differential equation as input to the second equation, a feasible control for the second equation is derived with the help of an adequate Lyapunov function. The repeated application of these steps leads to the control law for the overall system in the last differential equation. Because the interim control variables, e.g. the state of the second equation, are not always at their desired values, error definitions are conducted during the procedure. Besides the control

law, update laws for the unknown parameters in the system are designed from the derivative of the Lyapunov functions. The design of the controller and the update laws is interlaced in adaptive Backstepping.
If applied, this procedure generates multiple update laws, meaning also parameter estimates, for an unknown parameter. The number of parameter estimates is identical to the number of differential equations of the system. This behavior is denoted overparametrization. The further development of the methodology illustrated in [70] and [69] reduces the overparametrization of adaptive Backstepping. Following this development, other Backstepping varieties evolved. [71] constitutes a contiguous illustration. The methodology of input-to-state stability Backstepping, for example, provides the ability to separate the update law and controller design. The requirement to handle time-varying parameters, bounded disturbances, and provide stability without adaptation lead to the implementation of nonlinear damping terms into the Backstepping methodologies, as presented in [71].
After its invention in 1991, the Backstepping methodology has been in the focus of research regularly. Different authors applied the Backstepping methodology to various types of systems. Besides the basic examples given in [71], the application of the Backstepping methodology to a jet engine compressor is illustrated in [72]. The possibility of utilizing Backstepping for the control of spacecraft is demonstrated in [146]. Starting 2003, the use of the Backstepping method for flight control was demonstrated and further developed. The results are available in [43], [44], and [133]. One of the first applications of the Backstepping methodology to missile control is shown in [92]. A more detailed treatment of Backstepping based missile control is illustrated in [128] and [131].
The available literature comprises examples for the utilization of the adaptive Backstepping methodology for aerospace systems. A control design for spacecraft which is based on adaptive Backstepping is presented in [77]. The first employment of this methodology to flight control is illustrated in [118]. Further detailed and elaborated adaptive Backstepping flight control designs are presented in [123], [124], and [139]. Recently, the application of adaptive Backstepping to flight control of an unmanned aerial vehicle was achieved. The design is available in [144]. Besides a Backstepping based missile control, [131] contains an adaptive Backstepping design.
The first employment of input-to-state stability Backstepping in missile control is illustrated in [137] and [138]. The presentation in [3] contains nonlinear damping terms. In addition, nonlinear damping terms are used in the designs illustrated in [131].
In the following, the theoretical background of the nonlinear control methodology Backstepping is presented. Starting from Backstepping designs for systems without uncertainties, more intricate designs are introduced successively, leading to the design procedure for parametric strict-feedback systems with uncertain control coefficients. It is augmented by nonlinear damping terms, finally. Besides adaptive Backstepping, augmented by nonlinear damping terms, none of the further developments mentioned above is introduced herein. This is motivated by the aims stated at the beginning of the thesis. Because at the moment no source presenting a nonlinear, adaptive flight control system which can be applied to a real endo-atmospheric dual-actuator interceptor is on hand, it is reasonable to develop such system first using adaptive Backstepping, before other methods are accounted for. The design procedures in this thesis are developed only for systems of two differential equations, because these are of importance for the design of the interceptor flight control system. The presentation of recursive design procedure for systems consisting out of more differential equations would not allow to stay in the desired scope.
The following introduction generates a solid foundation of understanding of the Backstepping method for the design of the interceptor flight control system in the following chapters. By separating the theoretical background from the design of the interceptor flight control system, a concentration on the interceptor specifics during the execution of the design process is possible.

4.2 Backstepping

4.2.1 Basic stability theorems

The following sections introduce the Backstepping methodology and illustrate its usage for the control of nonlinear systems. Strict-feedback systems composed of scalar equations as well as strict-feedback systems consisting of two ordinary differential equations are considered. As introduced above, strict-feedback systems have a lower triangular structure, where the individual differential equations contain only the states up to the considered equation plus the state of the next differential equation. The particular differential equations comprise two nonlinearities which depend on the states up to the actual equation. One of the nonlinearities is multiplied by the state of the following equation or the input respectively, if it is the lowest equation of the triangular system. For this class of systems the control tasks of regulation and tracking are covered. The boundedness and stability properties of the respective controlled systems are affiliated based on Lyapunov stability. Furthermore, the relationship between the control parameters and the transient performance of the respective controlled systems is illustrated.
Stability is the primary requirement for all control systems. Lyapunov stability constitutes an established and widely spread concept in control theory. Due to the fact that Lyapunov stability provides the basis for the derivation of the boundedness and stability properties of controlled systems in this thesis, related stability properties as well as stability theorems are introduced now. A detailed presentation of Lyapunov stability and connoted concepts is available in [66]. The latter, in combination with [71], forms the foundation for this introduction.
A nonlinear, non-autonomous system is given by (4.1), whereupon $\vec{x} \in \mathbb{R}^n$ and $f : \mathbb{R}^n \times \mathbb{R}_+ \to \mathbb{R}^n$ is piecewise continuous in t and locally Lipschitz in $\vec{x}$. The origin $\vec{x} = 0$ is an equilibrium of (4.1) at $t = 0$; (4.2) holds.

$$\dot{\vec{x}} = f(\vec{x}, t) \tag{4.1}$$

$$f(0, t) = 0, \quad \forall t \geq 0 \tag{4.2}$$

Then the equilibrium $\vec{x} = 0$ of (4.1) is

- *stable*, if for each $\varepsilon > 0$ there exists a $\delta = \delta(\varepsilon, t_0) > 0$ such that

$$\|\vec{x}(t_0)\| < \delta \Rightarrow \|\vec{x}(t)\| < \varepsilon, \quad \forall t \geq t_0 \geq 0 \tag{4.3}$$

- *uniformly stable*, if for each $\varepsilon > 0$ there is $\delta = \delta(\varepsilon) > 0$, independent of t_0, such that (4.3) is satisfied.

- *unstable*, if it is not stable.

- *asymptotically stable*, if it is stable, and there is a positive constant $c = c(t_0)$ such that $\vec{x}(t) \to 0$ as $t \to \infty$, for all $\|\vec{x}(t_0)\| < c$.

- *uniformly asymptotically stable*, if it is uniformly stable, and there is a positive constant c, independent of t_0, such that $\vec{x}(t) \to 0$ as $t \to \infty$, for all $\|\vec{x}(t_0)\| < c$, uniformly in t_0; that is, for each $\eta > 0$, there is $T = T(\eta) > 0$ such that

$$\|\vec{x}(t)\| < \eta, \quad \forall t \geq t_0 + T(\eta), \quad \forall \|\vec{x}(t_0)\| < c \tag{4.4}$$

- *globally uniformly asymptotically stable*, if it is uniformly stable, $\delta(\varepsilon)$ can be chosen to satisfy $\lim_{\varepsilon \to \infty} \delta(\varepsilon) = \infty$, and for each pair of positive numbers η and c, there is $T = T(\eta, c) > 0$ such that

$$\|\vec{x}(t)\| < \eta, \quad \forall t \geq t_0 + T(\eta, c), \quad \forall \|\vec{x}(t_0)\| < c \tag{4.5}$$

Utilizing the stated stability property definitions, the following theorems are derived from [74] and [145]. These theorems constitute excellent tools for convergence analysis.

Theorem 4.1 (LaSalle-Yoshizawa, as in [71]) *Let $\vec{x} = 0$ be an equilibrium point of (4.1) and suppose $f(\vec{x}, t)$ is locally Lipschitz in $\vec{x}$ uniformly in t. Let $V : \mathbb{R}^n \to \mathbb{R}_+$ be a continuously differentiable, positive definite, and radially unbounded function $V(\vec{x})$ such that*

$$\dot{V}(\vec{x}) = \frac{\partial V(\vec{x})}{\partial \vec{x}} f(\vec{x}, t) \leq -W(\vec{x}) \leq 0, \quad \forall t \geq 0, \quad \forall \vec{x} \in \mathbb{R}^n, \tag{4.6}$$

whereupon $W : \mathbb{R}^n \to \mathbb{R}_+$ is a continuous function. Then, all solutions of (4.1) are globally uniformly bounded and satisfy

$$\lim_{t \to \infty} W(\vec{x}(t)) = 0. \tag{4.7}$$

In addition, if $W(\vec{x})$ is positive definite, then the equilibrium $\vec{x} = 0$ is globally uniformly asymptotically stable.

Theorem 4.2 (LaSalle, following [66]) *Let Ω be a positively invariant set of the nonlinear, autonomous system $\dot{\vec{x}} = f(\vec{x})$. Let $V : \Omega \to \mathbb{R}_+$ be a continuously differentiable function $V(\vec{x})$ such that*

$$\dot{V}(\vec{x}) \leq 0, \quad \forall \vec{x} \in \Omega. \tag{4.8}$$

Let $E = \left\{ \vec{x} \in \Omega \mid \dot{V}(\vec{x}) = 0 \right\}$, and let M be the largest invariant set contained in E. Then, every bounded solution $\vec{x}(t)$ starting in Ω converges to M as $t \to \infty$.

The mentioned property of radial unboundedness means that $V(\vec{x}) \to \infty$ for $\|\vec{x}\| \to \infty$. The definition of the concepts invariant set and positively invariant set is given in [66]. The term invariant set denotes as set which has the property that if the solution of the nonlinear, autonomous system belongs to the set at a certain time instant, it belongs to this set for all times; future and past. If the solution of a nonlinear, autonomous system belongs to a set starting at a distinct time instant and belongs to this set for all future times, the set is named positively invariant.
Theorem 4.2 allows to conclude that if $\vec{x} = 0$ is the only equilibrium of the nonlinear, autonomous system $\dot{\vec{x}} = f(\vec{x})$, $V : \mathbb{R}^n \to \mathbb{R}_+$ is a continuously differentiable, positive definite, radially unbounded function $V(\vec{x})$ such that (4.8) holds for all $\vec{x} \in \mathbb{R}^n$, $E = \left\{ \vec{x} \in \mathbb{R}^n \mid \dot{V}(\vec{x}) = 0 \right\}$ and no solution other than $\vec{x}(t) \equiv 0$ can stay forever in E, then the origin is globally asymptotically stable.
This stability properties and theorems are the foundation for the presentation of the basic principle of Backstepping and the recursive design procedure for strict-feedback systems in the following.

4.2.2 Strict-feedback systems

Before the recursive design procedure for strict-feedback systems is introduced, the basic principle of Backstepping is illustrated on the simple nonlinear system given by (4.9) and (4.10). The illustration follows [71].

$$\dot{x}_1 = f(x_1) + g(x_1) x_2 \tag{4.9}$$

$$\dot{x}_2 = u \tag{4.10}$$

Assuming that the nonlinear system would only consist of (4.9) and that the state x_2 would be the input u, (4.11) would result. The nonlinearity $f(x_1)$ in (4.11) is presumed to fulfill (4.12).

$$\dot{x}_1 = f(x_1) + g(x_1)\, u \tag{4.11}$$

$$f(0) = 0 \tag{4.12}$$

A feasible controller for (4.11) is designed by using the following approach. First, a Lyapunov function $V_1(x_1)$ is chosen like (4.13). $V_1(x_1)$ exhibits the properties of continuous differentiability, positive definiteness, and radial unboundedness stated in Theorem 4.1. The derivative of $V_1(x_1)$ is developed as (4.14) by using (4.11).

$$V_1(x_1) = \frac{1}{2} x_1^2 \tag{4.13}$$

$$\begin{aligned} \dot{V}_1(x_1) &= x_1 \dot{x}_1 \\ &= x_1 \left[f(x_1) + g(x_1)\, u \right] \end{aligned} \tag{4.14}$$

If the control u is chosen as (4.15), whereupon $c_1 \in \mathbb{R}_+$, the derivative of $V_1(x_1)$ simplifies to (4.16).

$$u = \frac{1}{g(x_1)} \left[-f(x_1) - c_1 x_1 \right] \tag{4.15}$$

$$\begin{aligned} \dot{V}_1(x_1) &= x_1 \left[f(x_1) + g(x_1) \cdot \frac{1}{g(x_1)} \left[-f(x_1) - c_1 x_1 \right] \right] \\ &= x_1 \left[f(x_1) - f(x_1) - c_1 x_1 \right] \\ &= -c_1 x_1^2 \end{aligned} \tag{4.16}$$

Because $c_1 \in \mathbb{R}_+$ is given, as mentioned above, (4.17) holds.

$$\dot{V}_1(x_1) = -c_1 x_1^2 \leq 0, \quad \forall x_1 \in \mathbb{R} \tag{4.17}$$

Referring back to Theorem 4.1, it becomes clear that the latter guarantees that all solutions $x_1(t)$ of (4.11) are globally bounded. Identifying $W(x_1(t))$ as $W(x_1(t)) = c_1 x_1^2$ in terms of Theorem 4.1, it is obvious that $W(x_1(t)) = 0$ for $t \to \infty$ as stated in (4.7). Because $W(x_1(t))$ is also positive definite, the equilibrium $x_1 = 0$ of (4.11) is guaranteed to be globally asymptotically stable by Theorem 4.1.
Considering $\mathbb{R}$ as Ω in Theorem 4.2 and noticing that $V_1 : \mathbb{R} \to \mathbb{R}_+$ as well as (4.8) is equal to (4.17), Theorem 4.2 guarantees that $x_1(t)$ converges to the largest invariant set M contained in the set $E = \{x_1 \in \mathbb{R} \mid W(x_1) = 0\}$. It is evident that the E as well as M encompass only the point $x_1 = 0$ in this case, because of $c_1 \in \mathbb{R}_+$.
Coming back to (4.9) and (4.10), it becomes clear that u, as chosen in (4.15), can not be used to control x_1, due to the fact that (4.9) only contains x_2. Therefore, x_1 is controlled via x_2. The latter itself is not specifiable directly, but can be influenced by u in (4.10). (4.15) is understood as the desired x_2, because it leads to the derived boundedness and stability properties. Because x_2 will differ from the desired value of (4.15), an error variable z is defined as stated in (4.18). The desired value of x_2 is represented by $\alpha(x_1)$, the stabilizing function, following the denotation in [71].

$$z = x_2 - \alpha(x_1) \tag{4.18}$$

By using (4.18) as well as the derivative of z, (4.9) and (4.10) are rewritten as (4.19) and (4.20).

$$\dot{x}_1 = f(x_1) + g(x_1)[z + \alpha(x_1)] \tag{4.19}$$

$$\dot{z} = u - \frac{\partial \alpha(x_1)}{\partial x_1}[f(x_1) + g(x_1)[z + \alpha(x_1)]] \tag{4.20}$$

Defining the Lyapunov function $V_2(x_1, z)$ as (4.21), whereupon $V_1(x_1)$ is given by (4.13), the derivative $\dot{V}_2(x_1, z)$ is written as (4.22). (4.16) is used in the latter derivation. The functions are written without their arguments to enhance readability.

$$\begin{aligned} V_2(x_1, z) &= V_1(x_1) + \frac{1}{2}z^2 \\ &= \frac{1}{2}x_1^2 + \frac{1}{2}z^2 \end{aligned} \tag{4.21}$$

$$\begin{aligned} \dot{V}_2(x_1, z) &= x_1\dot{x}_1 + z\dot{z} \\ &= x_1[f + gz + g\alpha] + z\left[u - \frac{\partial \alpha}{\partial x_1}(f + gz + g\alpha)\right] \\ &= x_1[f + g\alpha] + z\left[u - \frac{\partial \alpha}{\partial x_1}(f + gz + g\alpha) + x_1 g\right] \end{aligned} \tag{4.22}$$

$\alpha(x_1)$, which is the desired value of x_2 according to (4.15), as introduced above, is implemented in (4.22).

$$\begin{aligned} \dot{V}_2(x_1, z) &= x_1\left[f + g\frac{1}{g}(-f - c_1 x_1)\right] + z\left[u - \frac{\partial \alpha}{\partial x_1}\left(f + gz + g\frac{1}{g}(-f - c_1 x_1)\right) + x_1 g\right] \\ &= x_1[f - f - c_1 x_1] + z\left[u - \frac{\partial \alpha}{\partial x_1}(f + gz - f - c_1 x_1) + x_1 g\right] \\ &= -c_1 x_1^2 + z\left[u - \frac{\partial \alpha}{\partial x_1}(gz - c_1 x_1) + x_1 g\right] \end{aligned} \tag{4.23}$$

Choosing the control u as given in (4.24), with $c_2 \in \mathbb{R}_+$, Equation (4.23) is simplified to (4.25).

$$u = -c_2 z + \frac{\partial \alpha}{\partial x_1}(gz - c_1 x_1) - x_1 g \tag{4.24}$$

$$\dot{V}_2(x_1, z) = -c_1 x_1^2 - c_2 z^2 \tag{4.25}$$

Because (4.26) holds, Theorem 4.1 guarantees global boundedness of $x_1(t)$ and $z(t)$. Hence, all solutions of (4.19) and (4.20) are globally bounded. The boundedness of $x_1(t)$ and $z(t)$ in combination with (4.18) guarantees global boundedness of $x_2(t)$. Therefore, all solutions of (4.9) and (4.10) are globally bounded. In addition, $W(x_1(t), z(t)) = c_1 x_1^2 + c_2 z^2$ is regulated according to (4.27). The positive definiteness of $W(x_1(t), z(t))$ leads to the global asymptotic stability of $x_1 = 0$, $z = 0$ via Theorem 4.1. This implies that $x_1 = 0$, $x_2 = 0$ is the global asymptotic stable equilibrium of (4.9) and (4.10).

$$\dot{V}_2(x_1, z) = -c_1 x_1^2 - c_2 z^2 \leq 0, \quad \forall x_1 \in \mathbb{R}, \quad \forall z \in \mathbb{R} \tag{4.26}$$

$$\lim_{t \to \infty} W(x_1(t), z(t)) = 0 \tag{4.27}$$

Theorem 4.2 guarantees convergence of $\begin{bmatrix} x_1(t) & z(t) \end{bmatrix}^T$ to the largest invariant set contained in the set $\left\{ \begin{bmatrix} x_1(t) & z(t) \end{bmatrix}^T \in \mathbb{R}^2 \mid x_1 = 0, z = 0 \right\}$.

Design procedure for strict-feedback systems

After presenting the basic principle of Backstepping on a simple nonlinear system, the recursive design procedure for strict-feedback systems is introduced. The presentation is based on [71]. The strict-feedback system is given by (4.28) and (4.29).

$$\dot{x}_1 = f_1(x_1) + g_1(x_1)\, x_2 \tag{4.28}$$

$$\dot{x}_2 = f_2(x_1, x_2) + g_2(x_1, x_2)\, u \tag{4.29}$$

First, an error variable z is defined according to (4.30), following the example above. Utilizing this definition, (4.28) is rewritten as (4.31). The Lyapunov function $V_1(x_1)$ for (4.31) is chosen as (4.32). The derivative of $V_1(x_1)$ is given by (4.33).

$$z = x_2 - \alpha(x_1) \tag{4.30}$$

$$\dot{x}_1 = f_1(x_1) + g_1(x_1)\,[z + \alpha(x_1)] \tag{4.31}$$

$$V_1(x_1) = \frac{1}{2} x_1^2 \tag{4.32}$$

$$\begin{aligned} \dot{V}_1(x_1) &= x_1 \dot{x}_1 \\ &= x_1 \left[f_1(x_1) + g_1(x_1)\,[z + \alpha(x_1)] \right] \end{aligned} \tag{4.33}$$

Now, the stabilizing function $\alpha(x_1)$ is chosen according to (4.34), whereupon $c_1 \in \mathbb{R}_+$. Utilizing $\alpha(x_1)$ in (4.33) leads to (4.35). Because the sign of the last term in (4.35) is unknown, no conclusion about the stability properties of (4.35) can be drawn.

$$\alpha(x_1) = \frac{1}{g_1(x_1)} \left[-f_1(x_1) - c_1 x_1 \right] \tag{4.34}$$

$$\begin{aligned} \dot{V}_1(x_1) &= x_1 f_1(x_1) + x_1 g_1(x_1)\, z + x_1 g_1(x_1)\, \alpha(x_1) \\ &= -c_1 x_1^2 + x_1 g_1(x_1)\, z \end{aligned} \tag{4.35}$$

The derivative of z, which is given in (4.36), is further developed to (4.37). (4.29), (4.31), and (4.34) are used.

$$\dot{z} = \dot{x}_2 - \dot{\alpha}(x_1) \tag{4.36}$$

$$\begin{aligned} &= f_2(x_1, x_2) + g_2(x_1, x_2)\, u - \dot{\alpha}(x_1) \\ &= f_2(x_1, x_2) + g_2(x_1, x_2)\, u - \frac{\partial \alpha(x_1)}{\partial x_1} \dot{x}_1 \\ &= f_2(x_1, x_2) + g_2(x_1, x_2)\, u - \frac{\partial \alpha(x_1)}{\partial x_1} \left[f_1(x_1) + g_1(x_1)\,[z + \alpha(x_1)] \right] \\ &= f_2(x_1, x_2) + g_2(x_1, x_2)\, u - \frac{\partial \alpha(x_1)}{\partial x_1} \left[g_1(x_1)\, z - c_1 x_1 \right] \end{aligned} \tag{4.37}$$

The Lyapunov function $V_2(x_1, z)$ is defined in accordance with (4.38). The derivative of $V_2(x_1, z)$ is developed to (4.39) by employing (4.35) and (4.37).

$$V_2(x_1, z) = V_1(x_1) + \frac{1}{2} z^2$$

$$= \frac{1}{2}x_1^2 + \frac{1}{2}z^2 \tag{4.38}$$

$$\begin{aligned}\dot{V}_2(x_1, z) &= x_1\dot{x}_1 + z\dot{z} \\ &= -c_1x_1^2 + x_1g_1(x_1)z \\ &\quad + z\left[f_2(x_1, x_2) + g_2(x_1, x_2)u - \frac{\partial\alpha(x_1)}{\partial x_1}[g_1(x_1)z - c_1x_1]\right]\end{aligned} \tag{4.39}$$

By choosing the control u as stated in (4.40), with $c_2 \in \mathbb{R}_+$, (4.39) is written as (4.41).

$$u = \frac{1}{g_2(x_1, x_2)}\left[-f_2(x_1, x_2) + \frac{\partial\alpha(x_1)}{\partial x_1}[g_1(x_1)z - c_1x_1] - x_1g_1(x_1) - c_2z\right] \tag{4.40}$$

$$\dot{V}_2(x_1, z) = -c_1x_1^2 - c_2z^2 \tag{4.41}$$

Following the derivation of the boundedness and stability properties in the illustration of the basic principle of Backstepping, Theorem 4.1 guarantees global boundedness of $x_1(t)$ and $z(t)$, because (4.42) holds. The boundedness of $x_1(t)$ and $z(t)$ in combination with (4.30) guarantees global boundedness of $x_2(t)$. For this reason, all solutions of (4.28) and (4.29) are globally bounded. Additionally, $x_1(t)$ and $z(t)$ are regulated based on Theorem 4.1. Seeing (4.30) and (4.34), the regulation of $x_2(t)$ is evident, if $f_1(0) = 0$. Because the derivative of $V_2(x_1, z)$ is negative definite, Theorem 4.1 guarantees global asymptotic stability of $x_1 = 0$, $z = 0$. Provided $f_1(0) = 0$, this implies that $x_1 = 0$, $x_2 = 0$ is the global asymptotic stable equilibrium of the strict-feedback system given by (4.28) and (4.29).

$$\dot{V}_2(x_1, z) = -c_1x_1^2 - c_2z^2 \leq 0, \quad \forall x_1 \in \mathbb{R}, \quad \forall z \in \mathbb{R} \tag{4.42}$$

Theorem 4.2 guarantees the convergence of $\begin{bmatrix}x_1(t) & z(t)\end{bmatrix}^T$ to the largest invariant set contained in the set $\left\{\begin{bmatrix}x_1(t) & z(t)\end{bmatrix}^T \in \mathbb{R}^2 \mid x_1 = 0, z = 0\right\}$.
The necessary conditions for the derived boundedness and stability properties are $c_1 \in \mathbb{R}_+$ and $c_2 \in \mathbb{R}_+$. In addition, (4.43) and (4.44) must hold. Otherwise, the strict-feedback system (4.28) and (4.29) is not controllable, and $\alpha(x_1)$ as well as u are not defined. The concept of controllability is not treated further to stay inside the scope of this thesis. A detailed illustration is available in [125].

$$g_1(x_1) \neq 0, \quad \forall x_1 \in \mathbb{R} \tag{4.43}$$

$$g_2(x_1, x_2) \neq 0, \quad \forall x_1 \in \mathbb{R}, \quad \forall x_2 \in \mathbb{R} \tag{4.44}$$

It is clear from (4.41) that the derivative of $V_2(x_1, z)$ is proportional to c_1 and c_2. This means that the strict-feedback system converges to its global asymptotic stable equilibrium $x_1 = 0$, $x_2 = 0$ faster, if c_1 and c_2 are increased. In contrast, (4.40) shows that increasing c_1 and c_2 results in a higher control effort. Therefore, optimal c_1 and c_2, which guarantee maximum speed of convergence at an allowable control effort, exist.
After presenting the basic principle of Backstepping and the recursive design procedure for strict-feedback systems, more complex systems are treated in the following.

4.2.3 Block Backstepping

While scalar strict-feedback systems have been treated beforehand, the following paragraphs illustrate Backstepping for strict-feedback systems which systems equations are composed of two ordinary differential equations. The design procedure is presented and the boundedness

and stability properties are derived. According to [66] and [71], which constitute the basis for the following illustration, this use case of the Backstepping methodology is denoted as Block Backstepping.
The strict-feedback system is given by (4.45) and (4.46). The states of the system are $\vec{x}_1 \in \mathbb{R}^n$ and $\vec{x}_2 \in \mathbb{R}^n$. The vector $\vec{u} \in \mathbb{R}^n$ constitutes the control input. $F_1 : \mathbb{R}^n \to \mathbb{R}^n$ and $F_2 : \mathbb{R}^n \to \mathbb{R}^n$ are vector fields of smooth nonlinear functions. $G_1 : \mathbb{R}^n \to \mathbb{R}^n \times \mathbb{R}^n$ and $G_2 : \mathbb{R}^n \to \mathbb{R}^n \times \mathbb{R}^n$ are square matrices which are composed of vector fields of smooth nonlinear functions.

$$\dot{\vec{x}}_1 = F_1(\vec{x}_1) + G_1(\vec{x}_1)\,\vec{x}_2 \tag{4.45}$$

$$\dot{\vec{x}}_2 = F_2(\vec{x}_1, \vec{x}_2) + G_2(\vec{x}_1, \vec{x}_2)\,\vec{u} \tag{4.46}$$

Following the methodology for scalar strict-feedback systems, an error variable $\vec{z}$ is defined according to (4.47); $\vec{z} \in \mathbb{R}^n$ and the stabilizing function $\alpha(\vec{x}_1)$ constitutes a vector field $\alpha : \mathbb{R}^n \to \mathbb{R}^n$. Utilizing the definition of $\vec{z}$ in (4.45) leads to (4.48).

$$\vec{z} = \vec{x}_2 - \alpha(\vec{x}_1) \tag{4.47}$$

$$\dot{\vec{x}}_1 = F_1(\vec{x}_1) + G_1(\vec{x}_1)\,[\vec{z} + \alpha(\vec{x}_1)] \tag{4.48}$$

The Lyapunov function $V_1(\vec{x}_1)$ for (4.48) is chosen as (4.49). The derivative of $V_1(\vec{x}_1)$ is derived according to (4.50).

$$V_1(\vec{x}_1) = \frac{1}{2}\vec{x}_1^T\vec{x}_1 \tag{4.49}$$

$$\begin{aligned}\dot{V}_1(\vec{x}_1) &= \vec{x}_1^T\dot{\vec{x}}_1 \\ &= \vec{x}_1^T\,[F_1(\vec{x}_1) + G_1(\vec{x}_1)\,[\vec{z} + \alpha(\vec{x}_1)]]\end{aligned} \tag{4.50}$$

At this point, the stabilizing function $\alpha(\vec{x}_1)$ is taken as stated in (4.51), where $C_1 \in \mathbb{R}^n \times \mathbb{R}^n$ is positive definite, meaning that all eigenvalues of C_1 are positive. The derivative of $V_1(\vec{x}_1)$ is developed to (4.52) by employing (4.51) in (4.50).

$$\alpha(\vec{x}_1) = G_1^{-1}(\vec{x}_1)\,[-F_1(\vec{x}_1) - C_1\vec{x}_1] \tag{4.51}$$

$$\begin{aligned}\dot{V}_1(\vec{x}_1) &= \vec{x}_1^T F_1(\vec{x}_1) + \vec{x}_1^T G_1(\vec{x}_1)\,\vec{z} + \vec{x}_1^T G_1(\vec{x}_1)\,\alpha(\vec{x}_1) \\ &= -\vec{x}_1^T C_1\vec{x}_1 + \vec{x}_1^T G_1(\vec{x}_1)\,\vec{z}\end{aligned} \tag{4.52}$$

The unknown sign of the last term in (4.52) prevents a conclusion about the boundedness and stability properties of the strict-feedback system at this point of the procedure. Hence, the latter is continued exactly as for the scalar strict-feedback system. The derivative of $\vec{z}$, which is given by (4.53), is manipulated to (4.54). (4.46), (4.48), and (4.51) are used. The term $\frac{\partial\alpha(\vec{x}_1)}{\partial\vec{x}_1}$ constitutes the Jacobi-Matrix of $\alpha(\vec{x}_1)$.

$$\dot{\vec{z}} = \dot{\vec{x}}_2 - \dot{\alpha}(\vec{x}_1) \tag{4.53}$$

$$\begin{aligned}&= F_2(\vec{x}_1, \vec{x}_2) + G_2(\vec{x}_1, \vec{x}_2)\,\vec{u} - \dot{\alpha}(\vec{x}_1) \\ &= F_2(\vec{x}_1, \vec{x}_2) + G_2(\vec{x}_1, \vec{x}_2)\,\vec{u} - \frac{\partial\alpha(\vec{x}_1)}{\partial\vec{x}_1}\dot{\vec{x}}_1 \\ &= F_2(\vec{x}_1, \vec{x}_2) + G_2(\vec{x}_1, \vec{x}_2)\,\vec{u} - \frac{\partial\alpha(\vec{x}_1)}{\partial\vec{x}_1}\,[F_1(\vec{x}_1) + G_1(\vec{x}_1)\,[\vec{z} + \alpha(\vec{x}_1)]] \\ &= F_2(\vec{x}_1, \vec{x}_2) + G_2(\vec{x}_1, \vec{x}_2)\,\vec{u} - \frac{\partial\alpha(\vec{x}_1)}{\partial\vec{x}_1}\,[G_1(\vec{x}_1)\,\vec{z} - C_1\vec{x}_1]\end{aligned} \tag{4.54}$$

The Lyapunov function (4.49) is augmented according to (4.55). By employing (4.52) and (4.54), the derivative of $V_2(\vec{x}_1, \vec{z})$ is achieved. It is stated in (4.56).

$$\begin{aligned} V_2(\vec{x}_1, \vec{z}) &= V_1(\vec{x}_1) + \frac{1}{2}\vec{z}^T\vec{z} \\ &= \frac{1}{2}\vec{x}_1^T\vec{x}_1 + \frac{1}{2}\vec{z}^T\vec{z} \end{aligned} \tag{4.55}$$

$$\begin{aligned} \dot{V}_2(\vec{x}_1, \vec{z}) &= \vec{x}_1^T\dot{\vec{x}}_1 + \vec{z}^T\dot{\vec{z}} \\ &= -\vec{x}_1^T C_1\vec{x}_1 + \vec{x}_1^T G_1(\vec{x}_1)\vec{z} \\ &\quad + \vec{z}^T\Big[F_2(\vec{x}_1, \vec{x}_2) + G_2(\vec{x}_1, \vec{x}_2)\vec{u} \\ &\quad - \frac{\partial\alpha(\vec{x}_1)}{\partial\vec{x}_1}\left[G_1(\vec{x}_1)\vec{z} - C_1\vec{x}_1\right]\Big] \\ &= -\vec{x}_1^T C_1\vec{x}_1 + \vec{z}^T G_1^T(\vec{x}_1)\vec{x}_1 \\ &\quad + \vec{z}^T\Big[F_2(\vec{x}_1, \vec{x}_2) + G_2(\vec{x}_1, \vec{x}_2)\vec{u} \\ &\quad - \frac{\partial\alpha(\vec{x}_1)}{\partial\vec{x}_1}\left[G_1(\vec{x}_1)\vec{z} - C_1\vec{x}_1\right]\Big] \\ &= -\vec{x}_1^T C_1\vec{x}_1 \\ &\quad + \vec{z}^T\Big[F_2(\vec{x}_1, \vec{x}_2) + G_2(\vec{x}_1, \vec{x}_2)\vec{u} \\ &\quad - \frac{\partial\alpha(\vec{x}_1)}{\partial\vec{x}_1}\left[G_1(\vec{x}_1)\vec{z} - C_1\vec{x}_1\right] + G_1^T(\vec{x}_1)\vec{x}_1\Big] \end{aligned} \tag{4.56}$$

Now, the control $\vec{u}$ is chosen as (4.57). $C_2 \in \mathbb{R}^n \times \mathbb{R}^n$ is positive definite. Implementing $\vec{u}$ in (4.56) leads to (4.58) for the derivative of $V_2(\vec{x}_1, \vec{z})$.

$$\vec{u} = G_2^{-1}(\vec{x}_1, \vec{x}_2)\left[-F_2(\vec{x}_1, \vec{x}_2) + \frac{\partial\alpha(\vec{x}_1)}{\partial\vec{x}_1}\left[G_1(\vec{x}_1)\vec{z} - C_1\vec{x}_1\right] - G_1^T(\vec{x}_1)\vec{x}_1 - C_2\vec{z}\right] \tag{4.57}$$

$$\dot{V}_2(\vec{x}_1, \vec{z}) = -\vec{x}_1^T C_1\vec{x}_1 - \vec{z}^T C_2\vec{z} \tag{4.58}$$

Considering (4.59), global boundedness of $\vec{x}_1(t)$ and $\vec{z}(t)$ is guaranteed by Theorem 4.1. Combining this result with (4.47) provides the global boundedness of $\vec{x}_2(t)$. Hence, all solutions of the strict-feedback system (4.45), (4.46) are globally bounded. Theorem 4.1 guarantees the regulation of $\vec{x}_1(t)$ and $\vec{z}(t)$. Based on (4.47), this implies the regulation of $\vec{x}_2(t)$, if $F_1(0) = 0$. The negative definiteness of the derivative of $V_2(\vec{x}_1, \vec{z})$ in combination with Theorem 4.1 leads to global asymptotic stability of $\vec{x}_1 = 0, \vec{z} = 0$. Taking into account (4.47) and assuming $F_1(0) = 0$, the global asymptotic stable equilibrium of the strict-feedback system (4.45), (4.46) is given by $\vec{x}_1 = 0$ and $\vec{x}_2 = 0$.

$$\dot{V}_2(\vec{x}_1, \vec{z}) = -\vec{x}_1^T C_1\vec{x}_1 - \vec{z}^T C_2\vec{z} \leq 0, \quad \forall\vec{x}_1 \in \mathbb{R}^n, \quad \forall\vec{z} \in \mathbb{R}^n \tag{4.59}$$

Theorem 4.2 guarantees the convergence of $\begin{bmatrix}\vec{x}_1(t) & \vec{z}(t)\end{bmatrix}^T$ to the largest invariant set contained in the set $\left\{\begin{bmatrix}\vec{x}_1(t) & \vec{z}(t)\end{bmatrix}^T \in \mathbb{R}^{2n} \mid \vec{x}_1 = 0, \vec{z} = 0\right\}$.
The derived boundedness and stability properties of the strict-feedback system are based on the positive definiteness of $C_1 \in \mathbb{R}^n \times \mathbb{R}^n$ and $C_2 \in \mathbb{R}^n \times \mathbb{R}^n$. $G_1(\vec{x}_1)$ and $G_2(\vec{x}_1, \vec{x}_2)$ must be nonsingular in their domain to ensure the existence of their respective inverse which are utilized in (4.51) and (4.57).

4.2.4 Tracking

The presentations up to this point of the thesis considered scalar and vector strict-feedback systems. In either case, regulation has been the implicit aim of the control design. It is shown in the following that the Backstepping methodology allows to achieve the control task of tracking. The Backstepping control law is designed in such a way that the output of the strict-feedback system follows a known, smooth, and bounded reference signal. The related boundedness and stability properties are derived. This illustration augments [71] which does not treat tracking in the situation without uncertainties.
Following the design procedure for strict-feedback systems, the latter is given by (4.60) and (4.61). The output y of the strict-feedback system is defined in (4.62).

$$\dot{x}_1 = f_1(x_1) + g_1(x_1)\, x_2 \tag{4.60}$$
$$\dot{x}_2 = f_2(x_1, x_2) + g_2(x_1, x_2)\, u \tag{4.61}$$
$$y = x_1 \tag{4.62}$$

The known, smooth, and bounded reference signal, which y shall follow, is given by $x_{1,Ref}$. It is assumed that all derivatives of $x_{1,Ref}$ are known, smooth, and bounded.
First, two error variables z_1 and z_2 are defined according to (4.63) and (4.64). The derivative of z_1 is written as (4.65) by using (4.60) and (4.64).

$$z_1 = x_1 - x_{1,Ref} \tag{4.63}$$
$$z_2 = x_2 - \alpha(x_1, x_{1,Ref}, \dot{x}_{1,Ref}) \tag{4.64}$$

$$\begin{aligned}\dot{z}_1 &= \dot{x}_1 - \dot{x}_{1,Ref} \\ &= f_1(x_1) + g_1(x_1)\, x_2 - \dot{x}_{1,Ref} \\ &= f_1(x_1) + g_1(x_1)\,[z_2 + \alpha(x_1, x_{1,Ref}, \dot{x}_{1,Ref})] - \dot{x}_{1,Ref}\end{aligned} \tag{4.65}$$

The Lyapunov function $V_1(z_1)$ for (4.65) is chosen as (4.66). The derivative of $V_1(z_1)$ is calculated as stated in (4.67).

$$V_1(z_1) = \frac{1}{2} z_1^2 \tag{4.66}$$

$$\begin{aligned}\dot{V}_1(z_1) &= z_1 \dot{z}_1 \\ &= z_1\,[f_1(x_1) + g_1(x_1)\,[z_2 + \alpha(x_1, x_{1,Ref}, \dot{x}_{1,Ref})] - \dot{x}_{1,Ref}]\end{aligned} \tag{4.67}$$

The stabilizing function $\alpha(x_1, x_{1,Ref}, \dot{x}_{1,Ref})$ is chosen according to (4.68), with $c_1 \in \mathbb{R}_+$. The derivative of $V_1(z_1)$ simplifies to (4.69) with this choice.

$$\alpha(x_1, x_{1,Ref}, \dot{x}_{1,Ref}) = \frac{1}{g_1(x_1)}\,[-f_1(x_1) + \dot{x}_{1,Ref} - c_1 z_1] \tag{4.68}$$

$$\dot{V}_1(z_1) = -c_1 z_1^2 + z_1 g_1(x_1)\, z_2 \tag{4.69}$$

A conclusion about the stability properties is not possible, because the sign of the second term in (4.69) is unknown. Now, the derivative of z_2 is affiliated according to (4.70). (4.61) is employed in the derivation of (4.70).

$$\begin{aligned}\dot{z}_2 &= \dot{x}_2 - \dot{\alpha}(x_1, x_{1,Ref}, \dot{x}_{1,Ref}) \\ &= f_2(x_1, x_2) + g_2(x_1, x_2)\, u - \dot{\alpha}(x_1, x_{1,Ref}, \dot{x}_{1,Ref})\end{aligned} \tag{4.70}$$

The derivative of $\alpha\left(x_1, x_{1,Ref}, \dot{x}_{1,Ref}\right)$ in (4.70) is available as the analytic expression provided in (4.71).

$$\begin{aligned}\dot{\alpha}\left(x_1, x_{1,Ref}, \dot{x}_{1,Ref}\right) &= \frac{\partial \alpha\left(x_1, x_{1,Ref}, \dot{x}_{1,Ref}\right)}{\partial x_1}\dot{x}_1 \\ &\quad + \frac{\partial \alpha\left(x_1, x_{1,Ref}, \dot{x}_{1,Ref}\right)}{\partial x_{1,Ref}}\dot{x}_{1,Ref} + \frac{\partial \alpha\left(x_1, x_{1,Ref}, \dot{x}_{1,Ref}\right)}{\partial \dot{x}_{1,Ref}}\ddot{x}_{1,Ref} \\ &= \frac{\partial \alpha\left(x_1, x_{1,Ref}, \dot{x}_{1,Ref}\right)}{\partial x_1}\left[f_1\left(x_1\right) + g_1\left(x_1\right)x_2\right] \\ &\quad + \frac{\partial \alpha\left(x_1, x_{1,Ref}, \dot{x}_{1,Ref}\right)}{\partial x_{1,Ref}}\dot{x}_{1,Ref} + \frac{\partial \alpha\left(x_1, x_{1,Ref}, \dot{x}_{1,Ref}\right)}{\partial \dot{x}_{1,Ref}}\ddot{x}_{1,Ref}\end{aligned} \tag{4.71}$$

The Lyapunov function $V_2\left(z_1, z_2\right)$ is taken as (4.72), and it constitutes an augmented version of the choice in (4.66). The derivative of $V_2\left(z_1, z_2\right)$ is developed as given by (4.73), whereupon (4.69) and (4.70) are utilized. The arguments of $\alpha\left(x_1, x_{1,Ref}, \dot{x}_{1,Ref}\right)$ are not written in (4.73) to enhance readability.

$$\begin{aligned}V_2\left(z_1, z_2\right) &= V_1\left(z_1\right) + \frac{1}{2}z_2^2 \\ &= \frac{1}{2}z_1^2 + \frac{1}{2}z_2^2\end{aligned} \tag{4.72}$$

$$\begin{aligned}\dot{V}_2\left(z_1, z_2\right) &= z_1\dot{z}_1 + z_2\dot{z}_2 \\ &= -c_1 z_1^2 + z_1 g_1\left(x_1\right)z_2 \\ &\quad + z_2\Bigg[f_2\left(x_1, x_2\right) + g_2\left(x_1, x_2\right)u \\ &\quad - \frac{\partial \alpha}{\partial x_1}\dot{x}_1 - \frac{\partial \alpha}{\partial x_{1,Ref}}\dot{x}_{1,Ref} - \frac{\partial \alpha}{\partial \dot{x}_{1,Ref}}\ddot{x}_{1,Ref}\Bigg]\end{aligned} \tag{4.73}$$

With (4.74) for the control u, $c_2 \in \mathbb{R}_+$, the derivative of $V_2\left(z_1, z_2\right)$ simplifies to (4.75).

$$u = \frac{1}{g_2\left(x_1, x_2\right)}\left[-f_2\left(x_1, x_2\right) + \frac{\partial \alpha}{\partial x_1}\dot{x}_1 + \frac{\partial \alpha}{\partial x_{1,Ref}}\dot{x}_{1,Ref} + \frac{\partial \alpha}{\partial \dot{x}_{1,Ref}}\ddot{x}_{1,Ref} - z_1 g_1\left(x_1\right) - c_2 z_2\right] \tag{4.74}$$

$$\dot{V}_2\left(z_1, z_2\right) = -c_1 z_1^2 - c_2 z_2^2 \tag{4.75}$$

Respecting (4.76), Theorem 4.1 guarantees global boundedness of $z_1\left(t\right)$ and $z_2\left(t\right)$. All solutions of the error system, comprising the states z_1 and z_2, are globally bounded. In addition, Theorem 4.1 guarantees the regulation of $z_1\left(t\right)$ and $z_2\left(t\right)$. Because the derivative of $V_2\left(z_1, z_2\right)$ is negative definite, Theorem 4.1 guarantees global asymptotic stability of $z_1 = 0$, $z_2 = 0$ for the error system. The error system in vector notation is given in (4.77).

$$\dot{V}_2\left(z_1, z_2\right) = -c_1 z_1^2 - c_2 z_2^2 \leq 0, \quad \forall z_1 \in \mathbb{R}, \quad \forall z_2 \in \mathbb{R} \tag{4.76}$$

$$\begin{bmatrix}\dot{z}_1 \\ \dot{z}_2\end{bmatrix} = \begin{bmatrix}-c_1 & g_1\left(x_1\right) \\ -g_1\left(x_1\right) & -c_2\end{bmatrix}\begin{bmatrix}z_1 \\ z_2\end{bmatrix} \tag{4.77}$$

The derived boundedness and stability properties of (4.77) lead to the achievement of the control task of tracking. The global boundedness $z_1\left(t\right)$ means that the difference between $y\left(t\right)$,

which is equal to $x_1(t)$, and $x_{1,Ref}(t)$ is globally bounded. The regulation of $z_1(t)$ implies that $y(t)$ converges to $x_{1,Ref}(t)$ for $t \to \infty$. Based on the global asymptotic stability property of $z_1 = 0$, $z_2 = 0$, this convergence exhibits global asymptotical behavior. Hence, the control task of tracking of $x_{1,Ref}(t)$ is achieved globally and asymptotically.
Concerning the boundedness of the strict-feedback system given by (4.60) and (4.61), the following conclusions are drawn. The global boundedness of $z_1(t)$ as well as the boundedness of $x_{1,Ref}(t)$ in combination with (4.63) lead to the boundedness $x_1(t)$. This result in conjunction with the boundedness of $x_{1,Ref}(t)$ implies the boundedness of $\alpha(x_1, x_{1,Ref}, \dot{x}_{1,Ref})$. Considering (4.64), the boundedness of $z_2(t)$ is derived leading finally to the boundedness of $x_2(t)$. For this reason, all solutions of the strict-feedback system (4.60), (4.61) are globally bounded.
If $x_{1,Ref}(t) \to 0$ for $t \to \infty$, the regulation of $z_1(t)$ implies $x_1(t) \to 0$ for $t \to \infty$. Provided $f_1(0) = 0$, $\alpha(x_1, x_{1,Ref}, \dot{x}_{1,Ref}) \to 0$ for $t \to \infty$ which in turn leads to $x_2(t) \to 0$ for $t \to \infty$, based on the regulation of $z_2(t)$. $x_1 = 0$, $x_2 = 0$ is the globally stable equilibrium of the strict-feedback system (4.60), (4.61), if $f_1(0) = 0$.
Theorem 4.2 guarantees the convergence of $\begin{bmatrix} z_1(t) & z_2(t) \end{bmatrix}^T$ to the largest invariant set contained in the set $\left\{ \begin{bmatrix} z_1(t) & z_2(t) \end{bmatrix}^T \in \mathbb{R}^2 \mid z_1 = 0, z_2 = 0 \right\}$.
The derived boundedness and stability properties are based on the appropriate choices of $c_1 \in \mathbb{R}_+$ and $c_2 \in \mathbb{R}_+$. Furthermore, (4.43) and (4.44) must hold to guarantee controllability of the strict-feedback system as well as the existence of $\alpha(x_1, x_{1,Ref}, \dot{x}_{1,Ref})$ and u. The concept of controllability is illustrated in [125] and not treated further herein.
Due to the dependency of the derivative of $V_2(z_1, z_2)$ from c_1 and c_2, which is evident from (4.75), the speed of convergence to the global asymptotic stable equilibrium $z_1 = 0$, $z_2 = 0$ of (4.77) increases, if c_1 and c_2 are increased. This means that the speed at which the control task of tracking is achieved is proportional to c_1 and c_2. Vice versa, considering (4.74), it is obvious that increased c_1 and c_2 result in a higher control effort. Hence, c_1 and c_2 are optimizable with respect to tracking performance and control effort.
The given presentation showed the utilization of the Backstepping methodology for the control task of tracking of a known, smooth, and bounded reference signal. The boundedness and stability properties have been derived and it has been demonstrated that global asymptotic tracking of a known, smooth, and bounded reference signal is achieved. Because the interceptor flight control system is designed to follow commands which are calculated by the interceptor guidance the presented theoretical background is of high importance.
If all properties of the interceptor would be known exactly, the presented theoretical background would be sufficient for the design of the interceptor flight control system. As already introduced in Chapter 2, the exact determination of all interceptor properties is impossible. Therefore, the theoretical background is augmented further.

4.3 Adaptive Backstepping

4.3.1 Parametric strict-feedback systems

After the theoretical background for strict-feedback systems without uncertainties has been presented, the application of the Backstepping methodology to strict-feedback systems which do comprise uncertain constant parameters is shown. Following [71], this use case of Backstepping is denoted as adaptive Backstepping. Parametric strict-feedback systems as well as the latter systems with unknown control coefficients are treated. Regulation and tracking of a known, smooth, and bounded reference signal are considered. Based on Chapter 2, these illustrations are of importance to enable the interceptor flight control system to overcome uncertain constant

parameters.
To introduce the concept of adaptive Backstepping, the simple, scalar, parametric nonlinear system given by (4.78) and (4.79) is used. This also follows [71].

$$\dot{x}_1 = f(x_1)\,\theta + g(x_1)\,x_2 \tag{4.78}$$

$$\dot{x}_2 = u \tag{4.79}$$

Under the assumption that the parametric nonlinear system would only encompass (4.78) and that x_2 would constitute the input u, (4.80) would remain. At this point, it is assumed further that the nonlinearity $f(x_1)$ fulfills (4.81).

$$\dot{x}_1 = f(x_1)\,\theta + g(x_1)\,u \tag{4.80}$$

$$f(0) = 0 \tag{4.81}$$

For this reduced system, consisting only of (4.80), a controller would be derived in the following way. Initially, a Lyapunov function $V_1(x_1, \tilde{\theta}_1)$ is chosen according to (4.82). $\tilde{\theta}_1$ is the parameter error which results from the fact that the parameter estimate, denoted by $\hat{\theta}_1$, differs from the real parameter value θ. It is defined in (4.83). The variable γ_1 is called adaptation gain and exhibits the property $\gamma_1 \in \mathbb{R}_+$.

$$V_1\left(x_1, \tilde{\theta}_1\right) = \frac{1}{2}x_1^2 + \frac{1}{2\gamma_1}\tilde{\theta}_1^2 \tag{4.82}$$

$$\tilde{\theta}_1 = \theta - \hat{\theta}_1 \tag{4.83}$$

The chosen $V_1(x_1, \tilde{\theta}_1)$ is continuous differentiable, positive definite, and radially unbounded. Its derivative is developed to (4.84), whereupon (4.80) is employed.

$$\begin{aligned}\dot{V}_1\left(x_1, \tilde{\theta}_1\right) &= x_1\dot{x}_1 + \frac{1}{\gamma_1}\tilde{\theta}_1\dot{\tilde{\theta}}_1 \\ &= x_1\left[f(x_1)\,\theta + g(x_1)\,u\right] + \frac{1}{\gamma_1}\tilde{\theta}_1\dot{\tilde{\theta}}_1\end{aligned} \tag{4.84}$$

Because θ is assumed to be constant, $\dot{\tilde{\theta}}_1$ is equal to $-\dot{\hat{\theta}}_1$, which can be seen from (4.83). By implementing this as well as (4.83) itself into (4.84), (4.85) is derived.

$$\begin{aligned}\dot{V}_1\left(x_1, \tilde{\theta}_1\right) &= x_1\left[f(x_1)\left(\tilde{\theta}_1 + \hat{\theta}_1\right) + g(x_1)\,u\right] - \frac{1}{\gamma_1}\tilde{\theta}_1\dot{\hat{\theta}}_1 \\ &= x_1\left[f(x_1)\,\tilde{\theta}_1 + f(x_1)\,\hat{\theta}_1 + g(x_1)\,u\right] - \frac{1}{\gamma_1}\tilde{\theta}_1\dot{\hat{\theta}}_1 \\ &= x_1\left[f(x_1)\,\hat{\theta}_1 + g(x_1)\,u\right] + f(x_1)\,\tilde{\theta}_1 - \frac{1}{\gamma_1}\tilde{\theta}_1\dot{\hat{\theta}}_1 \\ &= x_1\left[f(x_1)\,\hat{\theta}_1 + g(x_1)\,u\right] + \tilde{\theta}_1\left[x_1 f(x_1) - \frac{1}{\gamma_1}\dot{\hat{\theta}}_1\right]\end{aligned} \tag{4.85}$$

The choice for the update law for $\dot{\hat{\theta}}_1$ according to (4.86) simplifies (4.85) to (4.87).

$$\dot{\hat{\theta}}_1 = \gamma_1 x_1 f(x_1) \tag{4.86}$$

$$\dot{V}_1\left(x_1, \tilde{\theta}_1\right) = x_1\left[f(x_1)\,\hat{\theta}_1 + g(x_1)\,u\right] \tag{4.87}$$

Based on the fact that $\hat{\theta}_1$ is available from (4.86) via integration, the feasible control u, as stated in (4.88), can be chosen; $c_1 \in \mathbb{R}_+$. This control employed in (4.87) leads to (4.89).

$$u = \frac{1}{g(x_1)} \left[-f(x_1)\,\hat{\theta}_1 - c_1 x_1 \right] \tag{4.88}$$

$$\dot{V}_1\left(x_1, \tilde{\theta}_1\right) = -c_1 x_1^2 \tag{4.89}$$

Given that (4.90) holds, Theorem 4.1 guarantees that $x_1(t)$ and $\tilde{\theta}_1(t)$ are globally bounded.

$$\dot{V}_1\left(x_1, \tilde{\theta}_1\right) = -c_1 x_1^2 \leq 0, \quad \forall x_1 \in \mathbb{R}, \quad \forall \tilde{\theta}_1 \in \mathbb{R} \tag{4.90}$$

Understanding $W(x_1(t)) = c_1 x_1^2$ with respect to Theorem 4.1, it becomes clear that $x_1(t)$ is regulated. If $x_1(t)$ is regulated, $\hat{\theta}_1(t)$ reaches a steady-state based on (4.86), implying further that u reaches the steady-state according to (4.91) for $t \to \infty$.

$$u_{SS} = \frac{1}{g(0)} \left[-f(0)\,\hat{\theta}_{1,SS} \right] \tag{4.91}$$

Because (4.81) holds and $x_1(t)$ is regulated, $x_1 = 0$ is the globally stable equilibrium of (4.80). Besides $\gamma_1 \in \mathbb{R}_+$ and $c_1 \in \mathbb{R}_+$, $g(x_1) \neq 0$ for all $x_1 \in \mathbb{R}$ is a mandatory prerequisite for this approach.

Widening the perspective to (4.78) and (4.79), it is evident that the designed u in (4.88) is not appropriate to control such parametric nonlinear system. On the other hand, the insights achieved by designing the control for the reduced system (4.80) help in finding the adequate control for the system (4.78) and (4.79).

As in the case without uncertainties, x_1 has to be controlled via x_2, because (4.78) does not contain u. The designed control for the reduced system according to (4.88) is considered as the desired x_2. Due to the fact that x_2 will differ from this desired value, the error z is defined as stated in (4.92). The stabilizing function, which represents the desired value of x_2, is now depending on x_1 as well as $\hat{\theta}_1$.

$$z = x_2 - \alpha\left(x_1, \hat{\theta}_1\right) \tag{4.92}$$

By employing (4.92) and the derivative of z, (4.78) and (4.79) are written as (4.93) and (4.94).

$$\dot{x}_1 = f(x_1)\,\theta + g(x_1)\left[z + \alpha\left(x_1, \hat{\theta}_1\right) \right] \tag{4.93}$$

$$\dot{z} = u - \frac{\partial \alpha\left(x_1, \hat{\theta}_1\right)}{\partial x_1}\left[f(x_1)\,\theta + g(x_1)\left[z + \alpha\left(x_1, \hat{\theta}_1\right) \right] \right] - \frac{\partial \alpha\left(x_1, \hat{\theta}_1\right)}{\partial \hat{\theta}_1}\dot{\hat{\theta}}_1 \tag{4.94}$$

The Lyapunov function $V_2(x_1, z, \tilde{\theta}_1, \tilde{\theta}_2)$ is defined as (4.95), with $\tilde{\theta}_2$ according to (4.96). The adaptation gain $\gamma_2 \in \mathbb{R}_+$. $\hat{\theta}_2$ in (4.96) is a second parameter estimate of θ. Although the system (4.78), (4.79) contains only one unknown parameter θ, the second parameter estimate $\hat{\theta}_2$, which implies $\tilde{\theta}_2$, is necessary to cancel the terms in the derivative of $V_2(x_1, z, \tilde{\theta}_1, \tilde{\theta}_2)$ originating from (4.94) later. $\hat{\theta}_2$ is independent from the parameter estimate $\hat{\theta}_1$, meaning two estimates for θ exist. Therefore, the overall resulting system is be overparametrized. This is a negative aspect of the adaptive Backstepping methodology. As introduced above, other methods are able to overcome the overparametrization, but they are not treated herein for the also stated reasons.

$$V_2\left(x_1, z, \tilde{\theta}_1, \tilde{\theta}_2\right) = V_1\left(x_1, \tilde{\theta}_1\right) + \frac{1}{2}z^2 + \frac{1}{2\gamma_2}\tilde{\theta}_2^2$$

$$= \frac{1}{2}x_1^2 + \frac{1}{2\gamma_1}\tilde{\theta}_1^2 + \frac{1}{2}z^2 + \frac{1}{2\gamma_2}\tilde{\theta}_2^2 \tag{4.95}$$

$$\tilde{\theta}_2 = \theta - \hat{\theta}_2 \tag{4.96}$$

The derivative of $V_2(x_1, z, \tilde{\theta}_1, \tilde{\theta}_2)$ is developed to (4.97). The functions are written without their arguments to provide readability.

$$\begin{aligned}
\dot{V}_2\left(x_1, z, \tilde{\theta}_1, \tilde{\theta}_2\right) &= x_1\dot{x}_1 + \frac{1}{\gamma_1}\tilde{\theta}_1\dot{\tilde{\theta}}_1 + z\dot{z} + \frac{1}{\gamma_2}\tilde{\theta}_2\dot{\tilde{\theta}}_2 \\
&= x_1\left[f\theta + gz + g\alpha\right] + \frac{1}{\gamma_1}\tilde{\theta}_1\dot{\tilde{\theta}}_1 \\
&\quad + z\dot{z} + \frac{1}{\gamma_2}\tilde{\theta}_2\dot{\tilde{\theta}}_2 \\
&= x_1\left[f\left(\tilde{\theta}_1 + \hat{\theta}_1\right) + gz + g\alpha\right] + \frac{1}{\gamma_1}\tilde{\theta}_1\dot{\tilde{\theta}}_1 \\
&\quad + z\dot{z} + \frac{1}{\gamma_2}\tilde{\theta}_2\dot{\tilde{\theta}}_2
\end{aligned} \tag{4.97}$$

The rearranging of terms in (4.97) and the use of the fact that $\dot{\tilde{\theta}}_1$ is equal to $-\dot{\hat{\theta}}_1$ leads to (4.98).

$$\begin{aligned}
\dot{V}_2\left(x_1, z, \tilde{\theta}_1, \tilde{\theta}_2\right) &= x_1\left[f\hat{\theta}_1 + gz + g\alpha\right] + \tilde{\theta}_1\left[x_1 f - \frac{1}{\gamma_1}\dot{\hat{\theta}}_1\right] \\
&\quad + z\dot{z} + \frac{1}{\gamma_2}\tilde{\theta}_2\dot{\tilde{\theta}}_2
\end{aligned} \tag{4.98}$$

Implementing (4.86) simplifies the latter to (4.99).

$$\begin{aligned}
\dot{V}_2\left(x_1, z, \tilde{\theta}_1, \tilde{\theta}_2\right) &= x_1\left[f\hat{\theta}_1 + gz + g\alpha\right] \\
&\quad + z\dot{z} + \frac{1}{\gamma_2}\tilde{\theta}_2\dot{\tilde{\theta}}_2
\end{aligned} \tag{4.99}$$

Now, the remaining terms are manipulated further and $\alpha(x_1, \hat{\theta}_1)$ which is given by (4.88) is employed.

$$\begin{aligned}
\dot{V}_2\left(x_1, z, \tilde{\theta}_1, \tilde{\theta}_2\right) &= x_1\left[f\hat{\theta}_1 + g\alpha\right] + x_1 gz \\
&\quad + z\dot{z} + \frac{1}{\gamma_2}\tilde{\theta}_2\dot{\tilde{\theta}}_2 \\
&= -c_1 x_1^2 + x_1 gz \\
&\quad + z\dot{z} + \frac{1}{\gamma_2}\tilde{\theta}_2\dot{\tilde{\theta}}_2
\end{aligned} \tag{4.100}$$

With the use of (4.94), the last line of (4.100) is expanded further. (4.86) is used in this derivation. Additionally, it is utilized that the derivative of $\tilde{\theta}_2$ equals $-\dot{\hat{\theta}}_2$, which can be seen from (4.96).

$$\begin{aligned}
\dot{V}_2\left(x_1, z, \tilde{\theta}_1, \tilde{\theta}_2\right) &= -c_1 x_1^2 + x_1 gz \\
&\quad + z\left[u - \frac{\partial\alpha}{\partial x_1}\left(f\theta + gz + g\alpha\right) - \frac{\partial\alpha}{\partial\hat{\theta}_1}\dot{\hat{\theta}}_1\right] + \frac{1}{\gamma_2}\tilde{\theta}_2\dot{\tilde{\theta}}_2
\end{aligned}$$

$$
\begin{aligned}
&= -c_1 x_1^2 + x_1 g z \\
&\quad + z\left[u - \frac{\partial \alpha}{\partial x_1}\left(f\theta + gz + g\alpha\right) - \frac{\partial \alpha}{\partial \hat{\theta}_1}\left(\gamma_1 x_1 f\right)\right] - \frac{1}{\gamma_2}\tilde{\theta}_2\dot{\hat{\theta}}_2 \qquad (4.101)
\end{aligned}
$$

At this point, the remaining θ in the second line of (4.101) is separated according to $\tilde{\theta}_2 + \hat{\theta}_2 = \theta$; the second, independent parameter estimate of θ is employed. Furthermore, the terms are once again rearranged.

$$
\begin{aligned}
\dot{V}_2\left(x_1, z, \tilde{\theta}_1, \tilde{\theta}_2\right) &= -c_1 x_1^2 + x_1 g z \\
&\quad + z\left[u - \frac{\partial \alpha}{\partial x_1}\left(f\left(\tilde{\theta}_2 + \hat{\theta}_2\right) + gz + g\alpha\right) - \frac{\partial \alpha}{\partial \hat{\theta}_1}\left(\gamma_1 x_1 f\right)\right] - \frac{1}{\gamma_2}\tilde{\theta}_2\dot{\hat{\theta}}_2 \\
&= -c_1 x_1^2 + x_1 g z \\
&\quad + z\left[u - \frac{\partial \alpha}{\partial x_1}\left(f\hat{\theta}_2 + gz + g\alpha\right) - \frac{\partial \alpha}{\partial \hat{\theta}_1}\left(\gamma_1 x_1 f\right)\right] \\
&\quad - z\frac{\partial \alpha}{\partial x_1} f\tilde{\theta}_2 - \frac{1}{\gamma_2}\tilde{\theta}_2\dot{\hat{\theta}}_2 \\
&= -c_1 x_1^2 + x_1 g z \\
&\quad + z\left[u - \frac{\partial \alpha}{\partial x_1}\left(f\hat{\theta}_2 + gz + g\alpha\right) - \frac{\partial \alpha}{\partial \hat{\theta}_1}\left(\gamma_1 x_1 f\right)\right] \\
&\quad - \tilde{\theta}_2\left[z\frac{\partial \alpha}{\partial x_1} f + \frac{1}{\gamma_2}\dot{\hat{\theta}}_2\right] \qquad (4.102)
\end{aligned}
$$

The last term in (4.102) is eliminated by choosing the update law for $\dot{\hat{\theta}}_2$ as (4.103). The control u is taken as (4.104); $c_2 \in \mathbb{R}_+$.

$$
\dot{\hat{\theta}}_2 = -\gamma_2 z\frac{\partial \alpha}{\partial x_1} f \qquad (4.103)
$$

$$
u = -c_2 z + \frac{\partial \alpha}{\partial x_1}\left(f\hat{\theta}_2 + gz + g\alpha\right) + \frac{\partial \alpha}{\partial \hat{\theta}_1}\left(\gamma_1 x_1 f\right) - x_1 g \qquad (4.104)
$$

The choices of (4.103) and (4.104) simplify the derivative of $V_2(x_1, z, \tilde{\theta}_1, \tilde{\theta}_2)$ to (4.105).

$$
\dot{V}_2\left(x_1, z, \tilde{\theta}_1, \tilde{\theta}_2\right) = -c_1 x_1^2 - c_2 z^2 \qquad (4.105)
$$

Given that (4.106) holds, Theorem 4.1 guarantees global boundedness of $x_1(t)$, $z(t)$, $\tilde{\theta}_1(t)$, and $\tilde{\theta}_2(t)$. This result leads to the global boundedness of $\alpha(x_1(t), \hat{\theta}_1(t))$. The combination of the global boundedness of $z(t)$ and $\alpha(x_1(t), \hat{\theta}_1(t))$ in (4.92) guarantees the identical property for $x_2(t)$. This achieves that all solutions of (4.78) and (4.79) are globally bounded.

$$
\dot{V}_2\left(x_1, z, \tilde{\theta}_1, \tilde{\theta}_2\right) = -c_1 x_1^2 - cz^2 \leq 0, \quad \forall x_1 \in \mathbb{R}, \quad \forall z \in \mathbb{R}, \quad \forall \tilde{\theta}_1 \in \mathbb{R}, \quad \forall \tilde{\theta}_2 \in \mathbb{R} \qquad (4.106)
$$

In addition, $x_1(t)$ and $z(t)$ are regulated, based on Theorem 4.1 implying that $\hat{\theta}_1(t)$ and $\hat{\theta}_2(t)$ reach a steady-state. This means that $\alpha(x_1(t), \hat{\theta}_1(t))$ reaches the steady-state value in (4.107) for $t \to \infty$.

$$
\alpha_{SS}\left(x_1, \hat{\theta}_1\right) = \frac{1}{g(0)}\left[-f(0)\,\hat{\theta}_{1,SS}\right] \qquad (4.107)
$$

Presumed (4.81) holds, $\alpha(x_1(t), \hat{\theta}_1(t)) \to 0$ for $t \to \infty$. In this case, $x_2(t) \to 0$ for $t \to \infty$, as can be seen from (4.92). In combination with the regulation of $x_1(t)$, this means that $x_1 = 0$,

$x_2 = 0$ is the globally stable equilibrium of the nonlinear parametric strict-feedback system (4.79), (4.80).
The already introduced prerequisites for the establishment of this procedure remain in effect. Additionally, $\gamma_2 \in \mathbb{R}_+$ and $c_2 \in \mathbb{R}_+$ are mandatory.

Design procedure for parametric strict-feedback systems
By combining the design procedure for strict-feedback systems without uncertainties with the concept of adaptive Backstepping, the design procedure for parametric strict-feedback system results. The derivation follows [71], but explicitly shows all steps of the design procedure.
The parametric strict-feedback system is stated by (4.108) and (4.109). $x_1 \in \mathbb{R}$ and $x_2 \in \mathbb{R}$ constitute the states. The control input is given by $u \in \mathbb{R}$. $F_1 : \mathbb{R} \to \mathbb{R}^{n\times 1}$ and $F_2 : \mathbb{R}^{2\times 1} \to \mathbb{R}^{n\times 1}$ are vector fields composed of known, smooth nonlinear functions. $g_1 : \mathbb{R} \to \mathbb{R}$ and $g_2 : \mathbb{R} \to \mathbb{R}$ are known, smooth nonlinear functions. $\vec{\theta} \in \mathbb{R}^q$ is a vector of uncertain constant parameters.

$$\dot{x}_1 = F_1^T(x_1)\,\vec{\theta} + g_1(x_1)\,x_2 \tag{4.108}$$

$$\dot{x}_2 = F_2^T(x_1, x_2)\,\vec{\theta} + g_2(x_1, x_2)\,u \tag{4.109}$$

Following (4.92), an error variable z is defined according to (4.110). Employing this definition, (4.108) is rewritten as (4.111).

$$z = x_2 - \alpha\left(x_1, \hat{\vec{\theta}}_1\right) \tag{4.110}$$

$$\dot{x}_1 = F_1^T(x_1)\,\vec{\theta} + g_1(x_1)\left[z + \alpha\left(x_1, \hat{\vec{\theta}}_1\right)\right] \tag{4.111}$$

At this point, the Lyapunov function $V_1(x_1, \tilde{\vec{\theta}}_1)$ is chosen according to (4.112), whereupon $\tilde{\vec{\theta}}_1$ constitutes the parameter error as defined in (4.113). The adaptation gain matrix $\Gamma_1 \in \mathbb{R}^q \times \mathbb{R}^q$ is positive definite. The derivative of $V_1(x_1, \tilde{\vec{\theta}}_1)$ is developed thereafter to (4.114).

$$V_1\left(x_1, \tilde{\vec{\theta}}_1\right) = \frac{1}{2}x_1^2 + \frac{1}{2}\tilde{\vec{\theta}}_1^T\Gamma_1^{-1}\tilde{\vec{\theta}}_1 \tag{4.112}$$

$$\tilde{\vec{\theta}}_1 = \vec{\theta} - \hat{\vec{\theta}}_1 \tag{4.113}$$

$$\begin{aligned}\dot{V}_1\left(x_1, \tilde{\vec{\theta}}_1\right) &= x_1\dot{x}_1 + \tilde{\vec{\theta}}_1^T\Gamma_1^{-1}\dot{\tilde{\vec{\theta}}}_1 \\ &= x_1\left[F_1^T(x_1)\,\vec{\theta} + g_1(x_1)\left[z + \alpha\left(x_1, \hat{\vec{\theta}}_1\right)\right]\right] + \tilde{\vec{\theta}}_1^T\Gamma_1^{-1}\dot{\tilde{\vec{\theta}}}_1\end{aligned} \tag{4.114}$$

Given that the vector $\vec{\theta}$ comprises uncertain constant parameters, (4.113) allows to conclude that $\dot{\tilde{\vec{\theta}}}_1$ is equal to $-\dot{\hat{\vec{\theta}}}_1$. Implementing this result in (4.114) results in (4.115).

$$\dot{V}_1\left(x_1, \tilde{\vec{\theta}}_1\right) = x_1\left[F_1^T(x_1)\,\vec{\theta} + g_1(x_1)\left[z + \alpha\left(x_1, \hat{\vec{\theta}}_1\right)\right]\right] - \tilde{\vec{\theta}}_1^T\Gamma_1^{-1}\dot{\hat{\vec{\theta}}}_1 \tag{4.115}$$

The stabilizing function $\alpha(x_1, \hat{\vec{\theta}}_1)$ is chosen adequately as (4.116), with $c_1 \in \mathbb{R}_+$. Employing (4.116) in (4.115) allows the calculation of (4.117).

$$\alpha\left(x_1, \hat{\vec{\theta}}_1\right) = \frac{1}{g_1(x_1)}\left[-F_1^T(x_1)\,\hat{\vec{\theta}}_1 - c_1x_1\right] \tag{4.116}$$

$$\begin{aligned}\dot{V}_1\left(x_1,\tilde{\vec{\theta}}_1\right) &= x_1 F_1^T(x_1)\,\vec{\theta} + x_1 g_1(x_1)\,z + x_1 g_1(x_1)\,\alpha\left(x_1,\hat{\vec{\theta}}_1\right) - \tilde{\vec{\theta}}_1^T\Gamma_1^{-1}\dot{\hat{\vec{\theta}}}_1 \\ &= -c_1 x_1^2 + x_1 g_1(x_1)\,z + x_1 F_1^T(x_1)\,\tilde{\vec{\theta}}_1 - \tilde{\vec{\theta}}_1^T\Gamma_1^{-1}\dot{\hat{\vec{\theta}}}_1 \\ &= -c_1 x_1^2 + x_1 g_1(x_1)\,z + \tilde{\vec{\theta}}_1^T\left[F_1(x_1)\,x_1 - \Gamma_1^{-1}\dot{\hat{\vec{\theta}}}_1\right] \end{aligned} \tag{4.117}$$

This achieved, the update law for $\dot{\hat{\vec{\theta}}}_1$ is taken as (4.118). Implementing this choice in (4.117) leads to (4.119) for the derivative of the $V_1(x_1,\tilde{\vec{\theta}}_1)$.

$$\dot{\hat{\vec{\theta}}}_1 = \Gamma_1 F_1(x_1)\,x_1 \tag{4.118}$$

$$\dot{V}_1\left(x_1,\tilde{\vec{\theta}}_1\right) = -c_1 x_1^2 + x_1 g_1(x_1)\,z \tag{4.119}$$

Because the sign of the last term in (4.119) is unknown, no conclusion about the stability properties is achievable. The derivative of z is developed to (4.120). The derivative of $\alpha(x_1,\hat{\vec{\theta}}_1)$ for this step of the process is given by the analytic expression (4.121).

$$\begin{aligned}\dot{z} &= \dot{x}_2 - \dot{\alpha}\left(x_1,\hat{\vec{\theta}}_1\right) \\ &= F_2^T(x_1,x_2)\,\vec{\theta} + g_2(x_1,x_2)\,u - \dot{\alpha}\left(x_1,\hat{\vec{\theta}}_1\right)\end{aligned} \tag{4.120}$$

$$\begin{aligned}\dot{\alpha}\left(x_1,\hat{\vec{\theta}}_1\right) &= \frac{\partial\alpha\left(x_1,\hat{\vec{\theta}}_1\right)}{\partial x_1}\dot{x}_1 + \frac{\partial\alpha\left(x_1,\hat{\vec{\theta}}_1\right)}{\partial\hat{\vec{\theta}}_1}\dot{\hat{\vec{\theta}}}_1 \\ &= \frac{\partial\alpha\left(x_1,\hat{\vec{\theta}}_1\right)}{\partial x_1}\left[F_1^T(x_1)\,\vec{\theta} + g_1(x_1)\,x_2\right] + \frac{\partial\alpha\left(x_1,\hat{\vec{\theta}}_1\right)}{\partial\hat{\vec{\theta}}_1}\left[\Gamma_1 F_1(x_1)\,x_1\right]\end{aligned} \tag{4.121}$$

The Lyapunov function $V_2(x_1,\tilde{\vec{\theta}}_1,z,\tilde{\vec{\theta}}_2)$ is stated in (4.122). $\tilde{\vec{\theta}}_2$ is defined in (4.123), whereupon $\hat{\vec{\theta}}_2$ constitutes a second parameter estimate of $\vec{\theta}$. Like in the beforehand presented approach, $\hat{\vec{\theta}}_2$ is independent from the parameter estimate $\hat{\vec{\theta}}_1$. Therefore, the overall system is overparametrized which is normal for adaptive Backstepping designs. $\Gamma_2 \in \mathbb{R}^q \times \mathbb{R}^q$ is positive definite and can differ from Γ_1.

$$\begin{aligned}V_2\left(x_1,\tilde{\vec{\theta}}_1,z,\tilde{\vec{\theta}}_2\right) &= V_1\left(x_1,\tilde{\vec{\theta}}_1\right) + \frac{1}{2}z^2 + \frac{1}{2}\tilde{\vec{\theta}}_2^T\Gamma_2^{-1}\tilde{\vec{\theta}}_2 \\ &= \frac{1}{2}x_1^2 + \frac{1}{2}\tilde{\vec{\theta}}_1^T\Gamma_1^{-1}\tilde{\vec{\theta}}_1 + \frac{1}{2}z^2 + \frac{1}{2}\tilde{\vec{\theta}}_2^T\Gamma_2^{-1}\tilde{\vec{\theta}}_2\end{aligned} \tag{4.122}$$

$$\tilde{\vec{\theta}}_2 = \vec{\theta} - \hat{\vec{\theta}}_2 \tag{4.123}$$

The derivative of $V_2(x_1,\tilde{\vec{\theta}}_1,z,\tilde{\vec{\theta}}_2)$ is manipulated to (4.124) by using (4.119) and (4.120). The arguments of the functions are left out in the derivation of (4.124) to provide readability.

$$\begin{aligned}\dot{V}_2\left(x_1,\tilde{\vec{\theta}}_1,z,\tilde{\vec{\theta}}_2\right) &= x_1\dot{x}_1 - \tilde{\vec{\theta}}_1^T\Gamma_1^{-1}\dot{\hat{\vec{\theta}}}_1 + z\dot{z} - \tilde{\vec{\theta}}_2^T\Gamma_2^{-1}\dot{\hat{\vec{\theta}}}_2 \\ &= -c_1 x_1^2 + x_1 g_1 z + z\left[F_2^T\vec{\theta} + g_2 u - \dot{\alpha}\right] - \tilde{\vec{\theta}}_2^T\Gamma_2^{-1}\dot{\hat{\vec{\theta}}}_2\end{aligned}$$

$$
\begin{aligned}
&= -c_1 x_1^2 + x_1 g_1 z \\
&\quad + z\left[F_2^T\vec{\theta} + g_2 u - \frac{\partial \alpha}{\partial x_1}\dot{x}_1 - \frac{\partial \alpha}{\partial \hat{\vec{\theta}}_1}\dot{\hat{\vec{\theta}}}_1\right] \\
&\quad - \tilde{\vec{\theta}}_2^T \Gamma_2^{-1}\dot{\hat{\vec{\theta}}}_2 \\
&= -c_1 x_1^2 + x_1 g_1 z \\
&\quad + z\left[F_2^T\vec{\theta} + g_2 u - \frac{\partial \alpha}{\partial x_1}\left[F_1^T\vec{\theta} + g_1 x_2\right] - \frac{\partial \alpha}{\partial \hat{\vec{\theta}}_1}\left[\Gamma_1 F_1 x_1\right]\right] \\
&\quad - \tilde{\vec{\theta}}_2^T \Gamma_2^{-1}\dot{\hat{\vec{\theta}}}_2
\end{aligned} \tag{4.124}
$$

The control u is chosen appropriately as (4.125), with $c_2 \in \mathbb{R}_+$. Implementing u in (4.124) leads to (4.126).

$$
u = \frac{1}{g_2}\left[-F_2^T\hat{\vec{\theta}}_2 - x_1 g_1 + \frac{\partial \alpha}{\partial x_1}\left[F_1^T\hat{\vec{\theta}}_2 + g_1 x_2\right] + \frac{\partial \alpha}{\partial \hat{\vec{\theta}}_1}\left[\Gamma_1 F_1 x_1\right] - c_2 z\right] \tag{4.125}
$$

$$
\begin{aligned}
\dot{V}_2\left(x_1, \tilde{\vec{\theta}}_1, z, \tilde{\vec{\theta}}_2\right) &= -c_1 x_1^2 + x_1 g_1 z \\
&\quad + z\left[F_2^T\left(\tilde{\vec{\theta}}_2 + \hat{\vec{\theta}}_2\right) + g_2 u - \frac{\partial \alpha}{\partial x_1}\left[F_1^T\left(\tilde{\vec{\theta}}_2 + \hat{\vec{\theta}}_2\right) + g_1 x_2\right] - \frac{\partial \alpha}{\partial \hat{\vec{\theta}}_1}\left[\Gamma_1 F_1 x_1\right]\right] \\
&\quad - \tilde{\vec{\theta}}_2^T \Gamma_2^{-1}\dot{\hat{\vec{\theta}}}_2 \\
&= -c_1 x_1^2 + x_1 g_1 z \\
&\quad + z\left[F_2^T\hat{\vec{\theta}}_2 + g_2 u - \frac{\partial \alpha}{\partial x_1}\left[F_1^T\hat{\vec{\theta}}_2 + g_1 x_2\right] - \frac{\partial \alpha}{\partial \hat{\vec{\theta}}_1}\left[\Gamma_1 F_1 x_1\right]\right] \\
&\quad + z F_2^T\tilde{\vec{\theta}}_2 - z\frac{\partial \alpha}{\partial x_1}F_1^T\tilde{\vec{\theta}}_2 - \tilde{\vec{\theta}}_2^T\Gamma_2^{-1}\dot{\hat{\vec{\theta}}}_2 \\
&= -c_1 x_1^2 - c_2 z^2 + F_2^T\tilde{\vec{\theta}}_2 z - \frac{\partial \alpha}{\partial x_1}F_1^T\tilde{\vec{\theta}}_2 z - \tilde{\vec{\theta}}_2^T\Gamma_2^{-1}\dot{\hat{\vec{\theta}}}_2 \\
&= -c_1 x_1^2 - c_2 z^2 + \tilde{\vec{\theta}}_2^T F_2 z - \frac{\partial \alpha}{\partial x_1}\tilde{\vec{\theta}}_2^T F_1 z - \tilde{\vec{\theta}}_2^T\Gamma_2^{-1}\dot{\hat{\vec{\theta}}}_2 \\
&= -c_1 x_1^2 - c_2 z^2 + \tilde{\vec{\theta}}_2^T\left[F_2 - \frac{\partial \alpha}{\partial x_1}F_1\right] z - \tilde{\vec{\theta}}_2^T\Gamma_2^{-1}\dot{\hat{\vec{\theta}}}_2
\end{aligned} \tag{4.126}
$$

By utilizing 4.127 as the update law for $\dot{\hat{\vec{\theta}}}_2$, (4.126) simplifies to (4.128).

$$
\dot{\hat{\vec{\theta}}}_2 = \Gamma_2\left[F_2 - \frac{\partial \alpha}{\partial x_1}F_1\right] z \tag{4.127}
$$

$$
\dot{V}_2\left(x_1, \tilde{\vec{\theta}}_1, z, \tilde{\vec{\theta}}_2\right) = -c_1 x_1^2 - c_2 z^2 \tag{4.128}
$$

Due to the fact that (4.129) holds, global boundedness of $x_1(t)$, $\tilde{\vec{\theta}}_1(t)$, $z(t)$, and $\tilde{\vec{\theta}}_2(t)$ is guaranteed by Theorem 4.1. The global boundedness of $x_1(t)$ and $\tilde{\vec{\theta}}_1(t)$, via (4.113), leads to the global boundedness of $\alpha(x_1(t), \hat{\vec{\theta}}_1(t))$. This guarantees global boundedness of $x_2(t)$ by 4.110. Hence,

all solutions of (4.108), (4.109) are globally bounded. Furthermore, Theorem 4.1 guarantees the regulation of $x_1(t)$ and $z(t)$.

$$\dot{V}_2\left(x_1, \tilde{\vec{\theta}}_1, z, \tilde{\vec{\theta}}_2\right) = -c_1 x_1^2 - c_2 z^2 \leq 0, \quad \forall x_1 \in \mathbb{R}, \quad \forall z \in \mathbb{R}, \quad \forall \tilde{\vec{\theta}}_1 \in \mathbb{R}^n, \quad \forall \tilde{\vec{\theta}}_2 \in \mathbb{R}^n \tag{4.129}$$

Since $x_1(t)$ and $z(t)$ are regulated, it is evident from (4.118) and (4.127) that $\dot{\tilde{\vec{\theta}}}_1(t) \to 0$ and $\dot{\hat{\vec{\theta}}}_2(t) \to 0$ for $t \to \infty$. Latter implies that $\dot{\hat{\vec{\theta}}}_1(t)$ and $\dot{\hat{\vec{\theta}}}_2(t)$ reach a steady-state value. It is concluded from (4.116) that $\alpha(x_1(t), \hat{\vec{\theta}}_1(t))$ reaches the steady-state value given in (4.130). If $F_1(x_1)$ exhibits the property (4.131), $\alpha(x_1(t), \hat{\vec{\theta}}_1(t)) \to 0$ for $t \to \infty$.

$$\alpha_{SS}\left(x_1, \hat{\vec{\theta}}_1\right) = \frac{1}{g_1(0)}\left[-F_1^T(0)\,\hat{\vec{\theta}}_{1,SS}\right] \tag{4.130}$$

$$F_1(0) = 0 \tag{4.131}$$

Provided (4.131) holds, $x_2(t) \to 0$ for $t \to \infty$, which is derived from (4.110). Under this condition, $x_1 = 0$, $x_2 = 0$ is the globally stable equilibrium of (4.108), (4.109).
The necessary conditions for the derived boundedness and stability properties are $c_1 \in \mathbb{R}_+$ and $c_2 \in \mathbb{R}_+$. Furthermore, $\Gamma_1 \in \mathbb{R}^q \times \mathbb{R}^q$ and $\Gamma_2 \in \mathbb{R}^q \times \mathbb{R}^q$ are required to be positive definite. In addition, (4.132) and (4.133) must hold.

$$g_1(x_1) \neq 0, \quad \forall x_1 \in \mathbb{R} \tag{4.132}$$

$$g_2(x_1, x_2) \neq 0, \quad \forall x_1 \in \mathbb{R}, \quad \forall x_2 \in \mathbb{R} \tag{4.133}$$

Design procedure for parametric strict-feedback systems in the case of tracking
The beforehand presented design procedure has been concerned with the regulation of parametric strict-feedback systems. Although this procedure itself constitutes an important step in the process of establishing a foundation from which the interceptor flight control system can be designed, the aim of the procedure is inappropriate for the interceptor flight control system design. For this reason, the control task of tracking is considered in the following. The design procedure for parametric strict-feedback systems in the case of tracking arises from the combination of the earlier results concerning tracking with the design procedure for parametric strict-feedback systems. This presentation exceeds the illustrations in [66] and [71]. These sources do not consider the control task of tracking in combination with adaptive Backstepping.
The parametric strict-feedback system, which constitutes the starting point for the design procedure, is given by (4.134) and (4.135). The states are $x_1 \in \mathbb{R}$ and $x_2 \in \mathbb{R}$. $u \in \mathbb{R}$ constitutes the control input. $F_1 : \mathbb{R} \to \mathbb{R}^{n\times 1}$ and $F_2 : \mathbb{R}^{2\times 1} \to \mathbb{R}^{n\times 1}$ are vectors fields of known, smooth nonlinear functions. $g_1 : \mathbb{R} \to \mathbb{R}$ and $g_2 : \mathbb{R} \to \mathbb{R}$ are known, smooth nonlinear functions. $\vec{\theta} \in \mathbb{R}^q$ constitutes a vector uncertain constant parameters.

$$\dot{x}_1 = F_1^T(x_1)\,\vec{\theta} + g_1(x_1)\,x_2 \tag{4.134}$$

$$\dot{x}_2 = F_2^T(x_1, x_2)\,\vec{\theta} + g_2(x_1, x_2)\,u \tag{4.135}$$

The output $y \in \mathbb{R}$ of the parametric strict-feedback system (4.134), (4.135) is equal to x_1. y shall follow the known, smooth, and bounded reference signal $x_{1,Ref} \in \mathbb{R}$. The derivatives of

$x_{1,Ref}$ are assumed to be known, smooth, and bounded.
Initially, two error variables $z_1 \in \mathbb{R}$ and $z_2 \in \mathbb{R}$ are defined according to (4.136) and (4.137).

$$z_1 = x_1 - x_{1,Ref} \tag{4.136}$$

$$z_2 = x_2 - \alpha\left(x_1, x_{1,Ref}, \dot{x}_{1,Ref}, \hat{\vec{\theta}}_1\right) \tag{4.137}$$

The Lyapunov function $V_1(z_1, \tilde{\vec{\theta}}_1)$ is chosen as (4.138). The parameter error $\tilde{\vec{\theta}}_1$ is defined in (4.139) and $\Gamma_1 \in \mathbb{R}^q \times \mathbb{R}^q$ is a positive definite adaptation gain matrix.

$$V_1\left(z_1, \tilde{\vec{\theta}}_1\right) = \frac{1}{2}z_1^2 + \frac{1}{2}\tilde{\vec{\theta}}_1^T \Gamma_1^{-1} \tilde{\vec{\theta}}_1 \tag{4.138}$$

$$\tilde{\vec{\theta}}_1 = \vec{\theta} - \hat{\vec{\theta}}_1 \tag{4.139}$$

The stabilizing function $\alpha(x_1, x_{1,Ref}, \dot{x}_{1,Ref}, \hat{\vec{\theta}}_1)$ is affiliated from the derivative of $V_1(z_1, \tilde{\vec{\theta}}_1)$ according to (4.140); $c_1 \in \mathbb{R}_+$. By employing $\alpha(x_1, x_{1,Ref}, \dot{x}_{1,Ref}, \hat{\vec{\theta}}_1)$ in the derivative of $V_1(z_1, \tilde{\vec{\theta}}_1)$, the update law for $\dot{\hat{\vec{\theta}}}_1$ becomes evident as given in (4.141).

$$\alpha\left(x_1, x_{1,Ref}, \dot{x}_{1,Ref}, \hat{\vec{\theta}}_1\right) = \frac{1}{g_1(x_1)}\left[-F_1^T(x_1)\,\hat{\vec{\theta}}_1 + \dot{x}_{1,Ref} - c_1 z_1\right] \tag{4.140}$$

$$\dot{\hat{\vec{\theta}}}_1 = \Gamma_1 F_1(x_1)\, z_1 \tag{4.141}$$

Because no conclusion about the stability properties of the parametric strict-feedback system is possible after (4.140) and (4.141) are implemented in the derivative of $V_1(z_1, \tilde{\vec{\theta}}_1)$, the derivative of z_2 is developed. Therein, the derivative of $\alpha(x_1, x_{1,Ref}, \dot{x}_{1,Ref}, \hat{\vec{\theta}}_1)$ is represented by an analytic expression. Afterwards, $V_2(z_1, \tilde{\vec{\theta}}_1, z_2, \tilde{\vec{\theta}}_2)$ is chosen as stated in (4.142), with $\tilde{\vec{\theta}}_2$ as (4.143). $\Gamma_2 \in \mathbb{R}^q \times \mathbb{R}^q$ is positive definite. $\hat{\vec{\theta}}_2$ in (4.143) constitutes a second parameter estimate of $\vec{\theta}$, which is independent from $\hat{\vec{\theta}}_1$, implying that the overall system is overparametrized also in the case of tracking.

$$V_2\left(z_1, \tilde{\vec{\theta}}_1, z_2, \tilde{\vec{\theta}}_2\right) = \frac{1}{2}z_1^2 + \frac{1}{2}\tilde{\vec{\theta}}_1^T \Gamma_1^{-1} \tilde{\vec{\theta}}_1 + \frac{1}{2}z_2^2 + \frac{1}{2}\tilde{\vec{\theta}}_2^T \Gamma_2^{-1} \tilde{\vec{\theta}}_2 \tag{4.142}$$

$$\tilde{\vec{\theta}}_2 = \vec{\theta} - \hat{\vec{\theta}}_2 \tag{4.143}$$

The calculation of the derivative of $V_2(z_1, \tilde{\vec{\theta}}_1, z_2, \tilde{\vec{\theta}}_2)$ leads finally to the control u given in (4.144), whereupon $c_2 \in \mathbb{R}_+$. Using u in the derivative of $V_2(z_1, \tilde{\vec{\theta}}_1, z_2, \tilde{\vec{\theta}}_2)$, the appropriate choice for the update law for $\dot{\hat{\vec{\theta}}}_2$ according to (4.145) becomes obvious. The arguments of the functions in (4.144) and (4.145) are left out to enhance readability.

$$\begin{aligned} u \;=\; & \frac{1}{g_2}\Bigg[-F_2^T\hat{\vec{\theta}}_2 - z_1 g_1 + \frac{\partial\alpha}{\partial x_1}\left[F_1^T\hat{\vec{\theta}}_2 + g_1 x_2\right] \\ & + \frac{\partial\alpha}{\partial x_{1,Ref}}\dot{x}_{1,Ref} + \frac{\partial\alpha}{\partial \dot{x}_{1,Ref}}\ddot{x}_{1,Ref} \\ & + \frac{\partial\alpha}{\partial \hat{\vec{\theta}}_1}\left[\Gamma_1 F_1 z_1\right] - c_2 z_2\Bigg] \end{aligned} \tag{4.144}$$

$$\dot{\tilde{\vec{\theta}}}_2 = \Gamma_2 \left[F_2 - \frac{\partial \alpha}{\partial x_1} F_1 \right] z_2 \tag{4.145}$$

(4.144) and (4.145) simplify the derivative of $V_2(z_1, \tilde{\vec{\theta}}_1, z_2, \tilde{\vec{\theta}}_2)$ to (4.146).

$$\dot{V}_2 \left(z_1, \tilde{\vec{\theta}}_1, z_2, \tilde{\vec{\theta}}_2 \right) = -c_1 z_1^2 - c_2 z_2^2 \tag{4.146}$$

Presuming (4.147) holds, Theorem 4.1 guarantees global boundedness of $z_1(t)$, $\tilde{\vec{\theta}}_1(t)$, $z_2(t)$, and $\tilde{\vec{\theta}}_2(t)$. Hence, all solutions of the error system which is given in (4.148) and (4.149) are globally bounded. Following [71], the abbreviations w_1 and w_2 are denoted regressor functions.

$$\dot{V}_2 \left(z_1, \tilde{\vec{\theta}}_1, z_2, \tilde{\vec{\theta}}_2 \right) = -c_1 z_1^2 - c_2 z_2^2 \leq 0, \quad \forall z_1 \in \mathbb{R}, \quad \forall z_2 \in \mathbb{R}, \quad \forall \tilde{\vec{\theta}}_1 \in \mathbb{R}^n, \quad \forall \tilde{\vec{\theta}}_2 \in \mathbb{R}^n \tag{4.147}$$

$$\begin{bmatrix} \dot{z}_1 \\ \dot{z}_2 \end{bmatrix} = \begin{bmatrix} -c_1 & g_1(x_1) \\ -g_1(x_1) & -c_2 \end{bmatrix} \begin{bmatrix} z_1 \\ z_2 \end{bmatrix} + \begin{bmatrix} w_1^T & 0 \\ 0 & w_2^T \end{bmatrix} \begin{bmatrix} \tilde{\vec{\theta}}_1 \\ \tilde{\vec{\theta}}_2 \end{bmatrix} \tag{4.148}$$

$$\begin{bmatrix} \dot{\tilde{\vec{\theta}}}_1 \\ \dot{\tilde{\vec{\theta}}}_2 \end{bmatrix} = \begin{bmatrix} \Gamma_1 & 0 \\ 0 & \Gamma_2 \end{bmatrix} \begin{bmatrix} w_1 & 0 \\ 0 & w_2 \end{bmatrix} \begin{bmatrix} z_1 \\ z_2 \end{bmatrix} \tag{4.149}$$

$$w_1 = F_1(x_1) \tag{4.150}$$

$$w_2 = F_2(x_1, x_2) - \frac{\partial \alpha \left(x_1, x_{1,Ref}, \dot{x}_{1,Ref}, \hat{\vec{\theta}}_1 \right)}{\partial x_1} F_1(x_1) \tag{4.151}$$

Theorem 4.1 guarantees regulation of $z_1(t)$ and $z_2(t)$. The regulation of $z_1(t)$ implies via (4.136) that $x_{1,Ref}$ is tracked globally. Therefore, the control task of tracking is achieved globally. Based on $z_1(t) \to 0$ and $z_2(t) \to 0$ for $t \to \infty$ as well as (4.141) and (4.145), $\hat{\vec{\theta}}_1(t)$ and $\hat{\vec{\theta}}_2(t)$ reach a steady-state for $t \to \infty$. $z_1 = 0$, $z_2 = 0$ is the globally stable equilibrium of the error system given in (4.148) and (4.149).

Reconsidering the parametric strict-feedback system stated in (4.134) and (4.135), the global boundedness of $z_1(t)$ and $x_{1,Ref}(t)$ achieves the global boundedness of $x_1(t)$. The global boundedness of $z_1(t)$, $x_{1,Ref}(t)$, and $\hat{\vec{\theta}}_1(t)$, which is derived from (4.139), generates the global boundedness of $\alpha(x_1, x_{1,Ref}, \dot{x}_{1,Ref}, \hat{\vec{\theta}}_1)$. This result in combination with the global boundedness of $z_2(t)$ provides the global boundedness of $x_2(t)$. Hence, all solutions of (4.134) and (4.135) are globally bounded.

Besides these results directly related to the case of tracking, some additional results are derivable, if special conditions apply. If $x_{1,Ref}(t) \to 0$ for $t \to \infty$, the regulation of $z_1(t)$ leads to $x_1(t) \to 0$ for $t \to \infty$. Taking into account the regulation of $z_1(t)$ and $z_2(t)$, which implies that the parameter estimates of $\vec{\theta}$ reach a steady-state, $\alpha(x_1, x_{1,Ref}, \dot{x}_{1,Ref}, \hat{\vec{\theta}}_1)$ converges to the steady-state given in (4.152).

$$\alpha_{SS} \left(x_1, x_{1,Ref}, \dot{x}_{1,Ref}, \hat{\vec{\theta}}_1 \right) = \frac{1}{g_1(0)} \left[-F_1^T(0) \hat{\vec{\theta}}_{1,SS} \right] \tag{4.152}$$

Provided $F_1(0) = 0$, $\alpha(x_1, x_{1,Ref}, \dot{x}_{1,Ref}, \hat{\vec{\theta}}_1) \to 0$ for $t \to \infty$. This result in combination with (4.137) is the basis for $x_2(t) \to 0$ for $t \to \infty$. Under the assumed conditions, $x_1 = 0$, $x_2 = 0$ is the globally stable equilibrium of (4.134), (4.135).

The derived boundedness and stability properties are founded on the appropriate choices of $c_1 \in \mathbb{R}_+$ and $c_2 \in \mathbb{R}_+$. In addition, the positive definiteness of $\Gamma_1 \in \mathbb{R}^q \times \mathbb{R}^q$ and $\Gamma_2 \in \mathbb{R}^q \times \mathbb{R}^q$ are prerequisites for the derived boundedness and stability properties. (4.153) and (4.154) are necessary to guarantee controllability of the parametric strict-feedback system as well as the existence of $\alpha(x_1, x_{1,Ref}, \dot{x}_{1,Ref}, \hat{\vec{\theta}}_1)$ and u.

$$g_1(x_1) \neq 0, \quad \forall x_1 \in \mathbb{R} \tag{4.153}$$

$$g_2(x_1, x_2) \neq 0, \quad \forall x_1 \in \mathbb{R}, \quad \forall x_2 \in \mathbb{R} \tag{4.154}$$

The provided illustrations showed how the Backstepping methodology is applied to strict-feedback systems containing uncertain constant parameters. The result of the design procedure for parametric strict-feedback systems demonstrated that global boundedness as well as global stability is achieved. Furthermore, the achievement of global tracking of a known, smooth, and bounded reference signal has been shown.
The introduced capabilities of the Backstepping methodology constitute a major milestone in establishing the theoretical background for the design of the interceptor flight control system. However, uncertain constant parameters have to be considered additionally as unknown control coefficients. The latter leads to a further augmentation of the introduced theory.

4.3.2 Unknown virtual control coefficients

The straightforward augmentation of the parametric strict-feedback systems considered beforehand by unknown control coefficients results in (4.155) and (4.156). This simple, nonlinear system is utilized to introduce the method which overcomes unknown control coefficients. The tools for this introduction are provided by [71], but latter does not comprise a self-contained presentation.
The unknown control coefficient in (4.155), (4.156) is denoted by b, with $b \in \mathbb{R}$. Although b is an uncertain constant parameter, the sign of b is supposed to be known.

$$\dot{x}_1 = f(x_1)\,\theta + b g(x_1)\,x_2 \tag{4.155}$$

$$\dot{x}_2 = u \tag{4.156}$$

If the beforehand system would only consist of the first equation and the input to this equation would be x_2, (4.157) would constitute the system to be accounted for.

$$\dot{x}_1 = f(x_1)\,\theta + b g(x_1)\,u \tag{4.157}$$

In this case, a controller and the respective update laws could be designed by the following approach. A Lyapunov function $V_1(x_1, \tilde{\theta}_1, \tilde{\varrho}_1)$ is defined according to (4.158). The parameter error $\tilde{\theta}_1$ is given by (4.159). $\tilde{\varrho}_1$, which is also a parameter error, is given by (4.160). The latter shows that instead of directly estimating the unknown parameter b, b^{-1} is estimated. The reason for this becomes evident from the upcoming steps. According to [71], the parameter estimate $\hat{\varrho}_1 = \hat{b}_1^{-1}$ is denoted unknown virtual control coefficient. $\gamma_{\theta_1} \in \mathbb{R}_+$ and $\gamma_{\varrho_1} \in \mathbb{R}_+$ are adaptation gains.

$$V_1\left(x_1, \tilde{\theta}_1, \tilde{\varrho}_1\right) = \frac{1}{2}x_1^2 + \frac{1}{2\gamma_{\theta_1}}\tilde{\theta}_1^2 + \frac{1}{2\gamma_{\varrho_1}}|b|\,\tilde{\varrho}_1^2 \tag{4.158}$$

$$\tilde{\theta}_1 = \theta - \hat{\theta}_1 \tag{4.159}$$

$$\tilde{\varrho}_1 = \varrho - \hat{\varrho}_1, \quad \varrho = b^{-1}, \quad \hat{\varrho}_1 = \hat{b}_1^{-1} \tag{4.160}$$

Considering Theorem 4.1, the defined $V_1(x_1, \tilde{\theta}_1, \tilde{\varrho}_1)$ is continuous differentiable, positive definite, and radially unbounded. Its derivative is developed according to (4.161) in the following. The fact that $\dot{\tilde{\theta}}_1 = -\dot{\hat{\theta}}_1$ and $\dot{\tilde{\varrho}}_1 = -\dot{\hat{\varrho}}_1$ are used in this derivation. These properties are evident from (4.159) and (4.160), keeping in mind that θ and $\varrho = b^{-1}$ are constant.

$$\begin{aligned}
\dot{V}_1\left(x_1, \tilde{\theta}_1, \tilde{\varrho}_1\right) &= x_1\dot{x}_1 + \frac{1}{\gamma_{\theta_1}}\tilde{\theta}_1\dot{\tilde{\theta}}_1 + \frac{1}{\gamma_{\varrho_1}}|b|\,\tilde{\varrho}_1\dot{\tilde{\varrho}}_1 \\
&= x_1\left[f(x_1)\,\theta + bg(x_1)\,u\right] + \frac{1}{\gamma_{\theta_1}}\tilde{\theta}_1\dot{\tilde{\theta}}_1 + \frac{1}{\gamma_{\varrho_1}}|b|\,\tilde{\varrho}_1\dot{\tilde{\varrho}}_1 \\
&= x_1\left[f(x_1)\,\theta + bg(x_1)\,u\right] - \frac{1}{\gamma_{\theta_1}}\tilde{\theta}_1\dot{\hat{\theta}}_1 - \frac{1}{\gamma_{\varrho_1}}|b|\,\tilde{\varrho}_1\dot{\hat{\varrho}}_1
\end{aligned} \tag{4.161}$$

At this point, the control u is chosen like (4.162); $c_1 \in \mathbb{R}_+$. Implementing this choice in (4.161) leads to (4.163).

$$u = \frac{\hat{\varrho}_1}{g(x_1)}\left[-f(x_1)\,\hat{\theta}_1 - c_1x_1\right] \tag{4.162}$$

$$\begin{aligned}
\dot{V}_1\left(x_1, \tilde{\theta}_1, \tilde{\varrho}_1\right) &= x_1\left[f(x_1)\,\theta + b\hat{\varrho}_1\left[-f(x_1)\,\hat{\theta}_1 - c_1x_1\right]\right] \\
&\quad -\frac{1}{\gamma_{\theta_1}}\tilde{\theta}_1\dot{\hat{\theta}}_1 - \frac{1}{\gamma_{\varrho_1}}|b|\,\tilde{\varrho}_1\dot{\hat{\varrho}}_1
\end{aligned} \tag{4.163}$$

It is desired to cancel the inner bracketed term in the first term of (4.163). This is done by finding an appropriate update law for $\dot{\hat{\varrho}}_1$. To establish a feasible design for this update law, it is necessary to remember that the sign of b is assumed to be known. Therefore, $\operatorname{sgn}(b)$ is available for update law design. Given that $|b|\operatorname{sgn}(b) = b$, the update law for $\dot{\hat{\varrho}}_1$ is taken as (4.164). With this choice, (4.163) is developed to (4.165). The fact that $\hat{\varrho}_1 + \tilde{\varrho}_1 = \varrho = b^{-1}$, available from (4.160), is utilized in this derivation.

$$\dot{\hat{\varrho}}_1 = -\gamma_{\varrho_1}\operatorname{sgn}(b)x_1\left[-f(x_1)\,\hat{\theta}_1 - c_1x_1\right] \tag{4.164}$$

$$\begin{aligned}
\dot{V}_1\left(x_1, \tilde{\theta}_1, \tilde{\varrho}_1\right) &= x_1\left[f(x_1)\,\theta + b\hat{\varrho}_1\left[-f(x_1)\,\hat{\theta}_1 - c_1x_1\right]\right] \\
&\quad -\frac{1}{\gamma_{\theta_1}}\tilde{\theta}_1\dot{\hat{\theta}}_1 + x_1|b|\operatorname{sgn}(b)\tilde{\varrho}_1\left[-f(x_1)\,\hat{\theta}_1 - c_1x_1\right] \\
&= x_1\left[f(x_1)\,\theta + b\left(\hat{\varrho}_1 + \tilde{\varrho}_1\right)\left[-f(x_1)\,\hat{\theta}_1 - c_1x_1\right]\right] \\
&\quad -\frac{1}{\gamma_{\theta_1}}\tilde{\theta}_1\dot{\hat{\theta}}_1 \\
&= x_1\left[f(x_1)\,\theta - f(x_1)\,\hat{\theta}_1 - c_1x_1\right] - \frac{1}{\gamma_{\theta_1}}\tilde{\theta}_1\dot{\hat{\theta}}_1 \\
&= x_1\left[f(x_1)\,\tilde{\theta}_1 - c_1x_1\right] - \frac{1}{\gamma_{\theta_1}}\tilde{\theta}_1\dot{\hat{\theta}}_1 \\
&= -c_1x_1^2 + x_1f(x_1)\,\tilde{\theta}_1 - \frac{1}{\gamma_{\theta_1}}\tilde{\theta}_1\dot{\hat{\theta}}_1
\end{aligned} \tag{4.165}$$

The update law for $\dot{\hat{\theta}}_1$ is now chosen as in the beforehand presented procedures as (4.166). This simplifies (4.165) to (4.167).

$$\dot{\hat{\theta}}_1 = \gamma_{\theta_1} x_1 f(x_1) \tag{4.166}$$

$$\dot{V}_1\left(x_1, \tilde{\theta}_1, \tilde{\varrho}_1\right) = -c_1 x_1^2 \tag{4.167}$$

Theorem 4.1 guarantees global boundedness of $x_1(t)$, $\tilde{\theta}_1(t)$, and $\tilde{\varrho}_1(t)$, based on the fact that (4.168) holds.

$$\dot{V}_1\left(x_1, \tilde{\theta}_1, \tilde{\varrho}_1\right) = -c_1 x_1^2 \leq 0, \quad \forall x_1 \in \mathbb{R}, \quad \forall \tilde{\theta}_1 \in \mathbb{R}, \quad \forall \tilde{\varrho}_1 \in \mathbb{R} \tag{4.168}$$

Furthermore, Theorem 4.1 guarantees that $x_1(t)$ is regulated, if $W(x_1(t)) = c_1 x_1^2$ is interpreted in terms of the theorem. As can be seen from (4.164) and (4.166), $\hat{\theta}_1(t)$ and $\hat{\varrho}_1(t)$ reach a steady-state due to the regulation of $x_1(t)$. Given that $f(0) = 0$, $x_1 = 0$ is the globally stable equilibrium of (4.157).
The prerequisites for the taken approach are $\gamma_{\theta_1} \in \mathbb{R}_+$, $\gamma_{\varrho_1} \in \mathbb{R}_+$, and $c_1 \in \mathbb{R}_+$. Additionally, $g(x_1) \neq 0$ for all $x_1 \in \mathbb{R}$ must hold, which is obvious from (4.162).
Returning to the system (4.155), (4.156), the beforehand derived design steps are employed to reach an overall controller for this system. Based on the rationale that the desired value of x_2 in this case would be according to (4.162), but this value can not be guaranteed to be achieved persistently, the error z is defined in (4.169).

$$z = x_2 - \alpha\left(x_1, \hat{\theta}_1, \hat{\varrho}_1\right) \tag{4.169}$$

Using (4.169) as well as the derivative of z, (4.155) and (4.156) are written as (4.170) and (4.171).

$$\dot{x}_1 = f(x_1)\theta + bg(x_1)\left[z + \alpha\left(x_1, \hat{\theta}_1, \hat{\varrho}_1\right)\right] \tag{4.170}$$

$$\begin{aligned} \dot{z} = {} & u - \frac{\partial \alpha\left(x_1, \hat{\theta}_1, \hat{\varrho}_1\right)}{\partial x_1}\left[f(x_1)\theta + bg(x_1)\left[z + \alpha\left(x_1, \hat{\theta}_1, \hat{\varrho}_1\right)\right]\right] \\ & - \frac{\partial \alpha\left(x_1, \hat{\theta}_1, \hat{\varrho}_1\right)}{\partial \hat{\theta}_1}\dot{\hat{\theta}}_1 - \frac{\partial \alpha\left(x_1, \hat{\theta}_1, \hat{\varrho}_1\right)}{\partial \hat{\varrho}_1}\dot{\hat{\varrho}}_1 \end{aligned} \tag{4.171}$$

The Lyapunov function $V_2(x_1, z, \tilde{\theta}_1, \tilde{\varrho}_1, \tilde{\theta}_2, \tilde{b}_2)$ is taken according to (4.172). The definitions of $\tilde{\theta}_2$ and $\tilde{b}_2$ are provided in (4.173) and (4.174) respectively, where $\hat{\theta}_2$ and $\hat{b}_2$ are second parameter estimates of θ and b. These second estimates are independent of the already introduced estimates $\hat{\theta}_1$ and $\hat{\varrho}_1$, showing that this control design leads to an overparametrized system. The adaptation gains are $\gamma_{\theta_2} \in \mathbb{R}_+$ and $\gamma_{b_2} \in \mathbb{R}_+$.

$$\begin{aligned} V_2\left(x_1, z, \tilde{\theta}_1, \tilde{\varrho}_1, \tilde{\theta}_2, \tilde{b}_2\right) = {} & V_1\left(x_1, \tilde{\theta}_1, \tilde{\varrho}_1\right) + \frac{1}{2}z^2 + \frac{1}{2\gamma_{\theta_2}}\tilde{\theta}_2^2 + \frac{1}{2\gamma_{b_2}}\tilde{b}_2^2 \\ = {} & \frac{1}{2}x_1^2 + \frac{1}{2\gamma_{\theta_1}}\tilde{\theta}_1^2 + \frac{1}{2\gamma_{\varrho_1}}|b|\,\tilde{\varrho}_1^2 \\ & + \frac{1}{2}z^2 + \frac{1}{2\gamma_{\theta_2}}\tilde{\theta}_2^2 + \frac{1}{2\gamma_{b_2}}\tilde{b}_2^2 \end{aligned} \tag{4.172}$$

$$\tilde{\theta}_2 = \theta - \hat{\theta}_2 \tag{4.173}$$

$$\tilde{b}_2 = b - \hat{b}_2 \tag{4.174}$$

Employing these equations, the derivative of $V_2(x_1, z, \tilde{\theta}_1, \tilde{\varrho}_1, \tilde{\theta}_2, \tilde{b}_2)$ is calculated as (4.175).

$$\begin{aligned}\dot{V}_2\left(x_1, z, \tilde{\theta}_1, \tilde{\varrho}_1, \tilde{\theta}_2, \tilde{b}_2\right) &= x_1\dot{x}_1 + \frac{1}{\gamma_{\theta_1}}\tilde{\theta}_1\dot{\tilde{\theta}}_1 + \frac{1}{\gamma_{\varrho_1}}|b|\,\tilde{\varrho}_1\dot{\tilde{\varrho}}_1 \\ &\quad + z\dot{z} + \frac{1}{\gamma_{\theta_2}}\tilde{\theta}_2\dot{\tilde{\theta}}_2 + \frac{1}{\gamma_{b_2}}\tilde{b}_2\dot{\tilde{b}}_2 \end{aligned} \tag{4.175}$$

Implementing the results from (4.162), (4.164), and (4.166) as well as the conclusions that $\dot{\tilde{\theta}}_2 = -\dot{\hat{\theta}}_2$ and $\dot{\tilde{b}}_2 = -\dot{\hat{b}}_2$, (4.175) is developed to (4.176). The functions are written without their arguments.

$$\begin{aligned}\dot{V}_2\left(x_1, z, \tilde{\theta}_1, \tilde{\varrho}_1, \tilde{\theta}_2, \tilde{b}_2\right) &= x_1\left[f\theta + bgz + bg\alpha\right] - \frac{1}{\gamma_{\theta_1}}\tilde{\theta}_1\dot{\hat{\theta}}_1 - \frac{1}{\gamma_{\varrho_1}}|b|\,\tilde{\varrho}_1\dot{\tilde{\varrho}}_1 \\ &\quad + z\dot{z} + \frac{1}{\gamma_{\theta_2}}\tilde{\theta}_2\dot{\tilde{\theta}}_2 + \frac{1}{\gamma_{b_2}}\tilde{b}_2\dot{\tilde{b}}_2 \\ &= x_1\left[f\theta + bgz + b\hat{\varrho}_1\left[-f\hat{\theta}_1 - c_1x_1\right]\right] - \frac{1}{\gamma_{\theta_1}}\tilde{\theta}_1\dot{\hat{\theta}}_1 - \frac{1}{\gamma_{\varrho_1}}|b|\,\tilde{\varrho}_1\dot{\tilde{\varrho}}_1 \\ &\quad + z\dot{z} + \frac{1}{\gamma_{\theta_2}}\tilde{\theta}_2\dot{\tilde{\theta}}_2 + \frac{1}{\gamma_{b_2}}\tilde{b}_2\dot{\tilde{b}}_2 \\ &= x_1\left[f\theta + bgz + b\left(\hat{\varrho}_1 + \tilde{\varrho}_1\right)\left[-f\hat{\theta}_1 - c_1x_1\right]\right] - \frac{1}{\gamma_{\theta_1}}\tilde{\theta}_1\dot{\hat{\theta}}_1 \\ &\quad + z\dot{z} + \frac{1}{\gamma_{\theta_2}}\tilde{\theta}_2\dot{\tilde{\theta}}_2 + \frac{1}{\gamma_{b_2}}\tilde{b}_2\dot{\tilde{b}}_2 \\ &= x_1\left[f\tilde{\theta}_1 + bgz - c_1x_1\right] - \frac{1}{\gamma_{\theta_1}}\tilde{\theta}_1\dot{\hat{\theta}}_1 \\ &\quad + z\dot{z} + \frac{1}{\gamma_{\theta_2}}\tilde{\theta}_2\dot{\tilde{\theta}}_2 + \frac{1}{\gamma_{b_2}}\tilde{b}_2\dot{\tilde{b}}_2 \\ &= -c_1x_1^2 + bgz + \tilde{\theta}_1\left[x_1f - \frac{1}{\gamma_{\theta_1}}\dot{\hat{\theta}}_1\right] \\ &\quad + z\dot{z} + \frac{1}{\gamma_{\theta_2}}\tilde{\theta}_2\dot{\tilde{\theta}}_2 + \frac{1}{\gamma_{b_2}}\tilde{b}_2\dot{\tilde{b}}_2 \\ &= -c_1x_1^2 + bgz \\ &\quad + z\left[u - \frac{\partial\alpha}{\partial x_1}\left(f\theta + bgz + bg\alpha\right) - \frac{\partial\alpha}{\partial\hat{\theta}_1}\dot{\hat{\theta}}_1 - \frac{\partial\alpha}{\partial\hat{\varrho}_1}\dot{\hat{\varrho}}_1\right] \\ &\quad - \frac{1}{\gamma_{\theta_2}}\tilde{\theta}_2\dot{\hat{\theta}}_2 - \frac{1}{\gamma_{b_2}}\tilde{b}_2\dot{\hat{b}}_2 \\ &= -c_1x_1^2 + bgz \\ &\quad + z\Bigg[u - \frac{\partial\alpha}{\partial x_1}\left(f\theta + bgz + bg\alpha\right) - \frac{\partial\alpha}{\partial\hat{\theta}_1}\left[\gamma_{\theta_1}x_1f\right] \\ &\quad - \frac{\partial\alpha}{\partial\hat{\varrho}_1}\left[-\gamma_{\varrho_1}\operatorname{sgn}(b)x_1\left[-f\hat{\theta}_1 - c_1x_1\right]\right]\Bigg] \\ &\quad - \frac{1}{\gamma_{\theta_2}}\tilde{\theta}_2\dot{\hat{\theta}}_2 - \frac{1}{\gamma_{b_2}}\tilde{b}_2\dot{\hat{b}}_2 \end{aligned} \tag{4.176}$$

The choice for the control u is stated in (4.177); $c_2 \in \mathbb{R}_+$. This leads to (4.178) for the derivative of $V_2(x_1, z, \tilde{\theta}_1, \tilde{\varrho}_1, \tilde{\theta}_2, \tilde{b}_2)$.

$$
\begin{aligned}
u &= -\hat{b}_2 g \\
&\quad + \frac{\partial \alpha}{\partial x_1}\left(f\hat{\theta}_2 + \hat{b}_2 g z + \hat{b}_2 g \alpha\right) + \frac{\partial \alpha}{\partial \hat{\theta}_1}\left[\gamma_{\theta_1} x_1 f\right] \\
&\quad + \frac{\partial \alpha}{\partial \hat{\varrho}_1}\left[-\gamma_{\varrho_1} \operatorname{sgn}(b) x_1 \left[-f\hat{\theta}_1 - c_1 x_1\right]\right] \\
&\quad - c_2 z
\end{aligned} \tag{4.177}
$$

$$
\begin{aligned}
\dot{V}_2\left(x_1, z, \tilde{\theta}_1, \tilde{\varrho}_1, \tilde{\theta}_2, \tilde{b}_2\right) &= -c_1 x_1^2 - c_2 z^2 + \tilde{b}_2 g z \\
&\quad + z\left[-\frac{\partial \alpha}{\partial x_1} f\tilde{\theta}_2 - \frac{\partial \alpha}{\partial x_1}\tilde{b}_2 g z - \frac{\partial \alpha}{\partial x_1}\tilde{b}_2 g \alpha\right] \\
&\quad - \frac{1}{\gamma_{\theta_2}}\tilde{\theta}_2\dot{\tilde{\theta}}_2 - \frac{1}{\gamma_{b_2}}\tilde{b}_2\dot{\tilde{b}}_2 \\
&= -c_1 x_1^2 - c_2 z^2 \\
&\quad + z\left[-\frac{\partial \alpha}{\partial x_1} f\tilde{\theta}_2\right] - \frac{1}{\gamma_{\theta_2}}\tilde{\theta}_2\dot{\tilde{\theta}}_2 \\
&\quad + z\left[\tilde{b}_2 g - \frac{\partial \alpha}{\partial x_1}\tilde{b}_2 g z - \frac{\partial \alpha}{\partial x_1}\tilde{b}_2 g \alpha\right] - \frac{1}{\gamma_{b_2}}\tilde{b}_2\dot{\tilde{b}}_2
\end{aligned} \tag{4.178}
$$

The update law for $\dot{\tilde{b}}_2$, defined as (4.179), simplifies the derivative of $V_2(x_1, z, \tilde{\theta}_1, \tilde{\varrho}_1, \tilde{\theta}_2, \tilde{b}_2)$ to (4.180).

$$
\dot{\tilde{b}}_2 = \gamma_{b_2} z\left[g - \frac{\partial \alpha}{\partial x_1} g z - \frac{\partial \alpha}{\partial x_1} g \alpha\right] \tag{4.179}
$$

$$
\begin{aligned}
\dot{V}_2\left(x_1, z, \tilde{\theta}_1, \tilde{\varrho}_1, \tilde{\theta}_2, \tilde{b}_2\right) &= -c_1 x_1^2 - c_2 z^2 \\
&\quad + z\left[-\frac{\partial \alpha}{\partial x_1} f\tilde{\theta}_2\right] - \frac{1}{\gamma_{\theta_2}}\tilde{\theta}_2\dot{\tilde{\theta}}_2
\end{aligned} \tag{4.180}
$$

(4.181) states the choice for the update law for $\dot{\tilde{\theta}}_2$. The derivative of $V_2(x_1, z, \tilde{\theta}_1, \tilde{\varrho}_1, \tilde{\theta}_2, \tilde{b}_2)$ simplifies to (4.182).

$$
\dot{\tilde{\theta}}_2 = -\gamma_{\theta_2} z \frac{\partial \alpha}{\partial x_1} f \tag{4.181}
$$

$$
\dot{V}_2\left(x_1, z, \tilde{\theta}_1, \tilde{\varrho}_1, \tilde{\theta}_2, \tilde{b}_2\right) = -c_1 x_1^2 - c_2 z^2 \tag{4.182}
$$

Because (4.183) holds for all arguments of $V_2(x_1, z, \tilde{\theta}_1, \tilde{\varrho}_1, \tilde{\theta}_2, \tilde{b}_2)$ in their respective domain, Theorem 4.1 guarantees global boundedness of $x_1(t)$, $z(t)$, $\tilde{\theta}_1(t)$, $\tilde{\varrho}_1(t)$, $\tilde{\theta}_2(t)$, and $\tilde{b}_2(t)$. This results in the global boundedness of $\alpha(x_1(t), \hat{\theta}_1(t), \hat{\varrho}_1(t))$. Via (4.169), the global boundedness of $z(t)$ and $\alpha(x_1(t), \hat{\theta}_1(t), \hat{\varrho}_1(t))$ leads to the global boundedness of $x_2(t)$. All solutions of (4.155) and (4.156) are globally bounded.

Furthermore, Theorem 4.1 guarantees regulation of $x_1(t)$ and $z(t)$. This implies that $\hat{\theta}_1(t)$, $\hat{\varrho}_1(t)$, $\hat{\theta}_2(t)$, and $\hat{b}_2(t)$ reach a steady-state for $t \to \infty$. Therefore, $\alpha(x_1(t), \hat{\theta}_1(t), \hat{\varrho}_1(t))$ reaches a steady-state value.

If $f(0) = 0$ holds, $\alpha(x_1(t), \hat{\theta}_1(t), \hat{\varrho}_1(t)) \to 0$ for $t \to \infty$. Via (4.169) in combination with the regulation of $z(t)$, this means that $x_2 \to 0$ for $t \to \infty$, leading to the fact that $x_1 = 0$, $x_2 = 0$ is the global stable equilibrium of (4.155) and (4.156), finally.

$$
\dot{V}_2\left(x_1, z, \tilde{\theta}_1, \tilde{\varrho}_1, \tilde{\theta}_2, \tilde{b}_2\right) = -c_1 x_1^2 - c_2 z^2 \leq 0 \tag{4.183}
$$

Design procedure for parametric strict-feedback systems with unknown control coefficients

With the basic concept to handle unknown control coefficients developed, the design procedure for parametric strict-feedback systems with unknown control coefficients is laid out in the following. This procedure evolves from the combination of the design procedure for parametric strict-feedback systems with the introduced methodology concerning unknown control coefficients. The latter are considered in every equation of the nonlinear system.

The parametric strict-feedback system with unknown control coefficients is given in (4.184) and (4.185). $x_1 \in \mathbb{R}$ and $x_2 \in \mathbb{R}$ constitute the states. $u \in \mathbb{R}$ is the control input. $F_1 : \mathbb{R}^n \to \mathbb{R}^n$ and $F_2 : \mathbb{R}^n \to \mathbb{R}^n$ are vector fields of known, smooth nonlinear functions. $g_1 : \mathbb{R} \to \mathbb{R}$ and $g_2 : \mathbb{R} \to \mathbb{R}$ are known, smooth nonlinear functions. $\theta \in \mathbb{R}^q$ is a vector of uncertain constant parameters, and $b_1 \in \mathbb{R}$ as well as $b_2 \in \mathbb{R}$ are uncertain constant parameters. The signs of b_1 and b_2 are known.

$$\dot{x}_1 = F_1^T(x_1)\,\vec{\theta} + b_1 g_1(x_1)\,x_2 \tag{4.184}$$

$$\dot{x}_2 = F_2^T(x_1, x_2)\,\vec{\theta} + b_2 g_2(x_1, x_2)\,u \tag{4.185}$$

The initial step of the procedure is the definition of an error variable z in (4.186). Using z in (4.184) leads to (4.187).

$$z = x_2 - \alpha\left(x_1, \hat{\vec{\theta}}_1, \hat{\varrho}_1\right) \tag{4.186}$$

$$\dot{x}_1 = F_1^T(x_1)\,\vec{\theta} + g_1(x_1)\left[z + \alpha\left(x_1, \hat{\vec{\theta}}_1, \hat{\varrho}_1\right)\right] \tag{4.187}$$

The Lyapunov function $V_1(x_1, \tilde{\vec{\theta}}_1, \tilde{b}_{11}, \tilde{\varrho}_1)$ is chosen as (4.188). The parameter errors $\tilde{\vec{\theta}}_1$, $\tilde{b}_{11}$, and $\tilde{\varrho}_1$ are defined according to (4.189), (4.190), and (4.191) respectively. $\hat{b}_{11}$ is a first estimate for the uncertain constant parameter b_1, whereas $\hat{\varrho}_1$ is an estimate for b_1^{-1}. Both estimates and its respective parameter errors, also represented in $V_1(x_1, \tilde{\vec{\theta}}_1, \tilde{b}_{11}, \tilde{\varrho}_1)$, are necessary for the conduct of the design procedure, as will be evident from the upcoming steps. The adaptation gain matrix $\Gamma_1 \in \mathbb{R}^q \times \mathbb{R}^q$ is positive definite.

$$V_1\left(x_1, \tilde{\vec{\theta}}_1, \tilde{b}_{11}, \tilde{\varrho}_1\right) = \frac{1}{2}x_1^2 + \frac{1}{2}\tilde{\vec{\theta}}_1^T \Gamma_1^{-1} \tilde{\vec{\theta}}_1 + \frac{1}{2\gamma_{b_{11}}}\tilde{b}_{11}^2 + \frac{1}{2\gamma_{\varrho_1}}|b_1|\,\tilde{\varrho}_1^2 \tag{4.188}$$

$$\tilde{\vec{\theta}}_1 = \vec{\theta} - \hat{\vec{\theta}}_1 \tag{4.189}$$

$$\tilde{b}_{11} = b_1 - \hat{b}_{11} \tag{4.190}$$

$$\tilde{\varrho}_1 = \varrho_1 - \hat{\varrho}_1, \quad \varrho_1 = b_1^{-1}, \quad \hat{\varrho}_1 = \hat{b}_1^{-1} \tag{4.191}$$

The derivative of $V_1(x_1, \tilde{\vec{\theta}}_1, \tilde{b}_{11}, \tilde{\varrho}_1 t)$ is calculated as (4.192), by utilizing the latter definitions as well as the fact that $\vec{\theta}$ and b_1 are presumed to be constant.

$$\begin{aligned}\dot{V}_1\left(x_1, \tilde{\vec{\theta}}_1, \tilde{b}_{11}, \tilde{\varrho}_1\right) &= x_1\left[F_1^T(x_1)\,\vec{\theta} + b_1 g_1(x_1)\left[z + \alpha\left(x_1, \hat{\vec{\theta}}_1, \hat{\varrho}_1\right)\right]\right] \\ &\quad -\tilde{\vec{\theta}}_1^T \Gamma_1^{-1} \dot{\hat{\vec{\theta}}}_1 - \frac{1}{\gamma_{b_{11}}}\tilde{b}_{11}\dot{\hat{b}}_{11} - \frac{1}{\gamma_{\varrho_1}}|b_1|\,\tilde{\varrho}_1\dot{\hat{\varrho}}_1\end{aligned} \tag{4.192}$$

The stabilizing function $\alpha(x_1, \hat{\vec{\theta}}_1, \hat{\varrho}_1)$ is defined by (4.193), with $c_1 \in \mathbb{R}_+$. (4.192) simplifies to (4.194).

$$\alpha\left(x_1, \hat{\vec{\theta}}_1, \hat{\varrho}_1\right) = \frac{\hat{\varrho}_1}{g_1(x_1)}\left[-F_1^T(x_1)\,\hat{\vec{\theta}}_1 - c_1 x_1\right] \tag{4.193}$$

$$\begin{aligned}\dot{V}_1\left(x_1, \tilde{\vec{\theta}}_1, \tilde{b}_{11}, \tilde{\varrho}_1\right) &= x_1\Big[F_1^T(x_1)\,\vec{\theta} + b_1 g_1(x_1)\,z \\ &\quad + b_1\hat{\varrho}_1\left[-F_1^T(x_1)\,\hat{\vec{\theta}}_1 - c_1 x_1\right]\Big] \\ &\quad - \tilde{\vec{\theta}}_1^T\Gamma_1^{-1}\dot{\hat{\vec{\theta}}}_1 - \frac{1}{\gamma_{b_{11}}}\tilde{b}_{11}\dot{\hat{b}}_{11} - \frac{1}{\gamma_{\varrho_1}}|b_1|\,\tilde{\varrho}_1\dot{\hat{\varrho}}_1\end{aligned} \tag{4.194}$$

The update law for $\dot{\hat{\varrho}}_1$ is chosen according to (4.195). The knowledge about the sign of b_1 allows this choice. The derivative of $V_1(x_1, \tilde{\vec{\theta}}_1, \tilde{b}_{11}, \tilde{\varrho}_1)$ shortens to (4.196), by implementing (4.195) in (4.194). From (4.196), appropriate choices for the update laws for $\dot{\hat{b}}_{11}$ and $\dot{\hat{\vec{\theta}}}_1$ according to (4.197) and (4.198) are obvious. The derivative of $V_1(x_1, \tilde{\vec{\theta}}_1, \tilde{b}_{11}, \tilde{\varrho}_1)$ simplifies further to (4.199).

$$\dot{\hat{\varrho}}_1 = -\gamma_{\varrho_1}\operatorname{sgn}(b_1)x_1\left[-F_1^T(x_1)\,\hat{\vec{\theta}}_1 - c_1 x_1\right] \tag{4.195}$$

$$\begin{aligned}\dot{V}_1\left(x_1, \tilde{\vec{\theta}}_1, \tilde{b}_{11}, \tilde{\varrho}_1\right) &= x_1\Big[F_1^T(x_1)\,\vec{\theta} + b_1 g_1(x_1)\,z \\ &\quad + b_1\left(\hat{\varrho}_1 + \tilde{\varrho}_1\right)\left[-F_1^T(x_1)\,\hat{\vec{\theta}}_1 - c_1 x_1\right]\Big] \\ &\quad - \tilde{\vec{\theta}}_1^T\Gamma_1^{-1}\dot{\hat{\vec{\theta}}}_1 - \frac{1}{\gamma_{b_{11}}}\tilde{b}_{11}\dot{\hat{b}}_{11} \\ &= x_1\left[F_1^T(x_1)\,\tilde{\vec{\theta}}_1 + b_1 g_1(x_1)\,z - c_1 x_1\right] \\ &\quad - \tilde{\vec{\theta}}_1^T\Gamma_1^{-1}\dot{\hat{\vec{\theta}}}_1 - \frac{1}{\gamma_{b_{11}}}\tilde{b}_{11}\dot{\hat{b}}_{11} \\ &= -c_1 x_1^2 + x_1 F_1^T(x_1)\,\tilde{\vec{\theta}}_1 + \left(\hat{b}_{11} + \tilde{b}_{11}\right)x_1 g_1(x_1)\,z \\ &\quad - \tilde{\vec{\theta}}_1^T\Gamma_1^{-1}\dot{\hat{\vec{\theta}}}_1 - \frac{1}{\gamma_{b_{11}}}\tilde{b}_{11}\dot{\hat{b}}_{11} \\ &= -c_1 x_1^2 + \hat{b}_{11}x_1 g_1(x_1)\,z \\ &\quad + \tilde{\vec{\theta}}_1^T\left[F_1(x_1)\,x_1 - \Gamma_1^{-1}\dot{\hat{\vec{\theta}}}_1\right] + \tilde{b}_{11}\left[x_1 g_1(x_1)\,z - \frac{1}{\gamma_{b_{11}}}\dot{\hat{b}}_{11}\right]\end{aligned} \tag{4.196}$$

$$\dot{\hat{b}}_{11} = \gamma_{b_{11}}x_1 g_1(x_1)\,z \tag{4.197}$$

$$\dot{\hat{\vec{\theta}}}_1 = \Gamma_1 F_1(x_1)\,x_1 \tag{4.198}$$

$$\dot{V}_1\left(x_1, \tilde{\vec{\theta}}_1, \tilde{b}_{11}, \tilde{\varrho}_1\right) = -c_1 x_1^2 + \hat{b}_{11}x_1 g_1(x_1)\,z \tag{4.199}$$

Because of the unknown sign of the last term in (4.199), neither a conclusion about the boundedness properties nor a conclusion about the stability properties is possible at this point. Therefore, the derivative of z is calculated in the following as (4.200).

$$\dot{z} = \dot{x}_2 - \dot{\alpha}\left(x_1, \hat{\vec{\theta}}_1, \hat{\varrho}_1\right)$$

$$
\begin{aligned}
&= F_2^T\left(x_1, x_2\right)\vec{\theta} + b_2 g_2\left(x_1, x_2\right) u \\
&\quad -\frac{\partial\alpha\left(x_1, \hat{\vec{\theta}}_1, \hat{\varrho}_1\right)}{\partial x_1}\left[F_1^T\left(x_1\right)\vec{\theta} + b_1 g_1\left(x_1\right) x_2\right] - \frac{\partial\alpha\left(x_1, \hat{\vec{\theta}}_1, \hat{\varrho}_1\right)}{\partial\hat{\vec{\theta}}_1}\left[\Gamma_1 F_1\left(x_1\right) x_1\right] \\
&\quad -\frac{\partial\alpha\left(x_1, \hat{\vec{\theta}}_1, \hat{\varrho}_1\right)}{\partial\hat{\varrho}_1}\left[-\gamma_{\varrho_1}\operatorname{sgn}\left(b_1\right) x_1\left[-F_1^T\left(x_1\right)\hat{\vec{\theta}}_1 - c_1 x_1\right]\right]
\end{aligned} \tag{4.200}
$$

The Lyapunov function $V_2(x_1, \tilde{\vec{\theta}}_1, \tilde{b}_{11}, \tilde{\varrho}_1, z, \tilde{\vec{\theta}}_2, \tilde{b}_{12}, \tilde{\varrho}_2)$ is defined in (4.201). The parameter errors $\tilde{\vec{\theta}}_2$, $\tilde{b}_{12}$, and $\tilde{\varrho}_2$ are defined following (4.189) to (4.191), and $\Gamma_2 \in \mathbb{R}^q \times \mathbb{R}^q$ is positive definite. $\hat{b}_{12}$ is a second estimate for the uncertain constant parameter b_1 in (4.184), but $\hat{\varrho}_2$ constitutes an estimate for b_2^{-1}. In contrast to the designs in [71], which neither considers unknown control coefficients in adaptive Backstepping designs nor elaborates the case with unknown control coefficients in every equation of the nonlinear system, the term comprising $\tilde{b}_{12}$ enters $V_2(x_1, \tilde{\vec{\theta}}_1, \tilde{b}_{11}, \tilde{\varrho}_1, z, \tilde{\vec{\theta}}_2, \tilde{b}_{12}, \tilde{\varrho}_2)$. This term provides the necessary degree of freedom to cancel b_1, which reappears in the remaining steps of the procedure.

$$
\begin{aligned}
V_2\left(x_1, \tilde{\vec{\theta}}_1, \tilde{b}_{11}, \tilde{\varrho}_1, z, \tilde{\vec{\theta}}_2, \tilde{b}_{12}, \tilde{\varrho}_2\right) &= V_1\left(x_1, \tilde{\vec{\theta}}_1, \tilde{b}_{11}, \tilde{\varrho}_1\right) \\
&\quad + \frac{1}{2} z^2 + \frac{1}{2}\tilde{\vec{\theta}}_2^T \Gamma_2^{-1}\tilde{\vec{\theta}}_2 + \frac{1}{2\gamma_{b_{12}}}\tilde{b}_{12}^2 + \frac{1}{2\gamma_{\varrho_2}}\left|b_2\right|\tilde{\varrho}_2^2 \\
&= \frac{1}{2} x_1^2 + \frac{1}{2}\tilde{\vec{\theta}}_1^T \Gamma_1^{-1}\tilde{\vec{\theta}}_1 + \frac{1}{2\gamma_{b_{11}}}\tilde{b}_{11}^2 + \frac{1}{2\gamma_{\varrho_1}}\left|b_1\right|\tilde{\varrho}_1^2 \\
&\quad + \frac{1}{2} z^2 + \frac{1}{2}\tilde{\vec{\theta}}_2^T \Gamma_2^{-1}\tilde{\vec{\theta}}_2 + \frac{1}{2\gamma_{b_{12}}}\tilde{b}_{12}^2 + \frac{1}{2\gamma_{\varrho_2}}\left|b_2\right|\tilde{\varrho}_2^2
\end{aligned} \tag{4.201}
$$

Employing (4.199), the derivative of $V_2(x_1, \tilde{\vec{\theta}}_1, \tilde{b}_{11}, \tilde{\varrho}_1, z, \tilde{\vec{\theta}}_2, \tilde{b}_{12}, \tilde{\varrho}_2)$ is developed to (4.202). The arguments of the functions are omitted for the sake of readability.

$$
\begin{aligned}
\dot{V}_2\left(x_1, \tilde{\vec{\theta}}_1, \tilde{b}_{11}, \tilde{\varrho}_1, z, \tilde{\vec{\theta}}_2, \tilde{b}_{12}, \tilde{\varrho}_2\right) &= x_1\dot{x}_1 - \tilde{\vec{\theta}}_1^T \Gamma_1^{-1}\dot{\hat{\vec{\theta}}}_1 - \frac{1}{\gamma_{b_{11}}}\tilde{b}_{11}\dot{\hat{b}}_{11} - \frac{1}{\gamma_{\varrho_1}}\left|b_1\right|\tilde{\varrho}_1\dot{\hat{\varrho}}_1 \\
&\quad + z\dot{z} - \tilde{\vec{\theta}}_2^T \Gamma_2^{-1}\dot{\hat{\vec{\theta}}}_2 - \frac{1}{\gamma_{b_{12}}}\tilde{b}_{12}\dot{\hat{b}}_{12} - \frac{1}{\gamma_{\varrho_2}}\left|b_2\right|\tilde{\varrho}_2\dot{\hat{\varrho}}_2 \\
&= -c_1 x_1^2 + \hat{b}_{11} x_1 g_1 z \\
&\quad + z\left[F_2^T\vec{\theta} + b_2 g_2 u - \frac{\partial\alpha}{\partial x_1}\left[F_1^T\vec{\theta} + b_1 g_1 x_2\right]\right. \\
&\quad \left. - \frac{\partial\alpha}{\partial\hat{\vec{\theta}}_1}\left[\Gamma_1 F_1 x_1\right] - \frac{\partial\alpha}{\partial\hat{\varrho}_1}\left[-\gamma_{\varrho_1}\operatorname{sgn}\left(b_1\right) x_1\left[-F_1^T\hat{\vec{\theta}}_1 - c_1 x_1\right]\right]\right] \\
&\quad - \tilde{\vec{\theta}}_2^T \Gamma_2^{-1}\dot{\hat{\vec{\theta}}}_2 - \frac{1}{\gamma_{b_{12}}}\tilde{b}_{12}\dot{\hat{b}}_{12} - \frac{1}{\gamma_{\varrho_2}}\left|b_2\right|\tilde{\varrho}_2\dot{\hat{\varrho}}_2
\end{aligned} \tag{4.202}
$$

The control u is chosen according to (4.203); $c_2 \in \mathbb{R}_+$. By additionally defining the update law for $\dot{\hat{\varrho}}_2$ as stated in (4.204), the derivative of $V_2(x_1, \tilde{\vec{\theta}}_1, \tilde{b}_{11}, \tilde{\varrho}_1, z, \tilde{\vec{\theta}}_2, \tilde{b}_{12}, \tilde{\varrho}_2)$ simplifies to (4.205).

$$
\begin{aligned}
u &= \frac{\hat{\varrho}_2}{g_2}\left[-F_2^T\hat{\vec{\theta}}_2 - \hat{b}_{11} x_1 g_1 + \frac{\partial\alpha}{\partial x_1}\left[F_1^T\hat{\vec{\theta}}_2 + \hat{b}_{12} g_1 x_2\right] + \frac{\partial\alpha}{\partial\hat{\vec{\theta}}_1}\left[\Gamma_1 F_1 x_1\right]\right. \\
&\quad \left. + \frac{\partial\alpha}{\partial\hat{\varrho}_1}\left[-\gamma_{b_{11}}\operatorname{sgn}\left(b_1\right) x_1\left[-F_1^T\hat{\vec{\theta}}_1 - c_1 x_1\right]\right] - c_2 z\right]
\end{aligned} \tag{4.203}
$$

$$\begin{aligned}\dot{\hat{\varrho}}_2 &= -\gamma_{\varrho_2}\operatorname{sgn}(b_2)z\Big[-F_2^T\hat{\vec{\theta}}_2-\hat{b}_{11}x_1g_1+\frac{\partial\alpha}{\partial x_1}\left[F_1^T\hat{\vec{\theta}}_2+\hat{b}_{12}g_1x_2\right]+\frac{\partial\alpha}{\partial\hat{\vec{\theta}}_1}\left[\Gamma_1F_1x_1\right]\\ &\quad+\frac{\partial\alpha}{\partial\hat{\varrho}_1}\left[-\gamma_{b_{11}}\operatorname{sgn}(b_1)x_1\left[-F_1^T\hat{\vec{\theta}}_1-c_1x_1\right]\right]-c_2z\Big] \qquad (4.204)\end{aligned}$$

$$\begin{aligned}\dot{V}_2\left(x_1,\tilde{\vec{\theta}}_1,\tilde{b}_{11},\tilde{\varrho}_1,z,\tilde{\vec{\theta}}_2,\tilde{b}_{12},\tilde{\varrho}_2\right) &= -c_1x_1^2+\hat{b}_{11}x_1g_1z\\ &\quad+z\left[F_2^T\tilde{\vec{\theta}}_2-\hat{b}_{11}x_1g_1-\frac{\partial\alpha}{\partial x_1}F_1^T\tilde{\vec{\theta}}_2-\frac{\partial\alpha}{\partial x_1}\tilde{b}_{12}g_1x_2-c_2z\right]\\ &\quad-\tilde{\vec{\theta}}_2^T\Gamma_2^{-1}\dot{\tilde{\vec{\theta}}}_2-\frac{1}{\gamma_{b_{12}}}\tilde{b}_{12}\dot{\tilde{b}}_{12}\\ &= -c_1x_1^2-c_2z^2\\ &\quad\tilde{\vec{\theta}}_2^T\left[F_2z-\frac{\partial\alpha}{\partial x_1}F_1z-\Gamma_2^{-1}\dot{\tilde{\vec{\theta}}}_2\right]\\ &\quad\tilde{b}_{12}\left[-z\frac{\partial\alpha}{\partial x_1}g_1x_2-\frac{1}{\gamma_{b_{12}}}\dot{\tilde{b}}_{12}\right] \qquad (4.205)\end{aligned}$$

Using (4.205) as basis, the update laws for $\dot{\tilde{b}}_{12}$ and $\dot{\tilde{\vec{\theta}}}_2$ are derived as (4.206) and (4.207), which finally provides the simplification of the derivative of $V_2(x_1,\tilde{\vec{\theta}}_1,\tilde{b}_{11},\tilde{\varrho}_1,z,\tilde{\vec{\theta}}_2,\tilde{b}_{12},\tilde{\varrho}_2)$ according to (4.208).

$$\dot{\tilde{b}}_{12}=-\gamma_{b_{12}}z\frac{\partial\alpha}{\partial x_1}g_1x_2 \qquad (4.206)$$

$$\dot{\tilde{\vec{\theta}}}_2=\Gamma_2\left[F_2-\frac{\partial\alpha}{\partial x_1}F_1\right]z \qquad (4.207)$$

$$\dot{V}_2\left(x_1,\tilde{\vec{\theta}}_1,\tilde{b}_{11},\tilde{\varrho}_1,z,\tilde{\vec{\theta}}_2,\tilde{b}_{12},\tilde{\varrho}_2\right)=-c_1x_1^2-c_2z^2 \qquad (4.208)$$

Due to the fact that (4.209) holds for all arguments of $V_2(x_1,\tilde{\vec{\theta}}_1,\tilde{b}_{11},\tilde{\varrho}_1,z,\tilde{\vec{\theta}}_2,\tilde{b}_{12},\tilde{\varrho}_2)$ in their respective domain, Theorem 4.1 guarantees global boundedness of $x_1(t)$, $\tilde{\vec{\theta}}_1(t)$, $\tilde{b}_{11}(t)$, $\tilde{\varrho}_1(t)$, $z(t)$, $\tilde{\vec{\theta}}_2(t)$, $\tilde{b}_{12}(t)$, and $\tilde{\varrho}_2(t)$. Based on the global boundedness of the mentioned signals, $\alpha(x_1(t),\hat{\vec{\theta}}_1(t),\hat{\varrho}_1(t))$ is globally bounded. This further implies the global boundedness of $x_2(t)$ via definition (4.186). All solutions of (4.184) and (4.185) are globally bounded. The regulation of $x_1(t)$ and $z(t)$ is additionally guaranteed by Theorem 4.1.

$$\dot{V}_2\left(x_1,\tilde{\vec{\theta}}_1,\tilde{b}_{11},\tilde{\varrho}_1,z,\tilde{\vec{\theta}}_2,\tilde{b}_{12},\tilde{\varrho}_2\right)=-c_1x_1^2-c_2z^2\leq 0 \qquad (4.209)$$

It is evident from (4.195), (4.197), (4.198), (4.204), (4.206), and (4.207) that the regulation of $x_1(t)$ and $z(t)$ causes that $\hat{\vec{\theta}}_1(t)$, $\hat{b}_{11}(t)$, $\hat{\varrho}_1(t)$, $\hat{\vec{\theta}}_2(t)$, $\hat{b}_{12}(t)$, and $\hat{\varrho}_2(t)$ reach a steady-state value for $t\to\infty$. Hence, $\alpha(x_1(t),\hat{\vec{\theta}}_1(t),\hat{\varrho}_1(t))$ converges to the steady-state value given in (4.210) for $t\to\infty$.

$$\alpha_{SS}\left(x_1,\hat{\vec{\theta}}_1,\hat{\varrho}_1\right)=\frac{\hat{\varrho}_{1,SS}}{g_1(0)}\left[-F_1^T(0)\,\hat{\vec{\theta}}_{1,SS}\right] \qquad (4.210)$$

Presumed $F_1(0)=0$, $\alpha(x_1(t),\hat{\vec{\theta}}_1(t),\hat{\varrho}_1(t))\to 0$ for $t\to\infty$, which leads to $x_2(t)\to 0$ for $t\to\infty$. In this case, $x_1=0$, $x_2=0$ is the globally stable equilibrium of (4.184) and (4.185).
If $c_1\in\mathbb{R}_+$, $c_2\in\mathbb{R}_+$, $\gamma_{b_{11}}\in\mathbb{R}_+$, $\gamma_{b_{12}}\in\mathbb{R}_+$, $\gamma_{\varrho_1}\in\mathbb{R}_+$, and $\gamma_{\varrho_2}\in\mathbb{R}_+$, the derived boundedness

and stability properties are achieved. In addition, the positive definiteness of $\Gamma_1 \in \mathbb{R}^q \times \mathbb{R}^q$ and $\Gamma_2 \in \mathbb{R}^q \times \mathbb{R}^q$ as well as (4.211) and (4.212) are requirements for the derived boundedness and stability properties. $\hat{\varrho}_1 \neq 0$ and $\hat{\varrho}_2 \neq 0$ must hold.

$$g_1(x_1) \neq 0, \quad \forall x_1 \in \mathbb{R} \tag{4.211}$$

$$g_2(x_1, x_2) \neq 0, \quad \forall x_1 \in \mathbb{R}, \quad \forall x_2 \in \mathbb{R} \tag{4.212}$$

Design procedure for parametric strict-feedback systems with unknown control coefficients in the case of tracking

The preceding design procedure illustrated that adaptive Backstepping achieves global boundedness and global stability for parametric strict-feedback systems with unknown control coefficients. If global boundedness, global tracking of a known, smooth, and bounded reference signal, and global stability is achieved by a similar design procedure, the ability to withstand uncertain constant parameters is established for the design of the interceptor flight control system. For this reason, the control task of tracking is considered now.

The parametric strict-feedback system with unknown control coefficients is identical to the beforehand presented procedure. It is given by (4.184) and (4.185). The stated properties of the system remain unchanged. The output $y \in \mathbb{R}$, which is equal to x_1, is desired to follow a known, smooth, and bounded reference signal $x_{1,Ref} \in \mathbb{R}$. The derivatives of $x_{1,Ref}$ are known, smooth, and bounded.

Following prior presentations concerning tracking, two error variables $z_1 \in \mathbb{R}$ and $z_2 \in \mathbb{R}$ are defined by (4.213) and (4.214).

$$z_1 = x_1 - x_{1,Ref} \tag{4.213}$$

$$z_2 = x_2 - \alpha\left(x_1, x_{1,Ref}, \dot{x}_{1,Ref}, \hat{\vec{\theta}}_1, \hat{\varrho}_1\right) \tag{4.214}$$

The Lyapunov function $V_1(z_1, \tilde{\vec{\theta}}_1, \tilde{b}_{11}, \tilde{\varrho}_1)$ is given in (4.215), whereupon the respective parameter errors are defined in (4.216) to (4.218), $\gamma_{b_{11}} \in \mathbb{R}_+$, $\gamma_{\varrho_1} \in \mathbb{R}_+$, and the adaptation gain matrix $\Gamma_1 \in \mathbb{R}^q \times \mathbb{R}^q$ is positive definite.

$$V_1\left(z_1, \tilde{\vec{\theta}}_1, \tilde{b}_{11}, \tilde{\varrho}_1\right) = \frac{1}{2}z_1^2 + \frac{1}{2}\tilde{\vec{\theta}}_1^T \Gamma_1^{-1} \tilde{\vec{\theta}}_1 + \frac{1}{2\gamma_{b_{11}}}\tilde{b}_{11}^2 + \frac{1}{2\gamma_{\varrho_1}}|b_1|\,\tilde{\varrho}_1^2 \tag{4.215}$$

$$\tilde{\vec{\theta}}_1 = \vec{\theta} - \hat{\vec{\theta}}_1 \tag{4.216}$$

$$\tilde{b}_{11} = b_1 - \hat{b}_{11} \tag{4.217}$$

$$\tilde{\varrho}_1 = \varrho_1 - \hat{\varrho}_1, \quad \varrho_1 = b_1^{-1}, \quad \hat{\varrho}_1 = \hat{b}_1^{-1} \tag{4.218}$$

The derivative of $V_1(z_1, \tilde{\vec{\theta}}_1, \tilde{b}_{11}, \tilde{\varrho}_1)$ leads to the stabilizing function $\alpha(z_1, x_{1,Ref}, \dot{x}_{1,Ref}, \hat{\vec{\theta}}_1, \hat{\varrho}_1)$ as (4.219); $c_1 \in \mathbb{R}_+$. Furthermore, the update laws for $\dot{\hat{\varrho}}_1$, $\dot{\hat{b}}_{11}$, and $\dot{\hat{\vec{\theta}}}_1$ are derived from the derivative of $V_1(z_1, \tilde{\vec{\theta}}_1, \tilde{b}_{11}, \tilde{\varrho}_1)$ according to (4.220), (4.221), and (4.222).

$$\alpha\left(z_1, x_{1,Ref}, \dot{x}_{1,Ref}, \hat{\vec{\theta}}_1, \hat{\varrho}_1\right) = \frac{\hat{\varrho}_1}{g_1(x_1)}\left[-F_1^T(x_1)\,\hat{\vec{\theta}}_1 + \dot{x}_{1,Ref} - c_1 z_1\right] \tag{4.219}$$

$$\dot{\hat{\varrho}}_1 = -\gamma_{\varrho_1}\,\mathrm{sgn}(b_1) z_1\left[-F_1^T(x_1)\,\hat{\vec{\theta}}_1 + \dot{x}_{1,Ref} - c_1 z_1\right] \tag{4.220}$$

$$\dot{\hat{b}}_{11} = \gamma_{b_{11}} z_1 g_1 (x_1) z_2 \tag{4.221}$$

$$\dot{\tilde{\vec{\theta}}}_1 = \Gamma_1 F_1 (x_1) z_1 \tag{4.222}$$

$\alpha(z_1, x_{1,Ref}, \dot{x}_{1,Ref}, \hat{\vec{\theta}}_1, \hat{\varrho}_1)$ and the update laws are used in the derivative of $V_1(z_1, \tilde{\vec{\theta}}_1, \tilde{b}_{11}, \tilde{\varrho}_1)$. Afterwards, the Lyapunov function $V_2(z_1, \tilde{\vec{\theta}}_1, \tilde{b}_{11}, \tilde{\varrho}_1, z_2, \tilde{\vec{\theta}}_2, \tilde{b}_{12}, \tilde{\varrho}_2)$ is taken as stated in (4.223). The respective parameter errors $\tilde{\vec{\theta}}_2$, $\tilde{b}_{12}$, and $\tilde{\varrho}_2$ are given by (4.224) to (4.226). $\hat{\vec{\theta}}_2$ is a second parameter estimate for $\vec{\theta}$. $\hat{b}_{12}$ is second parameter estimate for b_1, where $\hat{\varrho}_2$ is only related to b_2. $\Gamma_2 \in \mathbb{R}^q \times \mathbb{R}^q$ constitutes a positive definite adaptation gain matrix independent of Γ_1, and $\gamma_{b_{12}} \in \mathbb{R}_+$ as well as $\gamma_{\varrho_2} \in \mathbb{R}_+$.

$$\begin{aligned} V_2\left(z_1, \tilde{\vec{\theta}}_1, \tilde{b}_{11}, \tilde{\varrho}_1, z_2, \tilde{\vec{\theta}}_2, \tilde{b}_{12}, \tilde{\varrho}_2\right) &= \frac{1}{2} z_1^2 + \frac{1}{2} \tilde{\vec{\theta}}_1^T \Gamma_1^{-1} \tilde{\vec{\theta}}_1 + \frac{1}{2\gamma_{b_{11}}} \tilde{b}_{11}^2 + \frac{1}{2\gamma_{\varrho_1}} |b_1| \, \tilde{\varrho}_1^2 \\ &\quad + \frac{1}{2} z_2^2 + \frac{1}{2} \tilde{\vec{\theta}}_2^T \Gamma_2^{-1} \tilde{\vec{\theta}}_2 + \frac{1}{2\gamma_{b_{12}}} \tilde{b}_{12}^2 + \frac{1}{2\gamma_{\varrho_2}} |b_2| \, \tilde{\varrho}_2^2 \end{aligned} \tag{4.223}$$

$$\tilde{\vec{\theta}}_2 = \vec{\theta} - \hat{\vec{\theta}}_2 \tag{4.224}$$

$$\tilde{b}_{12} = b_1 - \hat{b}_{12} \tag{4.225}$$

$$\tilde{\varrho}_2 = \varrho_2 - \hat{\varrho}_2, \quad \varrho_2 = b_2^{-1}, \quad \hat{\varrho}_2 = \hat{b}_2^{-1} \tag{4.226}$$

Via the derivative of $V_2(z_1, \tilde{\vec{\theta}}_1, \tilde{b}_{11}, \tilde{\varrho}_1, z_2, \tilde{\vec{\theta}}_2, \tilde{b}_{12}, \tilde{\varrho}_2)$ the control u is derived according to (4.227); $c_2 \in \mathbb{R}_+$. The update laws for $\dot{\hat{\varrho}}_2$, $\dot{\hat{b}}_{12}$, and $\dot{\hat{\vec{\theta}}}_2$ are appropriately chosen as (4.228), (4.229), and (4.230). The respective arguments of the functions are left out for readability.

$$\begin{aligned} u &= \frac{\hat{\varrho}_2}{g_2} \Bigg[-F_2^T \hat{\vec{\theta}}_2 - \hat{b}_{11} z_1 g_1 + \frac{\partial \alpha}{\partial x_1} \left[F_1^T \hat{\vec{\theta}}_2 + \hat{b}_{12} g_1 x_2 \right] \\ &\quad + \frac{\partial \alpha}{\partial x_{1,Ref}} \dot{x}_{1,Ref} + \frac{\partial \alpha}{\partial \dot{x}_{1,Ref}} \ddot{x}_{1,Ref} + \frac{\partial \alpha}{\partial \hat{\theta}_1} \left[\Gamma_1 F_1 z_1 \right] \\ &\quad + \frac{\partial \alpha}{\partial \hat{\varrho}_1} \left[-\gamma_{b_{11}} \operatorname{sgn}(b_1) z_1 \left[-F_1^T \hat{\vec{\theta}}_1 + \dot{x}_{1,Ref} - c_1 z_1 \right] \right] - c_2 z_2 \Bigg] \end{aligned} \tag{4.227}$$

$$\begin{aligned} \dot{\hat{\varrho}}_2 &= -\gamma_{\varrho_2} \operatorname{sgn}(b_2) z_2 \Bigg[-F_2^T \hat{\vec{\theta}}_2 - \hat{b}_{11} z_1 g_1 + \frac{\partial \alpha}{\partial x_1} \left[F_1^T \hat{\vec{\theta}}_2 + \hat{b}_{12} g_1 x_2 \right] \\ &\quad + \frac{\partial \alpha}{\partial x_{1,Ref}} \dot{x}_{1,Ref} + \frac{\partial \alpha}{\partial \dot{x}_{1,Ref}} \ddot{x}_{1,Ref} + \frac{\partial \alpha}{\partial \hat{\theta}_1} \left[\Gamma_1 F_1 z_1 \right] \\ &\quad + \frac{\partial \alpha}{\partial \hat{\varrho}_1} \left[-\gamma_{b_{11}} \operatorname{sgn}(b_1) z_1 \left[-F_1^T \hat{\vec{\theta}}_1 + \dot{x}_{1,Ref} - c_1 z_1 \right] \right] - c_2 z_2 \Bigg] \end{aligned} \tag{4.228}$$

$$\dot{\hat{b}}_{12} = -\gamma_{b_{12}} z_2 \frac{\partial \alpha}{\partial x_1} g_1 x_2 \tag{4.229}$$

$$\dot{\hat{\vec{\theta}}}_2 = \Gamma_2 \left[F_2 - \frac{\partial \alpha}{\partial x_1} F_1 \right] z_2 \tag{4.230}$$

Employing (4.227) and (4.228) to (4.230) in the derivative of $V_2(z_1, \tilde{\vec{\theta}}_1, \tilde{b}_{11}, \tilde{\varrho}_1, z_2, \tilde{\vec{\theta}}_2, \tilde{b}_{12}, \tilde{\varrho}_2)$ gives rise to (4.231).

$$\dot{V}_2\left(z_1, \tilde{\vec{\theta}}_1, \tilde{b}_{11}, \tilde{\varrho}_1, z_2, \tilde{\vec{\theta}}_2, \tilde{b}_{12}, \tilde{\varrho}_2\right) = -c_1 z_1^2 - c_2 z_2^2 \tag{4.231}$$

Because (4.232) holds, global boundedness of $z_1(t)$, $\tilde{\vec{\theta}}_1(t)$, $\tilde{b}_{11}(t)$, $\tilde{\varrho}_1(t)$, $z_2(t)$, $\tilde{\vec{\theta}}_2(t)$, $\tilde{b}_{12}(t)$, and $\tilde{\varrho}_2(t)$ is guaranteed by Theorem 4.1. All solutions of the error system, which is given in (4.233) to (4.242), are globally bounded. The comparison of (4.233) to (4.242) with (4.148) and (4.149) shows how the error system is modified and augmented due to the consideration of the unknown control coefficients.

$$\dot{V}_2\left(z_1, \tilde{\vec{\theta}}_1, \tilde{b}_{11}, \tilde{\varrho}_1, z_2, \tilde{\vec{\theta}}_2, \tilde{b}_{12}, \tilde{\varrho}_2\right) = -c_1 z_1^2 - c_2 z_2^2 \leq 0 \tag{4.232}$$

$$\begin{aligned}\begin{bmatrix}\dot{z}_1\\ \dot{z}_2\end{bmatrix} &= \begin{bmatrix}-c_1 & \hat{b}_{11} g_1(x_1)\\ -\hat{b}_{11} g_1(x_1) & -c_2\end{bmatrix}\begin{bmatrix}z_1\\ z_2\end{bmatrix} + \begin{bmatrix}w_1^T & 0\\ 0 & w_2^T\end{bmatrix}\begin{bmatrix}\tilde{\vec{\theta}}_1\\ \tilde{\vec{\theta}}_2\end{bmatrix}\\ &\quad + \begin{bmatrix}u + \hat{\varrho}_1 v_1 & 0\\ 0 & -\frac{\partial \alpha}{\partial x_1}(u + \hat{\varrho}_1 v_1)\end{bmatrix}\begin{bmatrix}\tilde{b}_{11}\\ \tilde{b}_{12}\end{bmatrix} + \begin{bmatrix}0\\ \hat{\varrho}_2 v_2\end{bmatrix}\tilde{b}_2\end{aligned} \tag{4.233}$$

$$\begin{bmatrix}\dot{\hat{\vec{\theta}}}_1\\ \dot{\hat{\vec{\theta}}}_2\end{bmatrix} = \begin{bmatrix}\Gamma_1 & 0\\ 0 & \Gamma_2\end{bmatrix}\begin{bmatrix}w_1 & 0\\ 0 & w_2\end{bmatrix}\begin{bmatrix}z_1\\ z_2\end{bmatrix} \tag{4.234}$$

$$\begin{bmatrix}\dot{\hat{\varrho}}_1\\ \dot{\hat{\varrho}}_2\end{bmatrix} = \begin{bmatrix}-\gamma_{\varrho_1}\operatorname{sgn}(b_1) v_1 & 0\\ 0 & -\gamma_{\varrho_2}\operatorname{sgn}(b_2) v_2\end{bmatrix}\begin{bmatrix}z_1\\ z_2\end{bmatrix} \tag{4.235}$$

$$\dot{\hat{b}}_{11} = \gamma_{b_{11}} u z_1 \tag{4.236}$$

$$\dot{\hat{b}}_{12} = -\gamma_{b_{12}}\frac{\partial \alpha}{\partial x_1} u x_2 \tag{4.237}$$

$$u = g_1(x_1) z_2 \tag{4.238}$$

$$v_1 = -F_1^T(x_1)\hat{\vec{\theta}}_1 + \dot{x}_{1,Ref} - c_1 z_1 \tag{4.239}$$

$$\begin{aligned}v_2 &= -F_2^T(x_1, x_2)\hat{\vec{\theta}}_2 - \hat{b}_{11} z_1 g_1(x_1) + \frac{\partial \alpha}{\partial x_1}\left[F_1^T(x_1)\hat{\vec{\theta}}_2 + \hat{b}_{12} g_1(x_1) x_2\right]\\ &\quad + \frac{\partial \alpha}{\partial x_{1,Ref}}\dot{x}_{1,Ref} + \frac{\partial \alpha}{\partial \dot{x}_{1,Ref}}\ddot{x}_{1,Ref} + \frac{\partial \alpha}{\partial \hat{\vec{\theta}}_1}\left[\Gamma_1 F_1(x_1) z_1\right]\\ &\quad + \frac{\partial \alpha}{\partial \hat{\varrho}_1}\left[-\gamma_{\varrho_1}\operatorname{sgn}(b_1) z_1\left[-F_1^T(x_1)\hat{\vec{\theta}}_1 + \dot{x}_{1,Ref} - c_1 z_1\right]\right] - c_2 z_2\end{aligned} \tag{4.240}$$

$$w_1 = F_1(x_1) \tag{4.241}$$

$$w_2 = F_2(x_1, x_2) - \frac{\partial \alpha}{\partial x_1} F_1(x_1) \tag{4.242}$$

In addition to global boundedness, Theorem 4.1 provides the regulation of $z_1(t)$ and $z_2(t)$. Given (4.213), this implies that $x_{1,Ref}$ is tracked globally. Hence, the control task of tracking of a known, smooth, and bounded reference signal is achieved globally.
Revisiting (4.220), (4.221), (4.222), (4.228), (4.229), and (4.230) as well as the regulation of $z_1(t)$ and $z_2(t)$, it is clear that $\hat{\vec{\theta}}_1(t)$, $\hat{b}_{11}(t)$, $\hat{\varrho}_1(t)$, $\hat{\vec{\theta}}_2(t)$, $\hat{b}_{12}(t)$, $\hat{\varrho}_2(t)$ reach a steady-state for $t \to \infty$. $z_1 = 0$, $z_2 = 0$ constitutes the globally stable equilibrium of the error system given in (4.233) to (4.242).
With respect to the parametric strict-feedback system given in (4.184) and (4.185), the global

boundedness of $z_1(t)$ and $x_{1,Ref}(t)$ achieves the global boundedness of $x_1(t)$. The global boundedness of $\hat{\vec{\theta}}_1(t)$ and $\hat{\varrho}_1(t)$, which is derived from (4.220) and (4.222), leads to the global boundedness of $\alpha(z_1, x_{1,Ref}, \dot{x}_{1,Ref}, \hat{\vec{\theta}}_1, \hat{\varrho}_1)$. The latter result provides the global boundedness of $x_2(t)$ based on (4.214). Therefore, all solutions of (4.184) and (4.185) are globally bounded.
Given $x_{1,Ref}(t) \to 0$ for $t \to \infty$, $x_1(t) \to 0$ for $t \to \infty$ is implied via the regulation of $z_1(t)$ and (4.213). Accounting for the regulation of $z_1(t)$ and $z_2(t)$, which leads to the convergence of $\hat{\vec{\theta}}_1(t)$, $\hat{b}_{11}(t)$, $\hat{\varrho}_1(t)$, $\hat{\vec{\theta}}_2(t)$, $\hat{b}_{12}(t)$, and $\hat{\varrho}_2(t)$ to a steady-state for $t \to \infty$, $\alpha(z_1, x_{1,Ref}, \dot{x}_{1,Ref}, \hat{\vec{\theta}}_1, \hat{\varrho}_1)$ converges to the steady-state stated in (4.243).

$$\alpha_{SS}\left(z_1, x_{1,Ref}, \dot{x}_{1,Ref}, \hat{\vec{\theta}}_1, \hat{\varrho}_1\right) = \frac{\hat{\varrho}_{1,SS}}{g_1(0)}\left[-F_1^T(0)\,\hat{\vec{\theta}}_{1,SS}\right] \tag{4.243}$$

If $F_1(x_1)$ exhibits the property $F_1(0) = 0$, $\alpha(z_1, x_{1,Ref}, \dot{x}_{1,Ref}, \hat{\vec{\theta}}_1, \hat{\varrho}_1) \to 0$ for $t \to \infty$. Founded on (4.214), $x_2(t) \to 0$ for $t \to \infty$. If the introduced conditions hold, $x_1 = 0$, $x_2 = 0$ is the globally stable equilibrium of (4.184) and (4.185).
$c_1 \in \mathbb{R}_+$, $c_2 \in \mathbb{R}_+$, $\gamma_{b_{11}} \in \mathbb{R}_+$, $\gamma_{b_{12}} \in \mathbb{R}_+$, $\gamma_{\varrho_1} \in \mathbb{R}_+$, and $\gamma_{\varrho_2} \in \mathbb{R}_+$ are prerequisites for the derived boundedness and stability properties. $\Gamma_1 \in \mathbb{R}^q \times \mathbb{R}^q$ and $\Gamma_2 \in \mathbb{R}^q \times \mathbb{R}^q$ are required to be positive definite. (4.244) and (4.245) are necessary to guarantee the controllability of (4.184) and (4.185) as well as the existence of $\alpha\left(z_1, x_{1,Ref}, \dot{x}_{1,Ref}, \hat{\vec{\theta}}_1, \hat{\varrho}_1\right)$ and u. Furthermore, $\hat{\varrho}_1 \neq 0$ and $\hat{\varrho}_2 \neq 0$ must hold.

$$g_1(x_1) \neq 0, \quad \forall x_1 \in \mathbb{R} \tag{4.244}$$

$$g_2(x_1, x_2) \neq 0, \quad \forall x_1 \in \mathbb{R}, \quad x_2 \in \mathbb{R} \tag{4.245}$$

This section introduced adaptive Backstepping, and demonstrated that this methodology is capable to overcome uncertain constant parameters in strict-feedback systems. Parametric strict-feedback systems as well as parametric strict-feedback systems with unknown control coefficients have been considered. The design procedures for regulation and tracking of a known, smooth, and bounded reference signal have been derived.
If the uncertainties which are implemented in the interceptor would only encompass uncertain constant parameters, the presented theoretical background of this thesis would be sufficient to design the interceptor flight control system. As introduced in Chapter 2, the interceptor comprises uncertain constant parameters and time-varying parameters. This means, the presented theoretical background must be further augmented. This augmentation constitutes the final step in the theoretical background presentation.

4.4 Nonlinear damping

The strict-feedback systems considered beforehand contained no uncertainties or uncertain constant parameters. As illustrated, Backstepping and adaptive Backstepping constitute appropriate methodologies to control such systems. Following Chapter 2, some properties of the interceptor are subject to permanent change. These properties constitute time-varying parameters. Because Backstepping and adaptive Backstepping in the presented form are inappropriate to deal with time-varying parameters in strict-feedback systems, another methodology is employed. This methodology is nonlinear damping. It is available in [71], which introduces the basic concept. The combination of nonlinear damping with the design procedures is illustrated in the following. Furthermore, it is shown that nonlinear damping guarantees global boundedness in partial absence of adaptation concerning the derived design procedures.

For the introduction of the concept of nonlinear damping, the nonlinear system given in (4.246) is considered. $x \in \mathbb{R}$ is the state, $u \in \mathbb{R}$ is the control input, $f : \mathbb{R} \to \mathbb{R}$, and $g : \mathbb{R} \to \mathbb{R}$ are known, smooth nonlinear functions. The nonlinearity $\Delta(t)$ is unknown, but uniformly bounded.

$$\dot{x} = f(x)\,\Delta(t) + g(x)\,u \tag{4.246}$$

The Lyapunov function $V(x)$ for (4.246) is chosen equal to (4.247). The derivative of $V(x)$ is developed to (4.248).

$$V(x) = \frac{1}{2}x^2 \tag{4.247}$$

$$\begin{aligned} \dot{V}(x) &= x\dot{x} \\ &= x\left[f(x)\,\Delta(t) + g(x)\,u\right] \end{aligned} \tag{4.248}$$

By choosing the control u in accordance with (4.249), where $c \in \mathbb{R}_+$ and $\kappa \in \mathbb{R}_+$, the derivative of $V(x)$ is calculated as (4.250).

$$u = \frac{1}{g(x)}\left[-cx - \kappa f^2(x)\,x\right] \tag{4.249}$$

$$\dot{V} = -cx^2 - \kappa f^2(x)\,x^2 + xf(x)\,\Delta(t) \tag{4.250}$$

The completion of squares in (4.250) leads to (4.251). The derivative of $V(x)$ is negative whenever (4.252) holds. Based on the fact that $\Delta(t)$ is uniformly bounded, the derivative of $V(x)$ is negative outside the set R given in (4.253). Because $V(x)$ is positive definite, $\|x(t)\|$ decreases whenever $x(t)$ is outside the set R. Hence, $x(t)$ is globally bounded.

$$\begin{aligned} \dot{V} &= -cx^2 - \kappa\left[xf(x) - \frac{\Delta(t)}{2\kappa}\right]^2 + \frac{\Delta(t)^2}{4\kappa} \\ &\leq -cx^2 + \frac{\Delta(t)^2}{4\kappa} \end{aligned} \tag{4.251}$$

$$|x(t)| > \frac{\Delta(t)}{2\sqrt{\kappa c}} \tag{4.252}$$

$$R = \left\{x : |x| \leq \frac{\|\Delta\|_\infty}{2\sqrt{\kappa c}}\right\} \tag{4.253}$$

Design procedure for robust strict-feedback systems

The repeated application of the introduced concept of nonlinear damping to a robust strict-feedback system establishes the design procedure for robust strict-feedback systems which is illustrated now. The steps of this procedure comprise the terms which are utilized in the following to augment the beforehand derived designs. [71] introduces this design procedure, but a more general form of system is considered herein.

The robust strict-feedback system is given in (4.254) and (4.255). $x_1 \in \mathbb{R}$ and $x_2 \in \mathbb{R}$ constitute the states. $u \in \mathbb{R}$ is the control input. $F_1 : \mathbb{R}^n \to \mathbb{R}^n$ and $F_2 : \mathbb{R}^n \to \mathbb{R}^n$ are vector fields composed of known, smooth nonlinear functions. $g_1 : \mathbb{R} \to \mathbb{R}$ and $g_2 : \mathbb{R} \to \mathbb{R}$ are known, smooth nonlinear functions. $\vec{\Delta}(t) \in \mathbb{R}^q$ is a vector of unknown, uniformly bounded nonlinearities.

$$\dot{x}_1 = F_1^T(x_1)\,\vec{\Delta}(t) + g_1(x_1)\,x_2 \tag{4.254}$$

$$\dot{x}_2 = F_2^T(x_1, x_2)\,\vec{\Delta}(t) + g_2(x_1, x_2)\,u \tag{4.255}$$

By defining an error variable z according to (4.256) and utilizing its definition, (4.254) is written as (4.257). The Lyapunov function $V_1(x_1)$ is chosen as (4.258).

$$z = x_2 - \alpha(x_1) \tag{4.256}$$

$$\dot{x}_1 = F_1^T(x_1)\,\vec{\Delta}(t) + g_1(x_1)\,[z + \alpha(x_1)] \tag{4.257}$$

$$V_1(x_1) = \frac{1}{2}x_1^2 \tag{4.258}$$

Then, the derivative of $V_1(x_1)$ is manipulated to (4.259). Afterwards, the stabilizing function $\alpha(x_1)$ is chosen like (4.260), with $c_1 \in \mathbb{R}_+$ and $\kappa_1 \in \mathbb{R}_+$. Implementing this in the derivative of $V_1(x_1)$ leads to (4.261).

$$\begin{aligned}
\dot{V}_1(x_1) &= x_1\dot{x}_1 \\
&= x_1\left[F_1^T(x_1)\,\vec{\Delta}(t) + g_1(x_1)\,[z + \alpha(x_1)]\right] \\
&= x_1 F_1^T(x_1)\,\vec{\Delta}(t) + x_1 g_1(x_1)\,z + x_1 g_1(x_1)\,\alpha(x_1) \\
&\leq |x_1|\,|F_1(x_1)|\,\|\,\vec{\Delta}\,\|_\infty + x_1 g_1(x_1)\,z + x_1 g_1(x_1)\,\alpha(x_1)
\end{aligned} \tag{4.259}$$

$$\alpha(x_1) = \frac{1}{g_1(x_1)}\left[-c_1 x_1 - \kappa_1\,|F_1(x_1)|^2\,x_1\right] \tag{4.260}$$

$$\begin{aligned}
\dot{V}_1(x_1) &\leq |x_1|\,|F_1(x_1)|\,\|\,\vec{\Delta}\,\|_\infty + x_1 g_1(x_1)\,z - c_1 x_1^2 - \kappa_1\,|F_1(x_1)|^2\,x_1^2 \\
&= -c_1 x_1^2 + x_1 g_1(x_1)\,z - \kappa_1\left[|x_1|\,|F_1(x_1)| - \frac{\|\,\vec{\Delta}\,\|_\infty}{2\kappa_1}\right]^2 + \frac{\|\,\vec{\Delta}\,\|_\infty^2}{4\kappa_1} \\
&\leq -c_1 x_1^2 + \frac{\|\,\vec{\Delta}\,\|_\infty^2}{4\kappa_1} + x_1 g_1(x_1)\,z
\end{aligned} \tag{4.261}$$

Because neither a conclusion about the boundedness properties nor a conclusion about the stability properties of the robust strict-feedback system is possible, the derivative of z is developed as (4.262). The Lyapunov function $V_2(x_1, z)$ is now given by (4.263). Utilizing (4.261) and (4.262), the derivative of $V_2(x_1, z)$ is developed to (4.264). The respective arguments of the functions are omitted to enhance readability.

$$\begin{aligned}
\dot{z} &= \dot{x}_2 - \dot{\alpha}(x_1) \\
&= F_2^T(x_1, x_2)\,\vec{\Delta}(t) + g_2(x_1, x_2)\,u - \frac{\partial\alpha(x_1)}{\partial x_1}\left[F_1^T(x_1)\,\vec{\Delta}(t) + g_1(x_1)\,x_2\right]
\end{aligned} \tag{4.262}$$

$$\begin{aligned}
V_2(x_1, z) &= V_1(x_1) + \frac{1}{2}z^2 \\
&= \frac{1}{2}x_1^2 + \frac{1}{2}z^2
\end{aligned} \tag{4.263}$$

$$\dot{V}_2(x_1, z) = x_1\dot{x}_1 + z\dot{z}$$

$$= -c_1 x_1^2 + \frac{\| \vec{\Delta} \|_\infty^2}{4\kappa_1} + x_1 g_1 z + z \left[F_2^T \vec{\Delta} + g_2 u - \frac{\partial \alpha}{\partial x_1} \left[F_1^T \vec{\Delta} + g_1 x_2 \right] \right] \tag{4.264}$$

The control u is chosen according to (4.265); $c_2 \in \mathbb{R}_+$ and $\kappa_2 \in \mathbb{R}_+$. Using (4.265) in (4.264), the derivative of $V_2(x_1, z)$ is simplified to (4.266).

$$u = \frac{1}{g_2} \left[-c_2 z - x_1 g_1 + \frac{\partial \alpha}{\partial x_1} g_1 x_2 - \kappa_2 \left| F_2 - \frac{\partial \alpha}{\partial x_1} F_1 \right|^2 z \right] \tag{4.265}$$

$$\begin{aligned}
\dot{V}_2(x_1, z) &= -c_1 x_1^2 + \frac{\| \vec{\Delta} \|_\infty^2}{4\kappa_1} \\
&\quad + z \left[F_2^T \vec{\Delta} - c_2 z - \kappa_2 \left| F_2 - \frac{\partial \alpha}{\partial x_1} F_1 \right|^2 z - \frac{\partial \alpha}{\partial x_1} F_1^T \vec{\Delta} \right] \\
&\leq -c_1 x_1^2 + \frac{\| \vec{\Delta} \|_\infty^2}{4\kappa_1} \\
&\quad - c_2 z^2 + |z| \left| F_2 - \frac{\partial \alpha}{\partial x_1} F_1 \right| \| \vec{\Delta} \|_\infty^2 - \kappa_2 \left| F_2 - \frac{\partial \alpha}{\partial x_1} F_1 \right|^2 z \\
&= -c_1 x_1^2 + \frac{\| \vec{\Delta} \|_\infty^2}{4\kappa_1} \\
&\quad - c_2 z^2 + \left[|z| \left| F_2 - \frac{\partial \alpha}{\partial x_1} F_1 \right| - \frac{\| \vec{\Delta} \|_\infty}{2\kappa_2} \right]^2 + \frac{\| \vec{\Delta} \|_\infty^2}{4\kappa_2} \\
&\leq -c_1 x_1^2 - c_2 z^2 + \frac{\| \vec{\Delta} \|_\infty^2}{4\kappa_1} + \frac{\| \vec{\Delta} \|_\infty^2}{4\kappa_2}
\end{aligned} \tag{4.266}$$

(4.266) shows that $x_1(t)$ and $z(t)$ are globally bounded. The global boundedness of $x_1(t)$ in combination with (4.260) leads to the global boundedness of $\alpha(x_1)$. Relying on (4.256), the global boundedness of $x_2(t)$ is concluded. Hence, all solutions of the robust strict-feedback system (4.254), (4.255) are globally bounded. All signals converge to the compact set given by (4.267).

$$R = \left\{ (x_1, z) : c_1 x_1^2 + c_2 z^2 \leq \frac{\| \vec{\Delta} \|_\infty^2}{4\kappa_1} + \frac{\| \vec{\Delta} \|_\infty^2}{4\kappa_2} \right\} \tag{4.267}$$

Interpreting $\vec{\Delta}(t)$ not as a vector of unknown, uniformly bounded nonlinearities, as introduced above, but as a vector of time-varying parameters, it is evident that the presented design procedure guarantees global boundedness for strict-feedback systems which comprise time-varying parameters.

Augmented design procedure for parametric strict-feedback systems with unknown control coefficients in the case of tracking

After the employment of nonlinear damping has been illustrated in the framework of a design procedure, Backstepping and nonlinear damping are combined. This combination leads to augmented design procedures for parametric strict-feedback systems. The latter provide the capabilities to handle uncertain constant parameters as well as time-varying parameters.

Because the combination of adaptive Backstepping and nonlinear damping is achieved by the straightforward and simultaneous employment of both methodologies, only the augmented design procedure for parametric strict-feedback systems with unknown control coefficients in the

case of tracking is derived herein to stay inside the scope of this thesis. This procedure encompasses the full spectrum of the introduced theoretical background. Based on its capabilities, this design procedure is the starting point for the design of the interceptor flight control system. The boundedness and stability properties which are achieved by this design procedure are derived. In addition, following the introduction for a simpler system in [71], it is shown that global boundedness in partial absence of adaptation is achieved.
The parametric strict-feedback system with unknown control coefficients is given by (4.184) and (4.185). The properties of the system remain unchanged. It is desired that the output $y \in \mathbb{R}$, which is equal to x_1, follows a known, smooth, and bounded reference signal $x_{1,Ref}$. The derivatives of $x_{1,Ref}$ are known, smooth, and bounded.
First, two error variables $z_1 \in \mathbb{R}$ and $z_2 \in \mathbb{R}$ are defined in (4.213) and (4.214). After developing the derivative of z_1, the Lyapunov function $V_1(z_1, \tilde{\vec{\theta}}_1, \tilde{b}_{11}, \tilde{\varrho}_1)$ is chosen according to (4.215), whereupon $\gamma_{b_{11}} \in \mathbb{R}_+$, $\gamma_{\varrho_1} \in \mathbb{R}_+$, and $\Gamma_1 \in \mathbb{R}^q \times \mathbb{R}^q$ is positive definite. The definition of the respective parameter errors is stated in (4.217) to (4.219).
The stabilizing function $\alpha(z_1, x_{1,Ref}, \dot{x}_{1,Ref}, \hat{\vec{\theta}}_1, \hat{\varrho}_1)$ is chosen as (4.268), based on the derivative of $V_1(z_1, \tilde{\vec{\theta}}_1, \tilde{b}_{11}, \tilde{\varrho}_1)$. The nonlinear damping terms, which were derived in the design procedure for robust strict-feedback systems, are taken into account for this choice of $\alpha(z_1, x_{1,Ref}, \dot{x}_{1,Ref}, \hat{\vec{\theta}}_1, \hat{\varrho}_1)$.

$$\alpha\left(z_1, x_{1,Ref}, \dot{x}_{1,Ref}, \hat{\vec{\theta}}_1, \hat{\varrho}_1\right) = \frac{\hat{\varrho}_1}{g_1(x_1)}\left[-F_1^T(x_1)\,\hat{\vec{\theta}}_1 + \dot{x}_{1,Ref} - c_1 z_1 - \kappa_1 \left|F_1(x_1)\right|^2 z_1\right] \quad (4.268)$$

By implementing $\alpha(z_1, x_{1,Ref}, \dot{x}_{1,Ref}, \hat{\vec{\theta}}_1, \hat{\varrho}_1)$ in the derivative of $V_1(z_1, \tilde{\vec{\theta}}_1, \tilde{b}_{11}, \tilde{\varrho}_1)$, the update law for $\dot{\hat{\varrho}}_1$ becomes obvious as (4.269). The update laws for $\dot{\hat{b}}_{11}$ and $\dot{\hat{\vec{\theta}}}_1$ are given in (4.221) and (4.222); they remain unchanged.

$$\dot{\hat{\varrho}}_1 = -\gamma_{\varrho_1}\operatorname{sgn}(b_1) z_1\left[-F_1^T(x_1)\,\hat{\vec{\theta}}_1 + \dot{x}_{1,Ref} - c_1 z_1 - \kappa_1\left|F_1(x_1)\right|^2 z_1\right] \quad (4.269)$$

The choice for the Lyapunov function $V_2(z_1, \tilde{\vec{\theta}}_1, \tilde{b}_{11}, \tilde{\varrho}_1, z_2, \tilde{\vec{\theta}}_2, \tilde{b}_{12}, \tilde{\varrho}_2)$ is stated in (4.223). The adaptation gain matrix $\Gamma_2 \in \mathbb{R}^q \times \mathbb{R}^q$ is positive definite, $\gamma_{b_{12}} \in \mathbb{R}_+$, and $\gamma_{\varrho_2} \in \mathbb{R}_+$. (4.224), (4.225), and (4.226) provide the parameter errors, where $\hat{\vec{\theta}}_2$ is a second parameter estimate for $\vec{\theta}$ and $\hat{b}_{12}$ constitutes a second parameter estimate for b_1.
Given the derivative of $V_2(z_1, \tilde{\vec{\theta}}_1, \tilde{b}_{11}, \tilde{\varrho}_1, z_2, \tilde{\vec{\theta}}_2, \tilde{b}_{12}, \tilde{\varrho}_2)$, the control u is chosen in accordance with (4.270). After u is employed, the update law for $\dot{\hat{\varrho}}_2$ is defined appropriately as (4.271). The nonlinear damping terms derived in the design procedure for robust strict-feedback systems enter u as well as the update law for $\dot{\hat{\varrho}}_2$, but the update laws for $\dot{\hat{b}}_{12}$ and $\dot{\hat{\vec{\theta}}}_2$ remain unchanged as stated in (4.229) and (4.230). The arguments of the functions are left out to enhance readability.

$$\begin{aligned} u \;=\; & \frac{\hat{\varrho}_2}{g_2}\Bigg[-F_2^T\hat{\vec{\theta}}_2 - \hat{b}_{11} z_1 g_1 + \frac{\partial\alpha}{\partial x_1}\left[F_1^T\hat{\vec{\theta}}_2 + \hat{b}_{12} g_1 x_2\right] \\ & + \frac{\partial\alpha}{\partial x_{1,Ref}}\dot{x}_{1,Ref} + \frac{\partial\alpha}{\partial \dot{x}_{1,Ref}}\ddot{x}_{1,Ref} + \frac{\partial\alpha}{\partial\hat{\theta}_1}\left[\Gamma_1 F_1 z_1\right] \\ & + \frac{\partial\alpha}{\partial\hat{\varrho}_1}\left[-\gamma_{b_{11}}\operatorname{sgn}(b_1) z_1\left[-F_1^T\hat{\vec{\theta}}_1 + \dot{x}_{1,Ref} - c_1 z_1 - \kappa_1\left|F_1\right|^2 z_1\right]\right] \\ & - c_2 z_2 - \kappa_2\left|F_2 - \frac{\partial\alpha}{\partial x_1}F_1\right|^2 z_2\Bigg] \end{aligned} \quad (4.270)$$

$$
\begin{aligned}
\dot{\hat{\varrho}}_2 &= -\gamma_{\varrho 2}\operatorname{sgn}(b_2) z_2 \Bigg[-F_2^T \hat{\vec{\theta}}_2 - \hat{b}_{11} z_1 g_1 + \frac{\partial \alpha}{\partial x_1}\left[F_1^T \hat{\vec{\theta}}_2 + \hat{b}_{12} g_1 x_2 \right] \\
&\quad + \frac{\partial \alpha}{\partial x_{1,Ref}} \dot{x}_{1,Ref} + \frac{\partial \alpha}{\partial \dot{x}_{1,Ref}} \ddot{x}_{1,Ref} + \frac{\partial \alpha}{\partial \hat{\theta}_1}\left[\Gamma_1 F_1 z_1 \right] \\
&\quad + \frac{\partial \alpha}{\partial \hat{\varrho}_1}\left[-\gamma_{b_{11}} \operatorname{sgn}(b_1) z_1 \left[-F_1^T \hat{\vec{\theta}}_1 + \dot{x}_{1,Ref} - c_1 z_1 - \kappa_1 |F_1|^2 z_1 \right] \right] \\
&\quad - c_2 z_2 - \kappa_2 \left| F_2 - \frac{\partial \alpha}{\partial x_1} F_1 \right|^2 z_2 \Bigg]
\end{aligned} \tag{4.271}
$$

The derivative of $V_2(z_1, \tilde{\vec{\theta}}_1, \tilde{b}_{11}, \tilde{\varrho}_1, z_2, \tilde{\vec{\theta}}_2, \tilde{b}_{12}, \tilde{\varrho}_2)$ is simplified to (4.272) by implementing u as well as the update laws (4.229), (4.230), and (4.271).

$$
\begin{aligned}
\dot{V}_2\left(z_1, \tilde{\vec{\theta}}_1, \tilde{b}_{11}, \tilde{\varrho}_1, z_2, \tilde{\vec{\theta}}_2, \tilde{b}_{12}, \tilde{\varrho}_2 \right) &= -c_1 z_1^2 - c_2 z_2^2 \\
&\quad - \kappa_1 |F_1|^2 z_1^2 - \kappa_2 \left| F_2 - \frac{\partial \alpha}{\partial x_1} F_1 \right|^2 z_2^2
\end{aligned} \tag{4.272}
$$

Due to the fact that (4.273) is valid for all arguments of $V_2(z_1, \tilde{\vec{\theta}}_1, \tilde{b}_{11}, \tilde{\varrho}_1, z_2, \tilde{\vec{\theta}}_2, \tilde{b}_{12}, \tilde{\varrho}_2)$ in their respective domain, the boundedness and stability properties of the augmented design procedure are similar to the design procedure for parametric strict-feedback systems with unknown control coefficients in the case of tracking. Theorem 4.1 provides global boundedness of $z_1(t)$, $\tilde{\vec{\theta}}_1(t)$, $\tilde{b}_{11}(t)$, $\tilde{\varrho}_1$, $z_2(t)$, $\tilde{\vec{\theta}}_2(t)$, $\tilde{b}_{12}(t)$, and $\tilde{\varrho}_2$, which implies that all solutions of the error system are globally bounded.

$$
\begin{aligned}
\dot{V}_2\left(z_1, \tilde{\vec{\theta}}_1, \tilde{b}_{11}, \tilde{\varrho}_1, z_2, \tilde{\vec{\theta}}_2, \tilde{b}_{12}, \tilde{\varrho}_2 \right) &= -c_1 z_1^2 - c_2 z_2^2 \\
&\quad - \kappa_1 |F_1|^2 z_1^2 - \kappa_2 \left| F_2 - \frac{\partial \alpha}{\partial x_1} F_1 \right|^2 z_2^2 \\
&\leq 0
\end{aligned} \tag{4.273}
$$

Furthermore, Theorem 4.1 guarantees the regulation of $z_1(t)$ and $z_2(t)$. Considering (4.213), the regulation of $z_1(t)$ leads to the global tracking of $x_{1,Ref}$. The regulation of $z_1(t)$ and $z_2(t)$ causes that $\hat{\vec{\theta}}_1(t)$, $\hat{b}_{11}(t)$, $\hat{\varrho}_1(t)$, $\hat{\vec{\theta}}_2(t)$, $\hat{b}_{12}(t)$, and $\hat{\varrho}_2(t)$ reach a steady-state for $t \to \infty$. $z_1 = 0$, $z_2 = 0$ is the globally stable equilibrium of the error system.
The global boundedness of $x_1(t)$ is achieved via the global boundedness of $z_1(t)$ and $x_{1,Ref}(t)$. Global boundedness of $\hat{\vec{\theta}}_1(t)$ and $\hat{\varrho}_1(t)$ implies global boundedness of $\alpha(z_1, x_{1,Ref}, \dot{x}_{1,Ref}, \hat{\vec{\theta}}_1, \hat{\varrho}_1)$, which leads to the global boundedness of $x_2(t)$. For this reason, all solutions of (4.184) and (4.185) are globally bounded in case of the augmented design procedure.
Assuming $x_{1,Ref}(t) \to 0$ for $t \to \infty$, $x_1(t) \to 0$ for $t \to \infty$ results. This ends up in the convergence of $\alpha(z_1, x_{1,Ref}, \dot{x}_{1,Ref}, \hat{\vec{\theta}}_1, \hat{\varrho}_1)$ to the steady-state value given in (4.274).

$$
\alpha_{SS}\left(z_1, x_{1,Ref}, \dot{x}_{1,Ref}, \hat{\vec{\theta}}_1, \hat{\varrho}_1 \right) = \frac{\hat{\varrho}_{1,SS}}{g_1(0)} \left[-F_1^T(0) \hat{\vec{\theta}}_{1,SS} \right] \tag{4.274}
$$

Provided $F_1(0) = 0$, $\alpha_{SS}(z_1, x_{1,Ref}, \dot{x}_{1,Ref}, \hat{\vec{\theta}}_1, \hat{\varrho}_1) \to 0$ and $x_2(t) \to 0$ for $t \to \infty$. This finally shows that $x_1 = 0$, $x_2 = 0$ is the globally stable equilibrium of (4.184) and (4.185).
The prerequisites for the augmented design procedure are identical to the design procedure for parametric strict-feedback systems with unknown control coefficients in the case of tracking. In

addition, $\kappa_1 \in \mathbb{R}_+$ and $\kappa_2 \in \mathbb{R}_+$ are required.
Besides the fact that the augmented design procedure achieves the identical boundedness and stability properties as the design procedure for parametric strict-feedback systems with unknown control coefficients in the case of tracking, the former provides another benefit. It guarantees global boundedness in partial absence of adaptation. The proof that all signals are globally bounded, even if parts of the adaptation algorithms comprised in the design procedure fail, is given in the following.

Global boundedness in partial absence of adaptation
The nonlinear system to be considered is (4.184) and (4.185), and the properties of this nonlinear system as well as the assumptions on $x_{1,Ref}$, which have been provided for the augmented design procedure for parametric strict-feedback systems with unknown control coefficients in the case of tracking, remain. The definitions of the respective error variables z_1 and z_2 are given by (4.213) and (4.214). In contrast to the beforehand presentation, the Lyapunov function $V_1(z_1, \tilde{b}_{11}, \tilde{\varrho}_1)$ is defined without $\tilde{\vec{\theta}}_1$ according to (4.275); $\Gamma_1 = 0$, $\gamma_{b_{11}} \in \mathbb{R}_+$, and $\gamma_{\varrho_1} \in \mathbb{R}_+$.

$$V_1\left(z_1, \tilde{b}_{11}, \tilde{\varrho}_1\right) = \frac{1}{2} z_1^2 + \frac{1}{2\gamma_{b_{11}}} \tilde{b}_{11}^2 + \frac{1}{2\gamma_{\varrho_1}} |b_1| \, \tilde{\varrho}_1^2 \tag{4.275}$$

By choosing the stabilizing function $\alpha(z_1, x_{1,Ref}, \dot{x}_{1,Ref}, \hat{\vec{\theta}}_{1,0}, \hat{\varrho}_1)$ as (4.276) and the update law for $\dot{\hat{\varrho}}_1$ according to (4.277), whereupon $c_1 \in \mathbb{R}_+$, $\kappa_1 \in \mathbb{R}_+$, and $\hat{\vec{\theta}}_{1,0} \in \mathbb{R}^q$ constitutes an initial, constant parameter estimate for $\vec{\theta}$, the derivative of $V_1(z_1, \tilde{b}_{11}, \tilde{\varrho}_1)$ is developed to (4.278). The update law for $\dot{\hat{b}}_{11}$ is given by (4.221).

$$\alpha\left(z_1, x_{1,Ref}, \dot{x}_{1,Ref}, \hat{\vec{\theta}}_{1,0}, \hat{\varrho}_1\right) = \frac{\hat{\varrho}_1}{g_1(x_1)} \left[-F_1^T(x_1) \, \hat{\vec{\theta}}_{1,0} + \dot{x}_{1,Ref} - c_1 z_1 - \kappa_1 |F_1(x_1)|^2 z_1\right] \tag{4.276}$$

$$\dot{\hat{\varrho}}_1 = -\gamma_{\varrho_1} \operatorname{sgn}(b_1) z_1 \left[-F_1^T(x_1) \, \hat{\vec{\theta}}_{1,0} + \dot{x}_{1,Ref} - c_1 z_1 - \kappa_1 |F_1(x_1)|^2 z_1\right] \tag{4.277}$$

$$\begin{aligned}
\dot{V}_1\left(z_1, \tilde{b}_{11}, \tilde{\varrho}_1\right) &= z_1 \dot{z}_1 - \frac{1}{\gamma_{b_{11}}} \tilde{b}_{11} \dot{\hat{b}}_{11} - \frac{1}{\gamma_{\varrho_1}} |b_1| \, \tilde{\varrho}_1 \dot{\hat{\varrho}}_1 \\
&= z_1 \left[F_1^T(x_1) \, \vec{\theta} + b_1 g_1(x_1) z_2 + b_1 g_1(x_1) \, \alpha(\dots) - \dot{x}_{1,Ref}\right] \\
&\quad - \frac{1}{\gamma_{b_{11}}} \tilde{b}_{11} \dot{\hat{b}}_{11} - \frac{1}{\gamma_{\varrho_1}} |b_1| \, \tilde{\varrho}_1 \dot{\hat{\varrho}}_1 \\
&= -c_1 z_1^2 + \hat{b}_{11} z_1 g_1(x_1) z_2 + z_1 F_1^T(x_1) \, \vec{\theta} - z_1 F_1^T(x_1) \, \hat{\vec{\theta}}_{1,0} - \kappa_1 |F_1(x_1)|^2 z_1^2 \\
&= -c_1 z_1^2 + \hat{b}_{11} z_1 g_1(x_1) z_2 + z_1 F_1^T(x_1) \, \tilde{\vec{\theta}}_{1,0} - \kappa_1 |F_1(x_1)|^2 z_1^2 \\
&\leq -c_1 z_1^2 + \hat{b}_{11} z_1 g_1(x_1) z_2 + |z_1| \, |F_1(x_1)| \left|\tilde{\vec{\theta}}_{1,0}\right| - \kappa_1 |F_1(x_1)|^2 z_1^2 \\
&= -c_1 z_1^2 + \hat{b}_{11} z_1 g_1(x_1) z_2 - \kappa_1 \left[|z_1| \, |F_1(x_1)| - \frac{\left|\tilde{\vec{\theta}}_{1,0}\right|}{2\kappa_1}\right]^2 + \frac{\left|\tilde{\vec{\theta}}_{1,0}\right|^2}{4\kappa_1} \\
&\leq -c_1 z_1^2 + \hat{b}_{11} z_1 g_1(x_1) z_2 + \frac{\left|\tilde{\vec{\theta}}_{1,0}\right|^2}{4\kappa_1}
\end{aligned} \tag{4.278}$$

Starting from the derivative of z_2, the Lyapunov function $V_2(z_1, \tilde{b}_{11}, \tilde{\varrho}_1, z_2, \tilde{b}_{12}, \tilde{\varrho}_2)$ is chosen as (4.279) accordingly. The latter does not contain $\tilde{\vec{\theta}}_2$. The adaptation gains $\gamma_{b_{12}}$ and $\gamma_{\varrho_2} \in \mathbb{R}_+$.

$$\begin{aligned} V_2\left(z_1, \tilde{b}_{11}, \tilde{\varrho}_1, z_2, \tilde{b}_{12}, \tilde{\varrho}_2\right) &= \frac{1}{2}z_1^2 + \frac{1}{2\gamma_{b_{11}}}\tilde{b}_{11}^2 + \frac{1}{2\gamma_{\varrho_1}}|b_1|\,\tilde{\varrho}_1^2 \\ &\quad + \frac{1}{2}z_2^2 + \frac{1}{2\gamma_{b_{12}}}\tilde{b}_{12}^2 + \frac{1}{2\gamma_{\varrho_2}}|b_2|\,\tilde{\varrho}_2^2 \end{aligned} \tag{4.279}$$

The derivative of $V_2(z_1, \tilde{b}_{11}, \tilde{\varrho}_1, z_2, \tilde{b}_{12}, \tilde{\varrho}_2)$ forms the basis for the appropriate choice of the control u in (4.280) as well as the update law for $\dot{\hat{\varrho}}_2$, which is given in (4.281); $c_2 \in \mathbb{R}_+$ and $\kappa_2 \in \mathbb{R}_+$. $\hat{\vec{\theta}}_{2,0} \in \mathbb{R}^q$ constitutes a second initial, constant parameter estimate for $\vec{\theta}$. The arguments of the functions are omitted.

$$\begin{aligned} u &= \frac{\hat{\varrho}_2}{g_2}\Big[-F_2^T\hat{\vec{\theta}}_{2,0} - \hat{b}_{11}z_1g_1 + \frac{\partial\alpha}{\partial x_1}\left[F_1^T\hat{\vec{\theta}}_{2,0} + \hat{b}_{12}g_1x_2\right] \\ &\quad + \frac{\partial\alpha}{\partial x_{1,Ref}}\dot{x}_{1,Ref} + \frac{\partial\alpha}{\partial\dot{x}_{1,Ref}}\ddot{x}_{1,Ref} \\ &\quad + \frac{\partial\alpha}{\partial\hat{\varrho}_1}\left[-\gamma_{b_{11}}\operatorname{sgn}(b_1)z_1\left[-F_1^T\hat{\vec{\theta}}_{1,0} + \dot{x}_{1,Ref} - c_1z_1 - \kappa_1|F_1|^2z_1\right]\right] \\ &\quad - c_2z_2 - \kappa_2\left|F_2 - \frac{\partial\alpha}{\partial x_1}F_1\right|^2 z_2\Big] \end{aligned} \tag{4.280}$$

$$\begin{aligned} \dot{\hat{\varrho}}_2 &= -\gamma_{\varrho_2}\operatorname{sgn}(b_2)z_2\Big[-F_2^T\hat{\vec{\theta}}_{2,0} - \hat{b}_{11}z_1g_1 + \frac{\partial\alpha}{\partial x_1}\left[F_1^T\hat{\vec{\theta}}_{2,0} + \hat{b}_{12}g_1x_2\right] \\ &\quad + \frac{\partial\alpha}{\partial x_{1,Ref}}\dot{x}_{1,Ref} + \frac{\partial\alpha}{\partial\dot{x}_{1,Ref}}\ddot{x}_{1,Ref} \\ &\quad + \frac{\partial\alpha}{\partial\hat{\varrho}_1}\left[-\gamma_{b_{11}}\operatorname{sgn}(b_1)z_1\left[-F_1^T\hat{\vec{\theta}}_{1,0} + \dot{x}_{1,Ref} - c_1z_1 - \kappa_1|F_1|^2z_1\right]\right] \\ &\quad - c_2z_2 - \kappa_2\left|F_2 - \frac{\partial\alpha}{\partial x_1}F_1\right|^2 z_2\Big] \end{aligned} \tag{4.281}$$

Utilizing u, the update law for $\dot{\hat{\varrho}}_2$, and the update law for $\dot{\hat{b}}_{12}$, which remains unchanged from (4.229), the derivative of $V_2(z_1, \tilde{b}_{11}, \tilde{\varrho}_1, z_2, \tilde{b}_{12}, \tilde{\varrho}_2)$ simplifies to (4.282).

$$\begin{aligned} \dot{V}_2\left(z_1, \tilde{b}_{11}, \tilde{\varrho}_1, z_2, \tilde{b}_{12}, \tilde{\varrho}_2\right) &= z_1\dot{z}_1 - \frac{1}{\gamma_{b_{11}}}\tilde{b}_{11}\dot{\hat{b}}_{11} - \frac{1}{\gamma_{\varrho_1}}|b_1|\,\tilde{\varrho}_1\dot{\hat{\varrho}}_1 \\ &\quad z_2\dot{z}_2 - \frac{1}{\gamma_{b_{12}}}\tilde{b}_{12}\dot{\hat{b}}_{12} - \frac{1}{\gamma_{\varrho_2}}|b_2|\,\tilde{\varrho}_2\dot{\hat{\varrho}}_2 \\ &\leq -c_1z_1^2 + \hat{b}_{11}z_1g_1z_2 + \frac{\left|\tilde{\vec{\theta}}_{1,0}\right|^2}{4\kappa_1} \\ &\quad + z_2\left[F_2^T\vec{\theta} + b_2g_2u\right] - \frac{1}{\gamma_{b_{12}}}\tilde{b}_{12}\dot{\hat{b}}_{12} - \frac{1}{\gamma_{\varrho_2}}|b_2|\,\tilde{\varrho}_2\dot{\hat{\varrho}}_2 \\ &\leq -c_1z_1^2 + \frac{\left|\tilde{\vec{\theta}}_{1,0}\right|^2}{4\kappa_1} \\ &\quad - c_2z_2^2 + |z_2|\left|F_2 - \frac{\partial\alpha}{\partial x_1}F_1\right|\left|\tilde{\vec{\theta}}_{2,0}\right| - \kappa_2\left|F_2 - \frac{\partial\alpha}{\partial x_1}F_1\right|^2 z_2^2 \end{aligned}$$

$$
\begin{aligned}
&= -c_1 z_1^2 + \frac{\left|\tilde{\vec{\theta}}_{1,0}\right|^2}{4\kappa_1} \\
&\quad -c_2 z_2^2 + \left[|z_2| \left| F_2 - \frac{\partial \alpha}{\partial x_1} F_1 \right| - \frac{\left|\tilde{\vec{\theta}}_{2,0}\right|}{2\kappa_2} \right]^2 + \frac{\left|\tilde{\vec{\theta}}_{2,0}\right|^2}{4\kappa_2} \\
&\leq -c_1 z_1^2 - c_2 z_2^2 + \frac{\left|\tilde{\vec{\theta}}_{1,0}\right|^2}{4\kappa_1} + \frac{\left|\tilde{\vec{\theta}}_{2,0}\right|^2}{4\kappa_2}
\end{aligned} \tag{4.282}
$$

The result achieved by (4.282) allows the following conclusions about the boundedness and stability properties of (4.184) and (4.185), based on the status of the adaptation algorithms comprised in the design.

If all of the adaptation algorithms are available and active, the derivative of the Lyapunov function $V_2(z_1, \tilde{\vec{\theta}}_1, \tilde{b}_{11}, \tilde{\varrho}_1, z_2, \tilde{\vec{\theta}}_2, \tilde{b}_{12}, \tilde{\varrho}_2)$ is given by (4.272). The respective boundedness and stability properties have been derived in conjunction with the augmented design procedure for parametric strict-feedback system with unknown control coefficients in the case of tracking.

The derivative of the Lyapunov function $V_2(z_1, \tilde{b}_{11}, \tilde{\varrho}_1, z_2, \tilde{b}_{12}, \tilde{\varrho}_2)$ is established by (4.282), if the adaptation algorithms for $\vec{\theta}$ fail. Because $\left|\tilde{\vec{\theta}}_{1,0}\right|$ and $\left|\tilde{\vec{\theta}}_{2,0}\right|$ are bounded, $z_1(t)$ and $z_2(t)$ are globally bounded; the tracking error is globally bounded. Via (4.213), the global boundedness of $x_1(t)$ is achieved. This leads to the global boundedness of $\hat{\varrho}_1(t)$, founded on (4.277), and $\alpha(z_1, x_{1,Ref}, \dot{x}_{1,Ref}, \hat{\vec{\theta}}_{1,0}, \hat{\varrho}_1)$. Accounting for (4.214), the global boundedness of $x_2(t)$ is achieved. For this reason, all solutions of (4.184) and (4.185) are globally bounded.

Because the derivative of $V_2\left(z_1, \tilde{b}_{11}, \tilde{\varrho}_1, z_2, \tilde{b}_{12}, \tilde{\varrho}_2\right)$ is negative outside the set defined in (4.283) and the Lyapunov function is positive definite, $z_1(t)$ and $z_2(t)$ converge to R. This means that the tracking error decreases until $z_1(t)$ and $z_2(t)$ reach R. Therefore, $x_{1,Ref}$ is tracked to a certain degree.

$$
R = \left\{ (z_1, z_2) : c_1 z_1^2 + c_2 z_2^2 \leq \frac{\left|\tilde{\vec{\theta}}_{1,0}\right|^2}{4\kappa_1} + \frac{\left|\tilde{\vec{\theta}}_{2,0}\right|^2}{4\kappa_2} \right\} \tag{4.283}
$$

The derived results are valid in the absence of adaptation for $\vec{\theta}$. The adaptation laws for $\dot{\hat{b}}_{11}$, $\dot{\hat{\varrho}}_1$, $\dot{\hat{b}}_{12}$, and $\dot{\hat{\varrho}}_2$ are employed based on the augmented design procedure for parametric strict-feedback system with unknown control coefficients in the case of tracking. With respect to the design and implementation of the interceptor flight control system, this means that the augmented design procedure provides capabilities for a failure of the adaptation mechanism for $\vec{\theta}$. Vice versa, the adaptation mechanism for $\dot{\hat{b}}_{11}$, $\dot{\hat{\varrho}}_1$, $\dot{\hat{b}}_{12}$, and $\dot{\hat{\varrho}}_2$ are required to be available and active in the presented design.

Chapter 5

Design of the flight control system

5.1 Performance requirements

After the theoretical background of the Backstepping methodology has been presented in Chapter 4, the design of the interceptor flight control system is conducted. The design process consists of seven consecutive steps. First, the performance requirements for the controlled interceptor are provided and analyzed. Thereafter, the overall interceptor flight control system architecture is designed. This leads to the detailed design of the respective control systems. Section 5.3 covers the design of the interceptor roll rate control system. The interceptor pitch acceleration control system is illustrated in Section 5.4, followed by Section 5.5 which shows the design of the interceptor yaw acceleration control system. In the sixth step, the control allocation algorithm as well as the reaction jet cartridge allocation mechanisms are designed. Finally, the parameters of the interceptor flight control system are optimized.
The design of the interceptor flight control system is governed by a set of performance requirements. These define the boundedness and stability properties which the interceptor flight control system shall guarantee. Furthermore, requirements concerning the dynamical behavior of the controlled interceptor exist.

- **Requirement 1** *The interceptor flight control system shall guarantee global boundedness of all signals of the controlled interceptor.*

- **Requirement 2** *Concerning the control task of regulation in absence of parameter uncertainties, the interceptor flight control system shall guarantee global asymptotic stability. In the presence of parameter uncertainties, the controlled interceptor shall be globally stable.*

- **Requirement 3** *The interceptor flight control system shall guarantee global asymptotic tracking of a known, smooth, and bounded reference signal, if parameter uncertainties are absent. In case of existing parameter uncertainties, the interceptor flight control system shall guarantee global tracking of a known, smooth, and bounded reference signal.*

- **Requirement 4** *The interceptor flight control system shall implement provision to overcome failures of the comprised adaptation algorithms. Global boundedness shall be preserved under this conditions, and tracking of known, smooth, and bounded reference signal should be achieved.*

- **Requirement 5** *The controlled interceptor shall maintain* $\left(p_K^{0B}\right)_B = 90\,[deg/s]$ *during the terminal flight phase, which encompasses the last* $10\,[s]$ *of the interceptor time of flight, in the presence of parameter uncertainties.* $\left(p_K^{0B}\right)_B$ *shall not vary more than* $\pm 50\,[\%]$ *to*

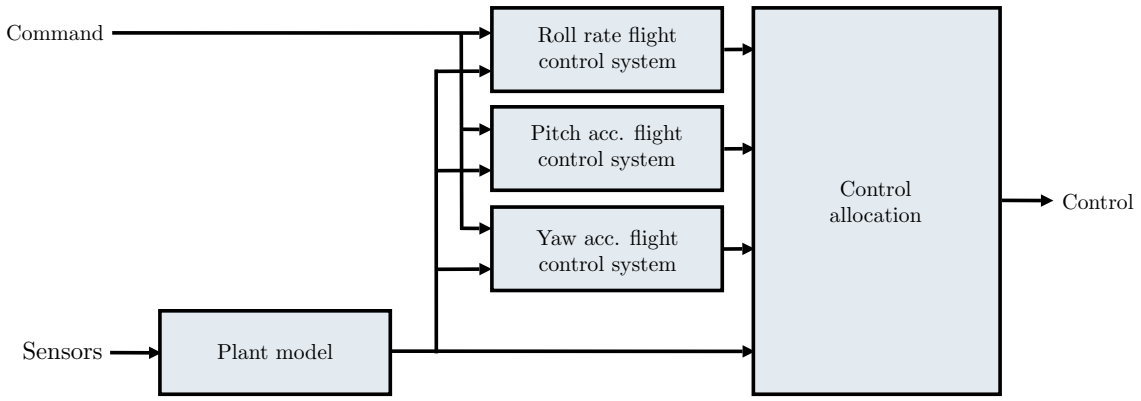

Figure 5.1: Interceptor flight control system architecture

guarantee availability of reaction jet cartridges for longitudinal as well as lateral maneuvers of the interceptor.

- **Requirement 6** *The controlled interceptor shall demonstrate a time constant of* $T = 0.1\,[s]$ *or smaller during the terminal flight phase for longitudinal and lateral acceleration maneuvers in the presence of parameter uncertainties. The time constant is understood as one third of the time the controlled interceptor needs to reach* $90\,[\%]$ *of the commanded acceleration. The overshoot shall not exceed* $15\,[\%]$ *of the acceleration command. The settling time to* $\pm 5\,[\%]$ *of the acceleration command shall be below* $0.5\,[s]$.

- **Requirement 7** *The interceptor flight control system should utilize both actuator sections of the interceptor during the terminal flight phase to guarantee maximum longitudinal and lateral agility. The reaction jet cartridge consumption shall not exceed* $50\,[\%]$ *during the terminal flight phase to guarantee availability of reaction jet cartridges for longitudinal as well as lateral maneuvers of the interceptor.*

While Requirement 1 to Requirement 4 must be achieved by the control methodology employed in the interceptor flight control system, the remaining requirements are depended on the flight control system parameters. The latter need to be determined appropriately so that the controlled interceptor exhibits the fast and accurate responses as well as correct properties mandatory to fulfill Requirement 5 to Requirement 7.

5.2 Flight control system architecture

The definition of the overall interceptor flight control system architecture constitutes the first step of the actual design work. It is influenced by the properties of the interceptor, the capabilities of the internal sensor system, and the given requirements. Figure 5.1 displays the defined interceptor flight control system architecture. As illustrated, the interceptor flight control system consists of five subsystems.
The lower left subsystem in Figure 5.1 which is denoted plant model comprises a model of the interceptor dynamics as well as representations of the interceptor subsystems. Because the internal sensor system provides only a subset of the states and the signals of the interceptor, this subsystem is necessary to make all states and signals of the interceptor available for the control systems as well as the control allocation. The output of the internal sensor system constitutes

the input to this subsystem. Besides driving the modeled interceptor dynamics and the representations of the interceptor subsystems, the input passes this subsystem without modification. Hence, the output of the internal sensor system is available to the control systems and the control allocation. In addition, the internally in the plant model generated states and signals are available to the control systems and the control allocation. The structure of the subsystem follows the presentation in Chapter 2. The aerodynamic control surface actuator modules are omitted in the plant model, because all signals of these modules are available from the internal sensor system. For the conduct of simulations, this subsystem is initialized with the identical initial conditions as the interceptor. Furthermore, neither uncertain constant parameters nor time-varying parameters exist in the plant model.
The center upper part of Figure 5.1 displays the interceptor roll rate control system. The reason for the separate implementation of this subsystem is twofold. First, it supports the fulfillment of the requirements. Based on Requirement 5, the interceptor shall maintain $\left(p_K^{0B}\right)_B = 90\,[deg/s]$ during the terminal flight phase. By this separate implementation, Requirement 5 is individually addressed and the subsystem is specifically designed to fulfill this requirement. Second, the separate implementation takes into account the structure of the nonlinear rigid body equations of motion of the interceptor. Considering (2.21), (2.37), (2.50), (2.56), and (2.59), the differential equation describing $\left(p_K^{0B}\right)_B$ is a first order system. Therefore, this subsystem is separated from control systems for higher order dynamics. The subsystem filters the incoming roll rate command $\left(p_K^{0B}\right)_{B,Cmd}$ and calculates the roll rate error $\left(p_K^{0B}\right)_{B,Err}$, the parameter estimates, and the roll deflection command $\delta_{L,Cmd}$. $\delta_{L,Cmd}$ constitutes the output of this subsystem being handed over to the control allocation.
In the center lower part, Figure 5.1 shows the interceptor pitch and yaw acceleration control system. The rational behind the separation of these subsystems from the interceptor roll rate control system has been illustrated beforehand. The separation of both subsystems provides the capability to design, implement, optimize, and analyze each subsystem individually. Furthermore, it is possible to achieve Requirement 6 stepwise with the chosen interceptor flight control system architecture. The incoming acceleration commands and the output of the plant model are inputs to these subsystems. Based on these inputs, the subsystems calculate the pitch deflection command $\delta_{M,Cmd}$ and the yaw deflection command $\delta_{N,Cmd}$ respectively. These are provided to the control allocation.
The last subsystem in the interceptor flight control system architecture is the control allocation. It is displayed on the right side of Figure 5.1. This subsystem consists of the control allocation algorithm and the reaction jet cartridge allocation. Because $\delta_{L,Cmd}$, $\delta_{M,Cmd}$, and $\delta_{N,Cmd}$ need to be blended to the reaction jet actuator section and the aerodynamic actuator section of the interceptor, a separate subsystem is required. In addition, this subsystem in the overall interceptor flight control system architecture addresses Requirement 7 individually. It offers the capability to be designed specifically in order to fulfill this requirement. Besides $\delta_{L,Cmd}$, $\delta_{M,Cmd}$, and $\delta_{N,Cmd}$, the output of the plant model constitutes an input to the subsystem. The outputs of the subsystem are $\delta_{L,Cmd}$, $\delta_{M,Cmd}$, and $\delta_{N,Cmd}$ as well as the reaction jet cartridge deflection operator δ_{RJC} for the individual reaction jet cartridges.

5.3 Roll rate control system

The interceptor roll rate control system is the first control system in the interceptor flight control system architecture to be designed. Given Requirement 5 this subsystem shall control $\left(p_K^{0B}\right)_B$ to the specified value of $\left(p_K^{0B}\right)_B = 90\,[deg/s]$. From the architectural perspective of the overall interceptor flight control system, $\left(p_K^{0B}\right)_{B,Cmd}$ and the output of the plant model are inputs to

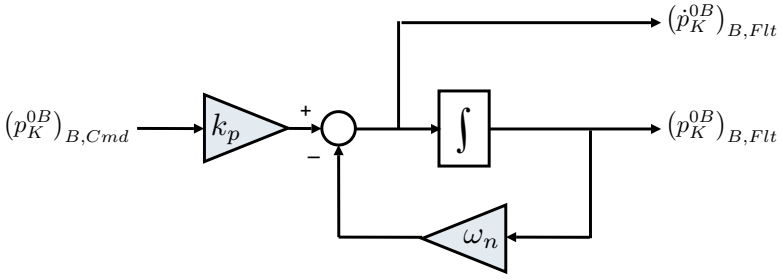

Figure 5.2: $\left(p_K^{0B}\right)_{B,Cmd}$ filter block diagram

the interceptor roll rate control system. These signals are the basis for the calculation of $\delta_{L,Cmd}$, which constitutes the output.
Considering (2.21), (2.37), (2.50), (2.56), and (2.59), while at the same time neglecting the dynamics of the aerodynamic control surface actuator modules, the system from the input $\delta_{L,Cmd}$ to the output $\left(p_K^{0B}\right)_B$ is a first order system. Although this implies that the Backstepping methodology is not required, because $\delta_{L,Cmd}$ and $\left(p_K^{0B}\right)_B$ appear in the same differential equation, the imparted theoretical background is employed to design the interceptor roll rate control system.
The augmented design procedure for parametric strict-feedback systems with unknown control coefficients in the case of tracking is used for the design. To adapt to the given first order system, this design procedure is modified. The nonlinear system is given by (4.184), where $x_2 \in \mathbb{R}$ considered as the control input $u \in \mathbb{R}$. (4.213) provides the respective error definition. The Lyapunov function $V_1(z_1, \tilde{\vec{\theta}}_1, \tilde{\varrho}_1)$ is stated in (4.215), whereupon the term concerning $\tilde{b}_{11}$ is not required in this case, and (4.217) as well as (4.219) provide the definition of the parameter errors. Based on the system order, the stabilizing function $\alpha(z_1, x_{1,Ref}, \dot{x}_{1,Ref}, \hat{\vec{\theta}}_1, \hat{\varrho}_1)$ according to (4.268) constitutes the control u in this special case. The update laws are given by (4.222) and (4.269).
To implement this design in the interceptor flight control system, the terms of the modified design procedure are substituted by variables of physical meaning. First, $x_{1,Ref}$ is replaced.
Following Chapter 4, $x_{1,Ref}$ is a known, smooth, and bounded reference signal. In addition, the derivatives of $x_{1,Ref}$ are assumed to be known, smooth, and bounded. Vice versa, $\left(p_K^{0B}\right)_{B,Cmd}$ is not guaranteed to be smooth, which means that the derivatives of $\left(p_K^{0B}\right)_{B,Cmd}$ may neither be smooth nor bounded. Hence, a first order, linear time invariant system is employed as filter for $\left(p_K^{0B}\right)_{B,Cmd}$ to ensure smoothness as well as boundedness. The outputs of the $\left(p_K^{0B}\right)_{B,Cmd}$ filter are used as $x_{1,Ref}$ and its derivatives in the modified design procedure. Figure 5.2 displays the block diagram of the $\left(p_K^{0B}\right)_{B,Cmd}$ filter.
The implementation of the update laws (4.222) and (4.269) as well as u requires the substitution of $F_1(x_1)$ and $g_1(x_1)$ in (4.184). Because (4.184) constitutes a scalar equation now, it is written as (5.1), where $f_1 : \mathbb{R} \to \mathbb{R}$ and $\theta \in \mathbb{R}$.

$$\dot{x}_1 = f_1(x_1)\,\theta + b g_1(x_1)\,u \tag{5.1}$$

Taking into account (2.7), (2.21), (2.37), and (2.50), the differential equation describing $\left(p_K^{0B}\right)_B$ is derived as (5.2).

$$
\begin{aligned}
\left(\dot{p}_K^{0B}\right)_B^B &= \frac{\left(M_{L,A}^G\right)_B}{\left(I_{XX}^G\right)_{BB}} \\
&= \frac{C_L \bar{q} S_{Ref} \bar{c}}{\left(I_{XX}^G\right)_{BB}} \\
&= \frac{\bar{q} S_{Ref} \bar{c}}{\left(I_{XX}^G\right)_{BB}} \Bigg[C_{L,0}\left(\alpha_K^G, \beta_K^G, M\right) \\
&\quad + C_{L,p}\left(\alpha_K^G, \beta_K^G, M\right) \cdot \frac{\left(p_K^{0B}\right)_B \bar{c}}{2\left(V_{K,Abs}^G\right)_B^I} + C_{L,\delta_L}\left(\alpha_K^G, \beta_K^G, M\right) \cdot \delta_L \Bigg]
\end{aligned} \tag{5.2}
$$

By rearranging the terms in (5.2) like (5.3), the structure of (5.1) is achieved. $\left(p_K^{0B}\right)_B$ substitutes x_1 and δ_L constitutes u. $f_1(x_1)$ and $g_1(x_1)$ are given by (5.4) and (5.5).

$$
\begin{aligned}
\left(\dot{p}_K^{0B}\right)_B^B &= \frac{\bar{q} S_{Ref} \bar{c}}{\left(I_{XX}^G\right)_{BB}} \left[C_{L,0}\left(\alpha_K^G, \beta_K^G, M\right) + C_{L,p}\left(\alpha_K^G, \beta_K^G, M\right) \cdot \frac{\left(p_K^{0B}\right)_B \bar{c}}{2\left(V_{K,Abs}^G\right)_B^I} \right] \\
&\quad + \frac{\bar{q} S_{Ref} \bar{c}}{\left(I_{XX}^G\right)_{BB}} \cdot C_{L,\delta_L}\left(\alpha_K^G, \beta_K^G, M\right) \cdot \delta_L
\end{aligned} \tag{5.3}
$$

$$
f_1(x_1) = \frac{\bar{q} S_{Ref} \bar{c}}{\left(I_{XX}^G\right)_{BB}} \left[C_{L,0}\left(\alpha_K^G, \beta_K^G, M\right) + C_{L,p}\left(\alpha_K^G, \beta_K^G, M\right) \cdot \frac{\left(p_K^{0B}\right)_B \bar{c}}{2\left(V_{K,Abs}^G\right)_B^I} \right] \tag{5.4}
$$

$$
g_1(x_1) = \frac{\bar{q} S_{Ref} \bar{c}}{\left(I_{XX}^G\right)_{BB}} \cdot C_{L,\delta_L}\left(\alpha_K^G, \beta_K^G, M\right) \tag{5.5}
$$

The analysis of (5.4) concerning the boundedness and stability properties, which have been derived for the augmented design procedure for parametric strict-feedback systems with unknown control coefficients in the case of tracking, shows that global boundedness as well as global tracking of the output of the $\left(p_K^{0B}\right)_{B,Cmd}$ filter is achieved under all conditions. Additionally, $f_1(0) = 0$, if $(\alpha_K^G)_B^I = 0\,[deg]$ and $(\beta_K^G)_B^I = 0\,[deg]$. In this case, $\left(p_K^{0B}\right)_B = 0\,[deg/s]$ is a globally stable equilibrium. Furthermore, $g_1(x_1) \neq 0$, except for $\bar{q}$ identical to zero. Because such condition is identical to $(V_{K,Abs}^G)_B^I = 0\,[m/s]$, this situation is negligible and the controllability of (5.1) as well as the existence of u is guaranteed.

The parameter uncertainties introduced in Chapter 2 are reflected in θ and b in (5.1). In the absence of parameter uncertainties, $\theta = 1$ and $b = 1$. If parameter uncertainties are present, they enter the system via (5.4) and (5.5), leading to $\theta \neq 1$ and $b \neq 1$. The individual parameter uncertainties of Chapter 2 are not represented separately, which constitutes a great advantage of the design derived in this thesis. Another advantage is $\theta = 1$ and $b = 1$ are reasonable initial conditions for the update laws.

After all elements of the modified design procedure are substituted, they are arranged in subsystems to the interceptor roll rate control system architecture displayed in Figure 5.3. The subsystems named $f_1(x_1)$ and $g_1(x_1)$ calculate the actual values of the respective terms, based on (5.4) and (5.5). The error calculation subsystem provides z according to (5.6), which results from (4.213) by considering the substitution of x_1 by $\left(p_K^{0B}\right)_B$ and the $\left(p_K^{0B}\right)_{B,Cmd}$ filter.

$$
z = \left(p_K^{0B}\right)_B - \left(p_K^{0B}\right)_{B,Flt} \tag{5.6}
$$

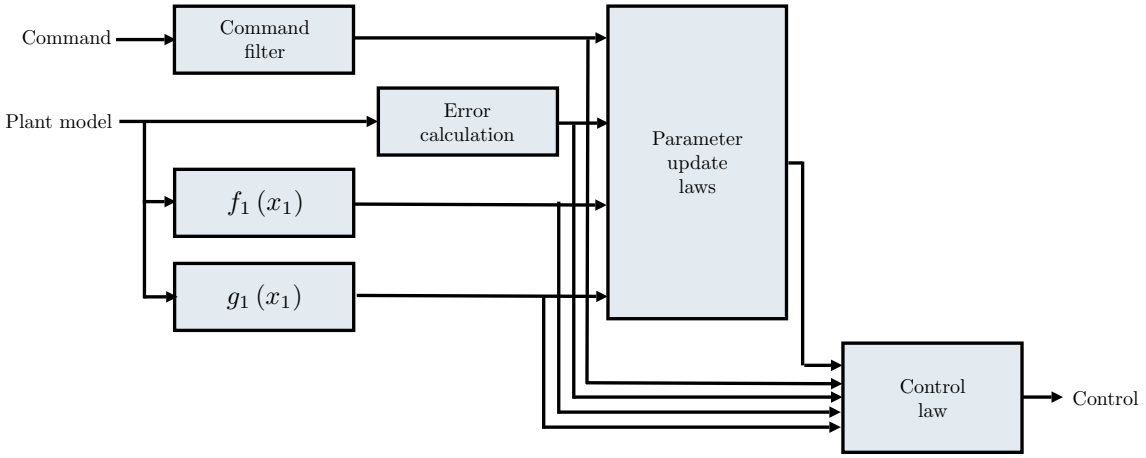

Figure 5.3: $\left(p_K^{0B}\right)_B$ control system architecture

The parameter update law subsystem comprises (4.222) and (4.269) and calculates the parameter estimates for θ and b. All calculated signals are forwarded to the subsystem illustrated as control law. It contains (4.268) and generates $\delta_{L,Cmd}$ as output.
Besides the enhanced readability and traceability of the signals in the interceptor roll rate control system, the implemented architecture supports a high degree of reusability. If the interceptor roll rate control system is applied to a different plant, only the subsystems denoted $f_1(x_1)$ and $g_1(x_1)$ require a redesign to implement the correct substitution of terms for the modified design procedure. The parameter update laws and the control law remain unchanged, because they use the naming convention of Chapter 4.

5.4 Pitch acceleration control system

The interceptor pitch acceleration control system is the second control system to be designed. This subsystem shall control the pitch acceleration of the interceptor to the acceleration commands provided by the interceptor guidance. Furthermore, the pitch acceleration of the interceptor shall demonstrate the dynamical behavior specified in Requirement 6. The pitch acceleration commands as well as the output of the plant model are inputs to the interceptor pitch acceleration control system; $\delta_{M,Cmd}$ is the output.
To be able to control the pitch acceleration of the interceptor, an equation describing the latter is derived first. (2.11) constitutes the starting point. By bringing the cross product to the left hand side of (2.11), an equation for the inertial acceleration of the center of gravity of the interceptor, specified in the body fixed frame, is achieved. The longitudinal acceleration of the center of gravity of the interceptor with respect to the inertial reference frame, specified in the body fixed frame, $\left(a_Z^G\right)_B^{II}$ is the third element of the vector on the left hand side. By combining the equation for $\left(a_Z^G\right)_B^{II}$ with the differential equation for $\left(q_K^{0B}\right)_B$, which is available from (2.7), (2.21), (2.37), and (2.51), a second order system from the input $\delta_{M,Cmd}$ to the output $\left(a_Z^G\right)_B^{II}$ is derived, whereupon the dynamics of the aerodynamic control surface actuator modules are neglected.
Unfortunately, this approach is inappropriate, because the second order system from $\delta_{M,Cmd}$ to $\left(a_Z^G\right)_B^{II}$ is non-minimum phase, as already introduced, substantiated, and analyzed in Chapter 3. This non-minimum phase property prevents the application of the theoretical background

introduced in Chapter 4; the Backstepping methodology can not be applied to non-minimum phase systems.

Longitudinal acceleration of an arbitrary reference point

To overcome the non-minimum phaseness and reach the desired control, as implied by Requirement 6, the longitudinal acceleration of an arbitrary reference point of the interceptor is defined as control variable. In terms of control theory, this approach means that the non-minimum phase output $\left(a_Z^G\right)_B^{II}$ is distorted in favor of the output longitudinal acceleration of an arbitrary reference point of the interceptor. If such reference point can be chosen so that the longitudinal acceleration at the respective position is minimum phase, the Backstepping methodology is applicable.

Picturing the physical effects behind the non-minimum phase property of $\left(a_Z^G\right)_B^{II}$, it becomes evident that the center of gravity of the interceptor rotates with respect to an instantaneous center of rotation during the initiation of longitudinal maneuvers, once the aerodynamic control surfaces are deflected. The instantaneous center of rotation is located ahead of the center of gravity of the interceptor. By choosing an arbitrary point in front of the instantaneous center of rotation as reference point for the longitudinal acceleration of the interceptor, minimum phaseness is guaranteed. This minimum phase property of such an output is proven via the derivation of the longitudinal acceleration of an arbitrary reference point of the interceptor.

The position of the arbitrary reference point P with respect to the inertial reference frame is given by (5.7), where G denotes the center of gravity of the interceptor.

$$\left(\vec{r}^{\,P}\right) = \left(\vec{r}^{\,G}\right) + \left(\vec{r}^{\,GP}\right) \tag{5.7}$$

The derivative of (5.7), which describes the velocity of P with respect to the inertial reference frame, is developed to (5.8). Because the interceptor is considered as a rigid body in this work, (5.9) is utilized in the derivation of (5.8).

$$\begin{aligned}
\left(\vec{V}^{\,P}\right)^I &= \left(\frac{\mathrm{d}}{\mathrm{d}t}\right)^I \left(\vec{r}^{\,P}\right) \\
&= \left(\frac{\mathrm{d}}{\mathrm{d}t}\right)^I \left(\vec{r}^{\,G}\right) + \left(\frac{\mathrm{d}}{\mathrm{d}t}\right)^I \left(\vec{r}^{\,GP}\right) \\
&= \left(\dot{\vec{r}}^{\,G}\right)^I + \left(\dot{\vec{r}}^{\,GP}\right)^B + \left(\vec{\omega}^{IB}\right) \times \left(\vec{r}^{\,GP}\right) \\
&= \left(\vec{V}^{\,G}\right)^I + \left(\vec{\omega}^{IB}\right) \times \left(\vec{r}^{\,GP}\right)
\end{aligned} \tag{5.8}$$

$$\left(\dot{\vec{r}}^{\,GP}\right)^B = 0 \tag{5.9}$$

Now, the derivative of (5.8) is developed according to (5.10), with (5.9) employed again. In addition, it is utilized that the cross product of equal vectors is identical to zero. (5.10) constitutes the acceleration of P with respect to the inertial reference frame.

$$\begin{aligned}
\left(\vec{a}^{\,P}\right)^{II} &= \left(\frac{\mathrm{d}}{\mathrm{d}t}\right)^I \left(\vec{V}^{\,G}\right)^I + \left(\frac{\mathrm{d}}{\mathrm{d}t}\right)^I \left[\left(\vec{\omega}^{IB}\right) \times \left(\vec{r}^{\,GP}\right)\right] \\
&= \left(\dot{\vec{V}}^{\,G}\right)^{II} + \left[\left(\dot{\vec{\omega}}^{IB}\right)^B + \left(\vec{\omega}^{IB}\right) \times \left(\vec{\omega}^{IB}\right)\right] \times \left(\vec{r}^{\,GP}\right) + \left(\vec{\omega}^{IB}\right) \times \left(\dot{\vec{r}}^{\,GP}\right)^I \\
&= \left(\dot{\vec{V}}^{\,G}\right)^{II} + \left(\dot{\vec{\omega}}^{IB}\right)^B \times \left(\vec{r}^{\,GP}\right) + \left(\vec{\omega}^{IB}\right) \times \left[\left(\dot{\vec{r}}^{\,GP}\right)^B + \left(\vec{\omega}^{IB}\right) \times \left(\vec{r}^{\,GP}\right)\right]
\end{aligned}$$

$$= \left(\vec{a}^{G}\right)^{II} + \left(\dot{\vec{\omega}}^{IB}\right)^{B} \times \left(\vec{r}^{GP}\right) + \left(\vec{\omega}^{IB}\right) \times \left[\left(\vec{\omega}^{IB}\right) \times \left(\vec{r}^{GP}\right)\right] \tag{5.10}$$

By expressing $\left(\vec{a}^{G}\right)^{II}$ via Newtons's second axiom, (5.11) results.

$$\left(\vec{a}^{P}\right)^{II} = \frac{1}{m}\sum \vec{F}^{G} + \left(\dot{\vec{\omega}}^{IB}\right)^{B} \times \left(\vec{r}^{GP}\right) + \left(\vec{\omega}^{IB}\right) \times \left[\left(\vec{\omega}^{IB}\right) \times \left(\vec{r}^{GP}\right)\right] \tag{5.11}$$

Considering the assumptions from Chapter 2, which lead to the employment of the flat earth representation and the inertial reference frame according to Appendix B, (5.11) is written as (5.12). The latter is specified in the body fixed frame.

$$\left(\vec{a}^{P}\right)_{B}^{II} = \frac{1}{m}\sum \left(\vec{F}^{G}\right)_{B} + \left(\dot{\vec{\omega}}_{K}^{0B}\right)_{B}^{B} \times \left(\vec{r}^{GP}\right)_{B} + \left(\vec{\omega}_{K}^{0B}\right)_{B} \times \left[\left(\vec{\omega}_{K}^{0B}\right)_{B} \times \left(\vec{r}^{GP}\right)_{B}\right] \tag{5.12}$$

The angular acceleration vector $(\dot{\vec{\omega}}_{K}^{0B})_{B}^{B}$ is given by (2.21). Assuming that P is located on the X_B axis of the interceptor, as stated in (5.13), $\left(a_{Z}^{P}\right)_{B}^{II}$ is extracted from (5.12) as (5.14).

$$\left(\vec{r}^{P}\right)_{B} = \begin{bmatrix} x^{P} & 0 & 0 \end{bmatrix}_{B}^{T} [m] \tag{5.13}$$

$$\left(a_{Z}^{P}\right)_{B}^{II} = \frac{1}{m}\sum \left(F_{Z}^{G}\right)_{B} - \left(\dot{q}_{K}^{0B}\right)_{B}^{B} \left(x^{P}\right)_{B} + \left(p_{K}^{0B}\right)_{B} \left(r_{K}^{0B}\right)_{B} \left(x^{P}\right)_{B} \tag{5.14}$$

Based on Requirement 5, the interceptor is a rolling airframe during the terminal flight phase. This implies that the influence of gravity on $\left(a_{Z}^{P}\right)_{B}^{II}$ varies permanently, depending on the interceptor attitude. Even in the case of $\Theta = 0\,[deg]$, the influence of gravity on $\left(a_{Z}^{P}\right)_{B}^{II}$ changes between none and full impact, due to the variation of Φ, as is evident from (2.35) in conjunction with (2.32). Hence, accounting for gravity in (5.14) while using $\left(a_{Z}^{P}\right)_{B}^{II}$ as control variable means an enormous effort.

Contemplating gravity from the system perspective, the interceptor guidance automatically compensates for the gravitation acting on the interceptor. Former subsystem commands any longitudinal acceleration being necessary to reach the desired target, even if gravity is neglected in (5.14). If gravity causes the interceptor to leave the desired collision course with the target, the interceptor guidance generates appropriate longitudinal acceleration commands to force the interceptor back on the desired flight path.

Given the two beforehand presented conclusions, gravity is neglected, which leaves (5.15) for the longitudinal acceleration of P with respect to the inertial reference frame, specified in the body fixed frame, without gravity.

$$\left(a_{Z}^{P}\right)_{B,woG}^{II} = \frac{1}{m}\sum \left(F_{Z}^{G}\right)_{B,woG} - \left(\dot{q}_{K}^{0B}\right)_{B}^{B} \left(x^{P}\right)_{B} + \left(p_{K}^{0B}\right)_{B} \left(r_{K}^{0B}\right)_{B} \left(x^{P}\right)_{B} \tag{5.15}$$

(5.15) reveals the desired insight into the mechanism guaranteeing the minimum phase property of the chosen output. Although the first term in (5.15) which constitutes the longitudinal acceleration of G with respect to the inertial reference frame, specified in the body fixed frame, without gravity exhibits non-minimum phase behavior, the second term in (5.15) which is the relative angular acceleration of P with respect to G, specified in the body fixed frame, renders $\left(a_{Z}^{P}\right)_{B,woG}^{II}$ minimum phase. If, for example, $\left(p_{K}^{0B}\right)_{B} = 0\,[deg]$, $\left(r_{K}^{0B}\right)_{B} = 0\,[deg]$, and $\left(x^{P}\right)_{B} > 0\,[m]$, then, the second term in (5.15) generates an relative angular acceleration which acts in the same direction as the longitudinal acceleration arising from the angle of attack between the interceptor fuselage and the surrounding airstream. These acceleration components

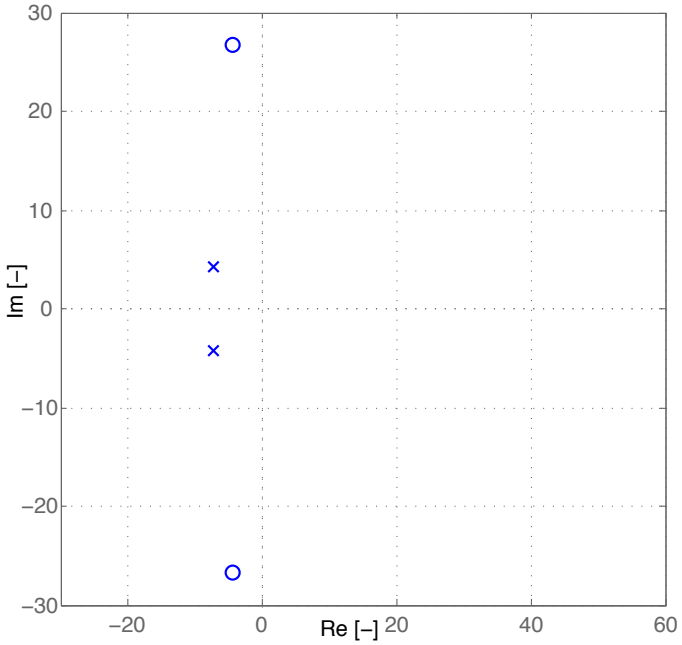

Figure 5.4: Pole-zero plot of $H_{\left(a_Z^P\right)^{II}_{B,woG}\delta_{M,Cmd}}(s)$ at $\left(x^P\right)_B = 1\,[m]$, $(V^G_{K,Abs})^I_B = 600\,[m/s]$, and $\left(z^G\right)_I = 10000\,[m]$ for the Short Period

oppose the longitudinal acceleration generated by the force originating from the aerodynamic control surfaces. By increasing $\left(x^P\right)_B$, the relative angular acceleration component is increased, the non-minimum phaseness is overwhelmed, and minimum phaseness of the output is achieved. A second proof of the minimum phase property of $\left(a_Z^P\right)^{II}_{B,woG}$ is provided via the linearized interceptor dynamics. (5.16) states the transfer function from $\delta_{M,Cmd}$ to $\left(a_Z^P\right)^{II}_{B,woG}$ for $(V^G_{K,Abs})^I_B = 600\,[m/s]$ and $\left(z^G\right)_I = 10000\,[m]$, whereupon $\left(x^P\right)_B = 1\,[m]$. Figure 5.4 shows the pole-zero plot of (5.16). It is evident that minimum phaseness is achieved by the presented approach. The comparison of (5.16) and Figure 5.4 with (3.53) and Figure 3.7 underpins this result.

$$H_{\left(a_Z^P\right)^{II}_{B,woG}\delta_{M,Cmd}}(s) = \frac{39.22 \cdot \left(s^2 + 8.54s + 734.50\right)}{s^2 + 11.38s + 78.02} \tag{5.16}$$

Pitch acceleration control system design

Utilizing the derived minimum phase output, the interceptor pitch acceleration control system is designed in the following, applying the full spectrum of theoretical background presented in Chapter 4.

The augmented design procedure for parametric strict-feedback systems with unknown control coefficients in the case of tracking is employed for the interceptor pitch acceleration control system. Following the design of the interceptor roll rate control system, the terms of latter design procedure are substituted by variables of physical meaning.

According to the design procedure, $x_{1,Ref}$ is a known, smooth, and bounded reference signal. Furthermore, the derivatives of $x_{1,Ref}$ are assumed to be known, smooth, and bounded. On the other hand, the smoothness of $\left(a_Z^P\right)^{II}_{B,woG,Cmd}$, which constitutes the input to the interceptor pitch acceleration control system, is not guaranteed. For this reason, the derivatives of

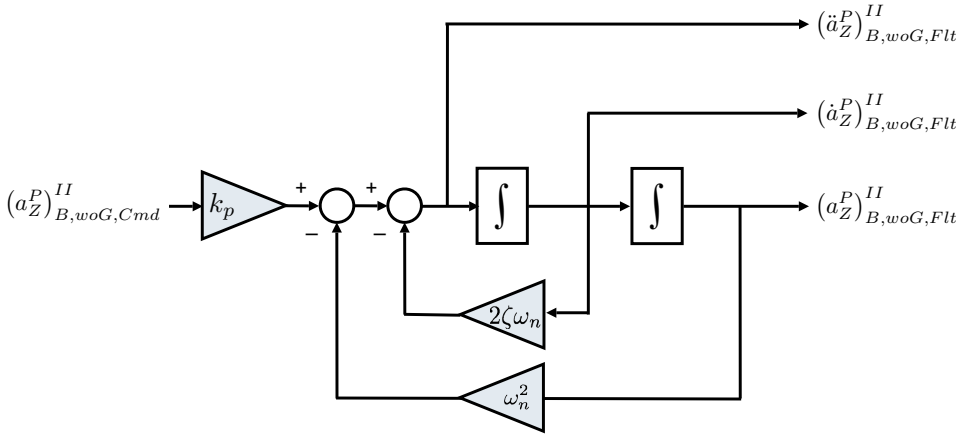

Figure 5.5: $\left(a_Z^P\right)_{B,woG,Cmd}^{II}$ filter block diagram

$\left(a_Z^P\right)_{B,woG,Cmd}^{II}$ are neither guaranteed to be smooth nor guaranteed to be bounded. To achieve the required smoothness and boundedness properties of $x_{1,Ref}$ as well as its derivatives, a second order, linear time invariant system is employed as $\left(a_Z^P\right)_{B,woG,Cmd}^{II}$ filter. Because the augmented design procedure for parametric strict-feedback systems with unknown control coefficients in the case of tracking contains $\ddot{x}_{1,Ref}$, a second order, linear time invariant system is necessary. The outputs of the $\left(a_Z^P\right)_{B,woG,Cmd}^{II}$ filter are used as $x_{1,Ref}$ and its respective derivatives. The block diagram of the $\left(a_Z^P\right)_{B,woG,Cmd}^{II}$ filter is illustrated in Figure 5.5.
The implementation of the terms of the augmented design procedure for parametric strict-feedback systems with unknown control coefficients in the case of tracking requires the substitution of x_1, x_2, u, and the nonlinearities in (4.184) as well as (4.185). Based on Requirement 6 and the presented derivation of a minimum phase output, x_1 is substituted by $\left(a_Z^P\right)_{B,woG}^{II}$. Following the attempt to control the acceleration of the center of gravity of the interceptor with respect to the inertial reference frame, specified in the body fixed frame, the equation for $\left(a_Z^P\right)_{B,woG}^{II}$ is combined with the differential equation describing $\left(q_K^{0B}\right)_B$. Hence, x_2 is substituted by $\left(q_K^{0B}\right)_B$. $\delta_{M,Cmd}$ replaces u.
To account for the dimension of the terms in the $\left(a_Z^P\right)_{B,woG}^{II}$ and the $\left(q_K^{0B}\right)_B$ equation, (4.184) and (4.185) are written as (5.17) and (5.18).

$$\dot{x}_1 = \begin{bmatrix} F_{1,11}(x_1) & 0 \end{bmatrix} \cdot \begin{bmatrix} \theta_{11} \\ \theta_{21} \end{bmatrix} + b_1 g_1(x_1)\, x_2 \tag{5.17}$$

$$\dot{x}_2 = \begin{bmatrix} 0 & F_{2,21}(x_1, x_2) \end{bmatrix} \cdot \begin{bmatrix} \theta_{11} \\ \theta_{21} \end{bmatrix} + b_2 g_2(x_1, x_2)\, u \tag{5.18}$$

The derivative of (5.15) is calculated according to (5.19), to identify the nonlinearities in (5.17) and (5.18). Assuming that $\left(z^G\right)_I$ varies slowly, the latter is considered steady in the derivation of (5.19). This implies that ρ_{Air} as well as the velocity of sound a are constant. The derivatives of $(V_{K,Abs}^G)_B^I$, $(\alpha_K^G)_B^I$, and $(\beta_K^G)_B^I$ are given by (2.15) to (2.17). $(M_{M,RJC}^G)_B$ and $(M_{N,RJC}^G)_B$ are according to (2.55).

$$
\begin{aligned}
\left(\dot{a}_Z^P\right)_{B,woG}^{II} \;=\;& \frac{\rho_{Air}\left(V_{K,Abs}^G\right)_B^I\left(\dot{V}_{K,Abs}^G\right)_B^I S_{Ref}}{m}\Bigg[C_{Z,0}\left(\alpha_K^G,\beta_K^G,M\right)\\
&+C_{Z,q}\left(\alpha_K^G,\beta_K^G,M\right)\frac{\left(q_K^{0B}\right)_B\bar{c}}{2\left(V_{K,Abs}^G\right)_B^I}+C_{Z,\delta_M}\left(\alpha_K^G,\beta_K^G,M\right)\delta_M\Bigg]\\
&+\frac{\bar{q}S_{Ref}}{m}\Bigg[\frac{\partial C_{Z,0}\left(\alpha_K^G,\beta_K^G,M\right)}{\partial\alpha_K^G}\left(\dot{\alpha}_K^G\right)_B^I+\frac{\partial C_{Z,0}\left(\alpha_K^G,\beta_K^G,M\right)}{\partial\beta_K^G}\left(\dot{\beta}_K^G\right)_B^I\\
&+\frac{\partial C_{Z,0}\left(\alpha_K^G,\beta_K^G,M\right)}{\partial M}\cdot\frac{\left(\dot{V}_{K,Abs}^G\right)_B^I}{a}\\
&+\frac{\partial C_{Z,q}\left(\alpha_K^G,\beta_K^G,M\right)}{\partial\alpha_K^G}\left(\dot{\alpha}_K^G\right)_B^I\frac{\left(q_K^{0B}\right)_B\bar{c}}{2\left(V_{K,Abs}^G\right)_B^I}\\
&+\frac{\partial C_{Z,q}\left(\alpha_K^G,\beta_K^G,M\right)}{\partial\beta_K^G}\left(\dot{\beta}_K^G\right)_B^I\frac{\left(q_K^{0B}\right)_B\bar{c}}{2\left(V_{K,Abs}^G\right)_B^I}\\
&+\frac{\partial C_{Z,q}\left(\alpha_K^G,\beta_K^G,M\right)}{\partial M}\cdot\frac{\left(\dot{V}_{K,Abs}^G\right)_B^I}{a}\cdot\frac{\left(q_K^{0B}\right)_B\bar{c}}{2\left(V_{K,Abs}^G\right)_B^I}\\
&+\frac{C_{Z,q}\left(\alpha_K^G,\beta_K^G,M\right)}{2\left(V_{K,Abs}^G\right)_B^I}\Bigg[\frac{\bar{q}S_{Ref}\bar{c}^2}{\left(I_{YY}^G\right)_{BB}}\Bigg[C_{M,0}\left(\alpha_K^G,\beta_K^G,M\right)\\
&+C_{M,q}\left(\alpha_K^G,\beta_K^G,M\right)\frac{\left(q_K^{0B}\right)_B\bar{c}}{2\left(V_{K,Abs}^G\right)_B^I}+C_{M,\delta_M}\left(\alpha_K^G,\beta_K^G,M\right)\delta_M\Bigg]\\
&+\frac{\bar{c}\left(M_{M,RJC}^G\right)_B}{\left(I_{YY}^G\right)_{BB}}-\frac{\left(I_{XX}^G\right)_{BB}-\left(I_{ZZ}^G\right)_{BB}}{\left(I_{YY}^G\right)_{BB}}\bar{c}\left(p_K^{0B}\right)_B\left(r_K^{0B}\right)_B\\
&-\bar{c}\left(q_K^{0B}\right)_B\frac{\left(\dot{V}_{K,Abs}^G\right)_B^I}{\left(V_{K,Abs}^G\right)_B^I}\Bigg]+\frac{\partial C_{Z,\delta_M}\left(\alpha_K^G,\beta_K^G,M\right)}{\partial\alpha_K^G}\left(\dot{\alpha}_K^G\right)_B^I\delta_M\\
&+\frac{\partial C_{Z,\delta_M}\left(\alpha_K^G,\beta_K^G,M\right)}{\partial\beta_K^G}\left(\dot{\beta}_K^G\right)_B^I\delta_M+\frac{\partial C_{Z,\delta_M}\left(\alpha_K^G,\beta_K^G,M\right)}{\partial M}\cdot\frac{\left(\dot{V}_{K,Abs}^G\right)_B^I}{a}\delta_M\\
&+C_{Z,\delta_M}\left(\alpha_K^G,\beta_K^G,M\right)\dot{\delta}_M\Bigg]\\
&-\left(x^P\right)_B\cdot\Bigg[\frac{\rho_{Air}\left(V_{K,Abs}^G\right)_B^I\left(\dot{V}_{K,Abs}^G\right)_B^I S_{Ref}\bar{c}}{\left(I_{YY}^G\right)_{BB}}\Bigg[C_{M,0}\left(\alpha_K^G,\beta_K^G,M\right)\\
&+C_{M,q}\left(\alpha_K^G,\beta_K^G,M\right)\frac{\left(q_K^{0B}\right)_B\bar{c}}{2\left(V_{K,Abs}^G\right)_B^I}+C_{M,\delta_M}\left(\alpha_K^G,\beta_K^G,M\right)\delta_M\Bigg]\\
&+\frac{\bar{q}S_{Ref}\bar{c}}{\left(I_{YY}^G\right)_{BB}}\Bigg[\frac{\partial C_{M,0}\left(\alpha_K^G,\beta_K^G,M\right)}{\partial\alpha_K^G}\left(\dot{\alpha}_K^G\right)_B^I+\frac{\partial C_{M,0}\left(\alpha_K^G,\beta_K^G,M\right)}{\partial\beta_K^G}\left(\dot{\beta}_K^G\right)_B^I
\end{aligned}
$$

$$
\begin{aligned}
&+\frac{\partial C_{M,0}\left(\alpha_K^G,\beta_K^G,M\right)}{\partial M}\cdot\frac{\left(\dot{V}_{K,Abs}^G\right)_B^I}{a}\\
&+\frac{\partial C_{M,q}\left(\alpha_K^G,\beta_K^G,M\right)}{\partial \alpha_K^G}\left(\dot{\alpha}_K^G\right)_B^I\frac{\left(q_K^{0B}\right)_B\bar{c}}{2\left(V_{K,Abs}^G\right)_B^I}\\
&+\frac{\partial C_{M,q}\left(\alpha_K^G,\beta_K^G,M\right)}{\partial \beta_K^G}\left(\dot{\beta}_K^G\right)_B^I\frac{\left(q_K^{0B}\right)_B\bar{c}}{2\left(V_{K,Abs}^G\right)_B^I}\\
&+\frac{\partial C_{M,q}\left(\alpha_K^G,\beta_K^G,M\right)}{\partial M}\cdot\frac{\left(\dot{V}_{K,Abs}^G\right)_B^I}{a}\cdot\frac{\left(q_K^{0B}\right)_B\bar{c}}{2\left(V_{K,Abs}^G\right)_B^I}\\
&+\frac{C_{M,q}\left(\alpha_K^G,\beta_K^G,M\right)}{2\left(V_{K,Abs}^G\right)_B^I}\left[\frac{\bar{q}S_{Ref}\bar{c}^2}{\left(I_{YY}^G\right)_{BB}}\left[C_{M,0}\left(\alpha_K^G,\beta_K^G,M\right)\right.\right.\\
&\left.\left.+C_{M,q}\left(\alpha_K^G,\beta_K^G,M\right)\frac{\left(q_K^{0B}\right)_B\bar{c}}{2\left(V_{K,Abs}^G\right)_B^I}+C_{M,\delta_M}\left(\alpha_K^G,\beta_K^G,M\right)\delta_M\right]\right.\\
&+\frac{\bar{c}\left(M_{M,RJC}^G\right)_B}{\left(I_{YY}^G\right)_{BB}}-\frac{\left(I_{XX}^G\right)_{BB}-\left(I_{ZZ}^G\right)_{BB}}{\left(I_{YY}^G\right)_{BB}}\bar{c}\left(p_K^{0B}\right)_B\left(r_K^{0B}\right)_B\\
&\left.-\bar{c}\left(q_K^{0B}\right)_B\frac{\left(\dot{V}_{K,Abs}^G\right)_B^I}{\left(V_{K,Abs}^G\right)_B^I}\right]+\frac{\partial C_{M,\delta_M}\left(\alpha_K^G,\beta_K^G,M\right)}{\partial \alpha_K^G}\left(\dot{\alpha}_K^G\right)_B^I\delta_M\\
&+\frac{\partial C_{M,\delta_M}\left(\alpha_K^G,\beta_K^G,M\right)}{\partial \beta_K^G}\left(\dot{\beta}_K^G\right)_B^I\delta_M+\frac{\partial C_{M,\delta_M}\left(\alpha_K^G,\beta_K^G,M\right)}{\partial M}\cdot\frac{\left(\dot{V}_{K,Abs}^G\right)_B^I}{a}\delta_M\\
&\left.+C_{M,\delta_M}\left(\alpha_K^G,\beta_K^G,M\right)\dot{\delta}_M\right]\\
&-\frac{\left(I_{XX}^G\right)_{BB}-\left(I_{ZZ}^G\right)_{BB}}{\left(I_{YY}^G\right)_{BB}}\left(r_K^{0B}\right)_B\left[\frac{\bar{q}S_{Ref}\bar{c}}{\left(I_{XX}^G\right)_{BB}}\left[C_{L,0}\left(\alpha_K^G,\beta_K^G,M\right)\right.\right.\\
&\left.\left.+C_{L,p}\left(\alpha_K^G,\beta_K^G,M\right)\frac{\left(p_K^{0B}\right)_B\bar{c}}{2\left(V_{K,Abs}^G\right)_B^I}+C_{L,\delta_L}\left(\alpha_K^G,\beta_K^G,M\right)\delta_L\right]\right]\\
&-\frac{\left(I_{XX}^G\right)_{BB}-\left(I_{ZZ}^G\right)_{BB}}{\left(I_{YY}^G\right)_{BB}}\left(p_K^{0B}\right)_B\left[\frac{\bar{q}S_{Ref}\bar{c}}{\left(I_{ZZ}^G\right)_{BB}}\left[C_{N,0}\left(\alpha_K^G,\beta_K^G,M\right)\right.\right.\\
&\left.\left.+C_{N,r}\left(\alpha_K^G,\beta_K^G,M\right)\frac{\left(r_K^{0B}\right)_B\bar{c}}{2\left(V_{K,Abs}^G\right)_B^I}+C_{N,\delta_N}\left(\alpha_K^G,\beta_K^G,M\right)\delta_N\right]\right.\\
&\left.+\frac{\left(M_{N,RJC}^G\right)_B}{\left(I_{ZZ}^G\right)_{BB}}-\frac{\left(I_{YY}^G\right)_{BB}-\left(I_{XX}^G\right)_{BB}}{\left(I_{ZZ}^G\right)_{BB}}\left(p_K^{0B}\right)_B\left(q_K^{0B}\right)_B\right]\right]\\
&+\left(x^P\right)_B\cdot\left[\left(r_K^{0B}\right)_B\left[\frac{\bar{q}S_{Ref}\bar{c}}{\left(I_{XX}^G\right)_{BB}}\left[C_{L,0}\left(\alpha_K^G,\beta_K^G,M\right)\right.\right.\right.
\end{aligned}
$$

$$
\begin{aligned}
&+C_{L,p}\left(\alpha_K^G,\beta_K^G,M\right)\frac{\left(p_K^{0B}\right)_B\bar{c}}{2\left(V_{K,Abs}^G\right)_B^I}+C_{L,\delta_L}\left(\alpha_K^G,\beta_K^G,M\right)\delta_L\Bigg]\Bigg]\\
&+\left(p_K^{0B}\right)_B\Bigg[\frac{\bar{q}S_{Ref}\bar{c}}{\left(I_{ZZ}^G\right)_{BB}}\Bigg[C_{N,0}\left(\alpha_K^G,\beta_K^G,M\right)\\
&+C_{N,r}\left(\alpha_K^G,\beta_K^G,M\right)\frac{\left(r_K^{0B}\right)_B\bar{c}}{2\left(V_{K,Abs}^G\right)_B^I}+C_{N,\delta_N}\left(\alpha_K^G,\beta_K^G,M\right)\delta_N\Bigg]\\
&+\frac{\left(M_{N,RJC}^G\right)_B}{\left(I_{ZZ}^G\right)_{BB}}-\frac{\left(I_{YY}^G\right)_{BB}-\left(I_{XX}^G\right)_{BB}}{\left(I_{ZZ}^G\right)_{BB}}\left(p_K^{0B}\right)_B\left(q_K^{0B}\right)_B\Bigg]\Bigg]
\end{aligned}
\tag{5.19}
$$

By utilizing the introduced substitution and rearranging terms, (5.19) is written in the structure of (5.17). δ_L, δ_M, δ_N, and $\dot{\delta}_M$ are considered as measurements provided by the internal sensor system to achieve the strict-feedback form of (5.17) and (5.18). This form is mandatory to apply the theoretical background of Chapter 4. The derivatives of the aerodynamic derivatives contained in (5.19) are implemented in the plant model as aerodynamic lookup tables. Hence, the actual values of these derivatives are available to the interceptor pitch acceleration control system. $F_{1,11}\left(x_1\right)$ and $g_1\left(x_1\right)$ are derived from the rearranged (5.19) according to (5.20) and (5.21).

$$
\begin{aligned}
F_{1,11}\left(x_1\right) \;=\;& \frac{\rho_{Air}\left(V_{K,Abs}^G\right)_B^I\left(\dot{V}_{K,Abs}^G\right)_B^I S_{Ref}}{m}\Bigg[C_{Z,0}\left(\alpha_K^G,\beta_K^G,M\right)+C_{Z,\delta_M}\left(\alpha_K^G,\beta_K^G,M\right)\delta_M\Bigg]\\
&+\frac{\bar{q}S_{Ref}}{m}\Bigg[\frac{\partial C_{Z,0}\left(\alpha_K^G,\beta_K^G,M\right)}{\partial\alpha_K^G}\left(\dot{\alpha}_K^G\right)_B^I+\frac{\partial C_{Z,0}\left(\alpha_K^G,\beta_K^G,M\right)}{\partial\beta_K^G}\left(\dot{\beta}_K^G\right)_B^I\\
&+\frac{\partial C_{Z,0}\left(\alpha_K^G,\beta_K^G,M\right)}{\partial M}\cdot\frac{\left(\dot{V}_{K,Abs}^G\right)_B^I}{a}\\
&+\frac{C_{Z,q}\left(\alpha_K^G,\beta_K^G,M\right)}{2\left(V_{K,Abs}^G\right)_B^I}\Bigg[\frac{\bar{q}S_{Ref}\bar{c}^2}{\left(I_{YY}^G\right)_{BB}}\Bigg[C_{M,0}\left(\alpha_K^G,\beta_K^G,M\right)+C_{M,\delta_M}\left(\alpha_K^G,\beta_K^G,M\right)\delta_M\Bigg]\\
&+\frac{\bar{c}\left(M_{M,RJC}^G\right)_B}{\left(I_{YY}^G\right)_{BB}}-\frac{\left(I_{XX}^G\right)_{BB}-\left(I_{ZZ}^G\right)_{BB}}{\left(I_{YY}^G\right)_{BB}}\bar{c}\left(p_K^{0B}\right)_B\left(r_K^{0B}\right)_B\Bigg]\\
&+\frac{\partial C_{Z,\delta_M}\left(\alpha_K^G,\beta_K^G,M\right)}{\partial\alpha_K^G}\left(\dot{\alpha}_K^G\right)_B^I\delta_M+\frac{\partial C_{Z,\delta_M}\left(\alpha_K^G,\beta_K^G,M\right)}{\partial\beta_K^G}\left(\dot{\beta}_K^G\right)_B^I\delta_M\\
&+\frac{\partial C_{Z,\delta_M}\left(\alpha_K^G,\beta_K^G,M\right)}{\partial M}\cdot\frac{\left(\dot{V}_{K,Abs}^G\right)_B^I}{a}\delta_M+C_{Z,\delta_M}\left(\alpha_K^G,\beta_K^G,M\right)\dot{\delta}_M\Bigg]\\
&-\left(x^P\right)_B\cdot\Bigg[\frac{\rho_{Air}\left(V_{K,Abs}^G\right)_B^I\left(\dot{V}_{K,Abs}^G\right)_B^I S_{Ref}\bar{c}}{\left(I_{YY}^G\right)_{BB}}\Bigg[C_{M,0}\left(\alpha_K^G,\beta_K^G,M\right)\\
&+C_{M,\delta_M}\left(\alpha_K^G,\beta_K^G,M\right)\delta_M\Bigg]\\
&+\frac{\bar{q}S_{Ref}\bar{c}}{\left(I_{YY}^G\right)_{BB}}\Bigg[\frac{\partial C_{M,0}\left(\alpha_K^G,\beta_K^G,M\right)}{\partial\alpha_K^G}\left(\dot{\alpha}_K^G\right)_B^I+\frac{\partial C_{M,0}\left(\alpha_K^G,\beta_K^G,M\right)}{\partial\beta_K^G}\left(\dot{\beta}_K^G\right)_B^I
\end{aligned}
$$

$$
\begin{aligned}
&+\frac{\partial C_{M,0}\left(\alpha_K^G,\beta_K^G,M\right)}{\partial M}\cdot\frac{\left(\dot{V}_{K,Abs}^G\right)_B^I}{a}\\
&+\frac{C_{M,q}\left(\alpha_K^G,\beta_K^G,M\right)}{2\left(V_{K,Abs}^G\right)_B^I}\left[\frac{\bar{q}S_{Ref}\bar{c}^2}{\left(I_{YY}^G\right)_{BB}}\left[C_{M,0}\left(\alpha_K^G,\beta_K^G,M\right)+C_{M,\delta_M}\left(\alpha_K^G,\beta_K^G,M\right)\delta_M\right]\right.\\
&\left.+\frac{\bar{c}\left(M_{M,RJC}^G\right)_B}{\left(I_{YY}^G\right)_{BB}}-\frac{\left(I_{XX}^G\right)_{BB}-\left(I_{ZZ}^G\right)_{BB}}{\left(I_{YY}^G\right)_{BB}}\bar{c}\left(p_K^{0B}\right)_B\left(r_K^{0B}\right)_B\right]\\
&+\frac{\partial C_{M,\delta_M}\left(\alpha_K^G,\beta_K^G,M\right)}{\partial\alpha_K^G}\left(\dot{\alpha}_K^G\right)_B^I\delta_M+\frac{\partial C_{M,\delta_M}\left(\alpha_K^G,\beta_K^G,M\right)}{\partial\beta_K^G}\left(\dot{\beta}_K^G\right)_B^I\delta_M\\
&+\frac{\partial C_{M,\delta_M}\left(\alpha_K^G,\beta_K^G,M\right)}{\partial M}\cdot\frac{\left(\dot{V}_{K,Abs}^G\right)_B^I}{a}\delta_M+C_{M,\delta_M}\left(\alpha_K^G,\beta_K^G,M\right)\dot{\delta}_M\Bigg]\\
&-\frac{\left(I_{XX}^G\right)_{BB}-\left(I_{ZZ}^G\right)_{BB}}{\left(I_{YY}^G\right)_{BB}}\left(r_K^{0B}\right)_B\left[\frac{\bar{q}S_{Ref}\bar{c}}{\left(I_{XX}^G\right)_{BB}}\left[C_{L,0}\left(\alpha_K^G,\beta_K^G,M\right)\right.\right.\\
&\left.\left.+C_{L,p}\left(\alpha_K^G,\beta_K^G,M\right)\frac{\left(p_K^{0B}\right)_B\bar{c}}{2\left(V_{K,Abs}^G\right)_B^I}+C_{L,\delta_L}\left(\alpha_K^G,\beta_K^G,M\right)\delta_L\right]\right]\\
&-\frac{\left(I_{XX}^G\right)_{BB}-\left(I_{ZZ}^G\right)_{BB}}{\left(I_{YY}^G\right)_{BB}}\left(p_K^{0B}\right)_B\left[\frac{\bar{q}S_{Ref}\bar{c}}{\left(I_{ZZ}^G\right)_{BB}}\left[C_{N,0}\left(\alpha_K^G,\beta_K^G,M\right)\right.\right.\\
&\left.\left.+C_{N,r}\left(\alpha_K^G,\beta_K^G,M\right)\frac{\left(r_K^{0B}\right)_B\bar{c}}{2\left(V_{K,Abs}^G\right)_B^I}+C_{N,\delta_N}\left(\alpha_K^G,\beta_K^G,M\right)\delta_N\right]\right.\\
&\left.+\frac{\left(M_{N,RJC}^G\right)_B}{\left(I_{ZZ}^G\right)_{BB}}\right]\Bigg]\\
&+\left(x^P\right)_B\cdot\left[\left(r_K^{0B}\right)_B\left[\frac{\bar{q}S_{Ref}\bar{c}}{\left(I_{XX}^G\right)_{BB}}\left[C_{L,0}\left(\alpha_K^G,\beta_K^G,M\right)+\right.\right.\right.\\
&\left.\left.\left.C_{L,p}\left(\alpha_K^G,\beta_K^G,M\right)\frac{\left(p_K^{0B}\right)_B\bar{c}}{2\left(V_{K,Abs}^G\right)_B^I}+C_{L,\delta_L}\left(\alpha_K^G,\beta_K^G,M\right)\delta_L\right]\right]\\
&+\left(p_K^{0B}\right)_B\left[\frac{\bar{q}S_{Ref}\bar{c}}{\left(I_{ZZ}^G\right)_{BB}}\left[C_{N,0}\left(\alpha_K^G,\beta_K^G,M\right)\right.\right.\\
&\left.\left.+C_{N,r}\left(\alpha_K^G,\beta_K^G,M\right)\frac{\left(r_K^{0B}\right)_B\bar{c}}{2\left(V_{K,Abs}^G\right)_B^I}+C_{N,\delta_N}\left(\alpha_K^G,\beta_K^G,M\right)\delta_N\right]\right.\\
&\left.+\frac{\left(M_{N,RJC}^G\right)_B}{\left(I_{ZZ}^G\right)_{BB}}\right]\Bigg]
\end{aligned}
\tag{5.20}
$$

$$
\begin{aligned}
g_1(x_1) \;=\; & \frac{\rho_{Air}\left(V^G_{K,Abs}\right)^I_B\left(\dot{V}^G_{K,Abs}\right)^I_B S_{Ref}}{m} C_{Z,q}\left(\alpha^G_K,\beta^G_K,M\right)\frac{\bar{c}}{2\left(V^G_{K,Abs}\right)^I_B} \\
& + \frac{\bar{q}S_{Ref}}{m}\left[\frac{\partial C_{Z,q}\left(\alpha^G_K,\beta^G_K,M\right)}{\partial \alpha^G_K}\left(\dot{\alpha}^G_K\right)^I_B\frac{\bar{c}}{2\left(V^G_{K,Abs}\right)^I_B}\right. \\
& + \frac{\partial C_{Z,q}\left(\alpha^G_K,\beta^G_K,M\right)}{\partial \beta^G_K}\left(\dot{\beta}^G_K\right)^I_B\frac{\bar{c}}{2\left(V^G_{K,Abs}\right)^I_B} \\
& + \frac{\partial C_{Z,q}\left(\alpha^G_K,\beta^G_K,M\right)}{\partial M}\cdot\frac{\left(\dot{V}^G_{K,Abs}\right)^I_B}{a}\cdot\frac{\bar{c}}{2\left(V^G_{K,Abs}\right)^I_B} \\
& \left. + \frac{C_{Z,q}\left(\alpha^G_K,\beta^G_K,M\right)}{4\left(\left(V^G_{K,Abs}\right)^I_B\right)^2}\left[\frac{\bar{q}S_{Ref}\bar{c}^3}{\left(I^G_{YY}\right)_{BB}}C_{M,q}\left(\alpha^G_K,\beta^G_K,M\right)-2\bar{c}\left(\dot{V}^G_{K,Abs}\right)^I_B\right]\right] \\
& - \left(x^P\right)_B\cdot\frac{\rho_{Air}\left(V^G_{K,Abs}\right)^I_B\left(\dot{V}^G_{K,Abs}\right)^I_B S_{Ref}\bar{c}}{\left(I^G_{YY}\right)_{BB}}C_{M,q}\left(\alpha^G_K,\beta^G_K,M\right)\frac{\bar{c}}{2\left(V^G_{K,Abs}\right)^I_B} \\
& - \left(x^P\right)_B\cdot\frac{\bar{q}S_{Ref}\bar{c}}{\left(I^G_{YY}\right)_{BB}}\left[\frac{\partial C_{M,q}\left(\alpha^G_K,\beta^G_K,M\right)}{\partial \alpha^G_K}\left(\dot{\alpha}^G_K\right)^I_B\frac{\bar{c}}{2\left(V^G_{K,Abs}\right)^I_B}\right. \\
& + \frac{\partial C_{M,q}\left(\alpha^G_K,\beta^G_K,M\right)}{\partial \beta^G_K}\left(\dot{\beta}^G_K\right)^I_B\frac{\bar{c}}{2\left(V^G_{K,Abs}\right)^I_B} \\
& + \frac{\partial C_{M,q}\left(\alpha^G_K,\beta^G_K,M\right)}{\partial M}\cdot\frac{\left(\dot{V}^G_{K,Abs}\right)^I_B}{a}\cdot\frac{\bar{c}}{2\left(V^G_{K,Abs}\right)^I_B} \\
& \left. + \frac{C_{M,q}\left(\alpha^G_K,\beta^G_K,M\right)}{4\left(\left(V^G_{K,Abs}\right)^I_B\right)^2}\left[\frac{\bar{q}S_{Ref}\bar{c}^3}{\left(I^G_{YY}\right)_{BB}}C_{M,q}\left(\alpha^G_K,\beta^G_K,M\right)-2\bar{c}\left(\dot{V}^G_{K,Abs}\right)^I_B\right]\right] \\
& - \left(x^P\right)_B\cdot\frac{\left(I^G_{XX}\right)_{BB}-\left(I^G_{ZZ}\right)_{BB}}{\left(I^G_{YY}\right)_{BB}}\left(p^{0B}_K\right)^2_B\left[-\frac{\left(I^G_{YY}\right)_{BB}-\left(I^G_{XX}\right)_{BB}}{\left(I^G_{ZZ}\right)_{BB}}\right] \\
& + \left(x^P\right)_B\left(p^{0B}_K\right)^2_B\left[-\frac{\left(I^G_{YY}\right)_{BB}-\left(I^G_{XX}\right)_{BB}}{\left(I^G_{ZZ}\right)_{BB}}\right] \qquad (5.21)
\end{aligned}
$$

For the substitution of terms in (5.18), the differential equation describing $\left(q^{0B}_K\right)_B$ is written as (5.22). It origins from (2.7), (2.21), (2.37), (2.51), and (2.55).

$$
\begin{aligned}
\left(\dot{q}^{0B}_K\right)^B_B \;=\; & \frac{\bar{q}S_{Ref}\bar{c}}{\left(I^G_{YY}\right)_{BB}}\left[C_{M,0}\left(\alpha^G_K,\beta^G_K,M\right)\right. \\
& \left. + C_{M,q}\left(\alpha^G_K,\beta^G_K,M\right)\cdot\frac{\left(q^{0B}_K\right)_B\bar{c}}{2\left(V^G_{K,Abs}\right)^I_B} + C_{M,\delta_M}\left(\alpha^G_K,\beta^G_K,M\right)\cdot\delta_M\right]
\end{aligned}
$$

$$+\frac{\left(M^G_{M,RJC}\right)_B}{\left(I^G_{YY}\right)_{BB}} - \frac{\left(I^G_{XX}\right)_{BB} - \left(I^G_{ZZ}\right)_{BB}}{\left(I^G_{YY}\right)_{BB}} \left(p^{0B}_K\right)_B \left(q^{0B}_K\right)_B \tag{5.22}$$

Employing the substitutions for x_1, x_2, and u, leads to (5.23) and (5.24) for $F_{2,21}(x_1, x_2)$ and $g_2(x_1, x_2)$.

$$\begin{aligned} F_{2,21}(x_1, x_2) &= \frac{\bar{q} S_{Ref} \bar{c}}{\left(I^G_{YY}\right)_{BB}} \left[C_{M,0}\left(\alpha^G_K, \beta^G_K, M\right) + C_{M,q}\left(\alpha^G_K, \beta^G_K, M\right) \cdot \frac{\left(q^{0B}_K\right)_B \bar{c}}{2\left(V^G_{K,Abs}\right)^I_B} \right] \\ &+ \frac{\left(M^G_{M,RJC}\right)_B}{\left(I^G_{YY}\right)_{BB}} - \frac{\left(I^G_{XX}\right)_{BB} - \left(I^G_{ZZ}\right)_{BB}}{\left(I^G_{YY}\right)_{BB}} \left(p^{0B}_K\right)_B \left(q^{0B}_K\right)_B \end{aligned} \tag{5.23}$$

$$g_2(x_1, x_2) = \frac{\bar{q} S_{Ref} \bar{c}}{\left(I^G_{YY}\right)_{BB}} C_{M,\delta_M}\left(\alpha^G_K, \beta^G_K, M\right) \tag{5.24}$$

As shown in Chapter 4, this design achieves global boundedness and global tracking of the output of the $\left(a^P_Z\right)^{II}_{B,woG,Cmd}$ filter under all conditions. Furthermore, analysis shows that $F_{1,11}(0) = 0$, if $(\alpha^G_K)^I_B = 0\,[deg]$, $(\dot{\alpha}^G_K)^I_B = 0\,[deg/s]$, $(\beta^G_K)^I_B = 0\,[deg]$, $(\dot{\beta}^G_K)^I_B = 0\,[deg/s]$, $\left(p^{0B}_K\right)_B = 0\,[deg/s]$, $\left(r^{0B}_K\right)_B = 0\,[deg/s]$, $\delta_L = 0\,[deg]$, $\delta_M = 0\,[deg]$, and $\delta_N = 0\,[deg]$. In this case, $\left(a^P_Z\right)^{II}_{B,woG} = 0\,[m/s^2]$, $\left(q^{0B}_K\right)_B = 0\,[deg/s]$ is a globally stable equilibrium. $g_1(x_1) \neq 0$ and $g_2(x_1, x_2) \neq 0$, except for $\bar{q}$ equal to zero, which means that $(V^G_{K,Abs})^I_B = 0\,[m/s]$. Therefore, the controllability of (5.17) and (5.18) as well as the existence of the stabilizing function and u is guaranteed, because this case is negligible.

Following the design of the interceptor roll rate control system, all parameter uncertainties introduced in Chapter 2 are reflected by $\vec{\theta}$, b_1, and b_2. $\vec{\theta} = \begin{bmatrix} 1 & 1 \end{bmatrix}^T$, $b_1 = 1$, and $b_2 = 1$, if parameter uncertainties are absent. If parameter uncertainties exist, they enter the system via (5.20), (5.21), (5.23), and (5.24), resulting in $\vec{\theta} \neq \begin{bmatrix} 1 & 1 \end{bmatrix}^T$, $b_1 \neq 1$, and $b_2 \neq 1$. The zero elements in $F_1(x_1)$ and $F_2(x_1, x_2)$ ensure that the introduced parameter uncertainties impact the $\left(a^P_Z\right)^{II}_{B,woG}$ or the $\left(q^{0B}_K\right)_B$ equation only. The particular parameter uncertainties of Chapter 2 are not considered individually in the presented approach, which reveals a great advantage of the chosen approach also for the pitch acceleration control system. In addition, $\vec{\theta} = \begin{bmatrix} 1 & 1 \end{bmatrix}^T$, $b_1 = 1$, and $b_2 = 1$, constitute reasonable initial conditions for the update laws contained in the augmented design procedure for parametric strict-feedback system with unknown control coefficients in the case of tracking.

After the substitution of all elements of the employed design procedure is finished, they are implemented in interceptor pitch acceleration control subsystem in the architecture illustrated in Figure 5.6. The subsystems denoted $F_1(x_1)$, $g_1(x_1)$, $F_2(x_1, x_2)$, and $g_2(x_1, x_2)$ provide the actual values of the terms, based on (5.20), (5.21), (5.23), and (5.24). The error calculation subsystem generates z_1 and z_2 according to (4.213) and (4.214), with (4.268) is employed to calculate $\alpha(z_1, x_{1,Ref}, \dot{x}_{1,Ref}, \hat{\vec{\theta}}_1, \hat{\varrho}_1)$. The parameter update law subsystem contains (4.221), (4.222), (4.229), (4.230), (4.269), and (4.271). $\delta_{M,Cmd}$ is calculated in the control law subsystem by utilizing (4.270).

As the interceptor roll rate control system architecture, the interceptor pitch acceleration control system architecture provides an enhanced readability as well as traceability of the signals. Furthermore, the comparison of Figure 5.6 with 5.3 underpins the earlier conclusion regarding reusability of the chosen architectural approach. By augmenting the interceptor roll rate control system with the $F_2(x_1, x_2)$ and $g_2(x_1, x_2)$ subsystem as well as redesigning the parameter

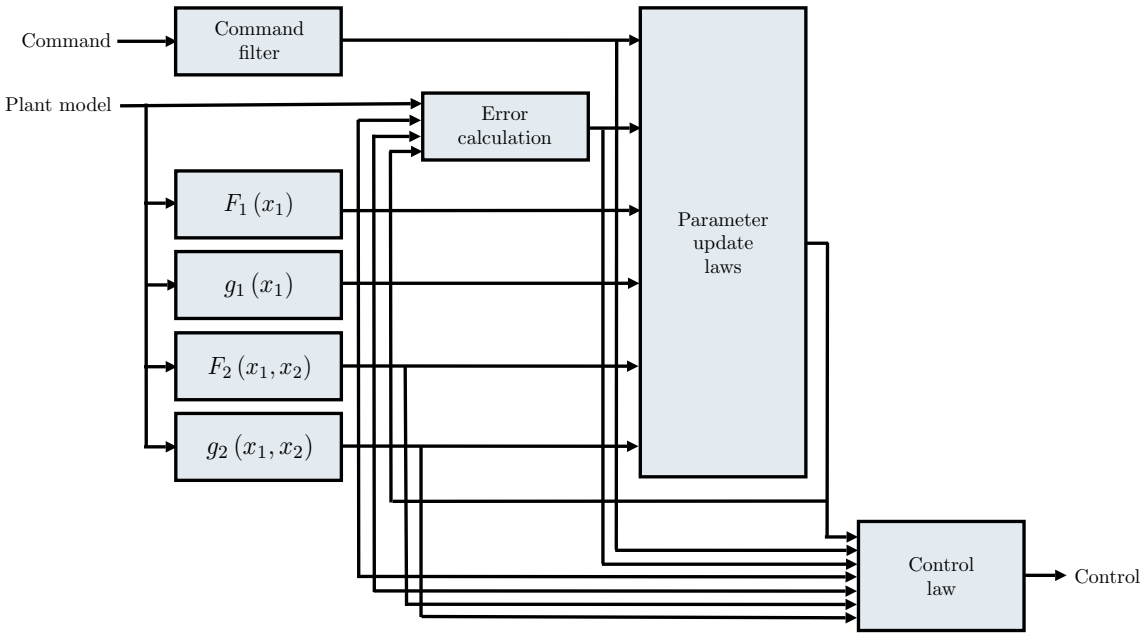

Figure 5.6: $\left(a_Z^P\right)_{B,woG}^{II}$ control system architecture

update law and the control law subsystem, the interceptor pitch acceleration control system is realized. The upcoming design of the interceptor yaw acceleration control system emphasizes the aspect of reusability even more.

5.5 Yaw acceleration control system

The last control system required to be designed is the interceptor yaw acceleration control system. This subsystem shall control the lateral acceleration of the interceptor. In addition, this subsystem shall ensure that the lateral acceleration of the interceptor demonstrates the dynamical behavior specified in Requirement 6. Inputs to the interceptor yaw acceleration control system are the lateral accelerations commands provided by the interceptor guidance and the output of the plant model. The subsystem generates $\delta_{N,Cmd}$ as output.
Requirement 6, which considers the longitudinal as well as the lateral acceleration performance of the controlled interceptor, imposes that the lateral acceleration of the interceptor is controlled. As illustrated in Chapter 3, the longitudinal and the lateral interceptor dynamics coincide, due to the cruciform configuration of the interceptor. This implies that the lateral acceleration of the center of gravity of the interceptor with respect to the inertial reference frame, specified in the body fixed frame, $\left(a_Y^G\right)_B^{II}$ exhibits the identical non-minimum phase property as $\left(a_Z^G\right)_B^{II}$. Hence, $\left(a_Y^G\right)_B^{II}$ is inappropriate to apply the theoretical background presented in Chapter 4.
Following the design of the interceptor pitch acceleration control system, the lateral acceleration of an arbitrary reference point P of the interceptor is defined as control variable to achieve a minimum phase output. Based on (5.12) and (5.13), the lateral acceleration of P with respect to the inertial reference frame, specified in the body fixed frame, $\left(a_Y^P\right)_B^{II}$ is given by (5.25).

$$\left(a_Y^P\right)_B^{II} = \frac{1}{m}\sum \left(F_Y^G\right)_B + \left(\dot{r}_K^{0B}\right)_B^B \left(x^P\right)_B + \left(p_K^{0B}\right)_B \left(q_K^{0B}\right)_B \left(x^P\right)_B \tag{5.25}$$

Implementing the negligence of gravity, because the conclusions given for the interceptor pitch acceleration control system are also valid for $\left(a_Y^P\right)_B^{II}$, leads to (5.26).

$$\left(a_Y^P\right)_{B,woG}^{II} = \frac{1}{m}\sum\left(F_Y^G\right)_{B,woG} + \left(\dot{r}_K^{0B}\right)_B^B\left(x^P\right)_B + \left(p_K^{0B}\right)_B\left(q_K^{0B}\right)_B\left(x^P\right)_B \tag{5.26}$$

$\left(a_Y^P\right)_{B,woG}^{II}$ is the desired minimum phase output. The proof of the minimum phaseness of this output is possible via the linearized interceptor dynamics, but is omitted here.
The interceptor yaw acceleration control system is designed by using the augmented design procedure for parametric strict-feedback systems with unknown control coefficients in the case of tracking. Following the earlier presentations, the terms of the design procedure are substituted by variables of physical meaning.
First, $x_{1,Ref}$ is substituted. Because the latter and its derivatives are assumed to be known, smooth, and bounded and $\left(a_Y^P\right)_{B,woG,Cmd}^{II}$ is not guaranteed to be smooth, a second order, linear time invariant system is employed as $\left(a_Y^P\right)_{B,woG,Cmd}^{II}$ filter to guarantee the required properties. The outputs of the $\left(a_Y^P\right)_{B,woG,Cmd}^{II}$ filter are utilized as $x_{1,Ref}$ and its derivatives in the terms of the design procedure. This approach follows the design of the interceptor pitch acceleration control system. The block diagram of the $\left(a_Y^P\right)_{B,woG,Cmd}^{II}$ filter is identical to the one displayed in Figure 5.5.
Second, x_1, x_2, u, and the nonlinearities in (4.184) as well as (4.185) are substituted. As the derivation of the minimum phase output implies, $\left(a_Y^P\right)_{B,woG}^{II}$ is taken as x_1. x_2 is substituted by $\left(r_K^{0B}\right)_B$ and $\delta_{N,Cmd}$ represents u.
By writing (4.184) and (4.185) in the form of (5.17) and (5.18), developing the derivative of (5.26), and restructuring the latter, $F_{1,11}\left(x_1\right)$ as well as $g_1\left(x_1\right)$ are calculated as stated in (5.27) and (5.28). $\left(z^G\right)_I$ is considered steady in the development of the derivative of (5.26). The derivatives of $(V_{K,Abs}^G)_B^I$, $(\alpha_K^G)_B^I$, and $(\beta_K^G)_B^I$ are provided in (2.15) to (2.17), and $(M_{M,RJC}^G)_B$ as well as $(M_{N,RJC}^G)_B$ are according to (2.55). Furthermore, δ_L, δ_M, δ_N, and $\dot{\delta}_N$ are taken into account as measured signals offered by the internal sensor system.

$$\begin{aligned}
F_{1,11}\left(x_1\right) \;=\; & \frac{\rho_{Air}\left(V_{K,Abs}^G\right)_B^I\left(\dot{V}_{K,Abs}^G\right)_B^I S_{Ref}}{m}\left[C_{Y,0}\left(\alpha_K^G,\beta_K^G,M\right) + C_{Y,\delta_N}\left(\alpha_K^G,\beta_K^G,M\right)\delta_N\right] \\
& + \frac{\bar{q}S_{Ref}}{m}\left[\frac{\partial C_{Y,0}\left(\alpha_K^G,\beta_K^G,M\right)}{\partial\alpha_K^G}\left(\dot{\alpha}_K^G\right)_B^I + \frac{\partial C_{Y,0}\left(\alpha_K^G,\beta_K^G,M\right)}{\partial\beta_K^G}\left(\dot{\beta}_K^G\right)_B^I\right. \\
& + \frac{\partial C_{Y,0}\left(\alpha_K^G,\beta_K^G,M\right)}{\partial M}\cdot\frac{\left(\dot{V}_{K,Abs}^G\right)_B^I}{a} \\
& + \frac{C_{Y,r}\left(\alpha_K^G,\beta_K^G,M\right)}{2\left(V_{K,Abs}^G\right)_B^I}\left[\frac{\bar{q}S_{Ref}\bar{c}^2}{\left(I_{ZZ}^G\right)_{BB}}\left[C_{N,0}\left(\alpha_K^G,\beta_K^G,M\right) + C_{N,\delta_N}\left(\alpha_K^G,\beta_K^G,M\right)\delta_N\right]\right. \\
& \left.\left. + \frac{\bar{c}\left(M_{N,RJC}^G\right)_B}{\left(I_{ZZ}^G\right)_{BB}} - \frac{\left(I_{YY}^G\right)_{BB} - \left(I_{XX}^G\right)_{BB}}{\left(I_{ZZ}^G\right)_{BB}}\bar{c}\left(p_K^{0B}\right)_B\left(q_K^{0B}\right)_B\right]\right. \\
& + \frac{\partial C_{Y,\delta_N}\left(\alpha_K^G,\beta_K^G,M\right)}{\partial\alpha_K^G}\left(\dot{\alpha}_K^G\right)_B^I\delta_N + \frac{\partial C_{Y,\delta_N}\left(\alpha_K^G,\beta_K^G,M\right)}{\partial\beta_K^G}\left(\dot{\beta}_K^G\right)_B^I\delta_N \\
& \left. + \frac{\partial C_{Y,\delta_N}\left(\alpha_K^G,\beta_K^G,M\right)}{\partial M}\cdot\frac{\left(\dot{V}_{K,Abs}^G\right)_B^I}{a}\delta_N + C_{Y,\delta_N}\left(\alpha_K^G,\beta_K^G,M\right)\dot{\delta}_N\right]
\end{aligned}$$

$$
\begin{aligned}
&+\left(x^{P}\right)_{B}\cdot\left[\frac{\rho_{Air}\left(V_{K,Abs}^{G}\right)_{B}^{I}\left(\dot{V}_{K,Abs}^{G}\right)_{B}^{I}S_{Ref}\bar{c}}{\left(I_{ZZ}^{G}\right)_{BB}}\left[C_{N,0}\left(\alpha_{K}^{G},\beta_{K}^{G},M\right)\right.\right.\\
&\left.\left.+C_{N,\delta_{N}}\left(\alpha_{K}^{G},\beta_{K}^{G},M\right)\delta_{N}\right]\right.\\
&+\frac{\bar{q}S_{Ref}\bar{c}}{\left(I_{ZZ}^{G}\right)_{BB}}\left[\frac{\partial C_{N,0}\left(\alpha_{K}^{G},\beta_{K}^{G},M\right)}{\partial\alpha_{K}^{G}}\left(\dot{\alpha}_{K}^{G}\right)_{B}^{I}+\frac{\partial C_{N,0}\left(\alpha_{K}^{G},\beta_{K}^{G},M\right)}{\partial\beta_{K}^{G}}\left(\dot{\beta}_{K}^{G}\right)_{B}^{I}\right.\\
&+\frac{\partial C_{N,0}\left(\alpha_{K}^{G},\beta_{K}^{G},M\right)}{\partial M}\cdot\frac{\left(\dot{V}_{K,Abs}^{G}\right)_{B}^{I}}{a}\\
&+\frac{C_{N,r}\left(\alpha_{K}^{G},\beta_{K}^{G},M\right)}{2\left(V_{K,Abs}^{G}\right)_{B}^{I}}\left[\frac{\bar{q}S_{Ref}\bar{c}^{2}}{\left(I_{ZZ}^{G}\right)_{BB}}\left[C_{N,0}\left(\alpha_{K}^{G},\beta_{K}^{G},M\right)+C_{N,\delta_{N}}\left(\alpha_{K}^{G},\beta_{K}^{G},M\right)\delta_{N}\right]\right.\\
&\left.+\frac{\bar{c}\left(M_{N,RJC}^{G}\right)_{B}}{\left(I_{ZZ}^{G}\right)_{BB}}-\frac{\left(I_{YY}^{G}\right)_{BB}-\left(I_{XX}^{G}\right)_{BB}}{\left(I_{ZZ}^{G}\right)_{BB}}\bar{c}\left(p_{K}^{0B}\right)_{B}\left(q_{K}^{0B}\right)_{B}\right]\\
&+\frac{\partial C_{N,\delta_{N}}\left(\alpha_{K}^{G},\beta_{K}^{G},M\right)}{\partial\alpha_{K}^{G}}\left(\dot{\alpha}_{K}^{G}\right)_{B}^{I}\delta_{N}+\frac{\partial C_{N,\delta_{N}}\left(\alpha_{K}^{G},\beta_{K}^{G},M\right)}{\partial\beta_{K}^{G}}\left(\dot{\beta}_{K}^{G}\right)_{B}^{I}\delta_{N}\\
&+\frac{\partial C_{N,\delta_{N}}\left(\alpha_{K}^{G},\beta_{K}^{G},M\right)}{\partial M}\cdot\frac{\left(\dot{V}_{K,Abs}^{G}\right)_{B}^{I}}{a}\delta_{N}+C_{N,\delta_{N}}\left(\alpha_{K}^{G},\beta_{K}^{G},M\right)\dot{\delta}_{N}\Big]\\
&-\frac{\left(I_{YY}^{G}\right)_{BB}-\left(I_{XX}^{G}\right)_{BB}}{\left(I_{ZZ}^{G}\right)_{BB}}\left(q_{K}^{0B}\right)_{B}\left[\frac{\bar{q}S_{Ref}\bar{c}}{\left(I_{XX}^{G}\right)_{BB}}\left[C_{L,0}\left(\alpha_{K}^{G},\beta_{K}^{G},M\right)\right.\right.\\
&\left.\left.+C_{L,p}\left(\alpha_{K}^{G},\beta_{K}^{G},M\right)\frac{\left(p_{K}^{0B}\right)_{B}\bar{c}}{2\left(V_{K,Abs}^{G}\right)_{B}^{I}}+C_{L,\delta_{L}}\left(\alpha_{K}^{G},\beta_{K}^{G},M\right)\delta_{L}\right]\right]\\
&-\frac{\left(I_{YY}^{G}\right)_{BB}-\left(I_{XX}^{G}\right)_{BB}}{\left(I_{ZZ}^{G}\right)_{BB}}\left(p_{K}^{0B}\right)_{B}\left[\frac{\bar{q}S_{Ref}\bar{c}}{\left(I_{YY}^{G}\right)_{BB}}\left[C_{M,0}\left(\alpha_{K}^{G},\beta_{K}^{G},M\right)\right.\right.\\
&\left.\left.+C_{M,q}\left(\alpha_{K}^{G},\beta_{K}^{G},M\right)\frac{\left(q_{K}^{0B}\right)_{B}\bar{c}}{2\left(V_{K,Abs}^{G}\right)_{B}^{I}}+C_{M,\delta_{M}}\left(\alpha_{K}^{G},\beta_{K}^{G},M\right)\delta_{M}\right]\right.\\
&\left.\left.+\frac{\left(M_{M,RJC}^{G}\right)_{B}}{\left(I_{YY}^{G}\right)_{BB}}\right]\right]\\
&+\left(x^{P}\right)_{B}\cdot\left[\left(q_{K}^{0B}\right)_{B}\left[\frac{\bar{q}S_{Ref}\bar{c}}{\left(I_{XX}^{G}\right)_{BB}}\left[C_{L,0}\left(\alpha_{K}^{G},\beta_{K}^{G},M\right)+\right.\right.\right.\\
&\left.\left.\left.C_{L,p}\left(\alpha_{K}^{G},\beta_{K}^{G},M\right)\frac{\left(p_{K}^{0B}\right)_{B}\bar{c}}{2\left(V_{K,Abs}^{G}\right)_{B}^{I}}+C_{L,\delta_{L}}\left(\alpha_{K}^{G},\beta_{K}^{G},M\right)\delta_{L}\right]\right]\right.\\
&+\left(q_{K}^{0B}\right)_{B}\left[\frac{\bar{q}S_{Ref}\bar{c}}{\left(I_{YY}^{G}\right)_{BB}}\left[C_{M,0}\left(\alpha_{K}^{G},\beta_{K}^{G},M\right)\right.\right.\\
&\left.\left.\left.+C_{M,q}\left(\alpha_{K}^{G},\beta_{K}^{G},M\right)\frac{\left(q_{K}^{0B}\right)_{B}\bar{c}}{2\left(V_{K,Abs}^{G}\right)_{B}^{I}}+C_{M,\delta_{M}}\left(\alpha_{K}^{G},\beta_{K}^{G},M\right)\delta_{M}\right]\right]
\end{aligned}
$$

$$+\frac{\left(M^G_{M,RJC}\right)_B}{\left(I^G_{YY}\right)_{BB}}\Bigg]\Bigg] \tag{5.27}$$

$$\begin{aligned}
g_1(x_1) \;=\; & \frac{\rho_{Air}\left(V^G_{K,Abs}\right)^I_B\left(\dot{V}^G_{K,Abs}\right)^I_B S_{Ref}}{m} C_{Y,r}\left(\alpha^G_K,\beta^G_K,M\right)\frac{\bar{c}}{2\left(V^G_{K,Abs}\right)^I_B} \\
& +\frac{\bar{q}S_{Ref}}{m}\Bigg[\frac{\partial C_{Y,r}\left(\alpha^G_K,\beta^G_K,M\right)}{\partial\alpha^G_K}\left(\dot{\alpha}^G_K\right)^I_B\frac{\bar{c}}{2\left(V^G_{K,Abs}\right)^I_B} \\
& +\frac{\partial C_{Y,r}\left(\alpha^G_K,\beta^G_K,M\right)}{\partial\beta^G_K}\left(\dot{\beta}^G_K\right)^I_B\frac{\bar{c}}{2\left(V^G_{K,Abs}\right)^I_B} \\
& +\frac{\partial C_{Y,r}\left(\alpha^G_K,\beta^G_K,M\right)}{\partial M}\cdot\frac{\left(\dot{V}^G_{K,Abs}\right)^I_B}{a}\cdot\frac{\bar{c}}{2\left(V^G_{K,Abs}\right)^I_B} \\
& +\frac{C_{Y,r}\left(\alpha^G_K,\beta^G_K,M\right)}{4\left(\left(V^G_{K,Abs}\right)^I_B\right)^2}\left[\frac{\bar{q}S_{Ref}\bar{c}^3}{\left(I^G_{ZZ}\right)_{BB}}C_{N,r}\left(\alpha^G_K,\beta^G_K,M\right)-2\bar{c}\left(\dot{V}^G_{K,Abs}\right)^I_B\right]\Bigg] \\
& +\left(x^P\right)_B\cdot\frac{\rho_{Air}\left(V^G_{K,Abs}\right)^I_B\left(\dot{V}^G_{K,Abs}\right)^I_B S_{Ref}\bar{c}}{\left(I^G_{ZZ}\right)_{BB}}C_{N,r}\left(\alpha^G_K,\beta^G_K,M\right)\frac{\bar{c}}{2\left(V^G_{K,Abs}\right)^I_B} \\
& +\left(x^P\right)_B\cdot\frac{\bar{q}S_{Ref}\bar{c}}{\left(I^G_{ZZ}\right)_{BB}}\Bigg[\frac{\partial C_{N,r}\left(\alpha^G_K,\beta^G_K,M\right)}{\partial\alpha^G_K}\left(\dot{\alpha}^G_K\right)^I_B\frac{\bar{c}}{2\left(V^G_{K,Abs}\right)^I_B} \\
& +\frac{\partial C_{N,r}\left(\alpha^G_K,\beta^G_K,M\right)}{\partial\beta^G_K}\left(\dot{\beta}^G_K\right)^I_B\frac{\bar{c}}{2\left(V^G_{K,Abs}\right)^I_B} \\
& +\frac{\partial C_{N,r}\left(\alpha^G_K,\beta^G_K,M\right)}{\partial M}\cdot\frac{\left(\dot{V}^G_{K,Abs}\right)^I_B}{a}\cdot\frac{\bar{c}}{2\left(V^G_{K,Abs}\right)^I_B} \\
& +\frac{C_{N,r}\left(\alpha^G_K,\beta^G_K,M\right)}{4\left(\left(V^G_{K,Abs}\right)^I_B\right)^2}\left[\frac{\bar{q}S_{Ref}\bar{c}^3}{\left(I^G_{ZZ}\right)_{BB}}C_{N,r}\left(\alpha^G_K,\beta^G_K,M\right)-2\bar{c}\left(\dot{V}^G_{K,Abs}\right)^I_B\right]\Bigg] \\
& +\left(x^P\right)_B\cdot\frac{\left(I^G_{YY}\right)_{BB}-\left(I^G_{XX}\right)_{BB}}{\left(I^G_{ZZ}\right)_{BB}}\left(p^{0B}_K\right)^2_B\left[-\frac{\left(I^G_{XX}\right)_{BB}-\left(I^G_{ZZ}\right)_{BB}}{\left(I^G_{YY}\right)_{BB}}\right] \\
& +\left(x^P\right)_B\cdot\left(p^{0B}_K\right)^2_B\left[-\frac{\left(I^G_{XX}\right)_{BB}-\left(I^G_{ZZ}\right)_{BB}}{\left(I^G_{YY}\right)_{BB}}\right]
\end{aligned} \tag{5.28}$$

The differential equation for $\left(r^{0B}_K\right)_B$, which is available from (2.7), (2.21), (2.37), (2.52), and (2.55), constitutes the foundation for the substitution of the terms in (5.18) concerning the interceptor yaw acceleration control system. Based on this differential equation and the replacements

for x_1, x_2, and u, $F_{2,21}(x_1, x_2)$ and $g_2(x_1, x_2)$ are derived according to (5.29) and (5.30).

$$F_{2,21}(x_1, x_2) = \frac{\bar{q} S_{Ref} \bar{c}}{\left(I^G_{ZZ}\right)_{BB}} \left[C_{N,0}\left(\alpha^G_K, \beta^G_K, M\right) + C_{N,r}\left(\alpha^G_K, \beta^G_K, M\right) \cdot \frac{\left(r^{0B}_K\right)_B \bar{c}}{2\left(V^G_{K,Abs}\right)^I_B} \right] + \frac{\left(M^G_{N,RJC}\right)_B}{\left(I^G_{ZZ}\right)_{BB}} - \frac{\left(I^G_{YY}\right)_{BB} - \left(I^G_{XX}\right)_{BB}}{\left(I^G_{ZZ}\right)_{BB}} \left(p^{0B}_K\right)_B \left(r^{0B}_K\right)_B \tag{5.29}$$

$$g_2(x_1, x_2) = \frac{\bar{q} S_{Ref} \bar{c}}{\left(I^G_{ZZ}\right)_{BB}} C_{N,\delta_N}\left(\alpha^G_K, \beta^G_K, M\right) \tag{5.30}$$

This design of the interceptor yaw acceleration control system guarantees global boundedness and global tracking of the output of the $\left(a^P_Y\right)^{II}_{B,woG,Cmd}$ filter independent of the flight condition of the interceptor, based on Chapter 4. Furthermore, $F_{1,11}(0) = 0$, if $(\alpha^G_K)^I_B = 0\,[deg]$, $(\dot{\alpha}^G_K)^I_B = 0\,[deg/s]$, $(\beta^G_K)^I_B = 0\,[deg]$, $(\dot{\beta}^G_K)^I_B = 0\,[deg/s]$, $\left(p^{0B}_K\right)_B = 0\,[deg/s]$, $\left(q^{0B}_K\right)_B = 0\,[deg/s]$, $\delta_L = 0\,[deg]$, $\delta_M = 0\,[deg]$, and $\delta_N = 0\,[deg]$. Under this conditions, $\left(a^P_Y\right)^{II}_{B,woG} = 0\,[m/s^2]$, $\left(r^{0B}_K\right)_B = 0\,[deg/s]$ is a globally stable equilibrium. Following the design of the interceptor pitch acceleration control system, the controllability of (5.17) and (5.18) as well as the existence of $\alpha(z_1, x_{1,Ref}, \dot{x}_{1,Ref}, \hat{\vec{\theta}}_1, \hat{\varrho}_1)$ and u is guaranteed, because $g_1(x_1) \neq 0$ and $g_2(x_1, x2) \neq 0$, except for $\bar{q}$ identical to zero.

The consideration of the parameter uncertainties introduced in Chapter 2 in the interceptor yaw acceleration control system follows exactly the interceptor pitch acceleration control system. $\vec{\theta}$, b_1, and b_2 account for all individual parameter uncertainties. Without parameter uncertainties present, $\vec{\theta} = \begin{bmatrix} 1 & 1 \end{bmatrix}^T$, $b_1 = 1$, and $b_2 = 1$. If parameter uncertainties exist, $\vec{\theta} \neq \begin{bmatrix} 1 & 1 \end{bmatrix}^T$, $b_1 \neq 1$, and $b_2 \neq 1$. The zero elements in (5.17) and (5.18) guarantee that the parameter uncertainty effects stay in the respective $\left(a^P_Y\right)^{II}_{B,woG}$ or $\left(r^{0B}_K\right)_B$ equation.

The implementation of the elements of the augmented design procedure for parametric strict-feedback systems with unknown control coefficients in the case of tracking inside the interceptor yaw acceleration control subsystem is identical to the interceptor pitch acceleration control system. The architecture of the $\left(a^P_Y\right)^{II}_{B,woG}$ control system is shown in Figure 5.6. The subsystems denoted $F_1(x_1)$, $g_1(x_1)$, $F_2(x_1, x_2)$, and $g_2(x_1, x_2)$ are redesigned according to (5.27) to (5.30). The fact that the implementation of interceptor yaw acceleration control system differs from the interceptor pitch acceleration control system only in the $F_1(x_1)$, $g_1(x_1)$, $F_2(x_1, x_2)$, and $g_2(x_1, x_2)$ subsystems underlines the superior reusability of the architectural approach chosen in this thesis.

5.6 Control allocation

5.6.1 Allocation algorithm

The control allocation subsystem inside the interceptor flight control system shall allocate $\delta_{L,Cmd}$, $\delta_{M,Cmd}$, and $\delta_{N,Cmd}$ to the two actuator sections of the interceptor, containing the total number of 184 actuators. Based on Requirement 7, the design of the control allocation should ensure that both actuator sections of the interceptor are employed and that the reaction jet cartridge consumption does not exceed 50 [%]. Therefore, standard control allocation methodologies are analyzed in the following concerning their capability to fulfill these requirements.

Standard control allocation methodologies

Available literature offers a wide spectrum of standard control allocation methodologies. [101] provides an overview to this spectrum and is based on [2], [6], [10], [13], [18], [19], [34], [35], [42], [75], [79], and [140]. In addition, the publication series consisting of [29], [30], [31], and [32] covers an enormous field of aspects related to control allocation, ranging from constrained controls to computational efficiency. Mathematical background touched in control allocation problems is available from [62], [96], and [99]. According to [101], control allocation methodologies are categorized into direct and optimization based algorithms. Daisy chaining is a control allocation methodology separate from these types.

[43] illustrates the successful application of optimization based algorithms to the control allocation of a modern fighter aircraft. Despite the availability of this important result, optimization based algorithms are inapplicable for this work. Such algorithms generate a solution for the control allocation problem which involves all available actuators. This means that the reaction jet actuator section of the interceptor would be driven permanently by the control allocation, even though the individual reaction jet cartridges can only be fired once. This behavior would lead to an excessive reaction jet cartridge consumption during the terminal flight phase of the interceptor. The results in [107] underpin the inapplicability of optimization based algorithms to this thesis, by showing that continuous reaction jet actuators are constantly driven in a similar situation.

The daisy chaining methodology constitutes a two step approach. First, all available actuators are sorted according to a priority order which is based primarily on measurable quantities, like actuator efficiency, maximum actuator deflection, etc., or possibly non-measurable quantities, e.g. predilection for an actuator by the system designer. Second, during system operation, all available actuators are driven according to the predefined priority order. If the actuator with the highest priority is saturated, the actuator which exhibits the second highest priority is driven with the remaining command that can not be implemented by the first actuator. This process continues until all available actuators are deflected to their limits. This is the case when the command exceeds the overall available actuator capability. The described operating principle of the daisy chaining methodology implies that the employment of all available actuators is not guaranteed. If, for example, a system operates at states where small commands which are below the saturation limit of the highest priority actuator need to be allocated, only this actuator is driven.

Based on the two actuator sections of the interceptor, two possible implementations of the daisy chaining methodology exist. Both exhibit different implications. If the reaction jet actuator section would be apportioned the highest priority, reaction jet cartridges would be utilized for every command, independent of the magnitude. Comparable to the optimization based algorithms, excessive reaction jet cartridge consumption would occur, preventing the fulfillment of Requirement 7. If the reaction jet actuator section would be given a priority lower than the aerodynamic actuator section, it would be possible that the reaction jet actuator section is not employed during the terminal flight phase of the interceptor, depending on the magnitude of the command, although beneficial effects for the agility of the interceptor could be achieved.

Although [27], following [10], [12], [35], [97], and [100], presented this priority order for aerospace vehicles comprising reaction control jets and aerodynamic control surfaces operating in endo-atmospheric conditions and derived a methodology to prevent control variable overshoot by accounting for the torques generated by the individual reaction control jets, this priority order is inappropriate for the interceptor flight control system, because it does not guarantee the utilization of both actuator sections of the interceptor during the terminal flight phase. Moreover, the cited method would lead to an enormous computational effort endangering the real time performance of the interceptor flight control system, due to the large number of individual reac-

tion jet cartridges in the reaction jet actuator section. Hence, the daisy chaining methodology is not usable herein.

Control allocation algorithm design

The inapplicability of the standard control allocation methodologies analyzed beforehand directs the search to simpler and straightforward solutions. Such solutions shall implement the following functionalities to fulfill Requirement 7.

The reaction jet actuator section shall not be driven by the control allocation when the interceptor is at a or close to a steady-state, meaning only small tracking errors exist, to prevent excessive reaction jet cartridge consumption. This functionality is extended to the situation when commands which are below a defined threshold need to be allocated. In this case, the reaction jet actuator section shall not be driven either. Small acceleration commands shall only be allocated to the aerodynamic actuator section to reduce reaction jet cartridge consumption. Vice versa, if large acceleration commands or tracking errors occur, the control allocation shall employ both actuator sections of the interceptor. The reaction jet actuator section, which exhibits a fast response time, supports the slower responding aerodynamic actuator section in the implementation of the commands. Furthermore, the control allocation should drive the reaction jet actuator section in discrete values up to the limit defined by (2.60).

Given this, the following control allocation algorithm design is defined. Because the reaction jet actuator section does not generate roll moments, which is evident from (2.55), $\delta_{L,Cmd}$ is completely allocated to the aerodynamic actuator section. $\delta_{M,Cmd}$ and $\delta_{N,Cmd}$ are also allocated to the aerodynamic actuator section. In contrast to these allocations, the tracking errors z_1 of the pitch and yaw acceleration control systems are forwarded to the reaction jet actuator section. (5.31) and (5.32) state the respective allocation.

$$\delta_{M,Cmd,RJC} = z_{1,Pitch} \tag{5.31}$$

$$\delta_{N,Cmd,RJC} = z_{1,Yaw} \tag{5.32}$$

$\delta_{M,Cmd}$ and $\delta_{N,Cmd}$ generated by the pitch and yaw acceleration control system are inappropriate to be used for the reaction jet actuator section, because $\delta_{M,Cmd} \neq 0$ or $\delta_{N,Cmd} \neq 0$, if the interceptor is at a steady-state. Therefore, the reaction jet actuator section would be driven, an excessive reaction jet cartridge consumption would result, and the defined requirements would not be achieved.

Because the individual reaction jet cartridges are dispersed on the circumference of the interceptor fuselage, as illustrated in Figure 2.1, (5.31) and (5.32) are transformed into polar coordinates. The magnitude of the reaction jet actuator section command $\delta_{Mag,Cmd,RJC}$ is calculated by (5.33).

$$\delta_{Mag,Cmd,RJC} = \sqrt{\delta^2_{M,Cmd,RJC} + \delta^2_{N,Cmd,RJC}} \tag{5.33}$$

Thereafter, $\delta_{Mag,Cmd,RJC}$ is quantized as stated in (5.34). The quantization is based on the reaction jet cartridge effectivity analyzed in Chapter 3. As Figure 3.11 shows, each reaction jet cartridge generates a $\left(a_Z^G\right)_B^{II}$ of $4\,[m/s^2]$ to $4.5\,[m/s^2]$, if positioned in the optimal attitude with respect to the command. A similar investigation for the chosen output $\left(a_Z^P\right)_{B,woG}^{II}$ leads to the result that an individual reaction jet cartridge gives rise to $6.9\,[m/s^2] \leq \left(a_Z^P\right)_{B,woG}^{II} \leq 7.2\,[m/s^2]$. $\delta_{Mag,Cmd,RJC}$ which represents the total acceleration tracking error, as can be seen from (5.31) to (5.33), is decreased by $\left(a_Z^P\right)_{B,woG}^{II}$ originating from the reaction jet cartridges, if the latter act in an adequate attitude. If, for example, $\delta_{Mag,Cmd,RJC} \approx 7\,[m/s^2]$ caused by $\delta_{M,Cmd,RJC} \approx 7\,[m/s^2]$, one reaction jet cartridge in the X_B - Z_B plane is sufficient to diminish the total

acceleration tracking error; tracking of the longitudinal acceleration is reestablished. Hence, the quantization expresses the amount of $\left(a_Z^P\right)_{B,woG}^{II}$ one or multiple reaction jet cartridges are capable to achieve. Presuming that the effects of individual reaction jet cartridges add up, (5.34) results. The integer interval to which the intervals of $\delta_{Mag,Cmd,RJC}$ are mapped is chosen in accordance with (2.60).

$$\delta^*_{Mag,Cmd,RJC} = \begin{cases} 0, & \text{if } 0 \leq \delta_{Mag,Cmd,RJC} < 7\,[m/s^2] \\ 1, & \text{if } 7\,[m/s^2] \leq \delta_{Mag,Cmd,RJC} < 14\,[m/s^2] \\ 2, & \text{if } 14\,[m/s^2] \leq \delta_{Mag,Cmd,RJC} < 21\,[m/s^2] \\ 3, & \text{if } \delta_{Mag,Cmd,RJC} \geq 21\,[m/s^2] \end{cases} \tag{5.34}$$

The last step of the control allocation algorithm guarantees $\delta^*_{Mag,Cmd,RJC} = 0$ for defined time interval between two successive reaction jet cartridge firings. This mechanism allows the reaction jet cartridge thrust profile, illustrated in Figure 2.4, to unfold, the respective forces and moments acting on the interceptor to develop, and by that prevents excessive reaction jet cartridge consumption during transition phases. The duration of the time interval is configurable and enables direct access to the reaction jet cartridge consumption in the terminal flight phase of the interceptor.
Although the designed control allocation algorithm is a straightforward approach, all required functionalities are fulfilled. The allocation of $\delta_{L,Cmd}$, $\delta_{M,Cmd}$, and $\delta_{N,Cmd}$ to the aerodynamic actuator section guarantees steady-state accuracy without the reaction jet actuator section driven. The control allocation algorithm uses the reaction jet actuator section in the presence of large commands and tracking errors with discrete values of reaction jet cartridges to be fired. In addition, the ability to directly influence the reaction jet cartridge consumption is implemented. The control allocation algorithm has no impact on the derived boundedness and stability properties, because the forces and moments generated by the reaction jet actuator section are considered in the employed design procedure.

5.6.2 Reaction jet cartridge allocation

The control allocation algorithm developed in the previous section generates $\delta^*_{Mag,Cmd,RJC}$ as output. $\delta^*_{Mag,Cmd,RJC}$ which expresses the amount of reaction jet cartridges to be fired needs to be mapped to reaction jet cartridge deflection operators δ_{RJC} of the individual reaction jet cartridge subsystems. The mapping is conducted in the reaction jet cartridge allocation. This process accounts for the positions and the attitudes of the individual reaction jet cartridges inside the interceptor fuselage as well as the availability of the particular reaction jet cartridges. The reaction jet cartridge allocation employs a four step approach. First, the optimal reaction jet cartridge angle with respect to the given commands is determined. Afterwards, the optimal reaction jet cartridge angle is corrected depending on $\left(p_K^{0B}\right)_B$ to account for the reaction jet cartridge fuze delay. Third, different reaction jet cartridge firing strategies are employed to fuze the amount of reaction jet cartridges given by $\delta^*_{Mag,Cmd,RJC}$. The reaction jet cartridge firing strategies depend on $\delta^*_{Mag,Cmd,RJC}$. Finally, two different reaction jet cartridge search algorithms are executed to find available reaction jet cartridges. Although the third and fourth step of the reaction jet cartridge allocation process are introduced separately, their execution inside the interceptor flight control system is interlaced.

Optimal reaction jet cartridge angle
The first step of the reaction jet cartridge allocation process searches the optimal reaction jet cartridge angle with respect to the given commands. Based on the dispersal of the reaction jet

cartridges on the circumference of the interceptor fuselage, the angle of $\delta^*_{Mag,Cmd,RJC}$, specified in the body fixed frame, needs to be calculated. $\delta_{M,Cmd,RJC}$ and $\delta_{N,Cmd,RJC}$ are employed in (5.35) to calculate the angle of $\delta^*_{Mag,Cmd,RJC}$.

$$\left(\varphi^{RJC}\right)_{B,Cmd} = \arctan\left(\frac{-\delta_{N,Cmd,RJC}}{\delta_{M,Cmd,RJC}}\right) \tag{5.35}$$

By comparing $\left(\varphi^{RJC}\right)_{B,Cmd}$ with the elements of $\left(\vec{\varphi}^{RJC}\right)_B$, as given in (2.4), the optimal reaction jet cartridge angle is found. The element of $\left(\vec{\varphi}^{RJC}\right)_B$ nearest to $\left(\varphi^{RJC}\right)_{B,Cmd}$ determines the optimal reaction jet cartridge angle.
The property $\left(p_K^{0B}\right)_B > 0\,[deg/s]$ of the interceptor, induced by Requirement 5, implies that the optimal reaction jet cartridge angle is a function of time. The calculated optimal reaction jet cartridge angle for a given $\delta^*_{Mag,Cmd,RJC}$ is inappropriate after a period of time and the adjacent element of $\left(\vec{\varphi}^{RJC}\right)_B$ becomes better suited. The reaction jet cartridge fuze delay displayed in Figure 2.4 contributes to this effect. Hence, the optimal reaction jet cartridge angle is corrected depending on $\left(p_K^{0B}\right)_B$. This mechanism ensures that the forces and moments generated by the reaction jet actuator section act in the plane specified by (5.35).
Considering $\left(p_K^{0B}\right)_B = 90\,[deg/s]$ and the reaction jet cartridge thrust profile, reaction jet cartridges which exhibit the optimal reaction jet cartridge angle for a given $\delta^*_{Mag,Cmd,RJC}$ rotate $0.45\,[deg]$ until the reaction jet cartridge fuze delay is elapsed, $1.35\,[deg]$ until the maximum reaction jet cartridge thrust unfolds, and $2.7\,[deg]$ until the reaction jet cartridge thrust diminishes. Compared to the angle of $10\,[deg]$ between adjacent reaction jet cartridges cartridge columns, these rotations are negligible. For this reason, no optimal reaction jet cartridge angle correction is necessary for $\left(p_K^{0B}\right)_B = 90\,[deg/s]$.
On the other hand, a correction of the optimal reaction jet cartridge angle becomes mandatory with increasing $\left|p_K^{0B}\right|_B$. To ensure reusability of the designed components, which has been defined as one of the aims of this work, the optimal reaction jet cartridge angle correction table according to Figure 5.7 is implemented in the reaction jet cartridge allocation. The table is based on considerations about $\left|p_K^{0B}\right|_B$ in relationship to the angle of $10\,[deg]$ between adjacent reaction jet cartridges cartridge columns.

Reaction jet cartridge firing strategies
After the determination of the optimal reaction jet cartridge angle, the individual reaction jet cartridge subsystems for the implementation of $\delta^*_{Mag,Cmd,RJC}$ are determined. This is the third step of the reaction jet cartridge allocation process. Depending on $\delta^*_{Mag,Cmd,RJC}$ as well as the availability of particular reaction jet cartridges, different reaction jet cartridge firing strategies are employed. In total, nine reaction jet cartridge firing strategies are designed in the framework of this thesis. All reaction jet cartridge firing strategies are displayed in Figure 5.8. Besides acting as an overview, Figure 5.8 illustrates the sequence in which the reaction jet cartridge firing strategies are utilized for different $\delta^*_{Mag,Cmd,RJC}$.
Reaction jet cartridge firing Strategy 1 relates to the case $\delta^*_{Mag,Cmd,RJC} = 1$. To generate forces and moments by reaction jet actuator section which are acting in the plane specified by the optimal reaction jet cartridge angle, it is desired to fire a reaction jet cartridge in the latter angle. Hence, Strategy 1 searches for an available reaction jet cartridge in the optimal reaction jet cartridge angle. Because the availability of such an reaction jet cartridge is not guaranteed, Strategy 1 incorporates the search in four adjacent reaction jet cartridge angles out of $\left(\vec{\varphi}^{RJC}\right)_B$, whereupon the sign of $\left(p_K^{0B}\right)_B$ is considered. If no available reaction jet cartridge is found in the total five considered reaction jet cartridge angles, Strategy 1 terminates without implementing $\delta^*_{Mag,Cmd,RJC}$. This termination prevents the generation of forces and moments by the reaction

Optimal reaction jet cartridge angle corrected by . . . available positions	$\left(p_K^{0B}\right)_B\ [rad/s]$
-3	$\left(p_K^{0B}\right)_B < -6\pi$
-2	$-6\pi \leq \left(p_K^{0B}\right)_B < -4\pi$
-1	$-4\pi \leq \left(p_K^{0B}\right)_B < -2\pi$
0	$-2\pi \leq \left(p_K^{0B}\right)_B < 2\pi$
1	$2\pi \leq \left(p_K^{0B}\right)_B < 4\pi$
2	$4\pi \leq \left(p_K^{0B}\right)_B < 6\pi$
3	$\left(p_K^{0B}\right)_B \geq 6\pi$

Figure 5.7: Optimal reaction jet cartridge angle correction table

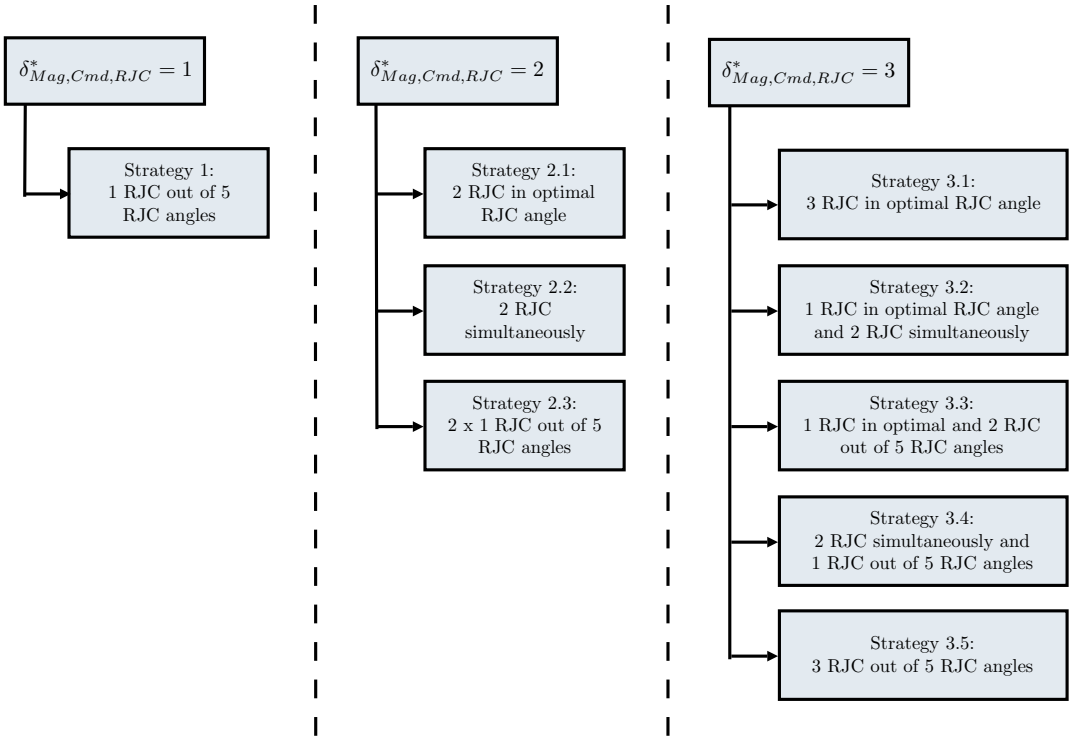

Figure 5.8: Reaction jet cartridge firing strategies

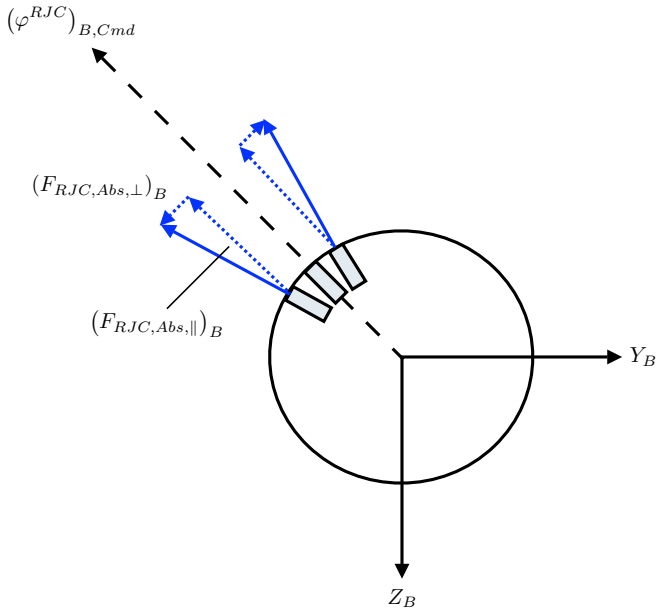

Figure 5.9: Reaction jet cartridge thrust forces at simultaneous firing

jet actuator section which act far outside the plane defined by the optimal reaction jet cartridge angle.

The case $\delta^*_{Mag,Cmd,RJC} = 2$ comprises three reaction jet cartridge firing strategies. These strategies are applied in the sequence shown in Figure 5.9. Strategy 2.1 searches for two available reaction jet cartridges in the optimal reaction jet cartridge angle. This constitutes the most desirable implementation of $\delta^*_{Mag,Cmd,RJC} = 2$. If such a pair of reaction jet cartridges is not available, Strategy 2.2 is employed.

Strategy 2.2 tries to implement $\delta^*_{Mag,Cmd,RJC} = 2$ by simultaneously firing two reaction jet cartridges which are positioned at the identical angle left- and right-hand side of the optimal reaction jet cartridge angle. As displayed in Figure 5.9, the simultaneous firing of two reaction jet cartridges gives rise to two reaction jet cartridge thrust forces. By splitting these reaction jet cartridge thrust forces into parallel thrust force components $\left(F_{RJC,Abs,\parallel}\right)_B$ and perpendicular thrust force components $(F_{RJC,Abs,\perp})_B$, it becomes evident that $(F_{RJC,Abs,\perp})_B$ of the two reaction jet cartridges cancel each other, while $\left(F_{RJC,Abs,\parallel}\right)_B$ remain. The remaining $\left(F_{RJC,Abs,\parallel}\right)_B$ act in the plane specified by the optimal reaction jet cartridge angle. If Strategy 2.2 can not be implemented, due to reaction jet cartridge non-availability, the third strategy for the case $\delta^*_{Mag,Cmd,RJC} = 2$ is used.

Strategy 2.3 constitutes a repeated application of Strategy 1. This repeated application ensures that a single, remaining reaction jet cartridge in the optimal reaction jet cartridge angle is utilized first, that $\delta^*_{Mag,Cmd,RJC} = 2$ is implemented, if possible, and that at least a partial implementation of $\delta^*_{Mag,Cmd,RJC} = 2$ is achieved, if only one available reaction jet cartridge remains in the considered reaction jet cartridge angles. In addition, it supports the modular, reusable design approach central to this thesis. In case Strategy 2.3 can not be implement $\delta^*_{Mag,Cmd,RJC}$ partially or totally, it is terminated.

The total number of five reaction jet cartridge firing strategies is related to the allocation $\delta^*_{Mag,Cmd,RJC} = 3$. Following Strategy 2.1, Strategy 3.1 tries to implement $\delta^*_{Mag,Cmd,RJC} = 3$ by firing three reaction jet cartridges in the optimal reaction jet cartridge angle. If the remaining availability of particular reaction jet cartridges does not allow such implementation Strategy 3.2

is employed, as illustrated in Figure 5.8.
Strategy 3.2 is designed for the case when one available reaction jet cartridge in the optimal reaction jet cartridge angle remains. Provided this availability, Strategy 3.2 tries to augment this partial implementation of $\delta^*_{Mag,Cmd,RJC} = 3$ by the simultaneous firing of two reaction jet cartridges positioned on either side of the optimal reaction jet cartridge angle. Hence, Strategy 3.2 is the superposition of the firing of one reaction jet cartridge in the optimal reaction jet cartridge angle and Strategy 2.2.
Following Strategy 3.2, Strategy 3.3 considers also the case when one reaction jet cartridge in the optimal reaction jet cartridge angle is available. In contrast to the former, Strategy 3.3 is employed, if a simultaneous firing of two reaction jet cartridges positioned on either side of the optimal reaction jet cartridge angle is not possible. Strategy 3.3 searches for two remaining reaction jet cartridges in the adjacent reaction jet cartridge angles. This strategy can be understood as repeated application of Strategy 1, where one reaction jet cartridge remains in the optimal reaction jet cartridge angle. If no reaction jet cartridge in the optimal reaction jet cartridge angle can be fired, Strategy 3.4 is executed.
Strategy 3.4 constitutes a combination of Strategy 1 and Strategy 2.2. First, Strategy 2.2 is employed to search for two reaction jet cartridges positioned on either side of the optimal reaction jet cartridge angle. If applicable reaction jet cartridges for a simultaneous firing are found, Strategy 1 is executed to identify an appropriate, individual reaction jet cartridge to augment the result of Strategy 2.2 and achieve $\delta^*_{Mag,Cmd,RJC} = 3$. If Strategy 2.2 can not be implemented successfully, the fifth strategy is employed.
The repeated application of Strategy 1 in the case $\delta^*_{Mag,Cmd,RJC} = 3$ is denoted Strategy 3.5. Although Strategy 3.5 is unable to identify an available reaction jet cartridge in the optimal reaction jet cartridge angle under this circumstances, based on the beforehand employed strategies, it provides the capability to implement $\delta^*_{Mag,Cmd,RJC} = 3$ partially or totally. If Strategy 3.5 is not able to realize $\delta^*_{Mag,Cmd,RJC}$ partially or totally, it terminates without implementation of the remaining $\delta^*_{Mag,Cmd,RJC}$. The creation of forces and moments by the reaction jet actuator section acting far outside the plane of the optimal reaction jet cartridge angle is prevented under all conditions by this approach.

Reaction jet cartridge search algorithms
The reaction jet cartridge firing strategies specify to which degree $\delta^*_{Mag,Cmd,RJC}$ is implemented. To identify the particular reaction jet cartridges and set the respective δ_{RJC}, the strategies rely on two reaction jet cartridge search algorithms. As introduced above, these algorithms constitute the fourth step in the reaction jet cartridge allocation process from the procedural perspective. With regard to implementation, their execution is interlaced with the reaction jet cartridge firing strategies.
The first of the reaction jet cartridge search algorithms identifies an available, individual reaction jet cartridge. Starting from the optimal reaction jet cartridge angle, the algorithm calculates a subset of $\left(\vec{\varphi}^{RJC}\right)_B$ which contains the optimal and four adjacent reaction jet cartridge angles. $\left(p_K^{0B}\right)_B$ is considered in this calculation, meaning that the adjacent reaction jet cartridge angles are becoming optimal through the rotation of the interceptor. After calculation of the subset of $\left(\vec{\varphi}^{RJC}\right)_B$, the algorithm searches for an available, individual reaction jet cartridge in the subset. The search is performed from the optimal reaction jet cartridge angle outwards, starting at each angle from the reaction jet cartridge exhibiting the largest lever arm to the center of gravity of the interceptor towards smaller lever arms. This methodology guarantees that the reaction jet cartridges with the highest control efficiency are utilized first. The first available reaction jet cartridge is the solution of this search algorithm and is handed over to the reaction jet cartridge

firing strategy.
The second reaction jet cartridge search algorithm allocates two available reaction jet cartridges for simultaneous firing. This algorithm is utilized in the reaction jet cartridge firing strategies related to $\delta^*_{Mag,Cmd,RJC} = 2$ and $\delta^*_{Mag,Cmd,RJC} = 3$. In its initial step, the search algorithm calculates a subset of $\left(\vec{\varphi}^{RJC}\right)_B$. This subset contains nine reaction jet cartridge angles, whereupon the optimal reaction jet cartridge angle constitutes the fifth angle in the subset. Beginning its search from reaction jet cartridges which exhibit the largest lever arm to the center of gravity of the interceptor towards reaction jet cartridges with smaller lever arms, the search algorithm moves from the reaction jet cartridge angle adjacent to the optimal angle outwards, while trying to identify an available reaction jet cartridge. If an available reaction jet cartridge is found, the algorithm searches the respective angle in the second half of the calculated subset for an available reaction jet cartridge that is appropriate for simultaneous firing. If an appropriate pair of reaction jet cartridges is identified, the latter is forwarded to the executed reaction jet cartridge firing strategy. If the search in the second half of the calculated subset of $\left(\vec{\varphi}^{RJC}\right)_B$ does not lead to an appropriate solution for simultaneous firing, the algorithm continues its search in the first half of the subset for the next available reaction jet cartridge. If no reaction jet cartridges for simultaneous firing can be identified or no available reaction jet cartridge remains in the first half of the subset, the algorithm terminates. The next reaction jet cartridge firing strategy is taken into account.
The derivation and implementation of the reaction jet cartridge allocation is the last step in the synthesis of the interceptor flight control system. Now, the parameters of the interceptor flight control system are adjusted to fulfill the given requirements.

5.7 Flight control system parameter optimization

The synthesis of the interceptor flight control system is the first main step in the design process presented in this thesis. To achieve the desired performance of the controlled interceptor, which is quantified in the requirements in Section 5.1, the parameters of the interceptor flight control system are adjusted appropriately. This is the second main step of the design process.
There are three sets of parameters in the interceptor flight control system to be adjusted. First, the position of the arbitrary acceleration reference point P, specified in the body fixed frame, is derived. Thereafter, the parameters of the respective control systems are determined. Finally, the parameters of the designed control allocation subsystem are defined.

Acceleration reference point
The design of the interceptor pitch and yaw acceleration control system is based on the availability of an arbitrary acceleration reference point P which guarantees that $\left(a_Z^P\right)^{II}_{B,woG}$ and $\left(a_Y^P\right)^{II}_{B,woG}$ are minimum phase. Following the presentation in Section 5.4 and Section 5.5, P is located ahead of the center of gravity of the interceptor and on the X_B axis. Besides these conditions, the exact location of P is undetermined and constitutes a design parameter. Therefore, an appropriate location of P is calculated in the following.
Considering the coincidence of the longitudinal and lateral interceptor dynamics, Requirement 6, and the equal design of the interceptor pitch and yaw acceleration control system, P is taken identical for $\left(a_Z^P\right)^{II}_{B,woG}$ and $\left(a_Y^P\right)^{II}_{B,woG}$. The derivation of appropriate locations for P is conducted by employing a modular toolbox which is developed in the framework of this thesis. This toolbox calculates the minimum distance between the center of gravity of the interceptor and P, specified in the body fixed frame, $|\vec{r}^{GP}|_{B,Min}$ for the interceptor flight envelope. Because this toolbox utilizes trim calculation results for steady-state horizontal flight as input, all prop-

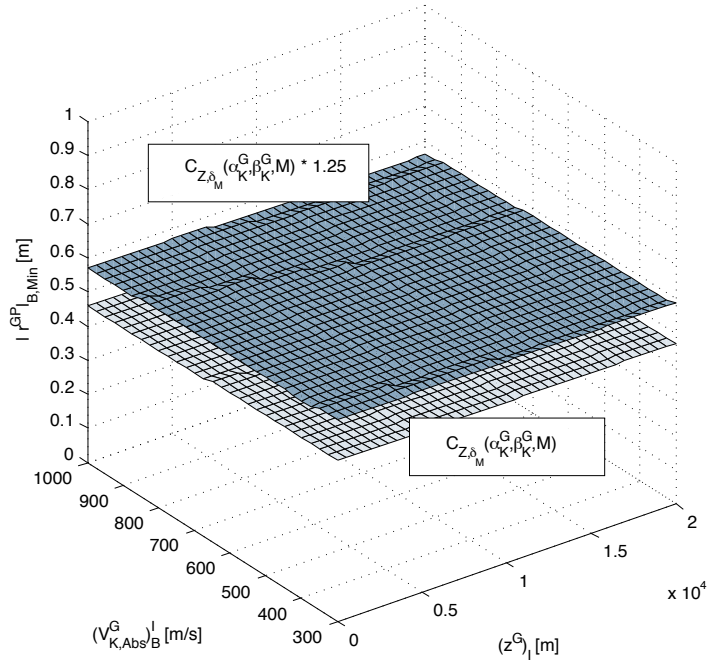

Figure 5.10: $\left|\vec{r}^{GP}\right|_{B,Min}$ in the nominal case and in case of increased $C_{Z,\delta_M}\left(\alpha_K^G, \beta_K^G, M\right)$

erties of the interceptor, including parameter uncertainties, are considered in the calculation of $|\vec{r}^{GP}|_{B,Min}$. The minimum and maximum possible values for $|\vec{r}^{GP}|_{B,Min}$ as well as the step size for the calculation are configurable. Hence, the toolbox calculates $|\vec{r}^{GP}|_{B,Min}$ with an arbitrary accuracy. $|\vec{r}^{GP}|_{B,Min}$ itself is determined via the real parts of the zeros of $H_{\left(a_Z^P\right)_{B,woG}^{II}\delta_{M,Cmd}}(s)$. $\left(\vec{r}^{GP}\right)_B$ is increased until the zeros of $H_{\left(a_Z^P\right)_{B,woG}^{II}\delta_{M,Cmd}}(s)$ cross the imaginary axis. If the zeros exhibit negative real parts, they are located in the open left half plane, minimum phaseness is achieved, and $|\vec{r}^{GP}|_{B,Min}$ is found. Besides the imaginary axis, the toolbox is able to consider any degree of minimum phaseness, represented by a parallel to the imaginary axis. This implies that the toolbox provides the capability to calculate $|\vec{r}^{GP}|_{B,Min}$ even in the case of unknown or non-modeled parameter uncertainties. The exact location of P follows from $|\vec{r}^{GP}|_{B,Min}$ in conjunction with (5.13).

The result for $|\vec{r}^{GP}|_{B,Min}$ for the interceptor flight envelope is illustrated in Figure 5.10. The lower surface in Figure 5.10 displays $|\vec{r}^{GP}|_{B,Min}$ in the absence of parameter uncertainties. The upper surface shows the result for the situation where $C_{Z,\delta_M}\left(\alpha_K^G, \beta_K^G, M\right)$, which enters the dynamics of the interceptor via (2.11), (2.36), and (2.49), is increased by 25 [%]. The increase of $C_{Z,\delta_M}\left(\alpha_K^G, \beta_K^G, M\right)$ implies an increased non-minimum phaseness of $\left(a_Z^G\right)_B^{II}$. An increased $|\vec{r}^{GP}|_{B,Min}$ to overcome this behavior results.

Based on the employment of the developed toolbox in the absence of parameter uncertainties as well as for different cases where parameter uncertainties are present, the location of P, specified in the body fixed frame, is chosen according to (5.36).

$$\left(\vec{r}^{P}\right)_B = \begin{bmatrix} 1.500 & 0 & 0 \end{bmatrix}_B^T [m] \tag{5.36}$$

Command filter parameters

Having P chosen adequately, the parameters of the control systems of the interceptor flight control system are determined in a two step approach. First, the parameters of the command filters are derived. Thereafter, all remaining parameters of the control systems are optimized.
The designed interceptor roll rate control system as well as the interceptor acceleration control systems comprise a command filter to guarantee the that the respective reference signals and its derivatives are smooth and bounded. The reference signals are tracked by the control systems. The choice of the parameters of the command filters in accordance with the given requirements constitutes the first step to fulfill the latter.
Specified in Requirement 5, the interceptor shall maintain $\left(p_K^{0B}\right)_B = 90\,[deg/s]$ during the terminal flight phase. This implies that $\left(p_K^{0B}\right)_{B,Cmd} = -90\,[deg/s]$. By initializing the command filter inside the interceptor roll rate control system with $\left(p_K^{0B}\right)_{B,Flt} = 90\,[deg/s]$, transients originating from the command filter are prevented. The filtered signal is constant. The parameters of the command filter can be chosen arbitrarily. Considering the linearized roll rate interceptor dynamics as given in (3.65), the natural frequency ω_n and the proportional gain k_P are defined according to (5.37) and (5.38).

$$\omega_n = 10\,[rad/s] \tag{5.37}$$

$$k_P = -10 \tag{5.38}$$

Requirement 6 imposes a specific behavior on the controlled interceptor with respect to the longitudinal and lateral acceleration dynamics. The dynamical behavior which is required is identical for longitudinal and lateral acceleration maneuvers. Therefore, the parameters of the command filters inside the interceptor pitch and yaw acceleration control system are chosen identical. Because no initial condition is available from the given requirement, the latter condition is defined to zero. The time constant of the controlled interceptor shall be $T = 0.1\,[s]$ or smaller. Hence, the natural frequency ω_n is defined as stated in (5.39).

$$\omega_n = 10\,[rad/s] \tag{5.39}$$

Following [81], the overshoot of a second order, linear time invariant system is given by (5.40). Due to the fact that the command filters inside the interceptor pitch and yaw acceleration control system belong to this class of system, (5.40) is used to derive a damping ratio ζ which guarantees the fulfillment of Requirement 6. Defining ζ like (5.41) results in an overshoot of $4.32\,[\%]$, being significantly below the threshold specified by the requirement. For this reason, ζ in (5.41) is appropriate and utilized in both command filters.

$$\Delta h = e^{-\frac{\pi\zeta}{\sqrt{1-\zeta^2}}} \tag{5.40}$$

$$\zeta = \frac{1}{2}\sqrt{2} \tag{5.41}$$

Considering the approximation stated in (5.42), which is available from [81], the choices (5.39) and (5.41) guarantee the fulfillment of Requirement 6 regarding the settling time to $\pm 5\,[\%]$ of the acceleration command. To ensure a static gain identical to one for the command filters inside the interceptor pitch and yaw acceleration control system, the proportional gain k_P is chosen according to (5.43).

$$T_{5\,[\%]} \approx \frac{3}{\zeta \cdot \omega_n} \tag{5.42}$$

$$k_P = -100 \tag{5.43}$$

Control system parameters

The choice of the parameters of the command filters guarantees that the reference signals of the interceptor flight control system are in accordance with Requirement 5 and Requirement 6. If the adjustment of the remaining parameters of the control systems achieves that the reference signals are tracked, these requirements are fulfilled. Furthermore, a reduction of the tracking errors of the interceptor flight control system implies an increased performance of the controlled interceptor with respect to the stated requirements. Moreover, by minimizing the tracking errors of the interceptor flight control system, the best possible fulfillment of Requirement 5 and Requirement 6 is achieved. Hence, the adjustment of the remaining parameters of the control systems constitutes an optimization problem from the mathematical perspective.

The remaining parameters of the control systems are categorized into three groups of parameters. The first group of parameters contains the parameters c_i utilized in the recursive design procedures. The c_i determine the dynamics of the error signals inside the control systems. In total, five c_i are comprised in the interceptor flight control system. The modified design procedure employed to design the interceptor roll rate control system contains one parameter. It is denoted c_{Roll}. The interceptor pitch and yaw acceleration control system exhibit two parameters each, which originate from the augmented design procedure for parametric strict-feedback systems with unknown control coefficients in the case of tracking. These parameters are denoted $c_{1,Pitch}$, $c_{2,Pitch}$, $c_{1,Yaw}$, and $c_{2,Yaw}$ respectively. Based on Requirement 6, $c_{1,Pitch}$ and $c_{1,Yaw}$ as well as $c_{2,Pitch}$ and $c_{2,Yaw}$ are defined to be identical, leading to the denotation c_1 and c_2.

The second group of parameters are the adaptation gain matrices Γ_j and the adaptation gains γ_k. The total number of 26 adaptation parameters is comprised in the interceptor flight control system, whereupon the elements of Γ_j are counted individually. By defining all non-main diagonal elements of Γ_j identical to zero to conveniently achieve the positive definiteness of Γ_j, the total number of adaptation parameters is reduced to 18. Considering Γ_j as multiples of the unit matrix as well as Requirement 6, the total number of eight adaptation parameters remains. The adaptation parameters are $\gamma_{1,Roll}$ and $\gamma_{\varrho_{1,Roll}}$ in the interceptor roll rate control systems and Γ_1, Γ_2, $\gamma_{b_{11}}$, $\gamma_{b_{12}}$, γ_{ϱ_1} as well as γ_{ϱ_2} inside the interceptor pitch and yaw acceleration control system, where Γ_1 and Γ_2 exhibit the beforehand mentioned structure.

The nonlinear damping gains κ_l form the third group of parameters. Following the first group, the third group contains five κ_l. κ_{Roll} is part of the interceptor roll rate control system. κ_1 and κ_2 are used with identical values in the interceptor pitch and yaw acceleration control system.

It is evident that no straightforward approach to determine the total number of 14 remaining parameters of the control systems optimally exists. The Backstepping methodology, as illustrated in [71] and introduced herein, provides no approach to calculate the optimal values for the remaining parameters of the control systems. Furthermore, no analytical approach which simultaneously accounts for multiple nonlinear adaptive control systems, as employed in the interceptor flight control system, is available that determines the optimal values for the remaining parameters.

To overcome this non-availability of an analytical approach and to provide the ability to optimize the remaining parameters of the control systems for the interceptor flight envelope, a modular parameter optimization toolbox has been employed. Figure 5.11 illustrates the parameter optimization toolbox architecture.

The flight envelope routine depicts the outer layer of the parameter optimization toolbox. It is initialized with an array of $(V^G_{K,Abs})^I_B$ and $\left(z^G\right)_I$ describing the interceptor flight envelope. The parameter optimization toolbox optimizes the remaining parameters of the control systems for all particular flight conditions of the interceptor specified in the flight envelope routine.

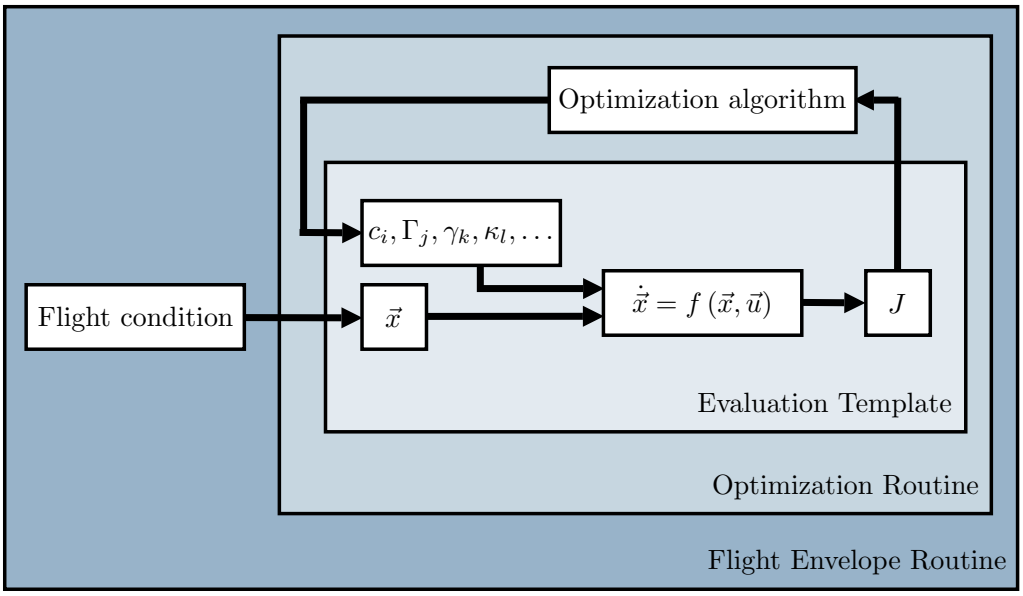

Figure 5.11: Parameter optimization toolbox architecture

The optimization routine is the middle layer of the parameter optimization toolbox. This layer conducts the optimization of the remaining parameters. The design of the parameter optimization toolbox allows any optimization algorithm to be used in this middle layer. The Downhill-Simplex-Algorithm, which is presented in [104], based on [95] as well as [38], [57], [103], [102], [109], [127], and [143], is used in this thesis. An initialization file provides the initial set of optimization parameters and parameters necessary for the process of optimization, e.g. the maximum number of iterations and the tolerance to be achieved. The Downhill-Simplex-Algorithm calculates the initial simplex and utilizes the methods of reflection, expansion, and contraction to modify the shape of the simplex volume to find the optimal set of parameters. Further details on the mentioned methods are available in the cited literature. To guarantee the boundedness and stability properties derived in Chapter 4, the Downhill-Simplex-Algorithm is modified in this work before implementation. This modification ensures that all parameters of the control systems, being subject to optimization, stay in $\mathbb{R}_+$. The optimization routine provides the actual set of optimization parameters to the inner layer of the parameter optimization toolbox; the evaluation template.

The evaluation template constitutes a construct that transforms the flight condition of the interceptor to the initial condition state vector of the interceptor, defines the actual set of optimization parameters as the parameters of the control systems, conducts the simulation of the terminal flight phase of the interceptor, and calculates the cost value J according to the defined cost function. J is forwarded from the evaluation template to the optimization routine, thereafter. Because the evaluation template simulates the terminal flight phase of the interceptor, the optimization of the remaining parameters of the control system is utilizable for any kind of input commands. In addition, the design of the evaluation template allows the parameter optimization toolbox to be utilized with any simulation model for any parameter optimization purpose with any cost function. Only minor changes to the evaluation template apply.

Considering the given requirements, the flight condition is defined by $\left(p_K^{0B}\right)_{B,Cmd} = 90\,[deg/s]$ only. Due to this, multiple $(V_{K,Abs}^G)_B^I$ and $\left(z^G\right)_I$ are considered for the optimization. The longitudinal and lateral acceleration control strings are each provided with representative step input

commands which vary during the terminal flight phase of the interceptor. Parameter uncertainties are absent for the employment of the parameter optimization toolbox.
The cost function for the optimization is chosen based on the rational to minimize the tracking errors of the interceptor flight control system. These tracking errors of the individual control systems are defined in (4.213). z_{Roll} denotes the tracking error of the interceptor roll rate control system. The tracking errors of the interceptor pitch and yaw acceleration control system are denoted by $z_{1,Pitch}$ and $z_{1,Yaw}$ respectively. Besides z_{Roll}, $z_{1,Pitch}$, and $z_{1,Yaw}$, the errors $z_{2,Pitch}$ and $z_{2,Yaw}$ of the interceptor pitch and yaw acceleration control system, which are given by (4.214), are reflected in the cost function to suppress oscillations. The resulting cost function is provided in (5.44), where t_{Sim} constitutes the terminal flight phase of the interceptor. The weighting factors in (5.44) are chosen appropriately as (5.45) and (5.46).

$$J = \int_{t_{Sim}} \left[k_1 z_{Roll}^2(\tau) + k_2 z_{1,Pitch}^2(\tau) + k_3 z_{2,Pitch}^2(\tau) + k_4 z_{1,Yaw}^2(\tau) + k_5 z_{2,Yaw}^2(\tau) \right] \mathrm{d}\tau \tag{5.44}$$

$$k_1 = k_2 = k_4 = 1 \tag{5.45}$$

$$k_3 = k_5 = 0.85 \tag{5.46}$$

Instead of directly optimizing all remaining parameters of the control systems, only c_i are subject to optimization initially. The designed adaptation algorithms as well as the nonlinear damping terms are distorted in this initial step. The absence of parameter uncertainties implies that optimal values for c_i are available without considering the second and third group of parameters in this case. The result for c_i constitutes the foundation for the optimization of the second and third group of parameters afterwards. In addition, this stepwise approach reduces the computational effort. The initial values for the optimization of c_i are chosen according to (5.47) and (5.48).

$$c_{Roll} = 10 \tag{5.47}$$

$$c_1 = c_2 = 2 \tag{5.48}$$

The result for the optimization of c_i for the flight condition $(V_{K,Abs}^G)_B^I = 600\,[m/s]$ and $\left(z^G\right)_I = 10000\,[m]$ is illustrated in Figure 5.12. The upper diagram of Figure 5.12 displays J over the number of iterations of the optimization. It is evident that J decreases during the optimization. The Downhill-Simplex-Algorithm continuously improves c_i towards smaller J, implying smaller tracking errors. The value of J for the final c_i is approximately one hundred times smaller than for the initial set. The lower diagram of Figure 5.12 displays the development of c_{Roll}, c_1, and c_2 during the optimization. The blue line shows c_{Roll}, the red line represents c_1, and c_2 is illustrated by the green line. By comparing the upper and the lower diagram, it is concluded that the decrease of J is achieved by increasing c_i. This behavior is fully in line with the theoretical background of Chapter 4. There it has been mentioned that the increase of c_i results in an increased speed of convergence. Faster convergence means reduced tracking errors, which results in a smaller J, if integrated over t_{Sim}. Furthermore, the lower diagram indicates that the Downhill-Simplex-Algorithm determines at least a local minimum of the cost function within the predefined tolerances, because c_{Roll}, c_1, and c_2 converge to steady-state values.
The implementation and test of the optimal values for c_{Roll}, c_1, and c_2 in the interceptor flight control system shows that rounding of the parameters is possible without recognizable influences to the performance of the controlled interceptor. This leads to the optimal values for c_{Roll}, c_1, and c_2 as given by (5.49) to (5.51) for the flight condition $(V_{K,Abs}^G)_B^I = 600\,[m/s]$ and $\left(z^G\right)_I = 10000\,[m]$.

$$c_{Roll} = 100 \tag{5.49}$$

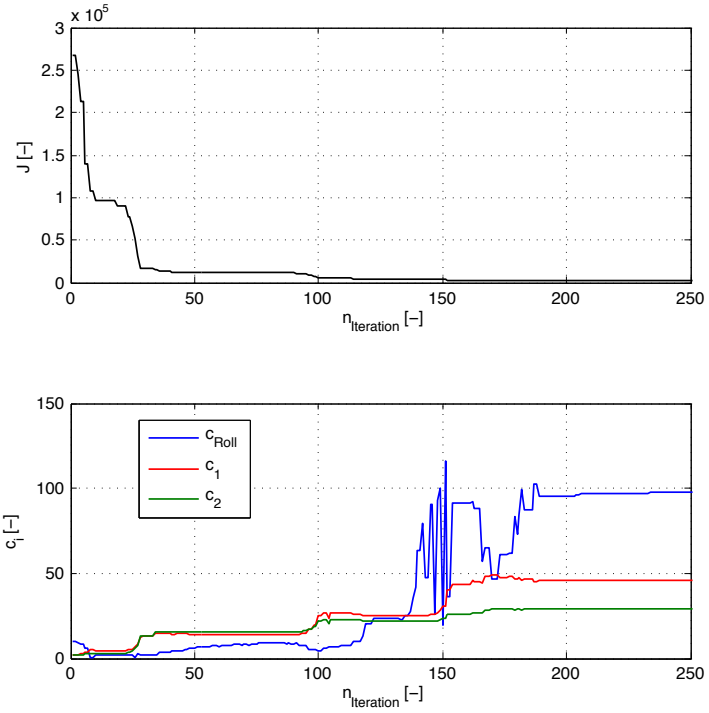

Figure 5.12: Optimization of c_i at $(V^G_{K,Abs})^I_B = 600\,[m/s]$ and $\left(z^G\right)_I = 10000\,[m]$

$$c_1 = 45 \tag{5.50}$$

$$c_2 = 25 \tag{5.51}$$

The c_i in (5.49) to (5.51) show very good results for other flight conditions and are therefore taken throughout the overall interceptor flight envelope.
After the optimization of c_i has been completed, the second and third group of parameters are optimized by using the developed toolbox. The flight conditions of the interceptor and the commands provided to the control strings remain unchanged. Parameter uncertainties are absent. The optimized parameters for the interceptor roll rate control system are given by (5.52) to (5.54).

$$\gamma_{1,Roll} = 1 \cdot 10^{-5} \tag{5.52}$$

$$\gamma_{\varrho 1,Roll} = 1 \cdot 10^{-5} \tag{5.53}$$

$$\kappa_{Roll} = 1 \cdot 10^{-6} \tag{5.54}$$

The results for the interceptor pitch and the yaw acceleration control system concerning the adaptation parameters are stated in (5.55) to (5.57). The respective optimized nonlinear damping gains are given in (5.58).

$$\Gamma_1 = \Gamma_2 = \begin{bmatrix} 1 \cdot 10^{-5} & 0 \\ 0 & 1 \cdot 10^{-5} \end{bmatrix} \tag{5.55}$$

$$\gamma_{b11} = \gamma_{b12} = 1 \cdot 10^{-5} \tag{5.56}$$

$$\gamma_{\varrho 1} = \gamma_{\varrho 2} = 1 \cdot 10^{-5} \tag{5.57}$$

$$\kappa_1 = \kappa_2 = 1 \cdot 10^{-6} \tag{5.58}$$

Control allocation parameters
With the parameters of the control systems inside the interceptor flight control system determined, only the parameters of the designed control allocation subsystem remain. Following Section 5.6, the duration of the time interval between two successive reaction jet cartridge firings constitutes the only adjustable parameter of the control allocation subsystem. Considering the reaction jet cartridge thrust profile visualized in Figure 2.4, the duration of this time interval is set to $0.025\,[s]$. After this time, the maximum thrust force of individual the reaction jet cartridges has developed and is acting on the interceptor. If under this condition $\delta_{Mag,Cmd,RJC}$ remains, the further use of reaction jet cartridges according to (5.34) is feasible.
After Chapter 4 presented the theoretical background utilized in this thesis, the preceding chapter illustrated the design of the interceptor flight control system. Now, the finalized design of the interceptor flight control system is evaluated against the requirements under various conditions, including situations where parameter uncertainties exist, to investigate its capabilities.

Chapter 6

Performance evaluation

6.1 Performance without parameter uncertainties

The design of the interceptor flight control system is the main work step in the engineering of the nonlinear adaptive flight control system for the endo-atmospheric dual-actuator interceptor. After completion of this step, the interceptor flight control system is implemented. To determine the performance of the design and explore its capabilities, it is tested under various conditions. Furthermore, it is evaluated, if the controlled interceptor meets the requirements of Chapter 5. This evaluation constitutes the foundation for a qualitative assessment of the designed interceptor flight control system concerning its applicability to highly agile systems.
The results of the testing as well as the evaluation are presented in the following. Although extensive testing and evaluation is conducted in the framework of this thesis, only the main results are provided herein. This introductory section illustrates the nominal case where parameter uncertainties are absent. Afterwards, two situations with existing uncertain constant parameters are covered, before time-varying parameters are introduced separately. Finally, combined uncertainties, meaning uncertain constant parameters as well as time-varying parameters, are considered, imposing the most difficult condition on the interceptor flight control system.
The first situation to be investigated is the nominal case; parameter uncertainties do not exist. Although this situation seems unrealistic, based on the presentations in Chapter 2, it is of importance for the overall testing and evaluation process. The nominal case constitutes the least difficult situation for the designed interceptor flight control system. If the interceptor flight control system is not able to meet the given requirements under these circumstances, a redesign of the interceptor flight control system becomes is necessary.
The properties of the interceptor in the nominal case are according to Chapter 2. The plant model inside the interceptor flight control system exhibits the identical properties. All parameters of the interceptor flight control system are adjusted following Chapter 5. Two separate scenarios are considered velocity-wise. The first scenario is defined by the initial conditions $(V_{K,Abs}^{G})_{B,IC}^{I} = 600\,[m/s]$ and $\left(z^{G}\right)_{I,IC} = 10000\,[m]$ and is denoted high velocity scenario in the following. In contrast, $(V_{K,Abs}^{G})_{B,IC}^{I} = 400\,[m/s]$ and $\left(z^{G}\right)_{I,IC} = 10000\,[m]$ are the initial conditions for the low velocity scenario. Both scenario are of operational relevance for a missile like the interceptor. As it is recognizable from Figure 3.3, the interceptor exhibits significantly different maneuver capabilities at these regions of the interceptor flight envelope. Especially in the low velocity scenario, the reduction of these capabilities, originating from the decreasing $(V_{K,Abs}^{G})_{B}^{I}$ due to the aerodynamic drag, will influence the performance of the controlled interceptor. Based on the introduced requirements, $\left(p_{K}^{0B}\right)_{B,Cmd} = 90\,[deg/s]$. The exemplary $\left(a_{Y}^{P}\right)_{B,woG,Cmd}^{II}$ and $\left(a_{Z}^{P}\right)_{B,woG,Cmd}^{II}$ sequence utilized for the investigation is displayed in Figure

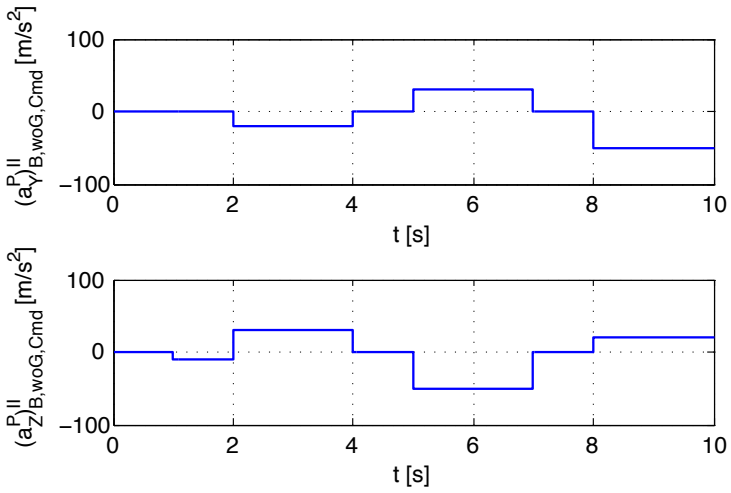

Figure 6.1: $\left(a_Y^P\right)_{B,woG,Cmd}^{II}$ and $\left(a_Z^P\right)_{B,woG,Cmd}^{II}$ sequence

6.1. This sequence does neither relate to a specific target nor scenario.

Interceptor performance in the nominal case at high velocity scenario
First, the signals of the plant model inside the interceptor flight control system are compared with the respective signals of the interceptor. This step validates the plant model as a representation of the interceptor. If the plant model represents the interceptor, its signals are appropriate to be used in the control subsystems. The comparison shows that the deviation of the signals of the plant model from the signals of the interceptor is significantly below 1 [%] during the terminal flight phase of the interceptor. Therefore, the signals of the plant model are used.
Given the beforehand derived result, the performance of the controlled interceptor in the nominal case is evaluated. Figure 6.2 displays $\left(p_K^{0B}\right)_B$, $\left(a_Y^P\right)_{B,woG}^{II}$, and $\left(a_Z^P\right)_{B,woG}^{II}$. The blue lines in the diagrams of Figure 6.2 indicate the signals measured by the internal sensor system, whereas the green lines show the known, smooth, and bounded reference signals generated by the command filters. Furthermore, the requirements provided in Chapter 5 are visualized.
It is obvious from the upper diagram of Figure 6.2 that $\left(p_K^{0B}\right)_B$ stays inside the boundaries given by Requirement 5. These are visualized by the horizontal dashed lines. The center and lower diagram of Figure 6.2 illustrate that the controlled interceptor demonstrates an appropriate time constant according to Requirement 6 for longitudinal and lateral acceleration maneuvers. The first vertical dashed lines are located 0.3 $[s]$ after the respective command. Because the interceptor reaches more than 90 [%] of the commanded acceleration in this time, the achieved time constant is smaller than the desired $T = 0.1\,[s]$. In addition, it is shown that the controlled interceptor does not exceed the overshoot threshold of Requirement 6. It is displayed by the outer horizontal dashed lines embracing a commanded acceleration value. The requirements given in Chapter 5 concerning settling time and settling range of the acceleration commanded, which are visualized by the vertical dashed line 0.5 $[s]$ after the respective command and the inner horizontal dashed lines embracing a command acceleration value, are fulfilled. The close-up view of $\left(a_Y^P\right)_{B,woG}^{II}$ underpins the results vividly.
In the nominal case at the high velocity scenario, $z_{1,Yaw}$ and $z_{1,Pitch}$ exhibit maximum values of $0.5\,[m/s^2]$ during the injection of a step input command. 1 $[s]$ after injection of an acceleration command, $z_{1,Yaw}$ and $z_{1,Pitch}$ are significantly below $0.2\,[m/s^2]$. This high tracking accuracy

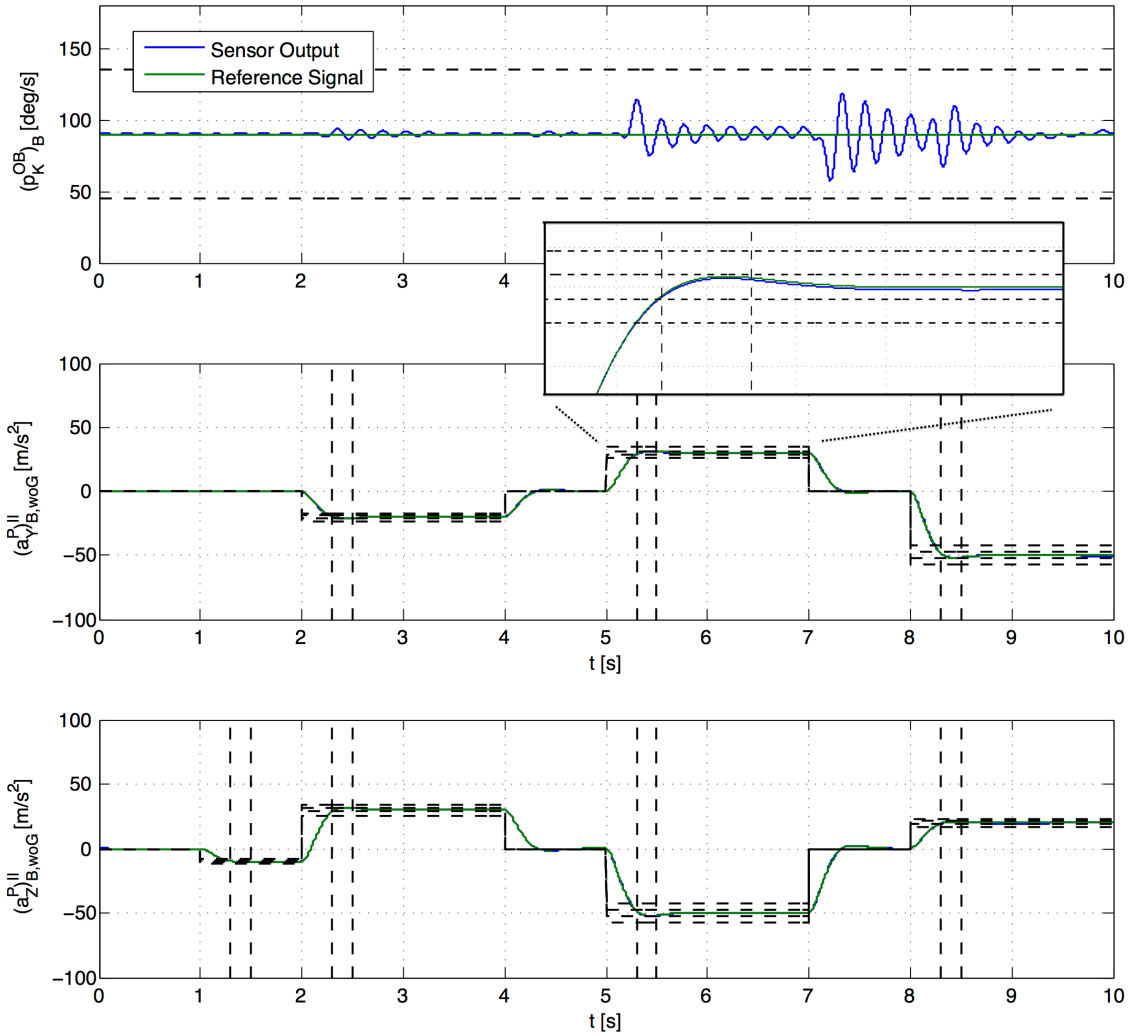

Figure 6.2: Interceptor performance in the nominal case at high velocity scenario

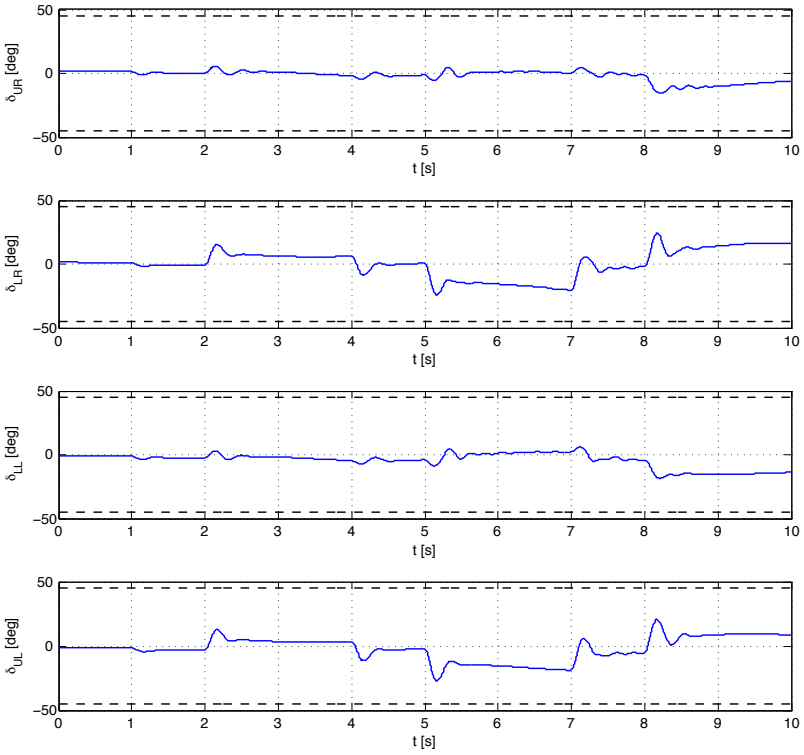

Figure 6.3: δ_{UR}, δ_{LR}, δ_{LL}, and δ_{UL} in the nominal case at high velocity scenario

with respect to the known, smooth, and bounded reference signals, generated by the linear time invariant systems acting as command filter, is also visible in the close-up view of the center diagram in Figure 6.2. As mentioned beforehand, it displays $\left(a_Y^P\right)^{II}_{B,woG}$ as the blue line and $\left(a_Y^P\right)^{II}_{B,woG,Flt}$ by the green line. Additionally, the thresholds of Requirement 6 are shown. The two signals nearly coincide.

Requirement 7 is evaluated for the high velocity scenario by using Figure 6.3. It depicts the positions of the aerodynamic control surfaces in the considered case. It is evident that the aerodynamic control surface actuator modules are driven by the control allocation. This contributes to the fulfillment of Requirement 7. Second, Figure 6.3 illustrates that the aerodynamic control surfaces are not reaching their position limit given in (2.58). The position limit is visualized for each aerodynamic control surface by the horizontal dashed lines. In the investigated situation, no reaction jet cartridges are consumed. The acceleration command sequence injected into the control strings is of operational relevance, but does not contain any commands which make the employment of both actuator sections of the interceptor necessary. The aerodynamic control surfaces realize the desired accelerations sufficiently fast and the acceleration control systems track the reference signals so precise that $\delta_{Mag,Cmd,RJC}$ stays significantly below the threshold of (5.34). Hence, Requirement 7 is fulfilled.

The last result underpins the considerations presented during the derivation of the allocation algorithm in Chapter 5. The $\left(a_Y^P\right)^{II}_{B,woG,Cmd}$ and $\left(a_Z^P\right)^{II}_{B,woG,Cmd}$ sequence displayed in Figure 6.1 would imply a permanent employment of the reaction jet actuator section, resulting in an excessive reaction jet cartridge consumption, if an optimization based allocation algorithm would have been used. The implementation of daisy chaining with the reaction jet actuator section exhibiting the highest actuator priority would have lead to the identical result. Therefore, the

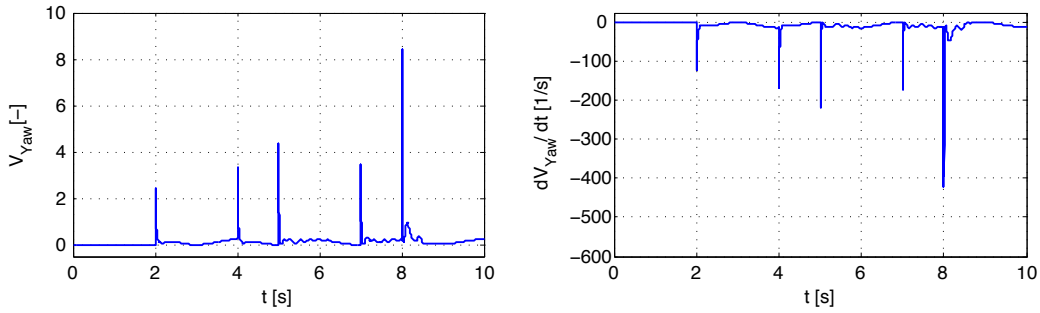

Figure 6.4: V_{Yaw} and $\dot{V}_{Yaw}$ in the nominal case at high velocity scenario

straightforward allocation algorithm is superior to standard allocation algorithms in this special application.
The functioning of the control systems regarding the theoretical background of Chapter 4 is available from Figure 6.4. It shows the Lyapunov function of the yaw acceleration control system V_{Yaw}, given by (4.223), in the left diagram and its derivative $\dot{V}_{Yaw}$ according to (4.272) in the right diagram. As anticipated, $V_{Yaw} \geq 0$ and $\dot{V}_{Yaw} \leq 0$. In addition, the following insight is revealed by Figure 6.4, pointing out the introduced theory. If an input command is given, V_{Yaw} and $\dot{V}_{Yaw}$ are diverted from zero, due to the initially existing $z_{1,Yaw}$ and $z_{2,Yaw}$. Because $\dot{V}_{Yaw} \leq 0$, V_{Yaw} is decreased. The designed control law (4.270) drives $z_{1,Yaw} \to 0$ and $z_{2,Yaw} \to 0$, resulting in $\dot{V}_{Yaw} \to 0$, as shown in the right half of Figure 6.4. V_{Yaw} reaches its steady-state when $\dot{V}_{Yaw} = 0$. The respective parameter estimates reach their steady-state with $z_{1,Yaw}$ and $z_{2,Yaw}$ disappearing. The steady-state value of V_{Yaw} origins from the remaining parameter errors in this situation. Hence, the control systems work as desired.
Summarizing the achieved results, the designed interceptor flight control system fulfills all given requirements in the nominal case at the chosen high velocity scenario. Because the requirements stated in Chapter 5 are not limited to this scenario, the low velocity scenario is investigated now.

Interceptor performance in the nominal case at low velocity scenario
The analysis for the low velocity scenario, given by $(V^G_{K,Abs})^I_{B,IC} = 400\,[m/s]$ and $\left(z^G\right)_{I,IC} = 10000\,[m]$, follows the scheme developed and employed for the high velocity scenario. Initially, the performance of the plant model in the interceptor flight control system is assessed. Because the signals inside the plant model differ from the signals of the interceptor at a rate clearly below 1 [%], the plant model is accepted as a valid representation of the interceptor and its signals are used in the control subsystems.
Figure 6.5 shows the interceptor performance in the nominal case at the low velocity scenario, meaning $\left(p_K^{0B}\right)_B$, $\left(a_Y^P\right)^{II}_{B,woG}$, and $\left(a_Z^P\right)^{II}_{B,woG}$ are plotted for the terminal flight phase. The signals gathered by the internal sensor system are displayed by the blue lines. The green lines depict the respective reference signals. Following Figure 6.2, the given requirements are illustrated by horizontal and vertical dashed lines.
The upper diagram of Figure 6.5 shows that $\left(p_K^{0B}\right)_B$ oscillates more than during the high velocity scenario considered above. During eleven oscillations $\left(p_K^{0B}\right)_B$ leaves the specified thresholds according to Requirement 5, but the interceptor keeps sufficient $\left(p_K^{0B}\right)_B$ to provide availability of reaction jet cartridges. If $\left(p_K^{0B}\right)_B$ would disappear completely, the usability of the reaction jet actuator section would be endangered. The center diagram displays that the controlled interceptor achieves a time constant for lateral acceleration maneuvers smaller than the specified

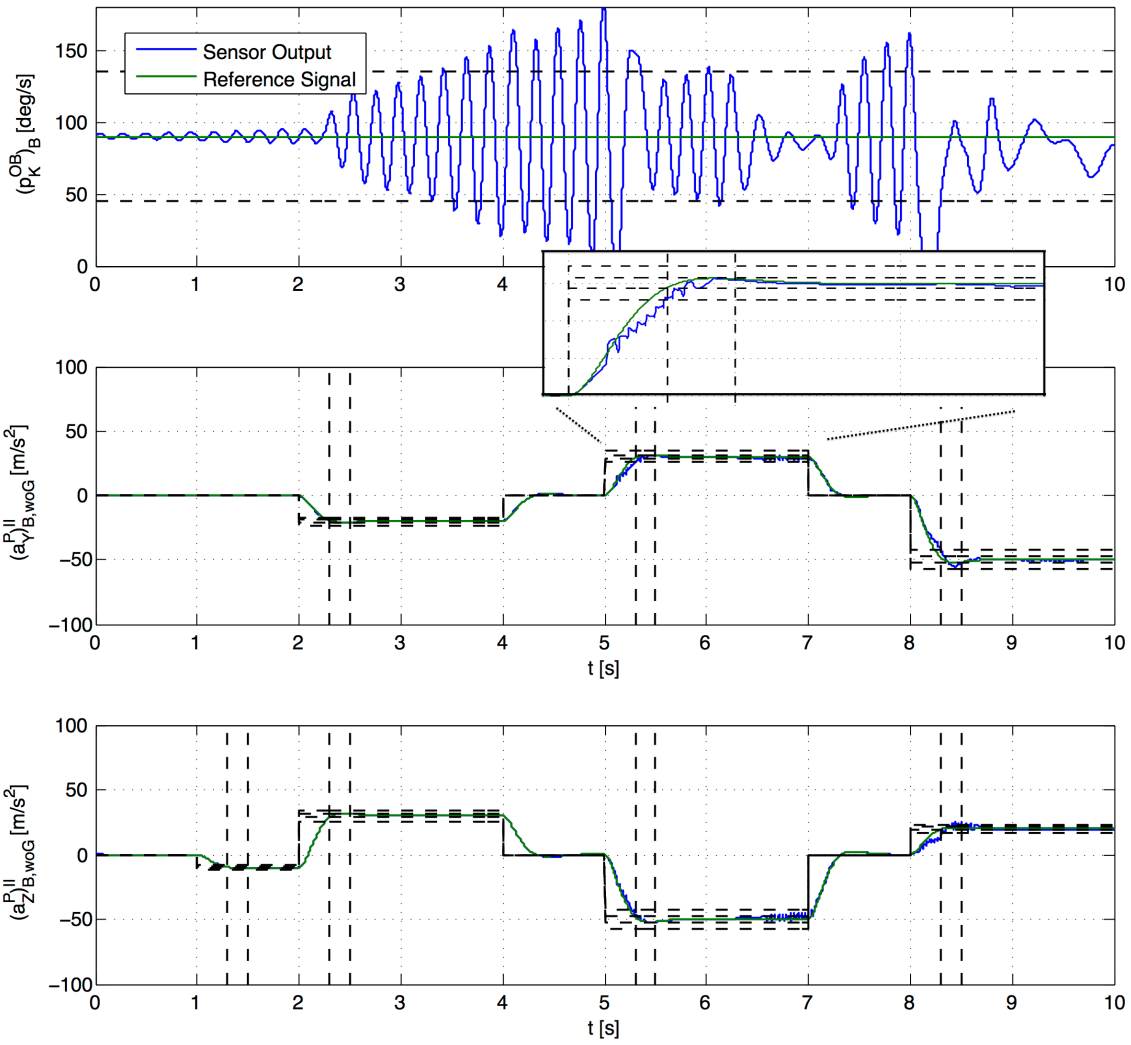

Figure 6.5: Interceptor performance in the nominal case at low velocity scenario

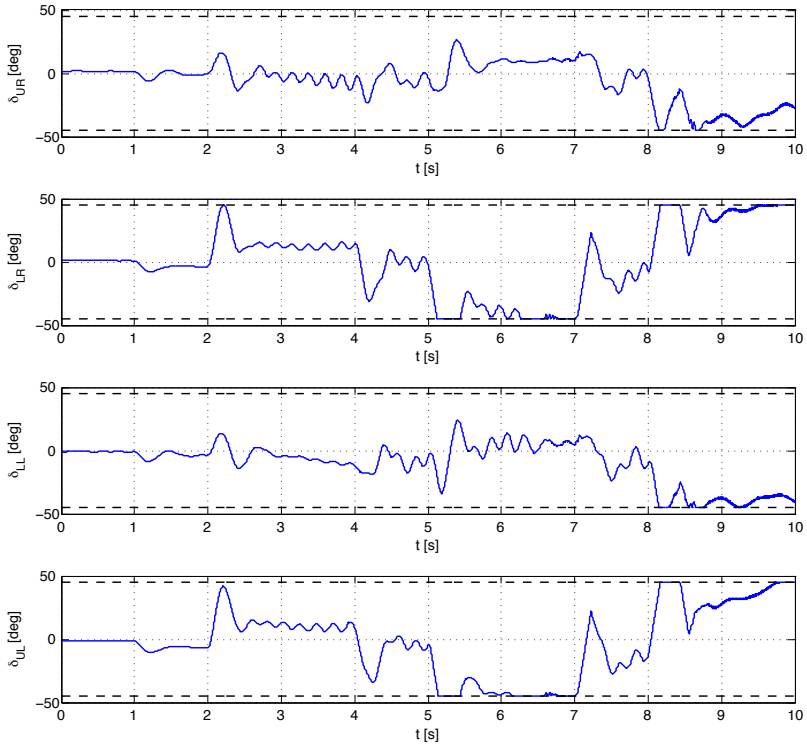

Figure 6.6: δ_{UR}, δ_{LR}, δ_{LL}, and δ_{UL} in the nominal case at low velocity scenario

$T = 0.1\,[s]$. More than $90\,[\%]$ of the acceleration command are achieved $0.3\,[s]$ after the individual commands. The close-up view vividly illustrates the details. The overshoot of $\left(a_Y^P\right)^{II}_{B,woG}$ does not exceed the given threshold of $15\,[\%]$ and the settling time as well as the settling range requirements are met. Therefore, the interceptor fulfills Requirement 6 for lateral acceleration maneuvers. The lower diagram of Figure 6.5 shows the results for the longitudinal acceleration performance. On one occasion, the reaction jet actuator section is used to control the interceptor back to the desired settling range. During the last acceleration command, the overshoot threshold is exceeded for $0.01\,[s]$ and the desired settling range is achieved with a delay of $0.05\,[s]$. Thereafter, the reference signal is tracked with high precision. Based on their endurance, these violations of the given requirements are considered as negligible with respect to the interceptor operational performance. Besides the details with regard to time constant, overshoot, settling time, and settling range, the close-up view indicates that the tracking errors are increased in this situation and that reaction jet cartridges are consumed.
The maximum $z_{1,Yaw}$ and $z_{1,Pitch}$ observed during the terminal flight phase in the nominal case at the low velocity scenario are $8.5\,[m/s^2]$. Referring back to (5.34), these errors are the reason for the employment of the reaction jet actuator section. $z_{1,Yaw}$ and $z_{1,Pitch}$ are reduced clearly below $1\,[m/s^2]$ $0.5\,[s]$ after an acceleration command has been injected. A high tracking accuracy is achieved during the steady-state, as recognizable from the close-up view in Figure 6.5.
The analysis of the aerodynamic control surface positions via Figure 6.6 reveals the reason behind the larger tracking errors occurring during the terminal flight phase. It is evident from Figure 6.6 that the aerodynamic control surfaces are driven by the control allocation, but reach their position limit (2.58), indicated by the horizontal dashed lines in the individual diagrams. Due to the decreased $(V^G_{K,Abs})^I_B$, implying a reduced $\bar{q}$, the aerodynamic control surface effectivity is diminished. The relationship is available from (2.11), (2.21), (2.36) to (2.38), and (2.47) to

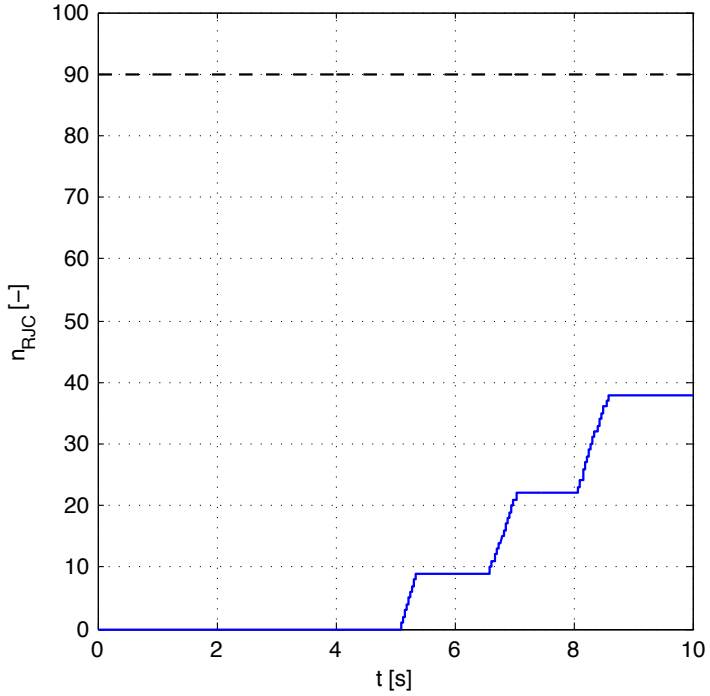

Figure 6.7: Reaction jet cartridge consumption in the nominal case at low velocity scenario

(2.52). Although the aerodynamic control surfaces are fully actuated, the interceptor is not able to follow the reference signals, leading to the increased $z_{1,Yaw}$ and $z_{1,Pitch}$. The control allocation therefore employs the reaction jet actuator section according to its design in Chapter 5 to decrease the tracking error. Reaction jet cartridges are consumed. In total, $n_{RJC} = 38$ reaction jet cartridges are fired in the considered situation, resulting in the superior tracking accuracy noticeable in the close-up view of Figure 6.5. This view allows to identify the individual firings of reaction jet cartridges and their positive effects with respect to tracking. Figure 6.7 illustrates the reaction jet cartridge consumption during the terminal flight phase of the interceptor. In terms of the requirements, the illustrated behavior implies the fulfillment of Requirement 7, due to the fact that both actuator sections of the interceptor are employed and the reaction jet cartridge consumption stays below the specified threshold.
Investigating the nominal case at the low velocity scenario concerning the theoretical background of Chapter 4 leads to the identical result as for the high velocity scenario. The control system works as desired. Hence, the designed interceptor flight control system fulfills nearly all requirements in the nominal case at the low velocity scenario. An operational relevant performance is achieved.
The derived results for the low velocity scenario indicate that the reaction jet actuator section in conjunction with the designed interceptor flight control system increases the operationally utilizable flight envelope of the interceptor. While at higher $(V^G_{K,Abs})^I_B$ the aerodynamic actuator section is sufficient to achieve the longitudinal and lateral acceleration maneuver requirement, the reaction jet actuator section realizes a significant part of the desired maneuverability at lower $(V^G_{K,Abs})^I_B$. Overall, the performance of the interceptor at lower $(V^G_{K,Abs})^I_B$ is adequate to fulfill nearly all the requirements and therefore, finally, leads to accomplishment of the interceptor mission in reality. Vice versa, the interceptor seems not being able to operate according to the requirements at the low velocity scenario without the reaction jet actuator section. This would

mean that the operational interceptor flight envelope would reduce to regions with sufficiently high $(V^G_{K,Abs})^I_B$. If it is proven that the combination of reaction jet actuator section and interceptor flight control system enlarges the operational interceptor flight envelope, the design derived in this thesis would provide a huge benefit for the employment of missiles like the interceptor. For this reason, the low velocity scenario is considered in the following without the reaction jet actuator section.

Interceptor performance in the nominal case at low velocity scenario without reaction jet actuator section

In the following paragraphs, the interceptor performance in the nominal case at the low velocity scenario without the reaction jet actuator section is investigated. Although situations in which the reaction jet actuator section are deliberately deactivated do not constitute an operational configuration, this analysis is of importance to verify the thesis that the combination of this actuator and the interceptor flight control system enhance the usable interceptor flight envelope. Besides the artificial negligence of the reaction jet actuator section, all parameters of and commands provided to the interceptor remain without changes.

The initial step of the analysis shows that the plant model inside the interceptor flight control system and the interceptor deviate not more than $1\,[\%]$ regarding the individual signals. This deviation allows to use the signals of the plant model inside the control subsystems.

Proceeding further from this result, the performance of the controlled interceptor is evaluated under these circumstances via Figure 6.8. It illustrates $\left(p^{0B}_K\right)_B$, $\left(a^P_Y\right)^{II}_{B,woG}$, and $\left(a^P_Z\right)^{II}_{B,woG}$ measured by the internal sensor system as well as the respective reference signals.

$\left(p^{0B}_K\right)_B$, which is plotted in the upper diagram of Figure 6.8, initially exhibits the identical oscillations as in the case with activated reaction jet actuator section. At a certain point of time, the performance concerning $\left(p^{0B}_K\right)_B$ deteriorates completely. Besides during the oscillations, $\left(p^{0B}_K\right)_B$ leaves the boundaries given by Requirement 5 for two extended periods. The center and lower diagram of Figure 6.8 display the performance of $\left(a^P_Y\right)^{II}_{B,woG}$ and $\left(a^P_Z\right)^{II}_{B,woG}$. During the first half of the terminal flight phase, the controlled interceptor demonstrates an appropriate time constant, which is recognizable from the displayed vertical dashed lines $0.3\,[s]$ after the individual commands. In the second half of the flight, the time constant drastically increases to maximum values of $T \approx 0.2\,[s]$; Requirement 6 is not met. The overshoot exceeds the given threshold on three occasions in the second half of the terminal flight phase. In addition, the controlled interceptor is no longer able to stay inside the desired settling range of $\pm 5\,[\%]$ of the acceleration command. Requirement 6 is also not fulfilled from this perspective.

$z_{1,Yaw}$ and $z_{1,Pitch}$ show maximum values of $15\,[m/s^2]$. After the reference signals have reached their steady-state, up to $8\,[m/s^2]$ remain. Compared to the situation analyzed beforehand, the maximum tracking errors are increased approximately by the factor two and the steady-state errors are more than ten times greater, showing that the performance of the controlled interceptor has been dramatically reduced.

The aerodynamic control surfaces are driven by the designed control allocation. Identical to the beforehand considered case, they reach their position limit according to (2.58). Because the reaction jet cartridges are deactivated, no further actuator supporting the aerodynamic control surfaces exists and they remain at their maximum deflection until the commanded acceleration is achieved. The periods in which the aerodynamic control surfaces are deflected to their maximum are significant. Figure 6.9 depicts δ_{LR} during the terminal flight phase. It is obvious from the diagram that δ_{LR} is at its position limit during extensive periods. The deflection of the aerodynamic control surfaces to the limit (2.58) is also the reason for $\left(p^{0B}_K\right)_B$ deteriorating. While all control surfaces are at their maximum position, the aerodynamic actuator section has

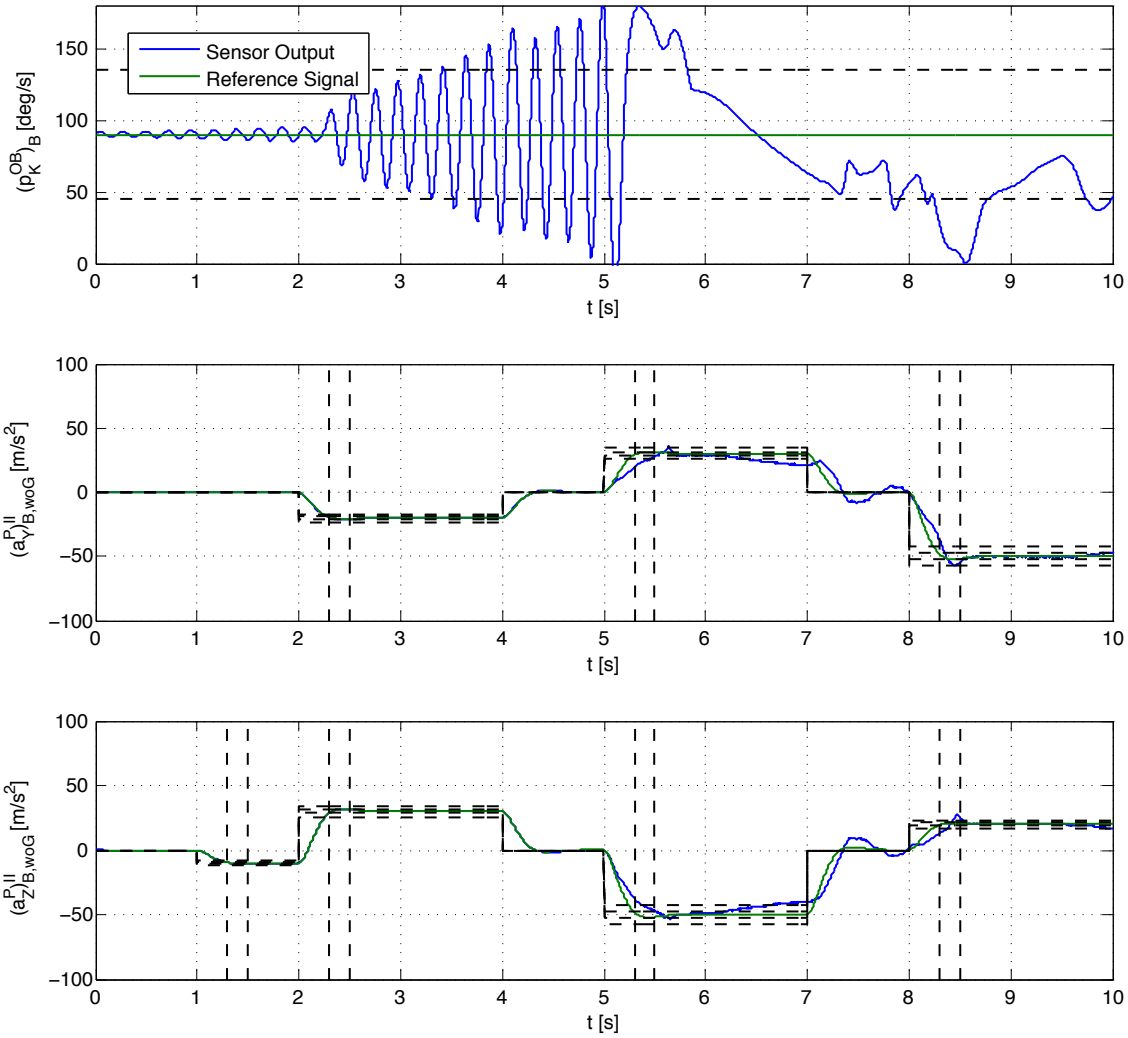

Figure 6.8: Interceptor performance in the nominal case at low velocity scenario without reaction jet actuator section

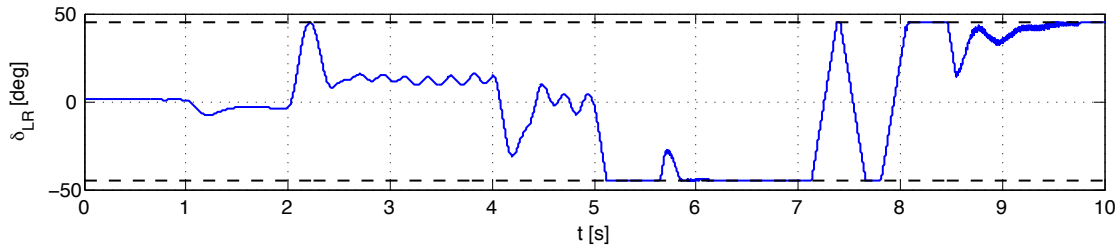

Figure 6.9: δ_{LR} in the nominal case at low velocity scenario without reaction jet actuator section

no capability left to sustain $\left(p_K^{0B}\right)_B$.
The presented results allow the conclusion that the controlled interceptor is not capable to fulfill the given requirements in the nominal case at the low velocity scenario without the reaction jet actuator section. The observed tracking errors give rise to doubts that the interceptor is able to accomplish its mission in the considered situation. Hence, without the reaction jet actuator section, the low velocity scenario can not be exploited from an operational point of view. On the other hand, the above conducted analysis at $(V_{K,Abs}^G)_{B,IC}^I = 400\,[m/s]$ and $\left(z^G\right)_{I,IC} = 10000\,[m]$ with the reaction jet cartridges activated showed that the controlled interceptor is able to achieve the requirements of Chapter 5. These two results imply that the combination of reaction jet actuator section and interceptor flight control system enlarges the usable interceptor flight envelope, as anticipated earlier. Therefore, the design derived in this thesis provides a large benefit for the operational employment of configurations like the interceptor.
This constitutes a profound basis for the further exploration of the capabilities of the interceptor flight control system. Because the deactivation of the reaction jet actuator section has been artificial, does not constitute the operational configuration, and has been conducted only proof the benefit of the derived design, it is not considered any further in the upcoming work. Instead, parameter uncertainties are introduced now. The following section considers uncertain constant parameters, where two different situations of such uncertainties are covered.

6.2 Performance in case of uncertain constant parameters

6.2.1 Total interceptor mass

After the nominal case has been analyzed in the preceding section, the controlled interceptor is tested and evaluated in the presence of uncertain constant parameters. Two different uncertain constant parameter situations are considered. First, the total interceptor mass constitutes the uncertain constant parameter. Thereafter, the reaction jet cartridge thrust profile deviates from the nominal profile.
As introduced in Chapter 2, the interceptor is propelled by a single stage, solid propellant rocket motor. It provides the interceptor with the ability to lift off from its static launch point, accelerate, and reach an aerodynamic flight. After burn out of the single stage, solid propellant rocket motor, the aerodynamic drag acting on the interceptor decelerates the latter persistently, resulting in a limited range.
In the nominal case, the solid propellant contained in the single stage rocket motor is consumed completely. The resulting total interceptor mass is given by (2.6). (2.7) states the respective inertia tensor with respect to the center of gravity of the interceptor. Because the consumption of the solid propellant is neither controlled nor monitored, which implies that the complete burn out of the single stage rocket motor is not guaranteed, it is possible that parts of the solid propellant remain. In addition, although all interceptor subsystems are specified concerning their mass and inertia properties, these properties are only guaranteed inside respective tolerances.
Comparing both effects, it is clear that the remaining solid propellant mass is lower bounded by zero; the nominal case. If the nominal case is not realized, the remaining solid propellant mass might take considerable sizes, based on the fact that, following [59], missiles may comprise up to 50 [%] of their total mass as solid propellant. Vice versa, the mass of the interceptor subsystems varies inside tolerances, implying an increase or decrease, whereupon the boundaries of the interval is well known from the individual subsystem specification. With regard to magnitude, the mass tolerances of the interceptor subsystems are at least one order smaller than the remaining solid propellant mass value range.
The illustrated circumstances lead to the fact that it is impossible to determine the total in-

terceptor mass at burn out condition of the single stage, solid propellant rocket motor exactly. Therefore, the total interceptor mass is considered as an uncertain constant parameter and the evaluation of the performance of the controlled interceptor under these conditions allows an assessment of the capabilities of the interceptor flight control system concerning the application to a real system.

Uncertain total interceptor mass implementation

The implementation of uncertain constant parameters according to Chapter 2 is employed. The level of uncertainty of the total interceptor mass $\Delta p_{m_{Empty}}$ is defined as given in (6.1), whereupon this value incorporates the effect of remaining solid propellant as well as varying interceptor subsystem masses.

$$\Delta p_{m_{Empty}} = 10\,[\%] \tag{6.1}$$

(2.61) is used to calculate the perturbed total interceptor mass $\tilde{m}_{Empty}$. Based on the considerations concerning the sign and the size of the individual effects influencing the total interceptor mass, it is ensured that $\tilde{m}_{Empty}$ is always greater than m_{Empty} provided in (2.6). In contrast, m_{Empty} utilized in the plant model inside the interceptor flight control system stays according to the nominal value. This ensures that the total interceptor mass constitutes an uncertain constant parameter during the terminal flight phase of the interceptor.

Besides the total interceptor mass, the inertia tensor with respect to the center of gravity of the interceptor, specified in the body fixed frame, is considered as uncertain constant parameter to account for the fact that the inertia changes, if the total interceptor mass and its distribution varies. The level of uncertainty of the inertia tensor $\Delta p_{\left(I^G_{Empty}\right)_{BB}}$ is set according to (6.2).

$$\Delta p_{\left(I^G_{Empty}\right)_{BB}} = 10\,[\%] \tag{6.2}$$

The perturbed inertia tensor with respect to the center of gravity of the interceptor, specified in the body fixed frame, $(\tilde{I}^G_{Empty})_{BB}$ is calculated via (2.61). $(\tilde{I}^G_{Empty})_{BB}$ is utilized in the interceptor, while $(I^G_{Empty})_{BB}$ according to (2.7) is implemented in the plant model inside the interceptor flight control system.

Multiple $\tilde{m}_{Empty}$ and $(\tilde{I}^G_{Empty})_{BB}$ are tested, but only one specific example is presented herein to stay inside the scope of this thesis. In this specific example, $\tilde{m}_{Empty}$ is given by (6.3). (6.4) states the respective $(\tilde{I}^G_{Empty})_{BB}$.

$$\tilde{m}_{Empty} = 156.35\,[kg] \tag{6.3}$$

$$\left(\tilde{I}^G_{Empty}\right)_{BB} = \begin{bmatrix} 5.05 & 0 & 0 \\ 0 & 403.76 & 0 \\ 0 & 0 & 403.76 \end{bmatrix} [kgm^2] \tag{6.4}$$

The other properties of the interceptor remain in accordance with Chapter 2. The parameters of the interceptor flight control system follow Chapter 5 and are identical to the nominal case. All adaptation algorithms designed are activated. The high velocity scenario, defined by $(V^G_{K,Abs})^I_{B,IC} = 600\,[m/s]$ and $\left(z^G\right)_{I,IC} = 10000\,[m]$, as well as the low velocity scenario are considered. Based on Requirement 5, $\left(p^{0B}_K\right)_{B,Cmd} = 90\,[deg/s]$. Figure 6.1 illustrates the $\left(a^P_Y\right)^{II}_{B,woG,Cmd}$ and $\left(a^P_Z\right)^{II}_{B,woG,Cmd}$ sequence. By using the identical command sequence as in the nominal case, the results become comparable.

Performance in case of uncertain total interceptor mass at high velocity scenario

Following the nominal case, the signals of the plant model are compared with the signals of the

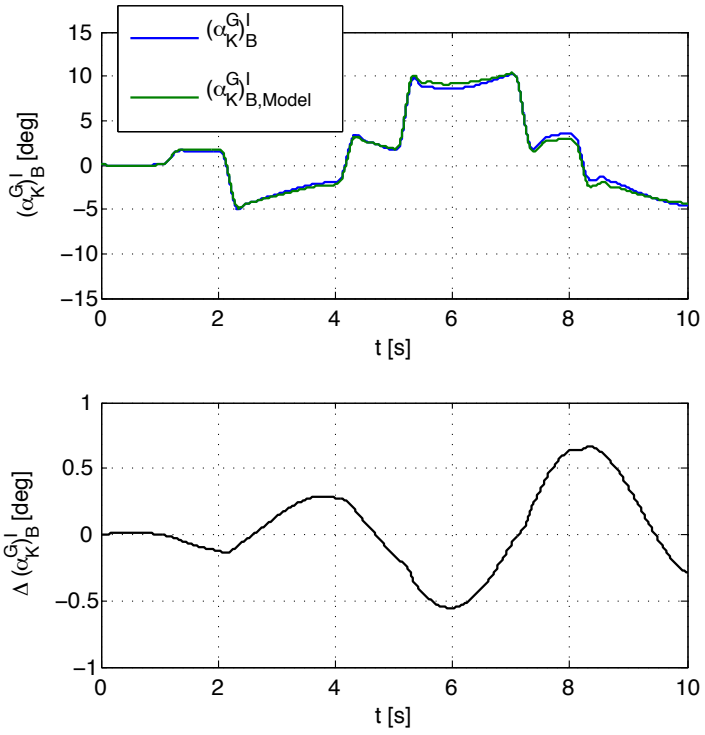

Figure 6.10: $(\alpha_K^G)_B^I$ and $\Delta(\alpha_K^G)_B^I$ in case of uncertain total interceptor mass at high velocity scenario

interceptor, first. The comparison reveals that the respective signals deviate. This originates from the fact that the properties of the plant model differ from the properties of the interceptor. The plant model constitutes a dynamical system which exhibits different parameters than the interceptor dynamical system. Hence, different dynamics result. Figure 6.10 illustrates the angle of attack $(\alpha_K^G)_B^I$ of the plant model as well as of the interceptor and the deviation of these variables $\Delta(\alpha_K^G)_B^I$. The upper diagram of Figure 6.10 displays $(\alpha_K^G)_B^I$, where the blue line constitutes $(\alpha_K^G)_B^I$ of the interceptor and the green line represents $(\alpha_K^G)_B^I$ of the plant model. The lower diagram shows $\Delta(\alpha_K^G)_B^I$. It is obvious from Figure 6.10 that $\Delta(\alpha_K^G)_B^I$ is negligibly small. The comparison of all signals of the plant model with the signals of the interceptor shows that the maximum deviation of two respective signals is approximately 10 [%]. This leads to the consideration of the plant model as a valid representation of the interceptor.
Proceeding with the evaluation of the performance of the controlled interceptor, it is assessed that Requirement 5 is fulfilled. $\left(p_K^{0B}\right)_B$ does not leave the boundaries imposed by Requirement 5. The fulfillment of Requirement 6 for $\left(a_Y^P\right)^{II}_{B,woG}$ is evident from Figure 6.11. It displays the $\left(a_Y^P\right)^{II}_{B,woG}$ performance of the controlled interceptor in this exemplary case of an uncertain total interceptor mass. $\left(a_Y^P\right)^{II}_{B,woG}$ demonstrates the required time constant, visualized in Figure 6.11 by the first vertical dashed line after a command. In addition, it is shown that the overshoot as well as the settling time and the settling range requirements which are visualized by vertical and horizontal dashed lines are met. The $\left(a_Z^P\right)^{II}_{B,woG}$ control string fulfills Requirement 6.
During the injection of the step input commands illustrated in Figure 6.1, $z_{1,Yaw}$ and $z_{1,Pitch}$ exhibit maximum values of 0.5 $[m/s^2]$ in presence of $\tilde{m}_{Empty}$ and $(\tilde{I}^G_{Empty})_{BB}$ according to (6.3) and (6.4). These values are identical to the nominal case. $z_{1,Yaw}$ and $z_{1,Pitch}$ are below 0.25 $[m/s^2]$

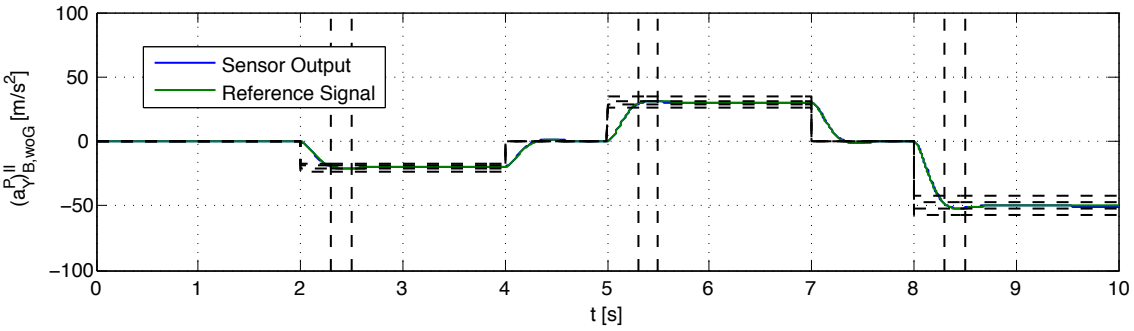

Figure 6.11: $\left(a_Y^P\right)^{II}_{B,woG}$ performance in case of uncertain total interceptor mass at high velocity scenario

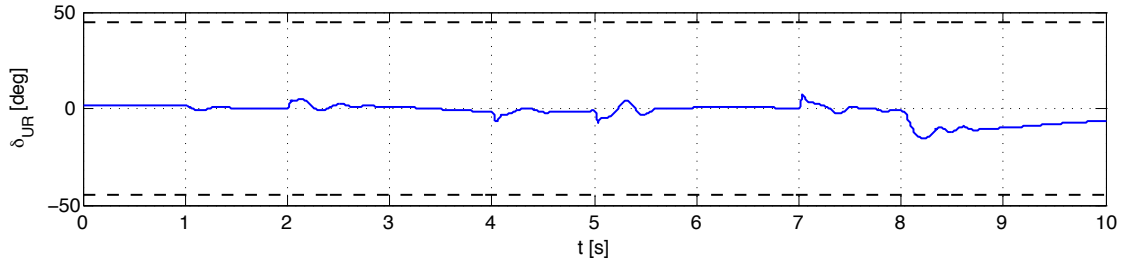

Figure 6.12: δ_{UR} in case of uncertain total interceptor mass at high velocity scenario

1 [s] after injection of the individual step input commands and $z_{1,Yaw}$ as well as $z_{1,Pitch}$ decrease slower than in the nominal case. The high tracking accuracy regarding the known, smooth, and bounded reference signals, although $\tilde{m}_{Empty}$ and $(\tilde{I}^G_{Empty})_{BB}$ are in effect, is underlined by Figure 6.11 in which the $\left(a_Y^P\right)^{II}_{B,woG}$ signal of the internal sensor system and the respective reference coincide.
The analysis of δ_{UR}, δ_{LR}, δ_{LL}, and δ_{UL} shows that none of the aerodynamic control surfaces is driven to its position limit (2.58). Figure 6.12, depicting δ_{UR} as well as the position limit, acts as an exemplary proof for this statement. As in the nominal case at the high velocity scenario, no reaction jet cartridges are consumed during the terminal flight phase of the interceptor. Therefore, Requirement 7 is fulfilled in this example.
The presented results lead to the assessment that the interceptor flight control system fulfills the specified requirements in the considered case of $\tilde{m}_{Empty}$ and $(\tilde{I}^G_{Empty})_{BB}$. In the next step, the low velocity scenario is accounted for.

Performance in case of uncertain total interceptor mass at low velocity scenario
For this step of the analysis, all properties of the interceptor as well as the parameters of the interceptor flight control system remain unchanged. As defined above, the scenario is given by $(V^G_{K,Abs})^I_{B,IC} = 400\,[m/s]$ and $\left(z^G\right)_{I,IC} = 10000\,[m]$. The $\left(a_Y^P\right)^{II}_{B,woG,Cmd}$ and $\left(a_Z^P\right)^{II}_{B,woG,Cmd}$ sequence is identical to Figure 6.1.
The comparison of the signals of the plant model and the respective signals of the interceptor leads to the result that the signals deviate; like above at the high velocity scenario. Although the deviations of the individual signals are different compared to the high velocity scenario, the signals of the plant model and the signals of the interceptor do not differ more than 10 [%]. The signals are used for the control subsystems.

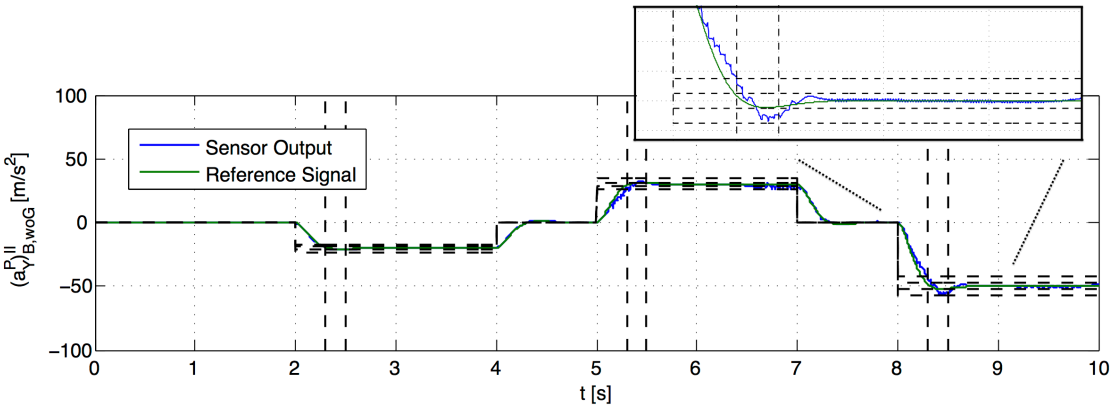

Figure 6.13: $\left(a_Y^P\right)^{II}_{B,woG}$ performance in case of uncertain total interceptor mass at low velocity scenario

As in the nominal case at the low velocity scenario, $\left(p_K^{0B}\right)_B$ oscillates more than for higher $(V^G_{K,Abs})^I_B$. On several occasions during these oscillations, $\left(p_K^{0B}\right)_B$ leaves the boundaries imposed by Requirement 5, but never deteriorates completely. A sufficient $\left(p_K^{0B}\right)_B$ always remains, enabling availability of unused reaction jet cartridges. The performance for $\left(a_Y^P\right)^{II}_{B,woG}$ is assessed using Figure 6.13. It shows $\left(a_Y^P\right)^{II}_{B,woG}$ measured by the internal sensor system as blue line and the $\left(a_Y^P\right)^{II}_{B,woG}$ reference signal as green line. It is evident from Figure 6.13, especially the close-up view, that the controlled interceptor demonstrates a time constant of $T = 0.1\,[s]$ and does not exceed the overshoot threshold. Once achieved, the interceptor stays in the settling range of $\pm 5\,[\%]$ of the acceleration command. Comparing Figure 6.13 with Figure 6.11, it becomes clear that the performance of the controlled interceptor for $\left(a_Y^P\right)^{II}_{B,woG}$ is nearly identical in both considered scenarios. The evaluation of the $\left(a_Z^P\right)^{II}_{B,woG}$ performance leads to the identical result.

The tracking errors, meaning $z_{1,Yaw}$ and $z_{1,Pitch}$, show maximum values of $8.5\,[m/s^2]$ for the considered $\tilde{m}_{Empty}$ and $(\tilde{I}^G_{Empty})_{BB}$ at $(V^G_{K,Abs})^I_{B,IC} = 400\,[m/s]$. $1\,[s]$ after each injected acceleration command, $z_{1,Yaw}$ and $z_{1,Pitch}$ are reduced to values below $2\,[m/s^2]$. Figure 6.14 depicts $z_{1,Yaw}$. The larger tracking errors during the transition phases lead to the employment of the reaction jet actuator section via the designed control allocation. A significant reduction of $z_{1,Yaw}$ and $z_{1,Pitch}$ results, as obvious for $\left(a_Y^P\right)^{II}_{B,woG}$ from the close-up view in Figure 6.13. This view also shows the high steady-state tracking accuracy achieved.

The aerodynamic control surfaces are deflected by the control allocation inside the interceptor flight control system. Like in the nominal case at the low velocity scenario, the control surfaces reach their position limit, given in (2.58), occasionally. δ_{UR} is visualized in Figure 6.15. The latter shows the two periods where δ_{UR} is at its position limit. The direct comparison of Figure 6.15 with Figure 6.12 reveals that this aerodynamic control surface, as an example for all surfaces, is deflected to a much greater extent at this scenario. The reduced aerodynamic control surface effectivity at $(V^G_{K,Abs})^I_{B,IC} = 400\,[m/s]$ constitutes the reason for this behavior. In addition to the control surfaces, the reaction jet actuator section is driven by the control allocation. The total number of $n_{RJC} = 33$ reaction jet cartridges is consumed during the terminal flight phase of the interceptor. Due to the fact that this number is below the imposed threshold and both actuator sections of the interceptor are employed, Requirement 7 is fulfilled for the low velocity

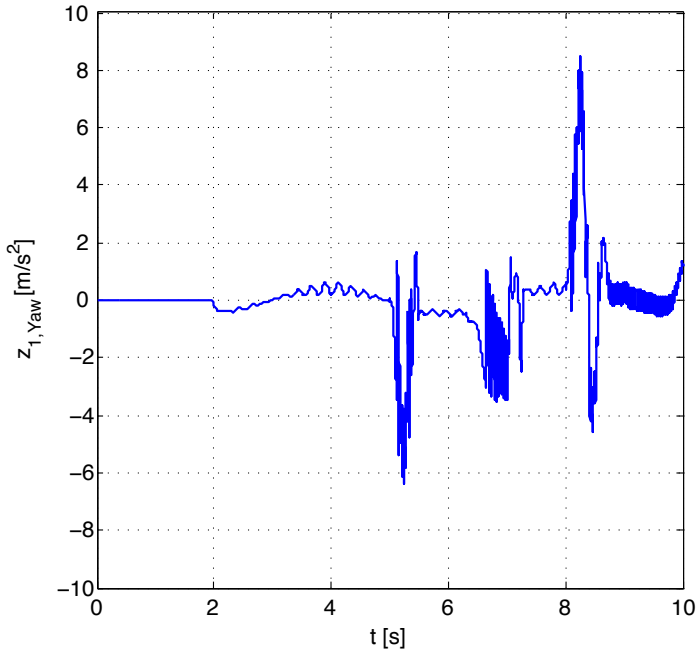

Figure 6.14: $z_{1,Yaw}$ in case of uncertain total interceptor mass at low velocity scenario

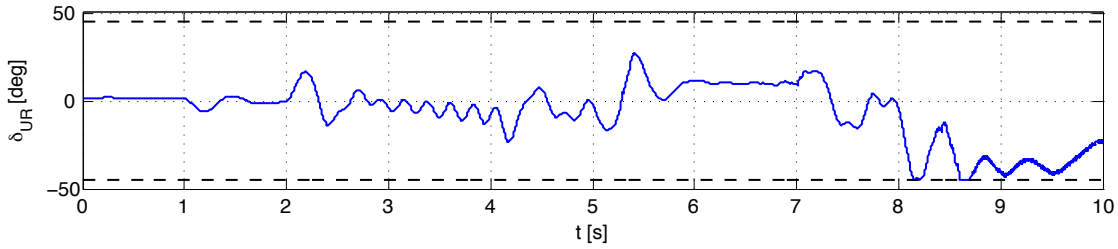

Figure 6.15: δ_{UR} in case of uncertain total interceptor mass at low velocity scenario

scenario in this example of $\tilde{m}_{Empty}$ and $(\tilde{I}^G_{Empty})_{BB}$.
The investigation of the designed control systems concerning their functioning in accordance with the theoretical background leads to a positive result. The Lyapunov functions as well as their derivatives behave as required. The individual parameter estimates reach steady-state values, once the errors z_i inside the control subsystems of the interceptor flight control system disappear.
Based on the presented results, it is assessed that the controlled interceptor fulfills nearly all given requirements for the introduced $\tilde{m}_{Empty}$ and $(\tilde{I}^G_{Empty})_{BB}$ at the low velocity scenario. Only Requirement 5 is violated occasionally. On the other hand, the controlled interceptor demonstrates a sufficient time constant and overshoot as well as a high tracking accuracy at the steady-state in its acceleration control strings. Because only a limited amount of reaction jet cartridges is consumed, the availability of the reaction jet actuator section is not endangered by the few occasions where Requirement 5 is not met. Therefore, it is concluded that the designed flight control system enables the interceptor to accomplish its mission at the low velocity scenario. In combination with the result derived for the high velocity scenario, this means that the interceptor flight control system is able to handle the $\tilde{m}_{Empty}$ and $(\tilde{I}^G_{Empty})_{BB}$ stated in (6.3) and (6.4).
Test with various combinations of $\tilde{m}_{Empty}$ and $(\tilde{I}^G_{Empty})_{BB}$, whereupon $\Delta p_{m_{Empty}}$ and $\Delta p_{\left(I^G_{Empty}\right)_{BB}}$ are given by (6.1) and (6.2), underpin this specific result. Therefore, the interceptor flight control system is capable to overcome uncertain total interceptor masses and uncertain inertias with respect to the center of gravity of the interceptor, specified in the body fixed frame, up to the considered $\Delta p_{m_{Empty}}$ and $\Delta p_{\left(I^G_{Empty}\right)_{BB}}$.

6.2.2 Reaction jet cartridge thrust force

The second uncertain constant parameter taken into consideration in this thesis, is the thrust force generated by the individual reaction jet cartridges. The rational behind this consideration are the various effects originating from the interaction of the reaction jet cartridge exhaust gases with the external airstream surrounding the interceptor. These effects lead to a resulting reaction jet cartridge thrust force which is dependent on the flight condition.
The investigation of the interaction effects generated by reaction jet injection in supersonic cross flow conditions and the consequences with respect to resulting forces and moments exhibits a long history. [147] is one of the first sources covering these topics. Besides other aspects of missile aerodynamics, the course containing [21] deals with the interaction effects and the consequences and relates these topics to missiles. Further publications are [14], [25], [26], [40], [78], [94], and [113]. While [14], [21], [40], [94], [113], and [116] consider missiles or projectiles as vehicle comprising the reaction jet, [25], [26], and [78] examine the interaction effects at a flat plate housing the reaction jet and experiencing the consequences of the reaction jet injection.
Following [78], the reaction jet injection in the external airstream surrounding the interceptor gives rise to a complex, three dimensional flow field, containing various shocks, vortices, and a flow separation area. As shown in the graphics in [78], [116], and [113], main components of the flow field are the separation shock lying in front of the reaction jet exhaust, the bow shock starting upfront of the reaction jet exhaust and bending downstream with the surrounding airstream, the barrel shock which is positioned downstream behind the bow shock and contains the reaction jet exhaust gases, and a set of vortices dominating the downstream flow behind the reaction jet exhaust. These main components of the flow field change the pressure distribution along the surface of the considered body. The changed pressure distribution leads to forces acting on the body that differ from the forces injected by the reaction jet. [116] presents such pressure

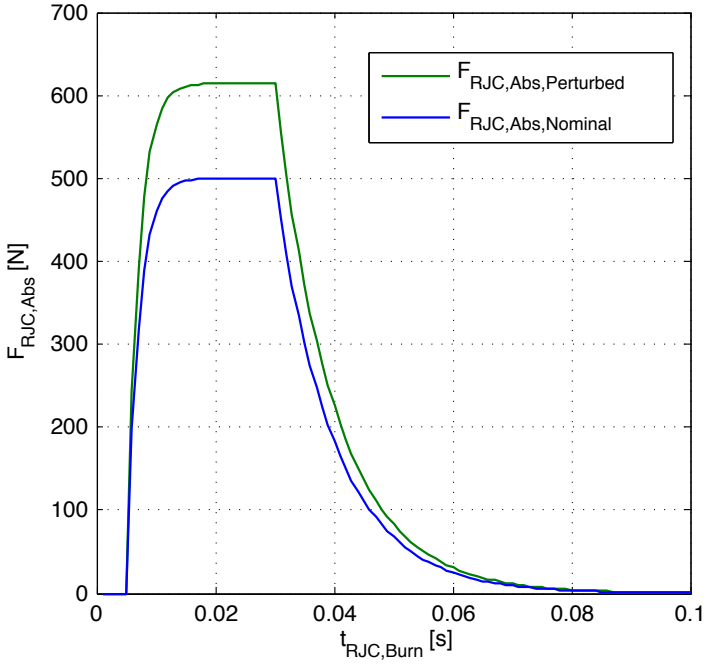

Figure 6.16: Nominal and perturbed reaction jet cartridge thrust profile

distributions.
Because the change in the pressure distribution is dependent on the flight condition, the influence of the latter on the forces injected by the reaction jet varies. This implies that forces acting on the body are dependent on the flight condition. As illustrated in these representative cases in [116], these acting forces can be significantly increased compared to the forces purely injected by the reaction jet.
Based on the fact that the pressure distribution along the surface of the interceptor is not modeled in this thesis, the reaction jet cartridge thrust force is accounted for as variable to implement the beforehand described effects. This choice allows to stay inside the scope of this work. Because the reaction jet cartridge thrust force deviates from the nominal reaction jet cartridge thrust force, which is utilized in the plant model, it constitutes an uncertain constant parameter.

Uncertain reaction jet cartridge thrust force implementation
The implementation of the uncertain reaction jet cartridge thrust force is done via the methodology presented in Chapter 2. Considering the influence of the flight condition as illustrated in [116], the level of uncertainty of the reaction jet cartridge thrust profile $\Delta p_{F_{RJC,Abs}}$ is defined according to (6.5).

$$\Delta p_{F_{RJC,Abs}} = 25\,[\%] \tag{6.5}$$

$\Delta p_{F_{RJC,Abs}}$ is employed in (2.61) to calculate the perturbed reaction jet cartridge thrust profile $\tilde{F}_{RJC,Abs}$ for the interceptor. The reaction jet cartridge thrust profile $F_{RJC,Abs}$ utilized in the plant model inside the interceptor flight control system remains in accordance with Chapter 2. Following earlier presentations, multiple $\tilde{F}_{RJC,Abs}$ profiles are tested, but only one specific example is illustrated herein. The $F_{RJC,Abs}$ profile is increased by 22.87 [%] in this specific example. Figure 6.16 illustrates the resulting reaction jet cartridge thrust profiles. The $F_{RJC,Abs}$ profile is displayed by the blue line, whereas the green line represents the $\tilde{F}_{RJC,Abs}$ profile. All other properties of the interceptor remain at the nominal values. The parameters of the intercep-

tor flight control system are adjusted as derived in Chapter 5. $(V^G_{K,Abs})^I_{B,IC} = 600\,[m/s]$ and $\left(z^G\right)_{I,IC} = 10000\,[m]$ describe the initial conditions of the high velocity scenario of the interceptor, whereas $(V^G_{K,Abs})^I_{B,IC} = 400\,[m/s]$ and $\left(z^G\right)_{I,IC} = 10000\,[m]$ represent the initial conditions of the low velocity scenario; $\left(p^{0B}_K\right)_{B,Cmd} = 90\,[deg/s]$. The $\left(a^P_Y\right)^{II}_{B,woG,Cmd}$ and $\left(a^P_Z\right)^{II}_{B,woG,Cmd}$ sequence is shown Figure 6.1.

Performance in case of uncertain reaction jet cartridge thrust force at high velocity scenario

The investigation of the nominal case as well as of the case of an uncertain total interceptor mass for the high velocity scenario showed that in neither of the two situations reaction jet cartridges are fired. The latter is also valid for the high velocity scenario in the presence of an uncertain reaction jet cartridge thrust force. The reaction jet actuator section is not employed; no reaction jet cartridges are fired during the terminal flight phase of the interceptor.

Because the implementation of the uncertain reaction jet cartridge thrust force implies that uncertainties exist only during the firing of reaction jet cartridges, the beforehand stated result means that the actually considered case is identical to the nominal case at the high velocity scenario. All results derived for this situation remain valid. The plant model constitutes a valid representation of the interceptor. The $\left(p^{0B}_K\right)_B$, $\left(a^P_Y\right)^{II}_{B,woG}$, and $\left(a^P_Z\right)^{II}_{B,woG}$ performance is identical to Figure 6.2. Excellent tracking accuracy is achieved by the controlled interceptor, and the aerodynamic control surfaces show the behavior illustrated in Figure 6.3. The statement on the functioning of the control systems with respect to the introduced methodologies in Chapter 4 as well as the exemplary visualization of V_{Yaw} and $\dot{V}_{Yaw}$ in Figure 6.4 remain valid.

The conclusion for the nominal case at the high velocity scenario is taken over. Therefore, the controlled interceptor fulfills all given requirements in the presence of the perturbed reaction jet cartridge thrust profile according to Figure 6.16 in this scenario. This result achieved, a detailed analysis is conducted for the low velocity scenario in the following. The latter encompasses the firing of reaction jet cartridges, meaning the implemented uncertainties are able to unfold their effects.

Performance in case of uncertain reaction jet cartridge thrust force at low velocity scenario

The first step of the analysis embraces the comparison of the signals of the plant model with the respective signals of the interceptor. The maximum deviation of two respective signals is $1\,[\%]$ during the terminal flight phase of the interceptor. Comparing this maximum deviation with the situations considered earlier, it is found that this maximum deviation is significantly smaller than in the case of an uncertain total interceptor mass and of the same magnitude as in the nominal case. This behavior originates from the already beforehand stated fact that the introduced uncertain constant parameter does not permanently exist in the system. It is only present in the system, if reaction jet cartridges are utilized. If no reaction jet cartridges are actually fired, parameter uncertainties are absent. The plant model and the interceptor exhibit identical properties during these phases of the terminal flight phase, implying that the uncertain reaction jet cartridge thrust force does not affect the system to the same degree as an uncertain total interceptor mass. Given these considerations as well as the observed maximum deviation of two respective signals of $1\,[\%]$, the plant model is identified as a valid representation of the interceptor.

Now, the performance of the controlled interceptor is evaluated. The comparison of $\left(p^{0B}_K\right)_B$ with the boundaries given by Requirement 5 shows that the latter is fulfilled, except on a few occasions where $\left(p^{0B}_K\right)_B$ is oscillating. This behavior is identical to the earlier analyzed low velocity

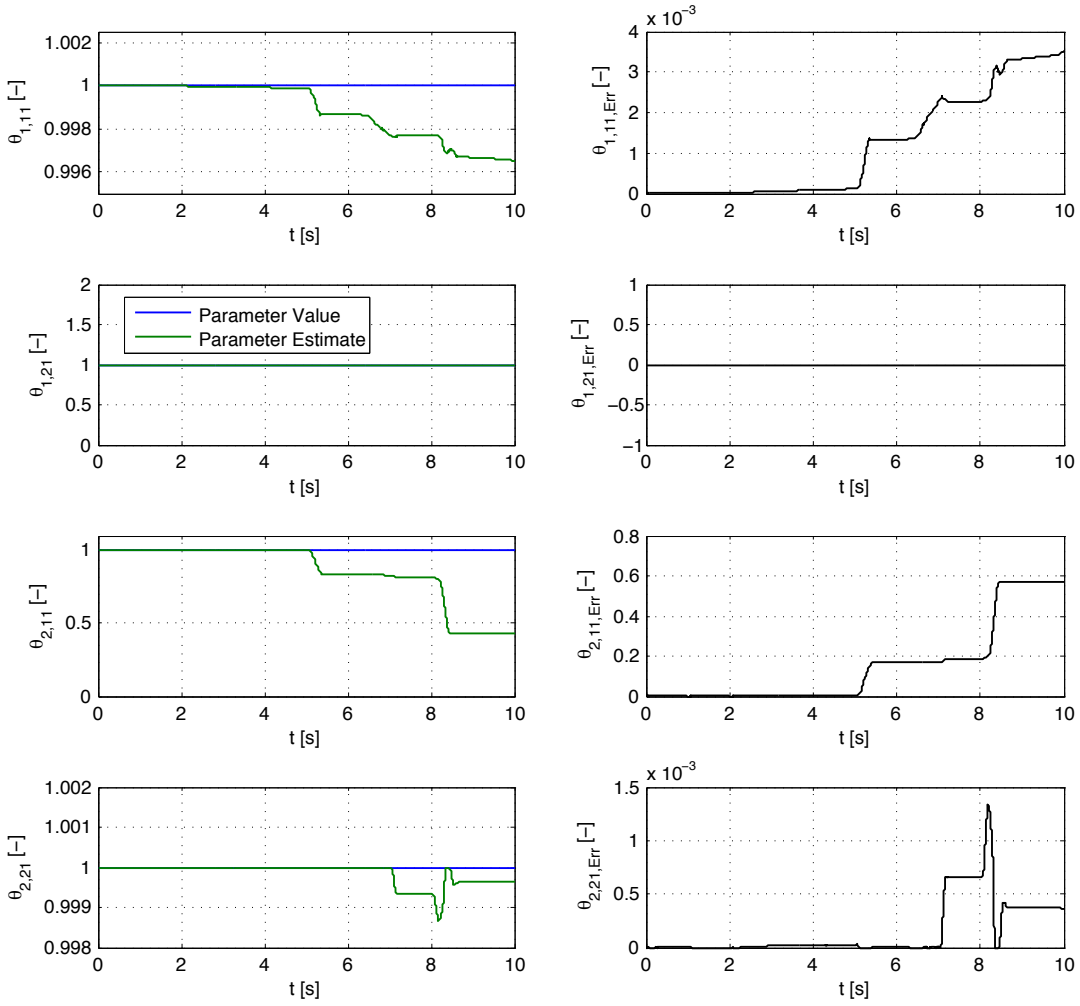

Figure 6.17: $\dot{\hat{\vec{\theta}}}_1$ and $\dot{\hat{\vec{\theta}}}_2$ update law performance in case of uncertain reaction jet cartridge thrust force at low velocity scenario

scenarios. $\left(a_Y^P\right)_{B,woG}^{II}$ and $\left(a_Z^P\right)_{B,woG}^{II}$ demonstrate the required time constant. In addition, the overshoot of $\left(a_Y^P\right)_{B,woG}^{II}$ stays below the threshold given by Requirement 6. On three occasions, $\left(a_Z^P\right)_{B,woG}^{II}$ exceeds the given overshoot threshold for approximately 0.01 $[s]$ by 3.5 $[m/s^2]$. Based on the duration of these violations, the latter are neglected from the perspective of requirements fulfillment. Furthermore, the desired settling time to the desired settling range is achieved by $\left(a_Y^P\right)_{B,woG}^{II}$ and $\left(a_Z^P\right)_{B,woG}^{II}$ with the used $\tilde{F}_{RJC,Abs}$ profile.
$z_{1,Yaw}$ and $z_{1,Pitch}$ show a behavior similar to the nominal case, underpinning the earlier consideration concerning the intermittent existence of the uncertain constant parameter. During injection of the step input commands, $z_{1,Yaw}$ and $z_{1,Pitch}$ reach maximum values of 8.5 $[m/s^2]$. 1 $[s]$ after the respective step input command, $z_{1,Yaw}$ and $z_{1,Pitch}$ are significantly below 1 $[m/s^2]$. Because of the similarities to the nominal case, a figure displaying the performance of the controlled interceptor in case of uncertain reaction jet cartridge thrust force is omitted here.

Instead, Figure 6.17 illustrates the performance of the update laws for $\dot{\hat{\vec{\theta}}}_1$ and $\dot{\hat{\vec{\theta}}}_2$ in the interceptor pitch acceleration control system. The left column of diagrams shows the elements of $\vec{\theta}$

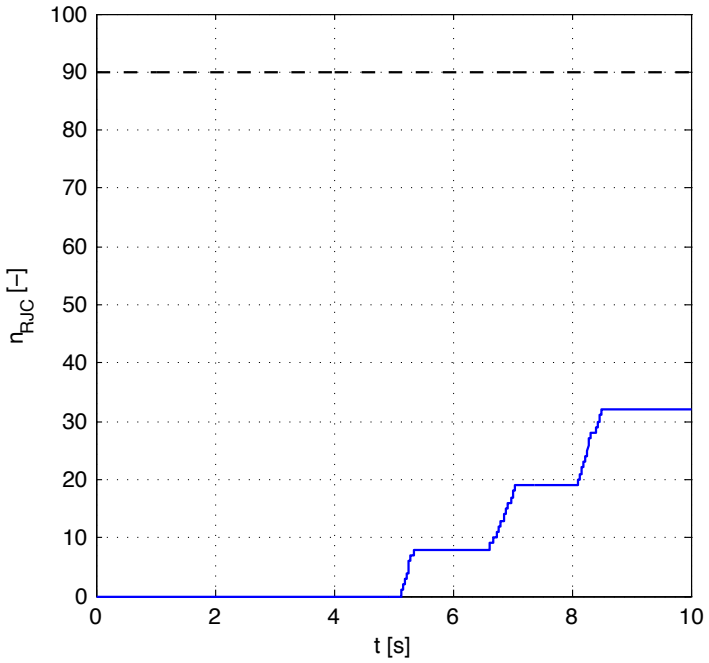

Figure 6.18: Reaction jet cartridge consumption in case of uncertain reaction jet cartridge thrust force at low velocity scenario

and $\hat{\vec{\theta}}_i$, whereupon $\vec{\theta}$ is displayed by the blue line and $\hat{\vec{\theta}}_i$ by the green line. The right column of diagrams visualizes the respective parameter errors $\tilde{\vec{\theta}}_i$. It is evident that the update laws for $\dot{\hat{\vec{\theta}}}_1$ and $\dot{\hat{\vec{\theta}}}_2$ function well. Furthermore, $\hat{\vec{\theta}}_i$ converge to steady-state values at significant speed; e.g. after $5\,[s]$ of the terminal flight phase of the interceptor. This underlines the adequacy of the result of the interceptor flight control system parameter optimization process conducted in Chapter 5.

The evaluation of Requirement 7 follows the earlier presented situations. The analysis of δ_{UR}, δ_{LR}, δ_{LL}, and δ_{UL} shows that the aerodynamic control surfaces are driven to its position limit during short timeframes; similar to the other examined low velocity scenarios. The total number of reaction jet cartridges utilized during the terminal flight phase in this specific example is $n_{RJC} = 32$. Figure 6.18 displays the reaction jet cartridge consumption. From the comparison of Figure 6.1 and Figure 6.18, it is clearly visible that the designed control allocation drives the reaction jet actuator section at step input commands in the $\left(a_Y^P\right)^{II}_{B,woG,Cmd}$ and $\left(a_Z^P\right)^{II}_{B,woG,Cmd}$ sequence. Hence, the desired functionality of the control allocation is achieved. The reaction jet cartridge consumption is below the threshold of Requirement 7, leading to the overall fulfillment of this requirement.

Following the evaluation of the nominal case, a short excursus demonstrates the operation of the control systems with respect to the theory of Chapter 4; at this point especially for the roll rate control system. The respective Lyapunov function V_{Roll}, stated in (4.215), and its derivative $\dot{V}_{Roll}$ are plotted in Figure 6.19. V_{Roll} and $\dot{V}_{Roll}$ show the expected properties of $V_{Roll} \geq 0$ and $\dot{V}_{Roll} \leq 0$ when $\left(p_K^{0B}\right)_B \neq 90\,[deg/s]$, meaning $z_{Roll} \neq 0$. The control law, in this case (4.268), enforces $z_{Roll} \to 0$ for $t \to \infty$. V_{Roll} is reduced due to $\dot{V}_{Roll} \leq 0$. When $z_{Roll} = 0$, the parameter estimates in the roll rate control system reach their steady-state value. The same is true for V_{Roll}, because $\dot{V}_{Roll} = 0$ with $z_{Roll} = 0$, underlining that the designed control achieves the

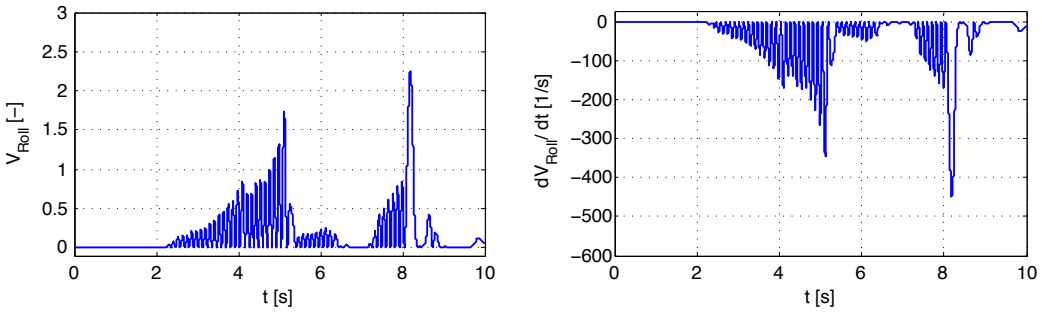

Figure 6.19: V_{Roll} and $\dot{V}_{Roll}$ in case of uncertain reaction jet cartridge thrust force at low velocity scenario

derived boundedness and stability properties.
Summarizing these results, nearly all requirements given in Chapter 5 are fulfilled for the low velocity scenario. The violation of Requirement 5 during the oscillations of $\left(p_K^{0B}\right)_B$ has no influence on the remaining performance of the controlled interceptor. In conjunction with the results for the high velocity scenario and those for various other $\tilde{F}_{RJC,Abs}$ profiles, it is concluded that the interceptor flight control system is capable to overcome uncertainties which originate from the interaction of the reaction jet cartridge exhaust gases with the external airstream surrounding the interceptor up to the considered $\Delta p_{F_{RJC,Abs}}$.
The presented results concerning uncertain total interceptor masses as well as uncertain reaction jet cartridges thrust forces demonstrate that the interceptor flight control system is able to achieve the required performance in the presence of uncertain constant parameters. This is an important result for the overall assessment. Besides uncertain constant parameters, time-varying parameters are of interest in this thesis. The capabilities of the interceptor flight control system in the presence of such parameters are explored in the following.

6.3 Robustness in case of time-varying parameters

The controlled interceptor is tested and evaluated in the presence of time-varying parameters in the following.
Based on the fact that the interceptor is affected by stochastic processes, properties of the interceptor change with time. Understanding that wind and turbulence are stochastic processes, the aerodynamic derivatives in (2.47) to (2.52) are distracted from their nominal values permanently, resulting in a change of the aerodynamic forces and moments acting on the interceptor. This implies that the dynamics of the interceptor change. Because it is impossible to measure the actual values of the aerodynamic derivatives, the plant model inside the interceptor flight control system utilizes the nominal aerodynamic derivatives. Therefore, the dynamics of the plant model no longer coincides with the dynamics of the interceptor. The aerodynamic derivatives constitute the time-varying parameters.

Time-varying aerodynamic derivatives implementation
The implementation of the time-varying aerodynamic derivatives follows Chapter 2. The levels of uncertainty for the aerodynamic derivatives are defined according to (6.6) to (6.11).

$$\Delta C_{X,0} = \Delta C_{X,Alt} = \Delta C_{X,Base} = \Delta C_{X,\delta_{Total}} = 10\,[\%] \tag{6.6}$$

$$\Delta C_{Y,0} = \Delta C_{Y,r} = \Delta C_{Y,\delta_N} = 2\,[\%] \tag{6.7}$$

$$\Delta C_{Z,0} = \Delta C_{Z,q} = \Delta C_{Z,\delta_M} = 2\,[\%] \tag{6.8}$$

$$\Delta C_{L,0} = \Delta C_{L,p} = \Delta C_{L,\delta_L} = 10\,[\%] \tag{6.9}$$

$$\Delta C_{M,0} = \Delta C_{M,q} = \Delta C_{M,\delta_M} = 10\,[\%] \tag{6.10}$$

$$\Delta C_{N,0} = \Delta C_{N,r} = \Delta C_{N,\delta_N} = 10\,[\%] \tag{6.11}$$

The sample rate which determines the frequency of the aerodynamic derivative changes is set to $1.5\,[s]$. The levels of uncertainty for the aerodynamic derivatives and the defined sample rate affect the interceptor during the terminal flight phase via (2.62). Vice versa, the aerodynamic derivatives used in the plant model remain at the nominal values. The outputs of the aerodynamic lookup tables in the plant model are not perturbed.
Because the use of (2.62) leads to stochastic properties of the interceptor, a large number of tests is conducted to explore and assess the capabilities of the interceptor flight control system. To stay inside the scope of this thesis, only one example out of these tests is presented for each velocity scenario. Besides the aerodynamic derivatives, all other properties of the interceptor remain in accordance with Chapter 2. The parameters of the interceptor flight control system are adjusted as presented in Chapter 5. Initially, the high velocity scenario is accounted for. Thereafter, the low velocity scenario is investigated. The input commands in this example are $\left(p_K^{0B}\right)_{B,Cmd} = 90\,[deg/s]$ as well as the $\left(a_Y^P\right)^{II}_{B,woG,Cmd}$ and $\left(a_Z^P\right)^{II}_{B,woG,Cmd}$ sequence shown in Figure 6.1.

Performance in case of time-varying aerodynamic derivatives at high velocity scenario
As first step, the signals of the plant model inside the interceptor flight control system are compared with the respective signals of the interceptor also in this case. This comparison shows that the signals of the plant model deviate from the respective signals of the interceptor to a maximum deviation of $1\,[\%]$. This deviation is smaller than in the case of an uncertain total interceptor mass and comparable to the nominal case. Hence, the plant model is considered a valid representation of the interceptor and its signals are used in the interceptor flight control system.
Proceeding from this result, the performance of the controlled interceptor in case of time-varying aerodynamic derivatives is explored. Figure 6.20 illustrates $\left(p_K^{0B}\right)_B$, $\left(a_Y^P\right)^{II}_{B,woG}$, and $\left(a_Z^P\right)^{II}_{B,woG}$ of the controlled interceptor in the considered example at the high velocity scenario. The signals measured by the internal sensor system are displayed by the blue lines. The green lines represent the reference signals generated by the particular command filters.
The upper diagram of Figure 6.20, which displays $\left(p_K^{0B}\right)_B$, evidently shows that latter does not leave the boundaries given by Requirement 5. The boundaries of this requirement are visualized by the horizontal dashed lines. Hence, Requirement 5 is fulfilled. The center diagram of Figure 6.20 shows the $\left(a_Y^P\right)^{II}_{B,woG}$ performance of the controlled interceptor. The vertical and horizontal dashed lines visualize the required time constant, the overshoot requirement, and the settling time to $\pm 5\,[\%]$ of the acceleration command according to Requirement 6. As illustrated in the diagram, $\left(a_Y^P\right)^{II}_{B,woG}$ fulfills the latter during the terminal flight phase of the interceptor. The lower diagram of Figure 6.20 displays the $\left(a_Z^P\right)^{II}_{B,woG}$ performance. It is obvious that $\left(a_Z^P\right)^{II}_{B,woG}$ fulfills Requirement 6. $\left(a_Z^P\right)^{II}_{B,woG}$ reaches $90\,[\%]$ of the acceleration command after less than three times the required time constant. Following [81] and the requirement definition, this means that the controlled interceptor exhibits the required time constant. The overshoot of $\left(a_Z^P\right)^{II}_{B,woG}$ stays significantly below the specified boundary, which is represented by the outer horizontal

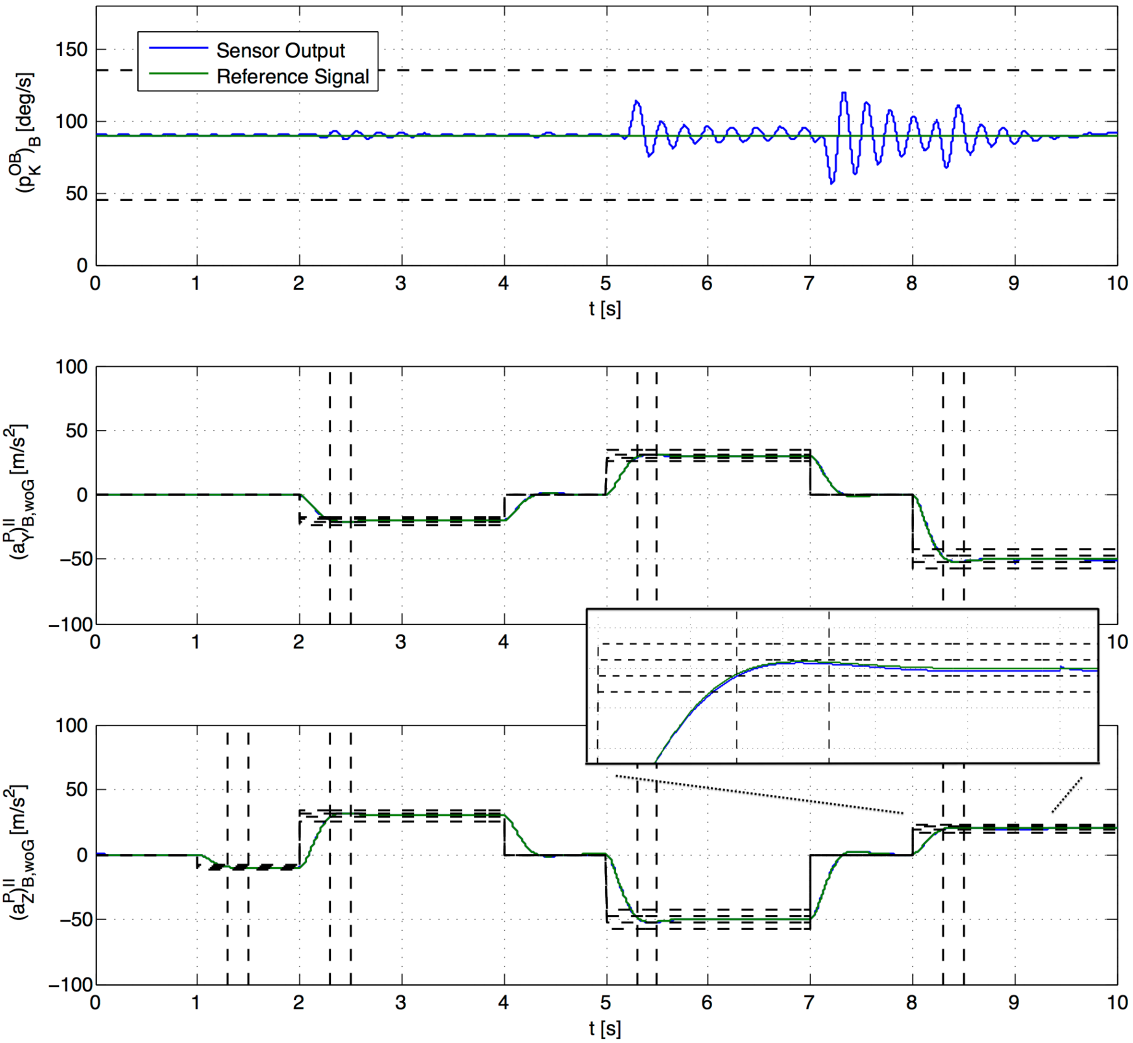

Figure 6.20: Interceptor performance in case of time-varying aerodynamic derivatives at high velocity scenario

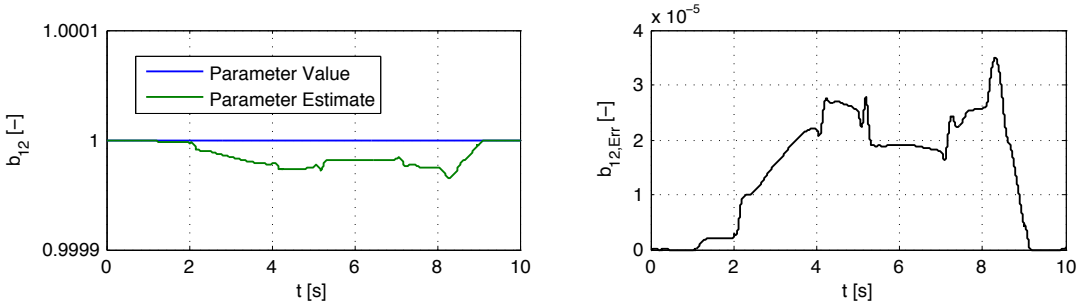

Figure 6.21: $\dot{\hat{b}}_{12}$ update law performance in case of time-varying aerodynamic derivatives at high velocity scenario

dashed lines. In addition, $\left(a_Z^P\right)^{II}_{B,woG}$ reaches the desired $\pm 5\,[\%]$ settling range of the acceleration command in the required settling time. The close-up view underlines this result.
In augmentation to the fulfillment of Requirement 6, the close-up view illustrates the influence of the time-varying aerodynamic derivatives on the interceptor flight control system. Based on the defined sample rate for the aerodynamic derivatives of $1.5\,[s]$, they change after $9.0\,[s]$ of the terminal flight phase of the interceptor. Considering the rational behind the time-varying aerodynamic derivatives, this change can be understood as a steady gust starting to affect the interceptor at this point of time. The aerodynamic forces and moments acting on the interceptor change, implying also a change in $\left(a_Y^P\right)^{II}_{B,woG}$ and $\left(a_Z^P\right)^{II}_{B,woG}$. This change is recognizable in the close-up view. $\left(a_Z^P\right)^{II}_{B,woG}$ increases after $9.0\,[s]$. The interceptor flight control system reacts on the increase and controls $\left(a_Z^P\right)^{II}_{B,woG}$ to the reference signal; $z_{1,Pitch}$ is controlled to zero. In this example, the interceptor flight control system eliminates $z_{1,Pitch}$ in approximately $0.05\,[s]$, whereupon $\left(a_Z^P\right)^{II}_{B,woG}$ does not leave the desired $\pm 5\,[\%]$ settling range.
The change of the aerodynamic derivatives induces that the adaptation algorithms are employed. Figure 6.21 illustrates the performance of the update law for $\dot{\hat{b}}_{12}$ in the interceptor pitch acceleration control system. The left diagram of Figure 6.21 displays b_{12} as blue line. $\hat{b}_{12}$ is represented by the green line. The right diagram shows $\tilde{b}_{12}$. The influence of the aerodynamic derivatives changes are vividly recognizable.
In the considered example, $z_{1,Yaw}$ and $z_{1,Pitch}$ reach maximum values of $0.6\,[m/s^2]$. These maximum values are observed after $5.01\,[s]$ of the terminal flight phase. As shown in Figure 6.1, $\left(a_Y^P\right)^{II}_{B,woG,Cmd}$ and $\left(a_Z^P\right)^{II}_{B,woG,Cmd}$ step input commands are injected simultaneously in the interceptor flight control system at this time, leading to these maximum values of $z_{1,Yaw}$ and $z_{1,Pitch}$. Compared to earlier considered high velocity scenario situations, $z_{1,Yaw}$ and $z_{1,Pitch}$ show increased maximum values. $1\,[s]$ after step input commands, $z_{1,Yaw}$ and $z_{1,Pitch}$ are below $0.2\,[m/s^2]$. This behavior is comparable to the beforehand investigated situations.
The evaluation concerning Requirement 7 leads to the following two results. The aerodynamic control surface actuator modules are driven inside their normal operating envelope. None of the aerodynamic control surfaces reaches its position or velocity limit given by (2.57) and (2.58) during the terminal flight phase. To allow traceability of this first result, δ_{LR} is provided in Figure 6.22 as an example; the horizontal dashed lines represent the position limit of the aerodynamic control surface actuator module. In analogy to the earlier situations considering the high velocity scenario, none reaction jet cartridge is fired. Requirement 7 is fulfilled.
Based on the achieved results, it is concluded that all requirements from Chapter 5 are fulfilled in the presented example. This leads directly to the investigation of the interceptor performance in

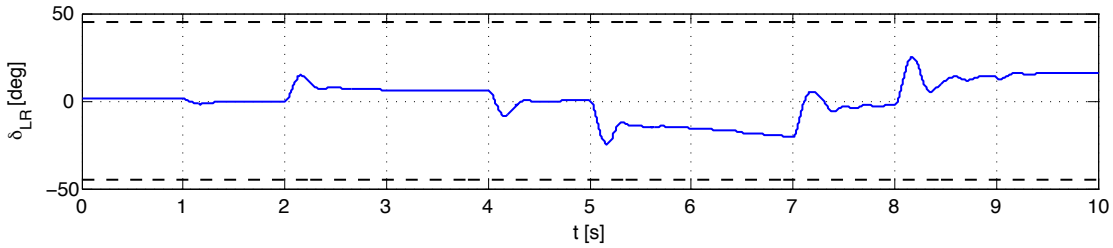

Figure 6.22: δ_{LR} in case of time-varying aerodynamic derivatives at high velocity scenario

the presence of the introduced time-varying aerodynamic derivatives at the low velocity scenario.

Performance in case of time-varying aerodynamic derivatives at low velocity scenario

The initial step of the analysis for this situation encompasses the comparison of the signals of the plant model with the signals of the interceptor. As result of this step, it is found that the respective signals show a maximum deviation of approximately 1 [%] during the terminal flight phase of the interceptor. This is comparable to the high velocity scenario. Based on the derived maximum deviation, the plant model inside the interceptor flight control system is accepted as a valid representation of the interceptor and its signals are used in the roll rate as well as the acceleration control systems.

In the next step, the performance of the interceptor is evaluated against Requirement 5 and Requirement 6. Figure 6.23 is utilized for this evaluation. It depicts $\left(p_K^{0B}\right)_B$, $\left(a_Y^P\right)_{B,woG}^{II}$, and $\left(a_Z^P\right)_{B,woG}^{II}$. Like in earlier performance plots, the blue lines display the signals measured by the internal sensor system, whereas the green lines depict the reference signals from the command filters. The black dashed lines represent the requirements.

As it is obvious from the upper diagram of Figure 6.23, $\left(p_K^{0B}\right)_B$ occasionally leaves the boundaries imposed by Requirement 5 for short durations. On the other hand, $\left(p_K^{0B}\right)_B$ does not deteriorate completely, like in the earlier considered situation of the nominal case at the low velocity scenario without the reaction jet actuator section. The center diagram of Figure 6.23 shows that the controlled interceptor demonstrates a sufficient time constant for $\left(a_Y^P\right)_{B,woG}^{II}$ during the first 8.0 $[s]$ of the terminal flight phase. After this point of time, the controlled interceptor is no longer able to reach 90 [%] of the commanded acceleration in three times $T = 0.1\,[s]$, indicated by the vertical dashed line. It takes the the controlled interceptor 0.025 $[s]$ longer to achieve this level of $\left(a_Y^P\right)_{B,woG}^{II}$. The overshoot boundary given by Requirement 6 is fulfilled for $\left(a_Y^P\right)_{B,woG}^{II}$. The same is true for the settling time and settling range during the first 8.0 $[s]$ of the terminal flight phase. Thereafter, the interceptor the settling range is achieved with a delay of approximately 0.075 $[s]$. The lower diagram of Figure 6.23 depicts the performance for $\left(a_Z^P\right)_{B,woG}^{II}$ which follows the $\left(a_Y^P\right)_{B,woG}^{II}$ behavior. The time constant is sufficient for the first part of the terminal flight phase. After 8.0 $[s]$, the interceptor reaches the desired level of acceleration with a delay of 0.025 $[s]$. In contrast to the lateral acceleration performance, the overshoot boundary is violated for three times due to the firing of reaction jet cartridges during the final stage of the terminal flight phase. The close-up view illustrates this evidently. The settling time and settling range behavior of $\left(a_Z^P\right)_{B,woG}^{II}$ is identical to the lateral control string. The 0.075 $[s]$ delay in reaching the settling range after 8.0 $[s]$ of the terminal flight phase is easily recognizable from the close-up view.

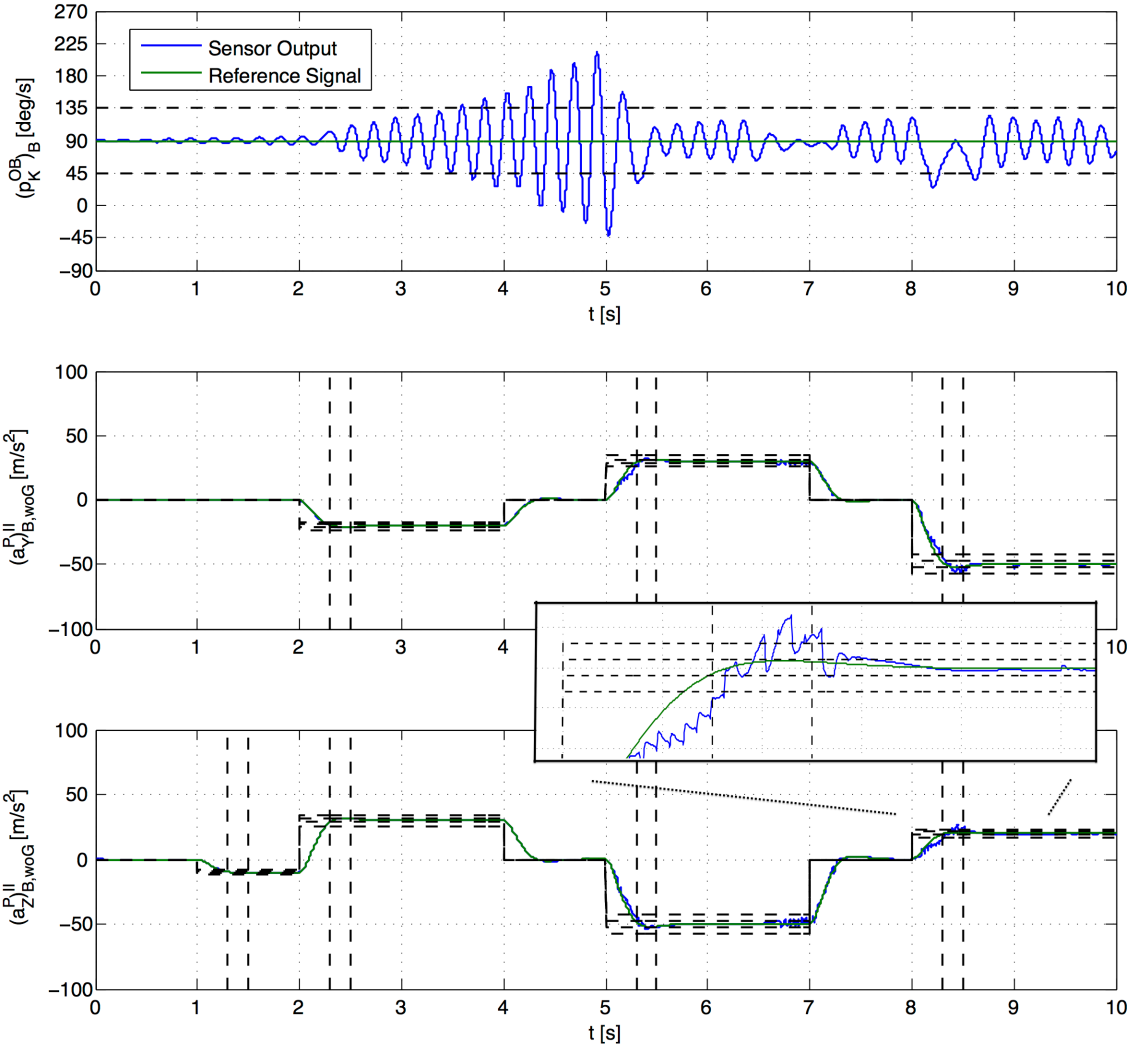

Figure 6.23: Interceptor performance in case of time-varying aerodynamic derivatives at low velocity scenario

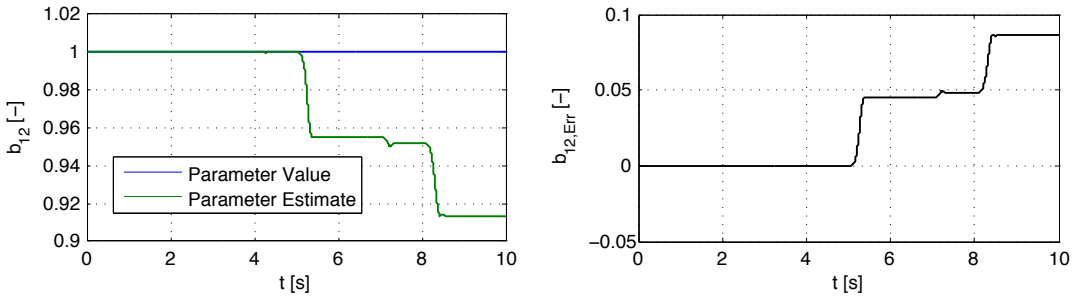

Figure 6.24: $\dot{\hat{b}}_{12}$ update law performance in case of time-varying aerodynamic derivatives at low velocity scenario

Although the described behavior may not be sufficient seen purely from the perspective of the given requirements, it is assessed that the interceptor does show a performance which enables it to fulfill its mission. The remaining $\left(p_K^{0B}\right)_B$ guarantees the availability of unused reaction jet cartridges. The latter support the achievement of the commanded accelerations in a very beneficial manner, as underpinned by the close-up view in Figure 6.23. Only minor delays with respect to the time constant and the settling time are observed in the final part of the terminal flight phase. The desired steady-state accuracy is achieved during the complete flight phase.
The regular change of the aerodynamic derivatives, illustrated already above for the high velocity scenario, is recognizable also in this case in the close-up view. After $9.0\,[s]$, $\left(a_Z^P\right)_{B,woG}^{II}$ increases based on the change of the aerodynamic forces and moments acting on the interceptor. $\left(a_Z^P\right)_{B,woG}^{II}$ does not leave the settling range of $\pm 5\,[\%]$. The interceptor flight control system reacts on the given $z_{1,Pitch}$ and controls $\left(a_Z^P\right)_{B,woG}^{II}$ to the desired value in approximately $0.04\,[s]$. Due to the existing $z_{1,Pitch}$, originating from the change of the aerodynamic derivatives, the adaptation algorithms of the interceptor flight control system are excited. The update law performance for $\dot{\hat{b}}_{12}$ in the interceptor pitch acceleration control system is displayed in Figure 6.24. The direct comparison of Figure 6.24 with Figure 6.21 shows that $\hat{b}_{12}$, represented by the green line, deviates much more from b_{12}, indicated by the blue line, at the low velocity scenario. Besides this increased deviation, the adaptation algorithm works as designed and convergence to the respective steady-state $\hat{b}_{12}$ is achieved considerably fast at low velocity scenario, which is vividly expressed in the right diagram of Figure 6.24, showing $\tilde{b}_{12}$.
The tracking errors $z_{1,Yaw}$ and $z_{1,Pitch}$ display maximum values of $8\,[m/s^2]$ during the injection of acceleration step input commands. After $1\,[s]$, the tracking errors are reduced below $1\,[m/s^2]$. This behavior follows the earlier accounted for situations at the low velocity scenario.
To evaluate the fulfillment of Requirement 7, the deflection of the aerodynamic control surfaces is investigated first. Figure 6.25 shows δ_{LR} as an example. The latter is chosen deliberately to provide comparability to Figure 6.22. It is obvious that the aerodynamic control surfaces are driven by the designed control allocation. Furthermore, it is evident that δ_{LR} shows much greater deflections at the low velocity scenario than in Figure 6.22, due to the reduced aerodynamic control surface effectivity. During seven periods, δ_{LR} reaches its position limit given in (2.58). This limit is indicated in Figure 6.25 by the horizontal dashed lines. Because the controlled interceptor in not able to follow the reference signals provided by the command filters, although the aerodynamic control surfaces are fully deflected, the reaction jet actuator section is employed by the designed control allocation. $n_{RJC} = 32$ reaction jet cartridges are consumed during the terminal flight phase of the interceptor in the considered example, leading

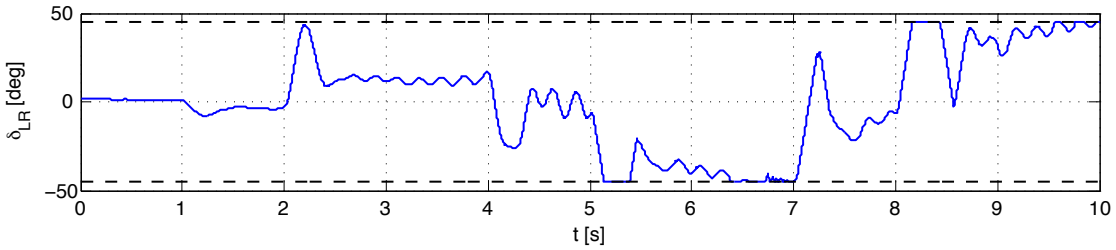

Figure 6.25: δ_{LR} in case of time-varying aerodynamic derivatives at low velocity scenario

to the beneficial increase of agility visible in the close-up view of Figure 6.23. The amount of reaction jet cartridges used is comparable to the low velocity scenarios investigated earlier and significantly below the imposed threshold. Given these results, Requirement 7 is fulfilled.
Summarizing the results for the case of time-varying aerodynamic derivatives at the low velocity scenario, not all requirements are persistently fulfilled. Requirement 5 as well as parts of Requirement 6 are violated occasionally during the terminal flight phase of the interceptor. Based on the duration and amount at which the given thresholds are exceeded, these violations are categorized as minor and not of importance with respect to the operation of the interceptor. In addition, given the results for the nominal case without the reaction jet actuator section, it is pointed out that the derived design constitutes the reason for the interceptor to be able to operate in the low velocity scenario; here including time-varying aerodynamic derivatives. Therefore, the conclusion is made that the designed interceptor flight control system is able to overcome the introduced time-varying parameters in the considered example and provide operational usability to the interceptor.
The repetition of the presented analysis for the high as well as the low velocity scenario in a large number of test cases with time-varying aerodynamic derivatives up to the levels of uncertainty specified in (6.6) to (6.11) leads to the identical results as presented beforehand. Hence, the interceptor flight control system owns the capability to handle time-varying aerodynamic derivatives up to the defined levels of uncertainty. Utilizing all derived results presented in this chapter up to this point, the interceptor flight control system is capable to resist all parameter uncertainties considered in this thesis, if they are present separately. This assessment is the basis for the exploration of the capabilities of the controlled interceptor in the case of combined uncertainties.

6.4 Performance under combined uncertainties

The conducted tests and evaluations in conjunction with the assessed capabilities of the interceptor flight control system allow to account for combined uncertainties at this point of the thesis. Combined uncertainties denote the simultaneous presence of uncertain constant parameters and time-varying parameters.
As mentioned in Section 6.1, the presence of combined uncertainties imposes the most difficult condition on the interceptor flight control system. In contrast, this case is the most realistic situation. Recapitulating the physical effects behind the uncertain constant parameters and the time-varying parameters, it is evident that an uncertain total interceptor mass, an uncertain reaction jet cartridge thrust force, and time-varying aerodynamic derivatives occur simultaneously in reality. This means that the evaluation of the performance of the controlled interceptor under combined uncertainties is of great importance and allows the most extensive assessment

concerning the capabilities of the derived interceptor flight control system design.

Combined uncertainty implementation
The implementation of the combined uncertainties is done as introduced in Chapter 2. Following Section 6.2.1, $\Delta p_{m_{Empty}}$ is defined by (6.1). (2.61) is used to calculate $\tilde{m}_{Empty}$ for the interceptor. m_{Empty} according to (2.6) is implemented in the plant model.
To account for changes in the inertia tensor with respect to the center of gravity of the interceptor, specified in the body fixed frame, resulting from a changed total interceptor mass as well as mass distribution, $\Delta p_{\left(I^G_{Empty}\right)_{BB}}$ is stated in (6.2). $(\tilde{I}^G_{Empty})_{BB}$ is calculated by employing (2.61). $(\tilde{I}^G_{Empty})_{BB}$ is implemented in the interceptor, while $(I^G_{Empty})_{BB}$ according to (2.7) is utilized in the plant model.
The $\tilde{F}_{RJC,Abs}$ profile is derived from (2.61), with $\Delta p_{F_{RJC,Abs}}$ as (6.5). The $\tilde{F}_{RJC,Abs}$ profile is utilized in the interceptor, whereas the $F_{RJC,Abs}$ profile is used in the plant model.
Although the introduced parameter uncertainties create a situation which exceeds the earlier considered cases, time-varying aerodynamic derivatives are introduced. Following Section 6.3, the levels of uncertainty for the aerodynamic derivatives are defined by (6.6) to (6.11). The time-varying aerodynamic derivatives are implemented in the interceptor via (2.62). Hence, the aerodynamic derivatives change frequently during the terminal flight phase of the interceptor. The sample rate determining the frequency of the aerodynamic derivative changes is chosen as $1.5\,[s]$. This choice follows Section 6.3.
To achieve a reliable assessment of the capabilities of the interceptor flight control system, multiple tests with the introduced combined uncertainties are conducted. One specific example is presented herein. The total interceptor mass is increased by $6.7\,[\%]$ in this example, leading to $\tilde{m}_{Empty}$ in (6.12). $(\tilde{I}^G_{Empty})_{BB}$ is given by (6.13).

$$\tilde{m}_{Empty} = 160.05\,[kg] \tag{6.12}$$

$$\left(\tilde{I}^G_{Empty}\right)_{BB} = \begin{bmatrix} 5.23 & 0 & 0 \\ 0 & 418.72 & 0 \\ 0 & 0 & 418.72 \end{bmatrix} [kgm^2] \tag{6.13}$$

The reaction jet cartridge thrust profile is increased by $1.6\,[\%]$. This results in a maximum reaction jet cartridge thrust force of $\tilde{F}_{RJC,Abs,Max} = 508.05\,[N]$. All remaining properties of the interceptor as well as all properties of the plant model are as presented in Chapter 2. The parameters of the interceptor flight control system are adjusted to the values derived in Chapter 5. The high velocity scenario of the interceptor is given by $(V^G_{K,Abs})^I_{B,IC} = 600\,[m/s]$ and $\left(z^G\right)_I = 10000\,[m]$, whereas the low velocity scenario is defined by the initial conditions $(V^G_{K,Abs})^I_{B,IC} = 400\,[m/s]$ and $\left(z^G\right)_{I,IC} = 10000\,[m]$. $\left(p^{0B}_K\right)_{B,Cmd} = 90[deg/s]$, following the requirements. The $\left(a^P_Y\right)^{II}_{B,woG,Cmd}$ and $\left(a^P_Z\right)^{II}_{B,woG,Cmd}$ sequence in this example is shown in Figure 6.1. This choice allows the direct comparison of the results achieved in the presence of combined uncertainties with the earlier investigated situations.

Performance in case of combined uncertainties at high velocity scenario
Before the performance of the controlled interceptor is evaluated, the signals of the plant model are compared with the signals of the interceptor to validate the plant model as a representation of the interceptor for this case. The comparison of the respective signals shows that the deviation of the signals of the plant model from the signals of the interceptor is generally increased during the terminal flight phase, compared to the earlier situations. This results from the fact that the plant model differs from the interceptor to the highest extend under combined uncertainties.

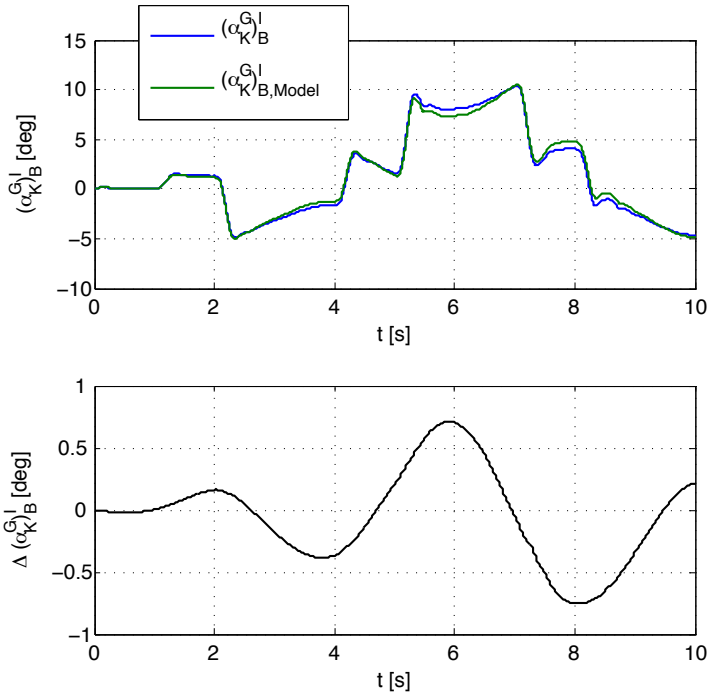

Figure 6.26: $(\alpha_K^G)_B^I$ and $\Delta(\alpha_K^G)_B^I$ in case of combined uncertainties at high velocity scenario

Figure 6.26 illustrates $(\alpha_K^G)_B^I$ and $\Delta(\alpha_K^G)_B^I$ for this example. The blue line in the upper diagram of Figure 6.26 displays $(\alpha_K^G)_B^I$ of the interceptor, whereas the green line represents $(\alpha_K^G)_B^I$ of the plant model. The deviation of the two signals during the terminal flight phase of the interceptor is obvious, if $\left|\alpha_K^G\right|_B^I > 5\,[deg]$. The lower diagram displays $\Delta(\alpha_K^G)_B^I$. The comparison of all signals of the plant model with the signals of the interceptor shows that the maximum deviation of two respective signals is approximately 15 [%]. Based on this, the plant model constitutes a valid representation of the interceptor; its signals are utilized in the control subsystems.
Continuing with the evaluation of the performance of the controlled interceptor, Requirement 5 is considered first. The upper diagram of Figure 6.27 shows the $\left(p_K^{0B}\right)_B$ performance during the terminal flight phase. The blue line displays the output of the internal sensor system. The reference signal is depicted by the green line.
$\left(p_K^{0B}\right)_B$ does not leave the boundaries given by the requirement. The latter is fulfilled. The center diagram displays the $\left(a_Y^P\right)_{B,woG}^{II}$ performance. The vertical and horizontal dashed lines visualize the time constant, the overshoot, the settling time, and the settling range specified in Requirement 6, following earlier performance plots. Due to the fact that $\left(a_Y^P\right)_{B,woG}^{II}$ reaches the commanded acceleration sufficiently fast, does not exceed the given overshoot boundary, and settles to the desired range of the acceleration command in the required settling time, it is concluded that Requirement 6 is fulfilled in this example at the high velocity scenario. The lower diagram of Figure 6.27 illustrates $\left(a_Z^P\right)_{B,woG}^{II}$. The analysis of this diagram shows that Requirement 6 is also fulfilled for $\left(a_Z^P\right)_{B,woG}^{II}$.
$z_{1,Yaw}$ and $z_{1,Pitch}$ exhibit greater values compared to the earlier presented situations at the high velocity scenario. Considering the amount of parameter uncertainties introduced, this behavior is a logical consequence. During the injection of step input commands, $z_{1,Yaw}$ and $z_{1,Pitch}$ reach maximum values of 5.0 $[m/s^2]$. 1 $[s]$ after the injection of a step input command, $z_{1,Yaw}$ and

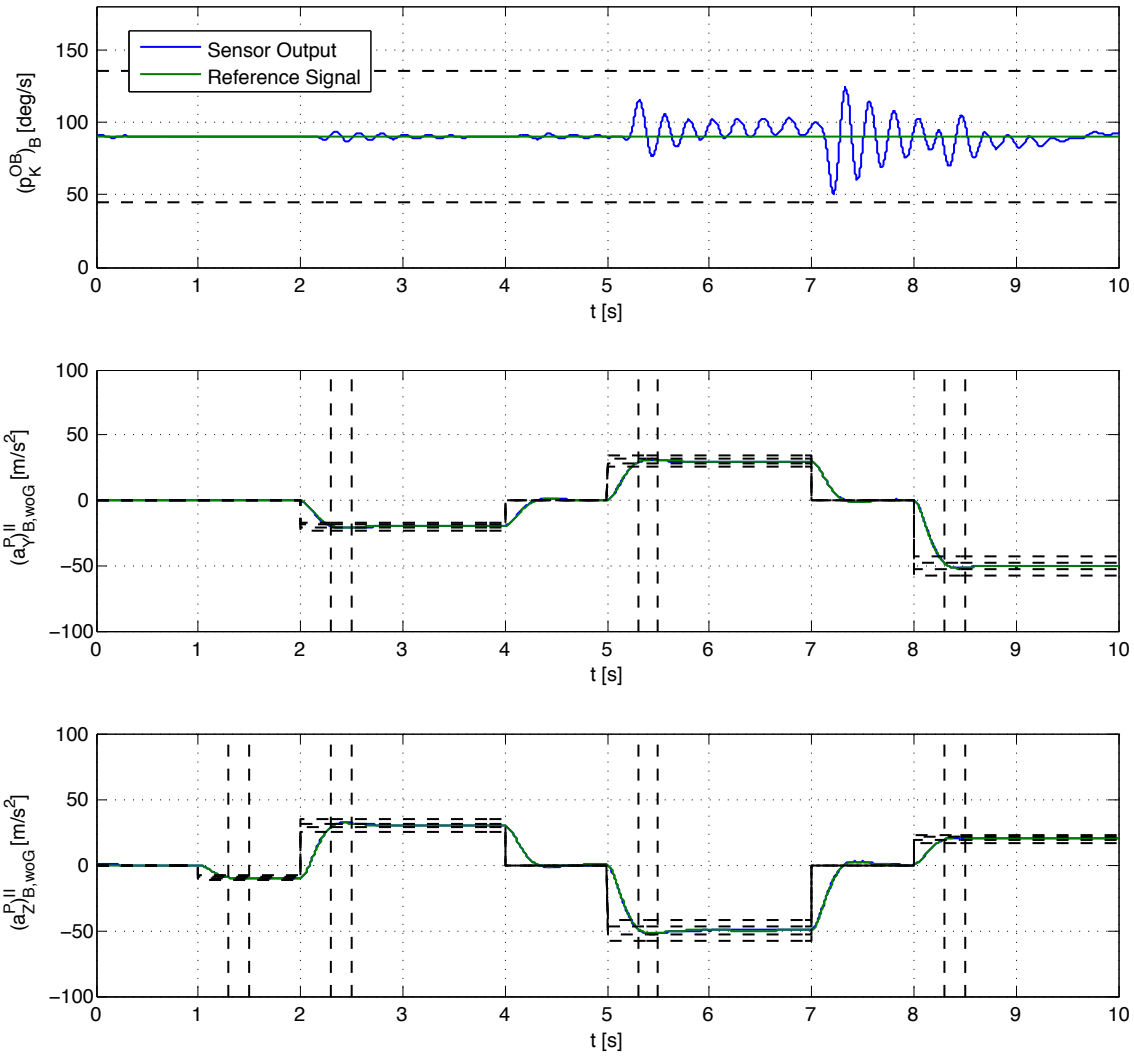

Figure 6.27: Interceptor performance in case of combined uncertainties at high velocity scenario

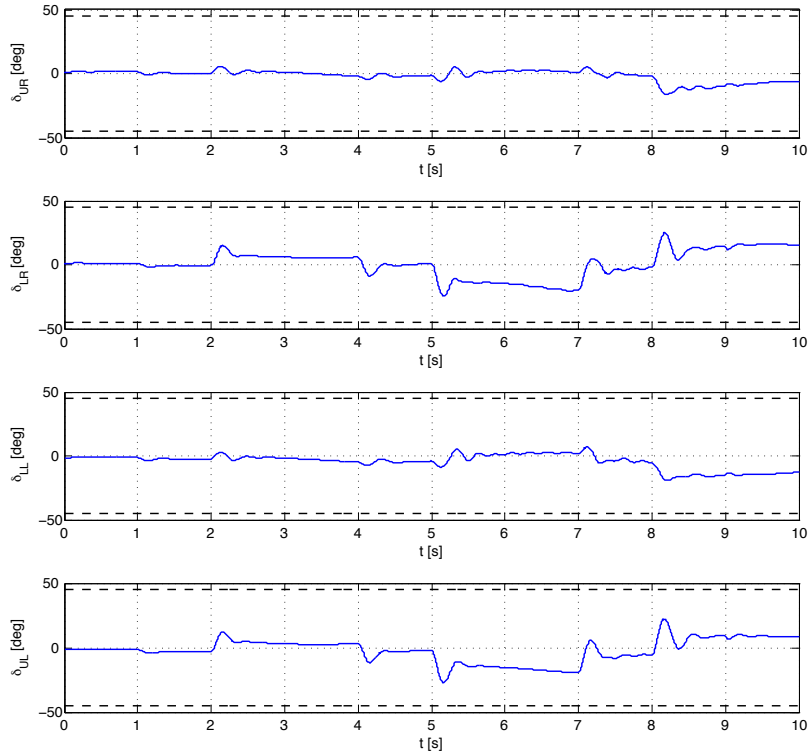

Figure 6.28: δ_{UR}, δ_{LR}, δ_{LL}, and δ_{UL} in case of combined uncertainties at high velocity scenario

$z_{1,Pitch}$ are reduced to approximately 0.5 $[m/s^2]$. Nevertheless, these tracking errors are so small that the signals in Figure 6.27 nearly coincide.
Given that Requirement 5 and Requirement 6 are fulfilled, the evaluation process continues with Requirement 7. First, δ_{UR}, δ_{LR}, δ_{LL}, and δ_{UL} are analyzed. Although remarkable uncertainties are introduced, the positions of the aerodynamic control surfaces exhibit only negligible deviations from the positions displayed in Figure 6.3. Figure 6.28 proofs this assessment by showing all aerodynamic control surface positions during the terminal flight phase, allowing the direct comparison of the two cases. The deviations of two respective surface positions are below 1 $[deg]$. None of the aerodynamic control surface actuator modules is driven to its position limit. Furthermore, none of the latter modules is driven to its velocity limit given in (2.57). No reaction jet cartridges are used during the terminal flight phase of the interceptor in the considered example. For this reason, Requirement 7 is fulfilled.
While the functioning of the yaw acceleration control system and the roll rate control system have been laid out earlier, Figure 6.29 depicts that the pitch acceleration control system works as designed in this case, viewed from the theoretical background. This figure displays the Lyapunov function (4.223) of the pitch acceleration control system V_{Pitch} in the left diagram and its respective derivative $\dot{V}_{Pitch}$, given by (4.272), in the right diagram. Caused by the input commands, $z_{1,Pitch}$ and $z_{2,Pitch}$ raise $V_{Pitch} \geq 0$ as well as $\dot{V}_{Pitch} \leq 0$. The control law (4.270) implemented in the control system drives $z_{1,Pitch} \to 0$ and $z_{2,Pitch} \to 0$. $\dot{V}_{Pitch} \leq 0$ decreases V_{Pitch}, as recognizable in Figure 6.29. With $z_{1,Pitch}$ and $z_{2,Pitch}$ faded away, the parameter estimates of the pitch acceleration control system reach steady-state values, $\dot{V}_{Pitch} = 0$, and V_{Pitch} remains steady. The system converges to the globally stable equilibrium $z_{1,Pitch} = 0$ and $z_{2,Pitch} = 0$ of the error system derived in Chapter 4.
With this results on hand, it is possible to assess that all given requirements are fulfilled in the

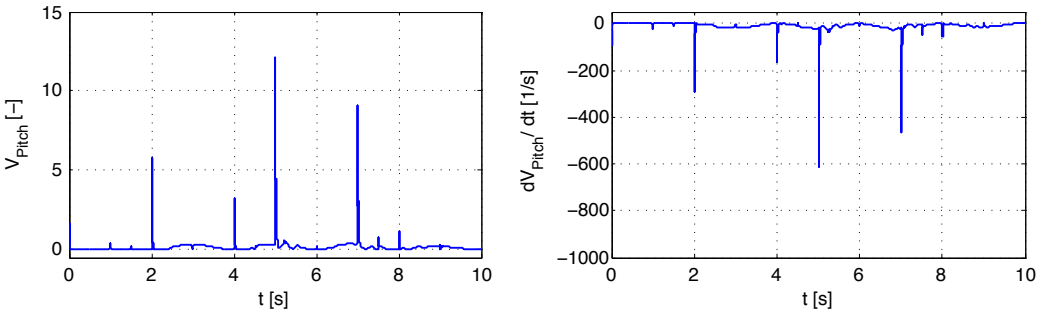

Figure 6.29: V_{Pitch} and $\dot{V}_{Pitch}$ in case of combined uncertainties at high velocity scenario

considered example of combined uncertainties at the high velocity scenario. Various simulations with other examples of combined uncertainties underpin this result. Therefore, the interceptor flight control system is capable to overcome combined uncertainties up to the levels of uncertainty defined in (6.1), (6.2), (6.5), and (6.6) to (6.11) at the high velocity scenario.
This achieved, the investigation and evaluation of the interceptor performance in the presence of combined uncertainties focusses on the low velocity scenario.

Performance in case of combined uncertainties at low velocity scenario
The investigation for the low velocity scenario, being defined by $(V^G_{K,Abs})^I_{B,IC} = 400\,[m/s]$ and $\left(z^G\right)_{I,IC} = 10000\,[m]$, starts again with the direct comparison of the signals of the plant model with the signals of the interceptor. As already observed for the case of combined uncertainties at the high velocity scenario, the signals deviate more than in earlier examined situations. $(\alpha^G_K)^I_B$ and $\Delta(\alpha^G_K)^I_B$ for this example are visualized in Figure 6.30. While the upper diagram of Figure 6.30 displays $(\alpha^G_K)^I_B$ of the interceptor as blue line and $(\alpha^G_K)^I_B$ of the plant model as green line, the lower diagram shows $\Delta(\alpha^G_K)^I_B$. The comparison of Figure 6.26 and Figure 6.30 reveals that $\Delta(\alpha^G_K)^I_B$ is increased in the low velocity scenario. The comparison of all signals of the plant model with the respective signals of the interceptor leads to a maximum deviation of two signals of 15 [%]. Although this constitutes the highest deviation observed in this thesis, the plant model is taken as a valid representation of the interceptor, because this deviation is only observed for one signal at one time instant.
In the next step, the performance of the controlled interceptor is evaluated against the given requirements. Figure 6.31 shows the performance for this example of combined uncertainties in the low velocity scenario.
The upper diagram of Figure 6.31 visualizes $\left(p^{0B}_K\right)_B$ as well as the thresholds imposed by Requirement 5. Like in earlier presented cases at the low velocity scenario, $\left(p^{0B}_K\right)_B$ shows oscillations and leaves the boundaries of Requirement 5 on several occasions for short periods. A sufficient $\left(p^{0B}_K\right)_B$ always remains to provide reaction jet cartridge availability. The center diagram of Figure 6.31 illustrates the $\left(a^P_Y\right)^{II}_{B,woG}$ performance. The signal measured by the internal sensor system is depicted by the blue line, whereas the green line displays the reference signal. The controlled interceptor is able to reach 90 [%] of the respective commanded acceleration in $T = 0.3\,[s]$. Hence, the time constant of the controlled interceptor is sufficient. The overshoot threshold of Requirement 6 is not violated by $\left(a^P_Y\right)^{II}_{B,woG}$. In addition, $\left(a^P_Y\right)^{II}_{B,woG}$ reaches the desired settling range in the specified settling time of $T = 0.5\,[s]$. The lower diagram of Figure 6.31 shows the performance of the controlled interceptor with regard to $\left(a^P_Z\right)^{II}_{B,woG}$. During the first part of the terminal flight phase, $\left(a^P_Z\right)^{II}_{B,woG}$ demonstrates the required time constant,

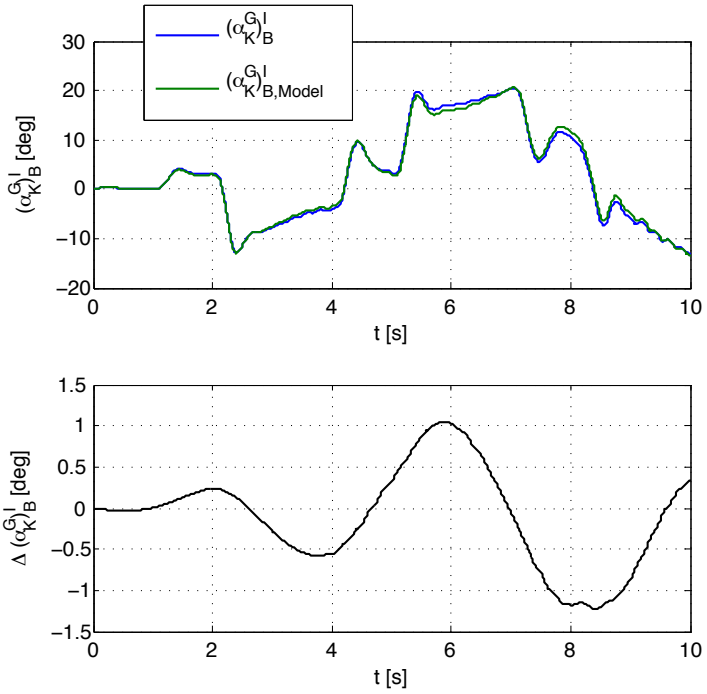

Figure 6.30: $(\alpha_K^G)_B^I$ and $\Delta(\alpha_K^G)_B^I$ in case of combined uncertainties at low velocity scenario

overshoot as well as settling time to the settling range of $\pm 5\,[\%]$ of the commanded acceleration. After $8.0\,[s]$ of the terminal flight phase, $90\,[\%]$ of the acceleration command is reached with a delay of $0.025\,[s]$. The given overshoot boundary is violated five times for $0.01\,[s]$ in this last section of the terminal flight phase. The settling range is reached with a delay of $0.1\,[s]$.
The observed violations of the given requirements are not considered as important for the operation of the interceptor at this point. $\left(p_K^{0B}\right)_B$ stays sufficiently high to guarantee the availability of unused reaction jet cartridges. The requirement violations of $\left(a_Z^P\right)_{B,woG}^{II}$ are to small concerning their size and to short with regard to their endurance to endanger the mission accomplishment of the interceptor. The settling range, being of most importance, because it defines that the trajectory of the interceptor is shaped according to the commanded accelerations, is achieved for the lateral and longitudinal acceleration control string throughout the whole terminal flight phase.
The tracking errors $z_{1,Yaw}$ and $z_{1,Pitch}$ in this example of combined uncertainties at the low velocity scenario display maximum values of $8.5\,[m/s^2]$. These errors occur during the injection of acceleration commands. They are reduced to values below $1.5\,[m/s^2]$ at $1\,[s]$ after the respective command injection. Such behavior is in line with the earlier considered situations at the low velocity scenario.
Figure 6.32 displays δ_{UR}, δ_{LR}, δ_{LL}, and δ_{UL} during the terminal flight phase of the interceptor, and allows the evaluation of Requirement 7 for this example. The aerodynamic control surfaces are driven throughout the terminal flight phase and reach their position limit according to (2.58) on several occasions. Based on the results of earlier investigated cases, this behavior is considered normal for this scenario. The comparison of Figure 6.32 with Figure 6.28 reveals the increase in deflection between the low velocity scenario and the high velocity scenario for the case of combined uncertainties, which originates from the reduced aerodynamic control surface effectivity at lower $(V_{K,Abs}^G)_B^I$. On the other hand, the comparison of Figure 6.6 and Figure 6.32

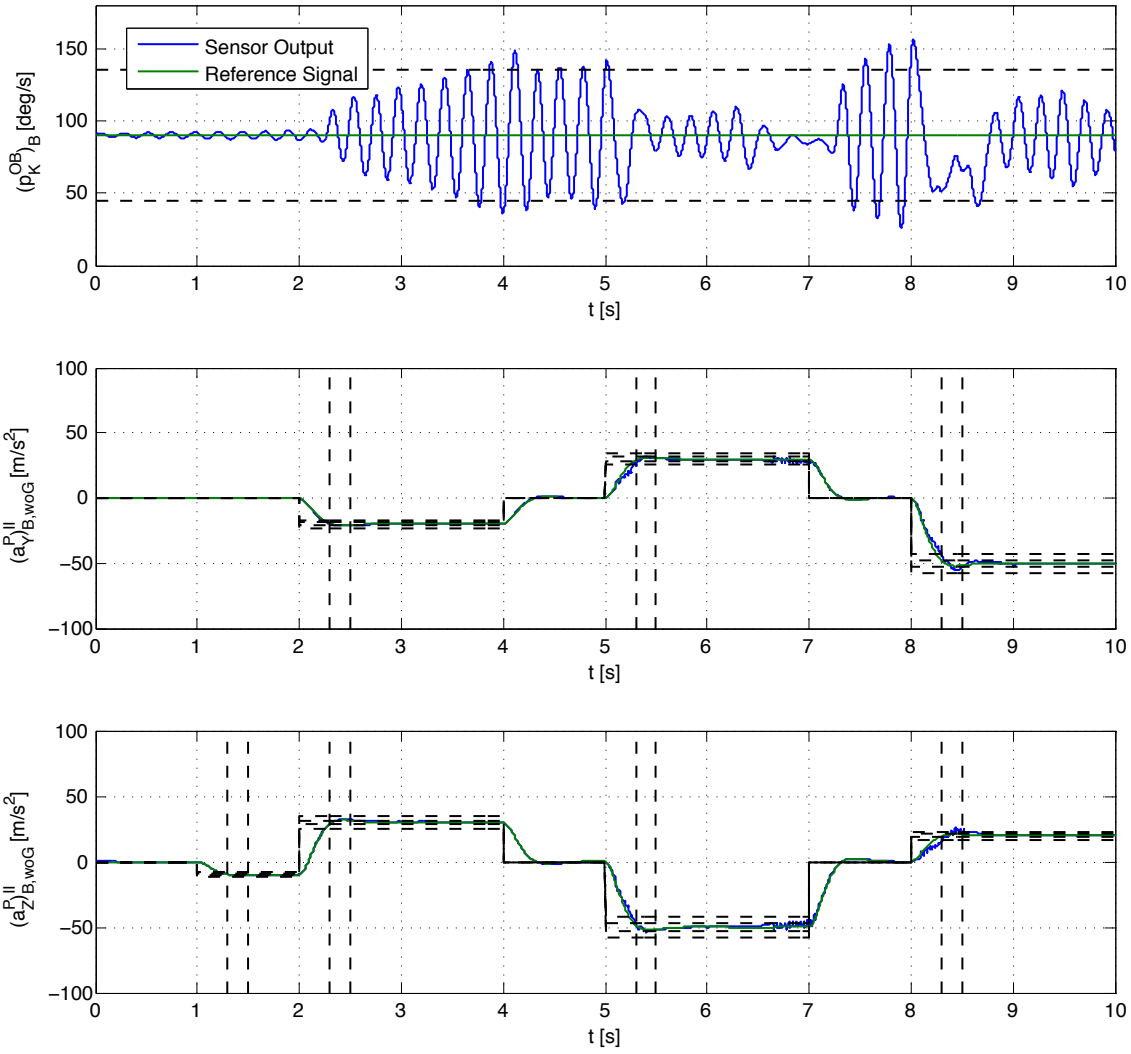

Figure 6.31: Interceptor performance in case of combined uncertainties at low velocity scenario

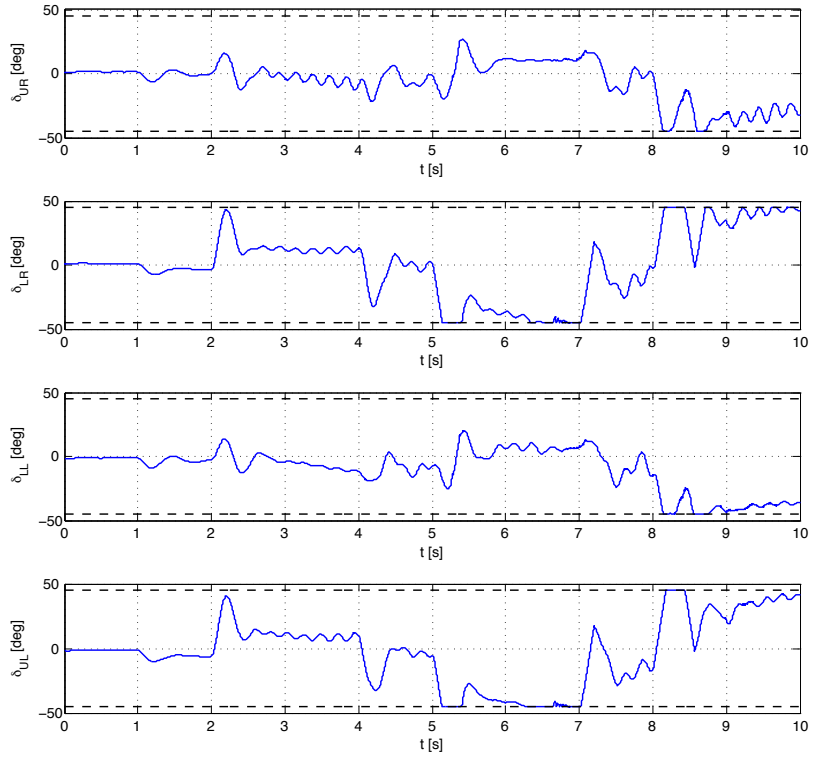

Figure 6.32: δ_{UR}, δ_{LR}, δ_{LL}, and δ_{UL} in case of combined uncertainties at low velocity scenario

provides the insight that δ_{UR}, δ_{LR}, δ_{LL}, and δ_{UL} differ only minor between the nominal case and the case of combined uncertainties, indicating the outstanding performance capabilities of the interceptor flight control system regarding uncertainties.
Besides the aerodynamic control surfaces, the reaction jet actuator section is driven by the designed control allocation to overcome the increased $z_{1,Yaw}$ and $z_{1,Pitch}$. The total number of $n_{RJC} = 34$ reaction jet cartridges is consumed during the terminal flight phase. Figure 6.33 visualizes this consumption. This is significantly below the given threshold, leading to the fulfillment of Requirement 7 in conjunction with the result achieved for the aerodynamic control surfaces.
Figure 6.34 illustrates the trajectory of the center of gravity of the interceptor as a final measure of evaluation for the performance of the controlled interceptor in the presented example. The $\left(a_Y^P\right)^{II}_{B,woG,Cmd}$ and $\left(a_Z^P\right)^{II}_{B,woG,Cmd}$ sequence in combination with $\left(p_K^{0B}\right)_{B,Cmd}$ generates an elliptical, counter clockwise corkscrew maneuver. Although this maneuver is rather complicated and combined uncertainties are present, the trajectory of the center of gravity of the interceptor is smooth and does not exhibit oscillations. This underlines that the generated reference signals are tracked persistently with a high accuracy during the terminal flight phase.
Summarizing the beforehand presented results, it is concluded that nearly all requirements are fulfilled in this specific example. The violations of the imposed requirements do not refrain the interceptor from mission accomplishment at the low velocity scenario in the presence of combined uncertainties. Even more, the designed interceptor flight control system enables the interceptor to operate in this domain of the flight envelope. Multiple tests with combined uncertainties, employing the levels of uncertainty given by (6.1), (6.2), (6.5), and (6.6) to (6.11), confirm these results.
The combination of the results for the high and the low velocity scenario lead to the final

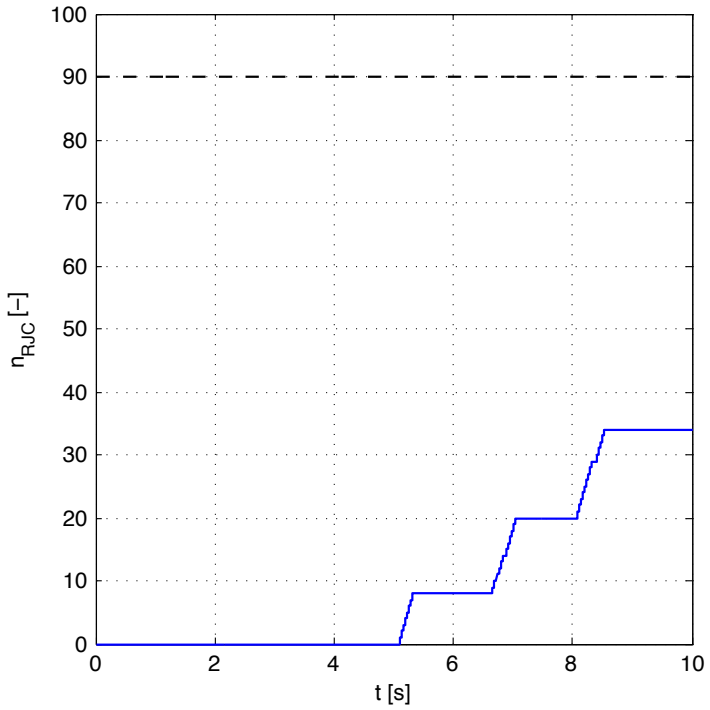

Figure 6.33: Reaction jet cartridge consumption in case of combined uncertainties at low velocity scenario

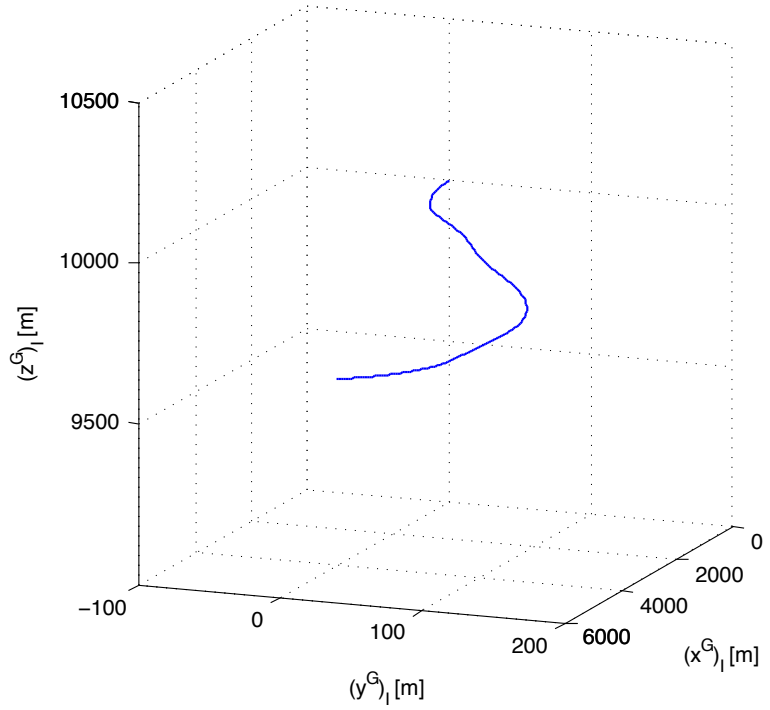

Figure 6.34: Interceptor trajectory in case of combined uncertainties at low velocity scenario

assessment that the designed interceptor flight control system, including the plant model, the Backstepping-based control systems, and the control allocation, exhibits the ability to withstand combined uncertainties up to the levels of uncertainty considered. Furthermore, the derived design seems to own the capabilities necessary to be applied to high agile, real world systems.

Chapter 7

Summary and perspectives

7.1 Summary

A nonlinear adaptive flight control system for an endo-atmospheric dual-actuator interceptor has been developed in this thesis. Aims of this development were to illustrate that the available nonlinear adaptive control methodologies can be applied successfully to high agile systems, that these methodologies have the properties to overcome the parameter uncertainties existing in real systems, and that specified requirements can be fulfilled at the same time. In detail, the developed interceptor flight control system design shall guarantee global boundedness of all signals, global tracking of known, smooth, and bounded reference signals, and global stability in the presence of uncertain constant parameters as well as time-varying parameters. In addition, the design shall be capable to overcome partial failures of the comprised adaptation algorithms. Furthermore, the controlled interceptor shall demonstrate a specified dynamical behavior.
As an introduction, the thesis provided an overview to the various categorizations available for missiles. By explaining the rational behind the categorizations, different types of missiles and their respective characteristics have been derived. The endo-atmospheric dual-actuator interceptor has been classified with respect to the presented categorizations. In addition, an overview of the development and the utilization of nonlinear adaptive control methods was given.
The starting point for the development of the nonlinear adaptive flight control system has been the detailed modeling of the interceptor dynamics as well as the interceptor subsystems. After presenting the geometrical properties, the mass properties, and the inertia properties of the interceptor, the nonlinear rigid body equations of motion were derived, based on Newton's second axiom. Thereafter, the modeling of the external forces and moments acting on the interceptor was presented. The description of the capabilities and the modeling of the interceptor subsystems followed. Afterwards, the modeling of uncertain constant parameters and time-varying parameters, which are both considered in this thesis, has been introduced.
Chapter 3 analyzed the interceptor flight dynamics. Multiple trim calculations were carried out for the endo-atmospheric dual-actuator interceptor; the interceptor flight envelope has been covered. Steady-state flight conditions and the maneuver capabilities of the interceptor have been derived. The former were utilized to derive the linearized interceptor dynamics, which provide insight into the inherent roll rate, longitudinal, and lateral dynamics of the interceptor as well as the change of the latter inside the interceptor flight envelope. In addition, the non-minimum phaseness of the interceptor dynamics as well as the effects originating from the reaction jet actuator section, which both constitute specialties of the endo-atmospheric dual-actuator interceptor, have been laid out.
The following chapter introduced the nonlinear control methodology Backstepping. After pro-

viding stability property definitions and stability theorems, Backstepping has been demonstrated for a simple example. Then, the design procedure for strict-feedback systems was derived. Thereafter, Block Backstepping has been presented. The control task of tracking of a known, smooth, and bounded reference signal has been considered in the following. It was shown that global asymptotic tracking is achieved. Afterwards, uncertain constant parameters were implemented in the strict-feedback systems, leading to adaptive Backstepping methodology. Starting from a simple example, the design procedure for parametric strict-feedback systems has been derived for the control task of regulation and tracking, including the respective boundedness and stability properties. In the following, unknown control coefficients were considered. It has been demonstrated that, by choosing an appropriate Lyapunov function, global boundedness of all signals and global tracking of a known, smooth, and bounded reference signal is achieved in the presence of uncertain constant parameters and unknown control coefficients. Finally, nonlinear damping was shown. The beforehand derived design procedures were augmented by nonlinear damping terms. It has been proven that this guarantees global boundedness of all signals in partial absence of adaptation.

The design process of the interceptor flight control system started with the formulation and analysis of requirements. Based on these requirements, the flight control system architecture was developed. A plant model, a roll rate control system, separate pitch and yaw acceleration control systems, and a control allocation have been identified as main architectural components. The interceptor roll rate control system was designed by utilizing the presented theoretical background. Due to the non-minimum phaseness of the pitch and lateral acceleration of the center of gravity of the interceptor with respect to the inertial reference frame, specified in the body fixed frame, the interceptor pitch and yaw acceleration control system can not be designed straightforward. Instead, the longitudinal and lateral acceleration of an arbitrary reference point with respect to the inertial reference frame, specified in the body fixed frame, have been defined as outputs. The minimum distance between the center of gravity of the interceptor and an arbitrary reference point to guarantee minimum phaseness of the defined outputs was calculated throughout the interceptor flight envelope, whereupon parameter uncertainties were considered. An appropriate location for the reference point has been chosen. The interceptor pitch and yaw acceleration control systems were designed thereafter, employing the full scope of the presented theoretical background, including nonlinear damping. Based on desired functionalities, a straightforward approach has been chosen for the control allocation. In the last step of the design process, the parameters of the interceptor flight control system were optimized.

The evaluation of the performance of the controlled interceptor showed that all requirements are fulfilled in the nominal case. Furthermore, it has been shown that the reaction jet actuator section in conjunction with the designed interceptor flight control system enables the endo-atmospheric dual-actuator interceptor to operate at low absolute velocity conditions. Different situations with existing parameter uncertainties have been considered afterwards. A high velocity scenario and a low velocity scenario have been investigated for all situations. Uncertain total interceptor masses as well as cases with uncertain reaction jet cartridge thrust force were investigated. Time-varying aerodynamic derivatives were introduced to assess the performance of the controlled interceptor in the presence of time-varying parameters. Finally, uncertain constant parameters and time-varying parameters were investigated in combination. It has been proven that the controlled interceptor is able to operate in all considered situations with existing parameter uncertainties.

Based on the results achieved in this work, it is assessed that the nonlinear adaptive control methodology Backstepping can be applied successfully to high agile systems, like the endo-atmospheric dual-actuator interceptor. The uncertainties taken into account allow the further conclusion that Backstepping owns the capability to overcome the parameter uncertainties exist-

ing in real systems, while at the same time being able to fulfill defined requirements. The derived interceptor flight control system design shows a significant potential to be further investigated, tested, and matured in order to reach an application in a real missile system.

7.2 Perspectives

The way ahead to an application of the derived interceptor flight control system design in a real missile system is at least threefold. The availability and continuity of the internal sensor system signals is assumed in this thesis. Although these signal properties are realizable from the technical point of view, the effects of non-availabilities of these signals as well as the outcomes of discretization of such signals should be investigated. The derived results could be utilized to harden the interceptor flight control system against partial failures of the internal sensor system. Second, the controlled interceptor should be augmented by a guidance algorithm and a sensor model. This would lead to an interceptor system simulation, which could be used to study the performance of the interceptor flight control system design on the system level. Measures to qualify the nonlinear adaptive interceptor flight control system should be developed in parallel to the two mentioned efforts. The actual certification requirements for flight control systems are oriented towards linear system theory.
From the perspective of future research, the illustrated interceptor flight control system design offers multiple opportunities to continue scientific work. First, it would be possible to reduce or eliminate the overparametrization of the control systems, pointed out during the introduction of the Backstepping methodology. While in this thesis the overparametrization has been accepted to reach an adaptive Backstepping-based design for this realistic application for the first time, further work could concentrate on the evolution of the derived design. This could be done by utilizing the Tuning Functions Design presented in [71]. The separation of the controller and identifier design would desirable. The theoretical framework of ISS-Backstepping seems promising. Introduced in [71], [137] and [138] applied this method to a simple representation of a missile.
Third, the invention of mechanisms in the fashion of nonlinear damping which overcome the total absence of adaptation in the presence of the considered parameter uncertainties would provide a very high benefit from the operational perspective.
Considering the application of the derived design to other aerospace vehicles or the combination of the chosen approach with other theories, e.g. other control allocation methodologies, one can figure out new research opportunities instantaneously.

Appendix A

Nomenclature

Position

The following appendix illustrates the nomenclature which is utilized throughout this thesis. It follows the nomenclature introduced in [47]. The denotation of position, velocity, acceleration, angular velocity, angular acceleration, force, and moment vectors as well as their scalar elements is illustrated.
The position of a point G with respect to the inertial reference frame is described by (A.1), whereupon the subscript B indicates the coordinate frame in which the vector is specified. The right hand side of (A.1) shows the scalar elements of the position vector.

$$\left(\vec{r}^{\,G}\right)_B = \begin{bmatrix} x^G \\ y^G \\ z^G \end{bmatrix}_B \tag{A.1}$$

The relative position of a point P with respect to a point G, specified in the coordinate frame B, is designated according to (A.2).

$$\left(\vec{r}^{\,GP}\right)_B = \begin{bmatrix} x^{GP} \\ y^{GP} \\ z^{GP} \end{bmatrix}_B \tag{A.2}$$

Velocity

The velocity of a point G with respect to the inertial reference frame, which herein is embedded in the flat earth representation, is denoted as stated in (A.3).

$$\left(\vec{V}_K^G\right)_B^I = \begin{bmatrix} u_K^G \\ v_K^G \\ w_K^G \end{bmatrix}_B^I \tag{A.3}$$

The outer superscript I indicates that the velocity is relative to the inertial reference frame. The outer subscript specifies that the velocity is specified in the coordinate frame B. The inner subscript K denotes the type of velocity; the kinematic velocity.

Acceleration

Accelerations are denoted in two different ways in this thesis. The first designation is derived from the beforehand presented nomenclature of velocities. (A.4) describes the acceleration of a

point G, whereupon the time derivative of the velocity relative to the inertial reference frame is derived with respect to the coordinate frame B. The outer subscript B indicates the coordinate frame in which the acceleration is specified. The type of acceleration is denoted by the inner subscript K. In this case the kinematic acceleration. The right hand side of (A.4) illustrates the respective designation of the scalar elements of the acceleration vector.

$$\left(\dot{\vec{V}}_K^G\right)_B^{IB} = \begin{bmatrix} \dot{u}_K^G \\ \dot{v}_K^G \\ \dot{w}_K^G \end{bmatrix}_B^{IB} \tag{A.4}$$

The second acceleration denotation possibility is shown in (A.5). The latter describes the acceleration of a point G, whereupon the time derivative of the velocity relative to the inertial reference frame is derived with respect to the inertial reference frame. The acceleration is specified in the coordinate frame B, which is indicated by the outer subscript. As illustrated in (A.5), the scalar elements of the acceleration vector are denoted according to the individual axis of the respective coordinate frame.

$$\left(\vec{a}^{\,G}\right)_B^{II} = \begin{bmatrix} a_X^G \\ a_Y^G \\ a_Z^G \end{bmatrix}_B^{II} \tag{A.5}$$

Angular velocity

The angular velocity of the coordinate frame B relative to the coordinate frame 0 is denoted according to (A.6). The outer subscript B indicates the coordinate frame in which the angular velocity is specified. The inner subscript K specifies the type of angular velocity.

$$\left(\vec{\omega}_K^{0B}\right)_B = \begin{bmatrix} p_K^{0B} \\ q_K^{0B} \\ r_K^{0B} \end{bmatrix}_B \tag{A.6}$$

Angular acceleration

The change, with respect to the coordinate frame 0, of the angular velocity of the coordinate frame B relative to the coordinate frame 0 is described as stated in (A.7). The right hand side of (A.7) shows the respective scalar elements of the angular acceleration vector.

$$\left(\dot{\vec{\omega}}_K^{0B}\right)_B^0 = \begin{bmatrix} \dot{p}_K^{0B} \\ \dot{q}_K^{0B} \\ \dot{r}_K^{0B} \end{bmatrix}_B^0 \tag{A.7}$$

The outer subscript indicates that the angular acceleration is specified in the coordinate frame B. The type of angular acceleration is described by the inner subscript K. In (A.7), a kinematic angular acceleration is designated.

Force

A force, acting on the point P, is designated according to (A.8). The outer subscript shows that the force is specified in the coordinate frame B. The inner subscript indicates the physical

origin of the force; in this case aerodynamics.

$$\left(\vec{F}_A^P\right)_B = \begin{bmatrix} F_{X,A}^P \\ F_{Y,A}^P \\ F_{Z,A}^P \end{bmatrix}_B \tag{A.8}$$

As shown on the right hand side of (A.8), the scalar elements of the force vector are denoted according to the individual axis along they are acting.

Moment

Moments with respect to a point P are denoted as stated in (A.9), whereupon the outer subscript indicates that the moments are specified in the coordinate frame B. The inner subscript describes the physical origin of the moment. In this example, the moment arises from the reaction jet actuator section. The scalar elements of the moment vector are denoted by their respective axis of rotation, whereupon L specifies a roll moment, M indicates a pitch moment, and N denotes a yaw moment.

$$\left(\vec{M}_{RJC}^P\right)_B = \begin{bmatrix} M_{L,RJC}^P \\ M_{M,RJC}^P \\ M_{N,RJC}^P \end{bmatrix}_B \tag{A.9}$$

Appendix B

Coordinate frames

Body fixed frame

This appendix illustrates the coordinate frames which are utilized in this thesis. Three coordinate frames are used in total. The body fixed frame constitutes the first coordinate frame, the North-East-Down frame the second, and the inertial reference frame the third and final coordinate frame. All frames are following [55] and [56]. The figures shown below are based on the illustrations in [16].
The origin of the body fixed frame resides in the center of gravity G of the vehicle and moves with the latter. The body fixed frame is denoted by the subscript B. The X_B and the Z_B axis of the coordinate frame B are lying in the plane of symmetry of the vehicle, whereupon the X_B axis points to the vehicle nose and the Z_B axis points downwards. The Y_B axis is oriented perpendicular to the plane of symmetry of the vehicle and points to the right hand side. Hence, the coordinate frame B constitutes a right hand coordinate system. The B frame is visualized in Figure B.1. In addition, Figure B.1 shows the absolute kinematic velocity $(V^G_{K,Abs})^I_B$ as well as the angle of attack $(\alpha^G_K)^I_B$ and the sideslip angle $(\beta^G_K)^I_B$, which relate $(V^G_{K,Abs})^I_B$ to the coordinate frame B.

North-East-Down frame

The origin of the North-East-Down frame is the center of gravity of the aerospace vehicle. Hence, the North-East-Down frame, commonly abbreviated NED, moves with the vehicle. The NED coordinate frame is denoted by the subscript 0. The X_0 axis of the coordinate frame NED points north persistently. The Y_0 axis invariably points east. The Z_0 axis of the coordinate frame points to the center of the earth, which implies that the X_0 - Y_0 plane is a tangent plane to the earth ellipsoid. The coordinate frame NED constitutes a right hand coordinate system. Based on the fact that a flat earth representation is employed in this thesis, the downward pointing axis Z_0 of the coordinate frame NED is perpendicular to the surface of the flat earth representation. Hence, the X_0 - Y_0 plane is parallel to the surface of the flat earth representation. The coordinate frame NED and the frame B are related via the Euler angles. The roll angle Φ constitutes the angle which the vehicle is rotated out of the X_0 - Y_0 plane, whereupon the X_B axis is the axis of rotation. The angle at which the vehicle is rotated about the Y_B axis constitutes the pitch angle Θ. Ψ denotes the angle that the vehicle is rotated in the X_0 - Y_0 plane, whereupon Z_0 is the axis of rotation. The coordinate frame NED as well as the Euler angles are visualized in Figure B.2.

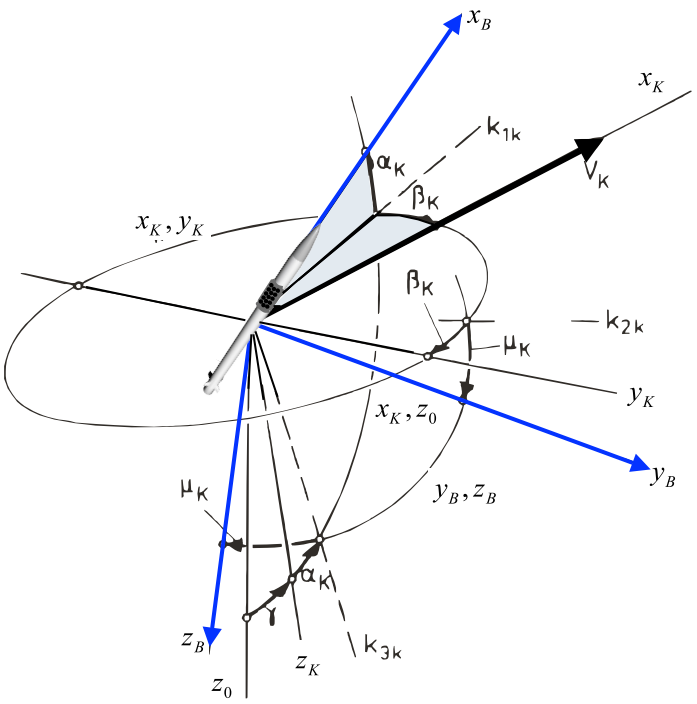

Figure B.1: Body fixed frame

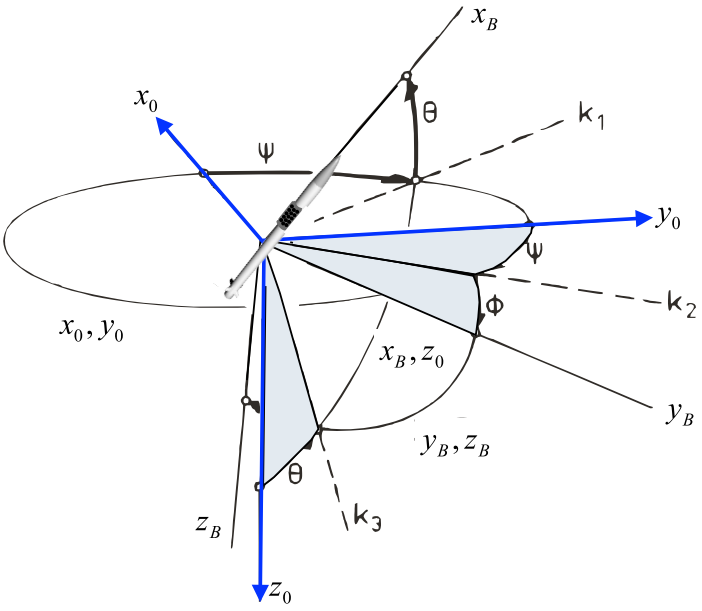

Figure B.2: North-East-Down frame

Inertial reference frame

The origin of the inertial reference frame, which is utilized in this thesis, resides in the surface of the flat earth representation. The inertial frame is denoted by the index I. Besides the Z_I axis, the coordinate frame I is oriented identically as the NED frame, meaning that the X_I axis points north and the Y_I axis points east. Hence, the X_I axis and the Y_I axis span the surface plane of the flat earth representation. The Z_I axis points upwards and describes the altitude above the surface of the flat earth representation.

Appendix C

Aerodynamic derivatives

Axial force derivatives

The following appendix displays the aerodynamic derivatives of the interceptor, which enter the application rules (2.47) to (2.52). The flight condition $(V^G_{K,Abs})^I_B = 600\,[m/s]$ and $\left(z^G\right)_I = 10000\,[m]$, which is exemplary employed throughout this thesis, is utilized for this illustration. The aerodynamic derivatives are grouped in the taxonomy of axial force derivatives, lateral force derivatives, longitudinal force derivatives, roll moment derivatives, pitch moment derivatives, and yaw moment derivatives. The aerodynamic derivative $C_{X,Alt}\left(\alpha^G_K, \left(z^G\right)_I, M\right)$ is identical to zero at the considered exemplary flight condition. Hence, it is not shown.

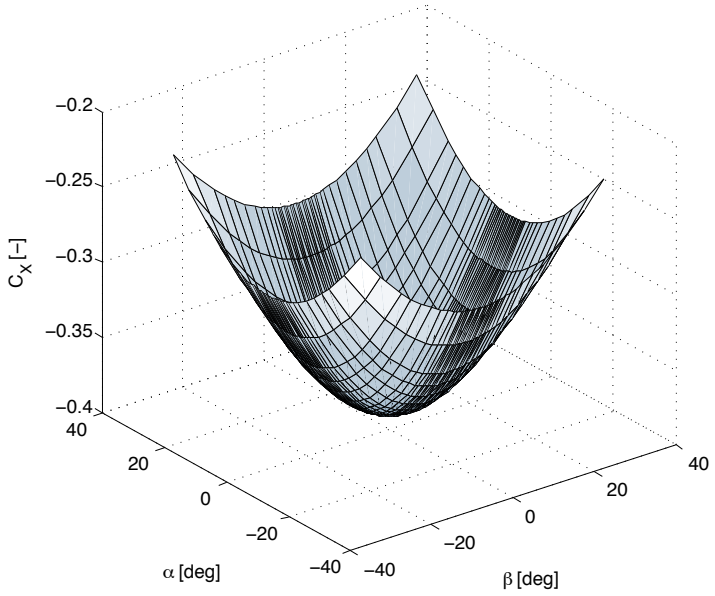

Figure C.1: $C_{X,0}\left(\alpha^G_K, \beta^G_K, M\right)$ at $(V^G_{K,Abs})^I_B = 600\,[m/s]$ and $\left(z^G\right)_I = 10000\,[m]$

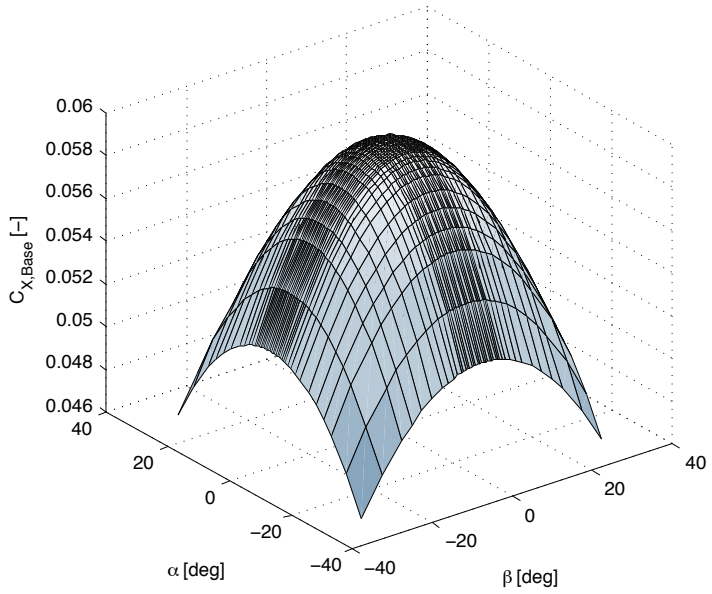

Figure C.2: $C_{X,Base}\left(\alpha_K^G, \beta_K^G, M\right)$ at $(V_{K,Abs}^G)_B^I = 600\,[m/s]$ and $\left(z^G\right)_I = 10000\,[m]$

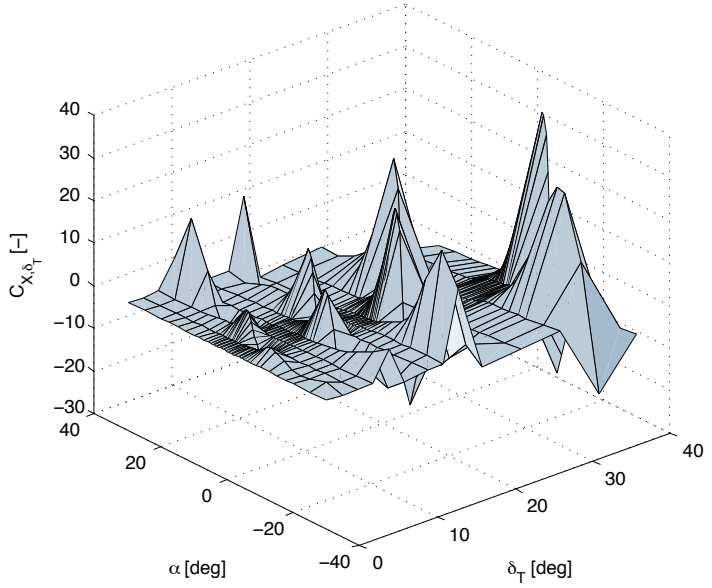

Figure C.3: $C_{X,\delta_{Total}}\left(\alpha_K^G, \delta_{Total}, M\right)$ at $(V_{K,Abs}^G)_B^I = 600\,[m/s]$ and $\left(z^G\right)_I = 10000\,[m]$

Lateral force derivatives

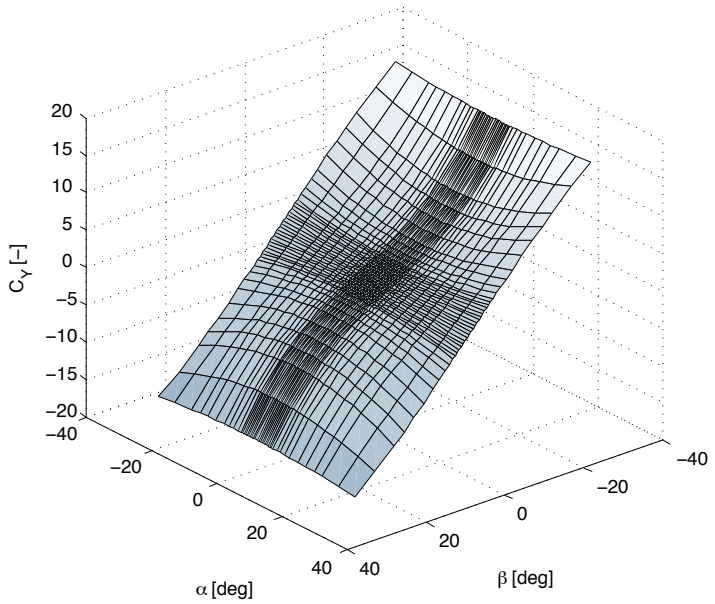

Figure C.4: $C_{Y,0}\left(\alpha_K^G, \beta_K^G, M\right)$ at $(V_{K,Abs}^G)_B^I = 600\,[m/s]$ and $\left(z^G\right)_I = 10000\,[m]$

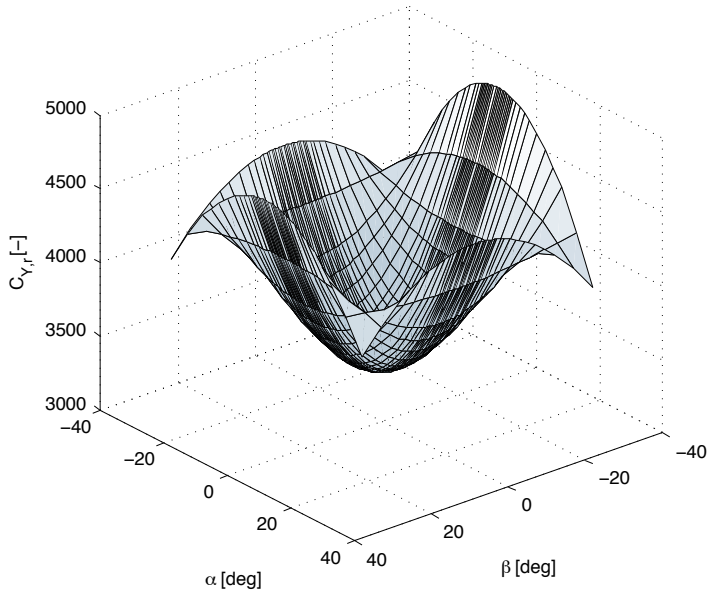

Figure C.5: $C_{Y,r}\left(\alpha_K^G, \beta_K^G, M\right)$ at $(V_{K,Abs}^G)_B^I = 600\,[m/s]$ and $\left(z^G\right)_I = 10000\,[m]$

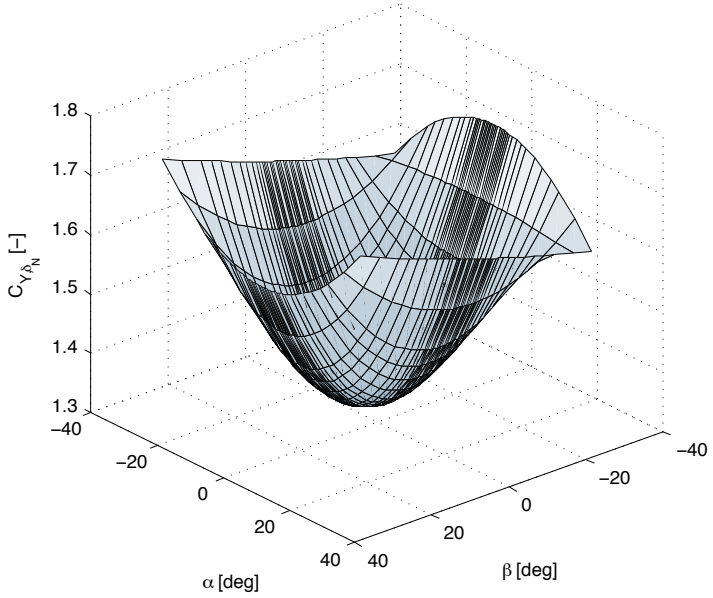

Figure C.6: $C_{Y,\delta_N}\left(\alpha_K^G, \beta_K^G, M\right)$ at $\left(V_{K,Abs}^G\right)_B^I = 600\,[m/s]$ and $\left(z^G\right)_I = 10000\,[m]$

Longitudinal force derivatives

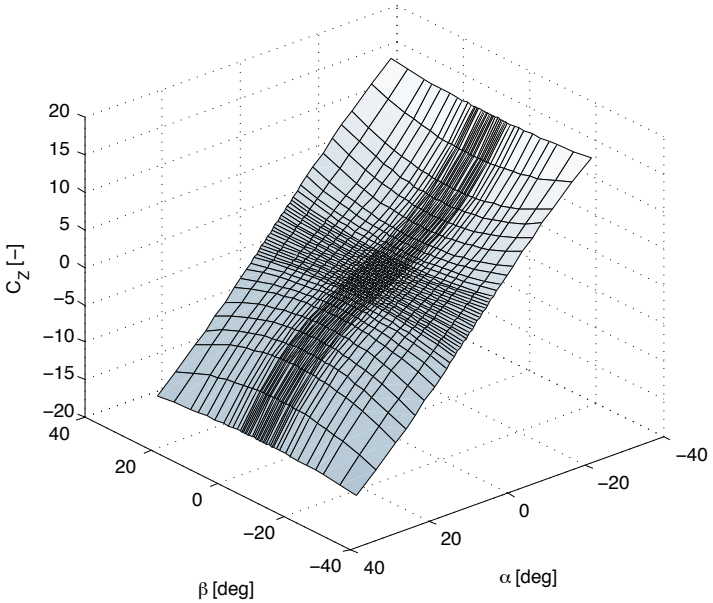

Figure C.7: $C_{Z,0}\left(\alpha_K^G, \beta_K^G, M\right)$ at $\left(V_{K,Abs}^G\right)_B^I = 600\,[m/s]$ and $\left(z^G\right)_I = 10000\,[m]$

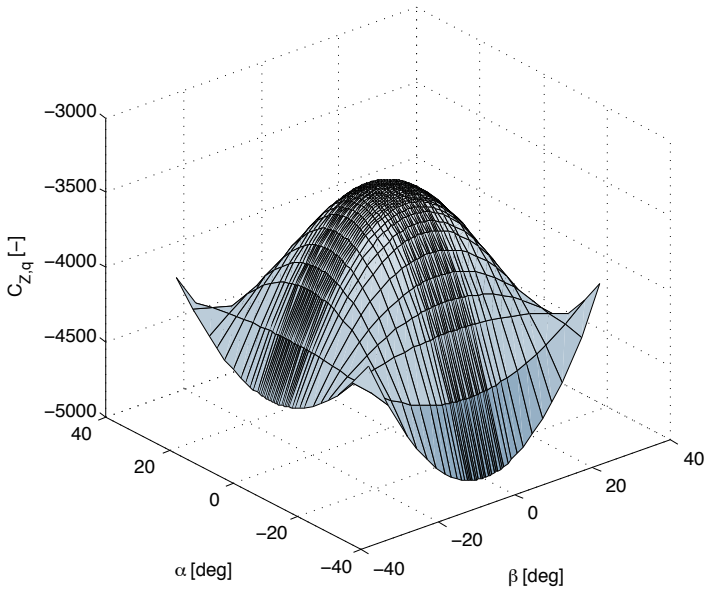

Figure C.8: $C_{Z,q}\left(\alpha_K^G, \beta_K^G, M\right)$ at $(V_{K,Abs}^G)_B^I = 600\,[m/s]$ and $\left(z^G\right)_I = 10000\,[m]$

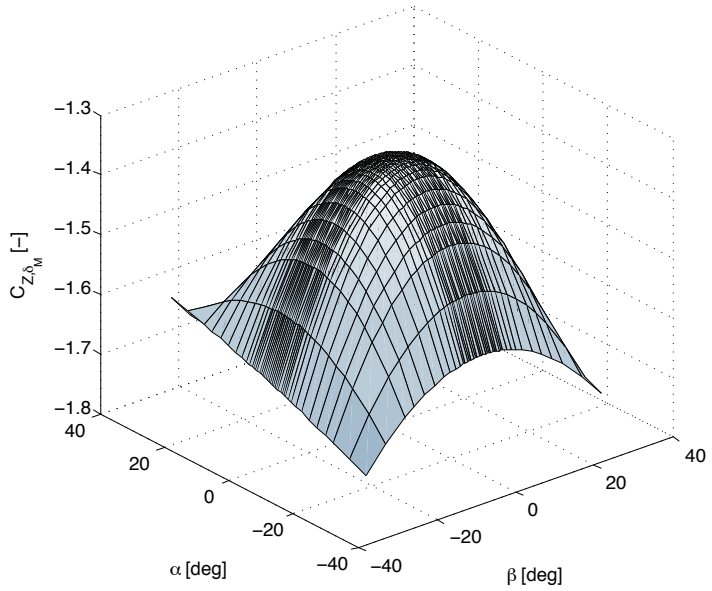

Figure C.9: $C_{Z,\delta_M}\left(\alpha_K^G, \beta_K^G, M\right)$ at $(V_{K,Abs}^G)_B^I = 600\,[m/s]$ and $\left(z^G\right)_I = 10000\,[m]$

Roll moment derivatives

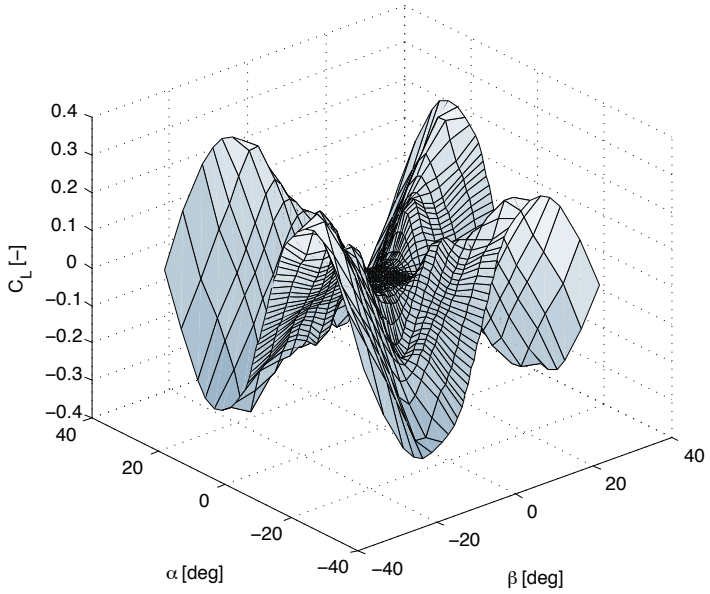

Figure C.10: $C_{L,0}\left(\alpha_K^G, \beta_K^G, M\right)$ at $(V_{K,Abs}^G)_B^I = 600\,[m/s]$ and $\left(z^G\right)_I = 10000\,[m]$

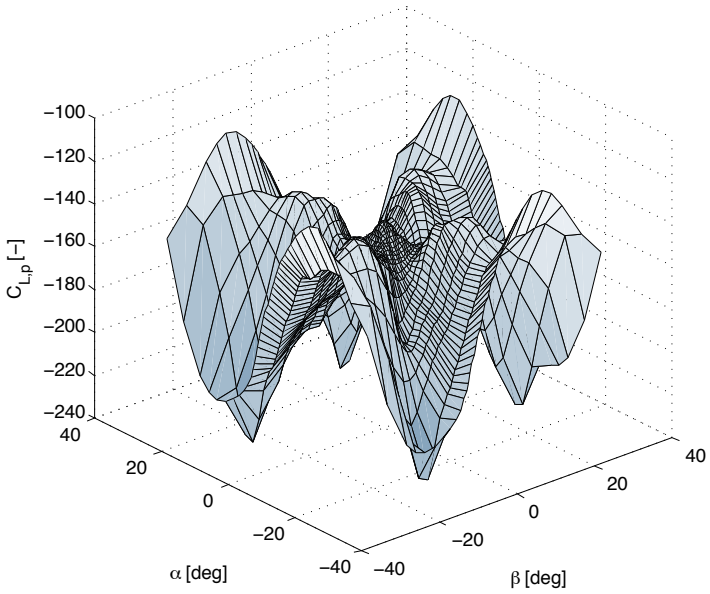

Figure C.11: $C_{L,p}\left(\alpha_K^G, \beta_K^G, M\right)$ at $(V_{K,Abs}^G)_B^I = 600\,[m/s]$ and $\left(z^G\right)_I = 10000\,[m]$

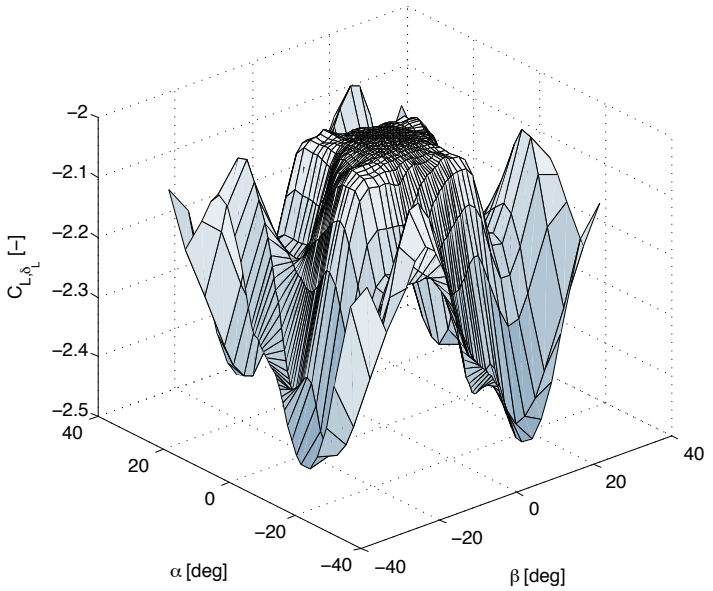

Figure C.12: $C_{L,\delta_L}\left(\alpha_K^G, \beta_K^G, M\right)$ at $(V_{K,Abs}^G)_B^I = 600\,[m/s]$ and $\left(z^G\right)_I = 10000\,[m]$

Pitch moment derivatives

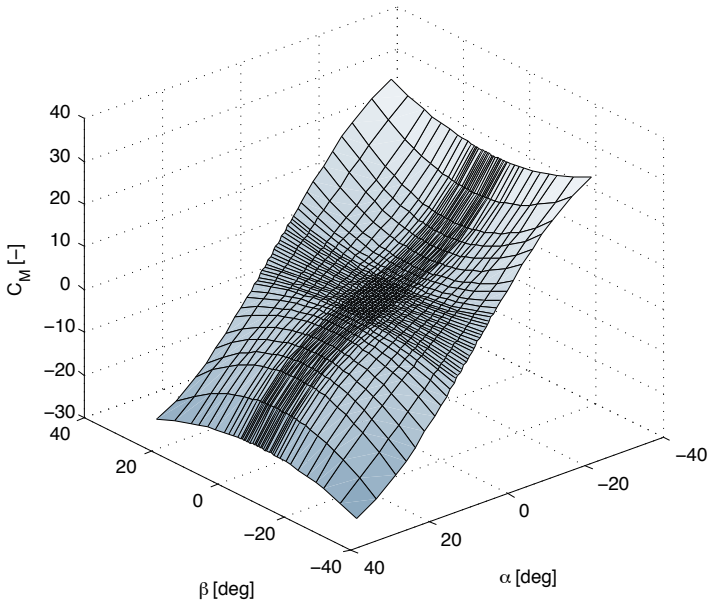

Figure C.13: $C_{M,0}\left(\alpha_K^G, \beta_K^G, M\right)$ at $(V_{K,Abs}^G)_B^I = 600\,[m/s]$ and $\left(z^G\right)_I = 10000\,[m]$

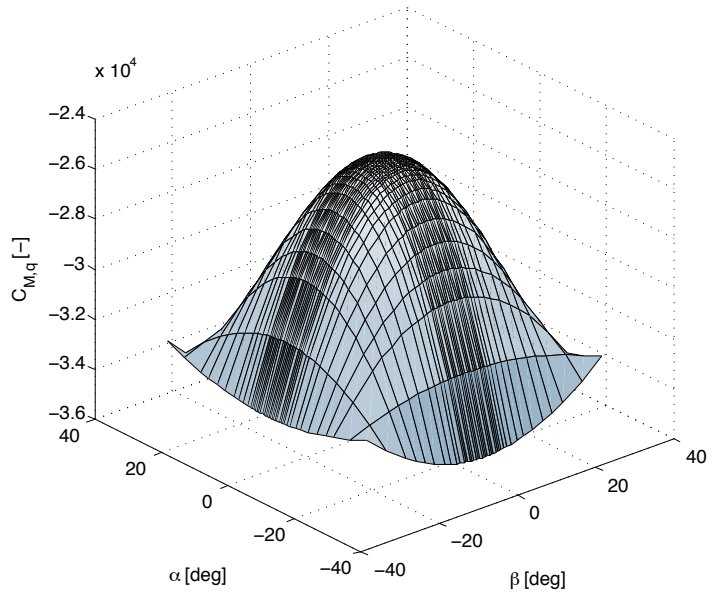

Figure C.14: $C_{M,q}\left(\alpha_K^G, \beta_K^G, M\right)$ at $(V_{K,Abs}^G)_B^I = 600\,[m/s]$ and $\left(z^G\right)_I = 10000\,[m]$

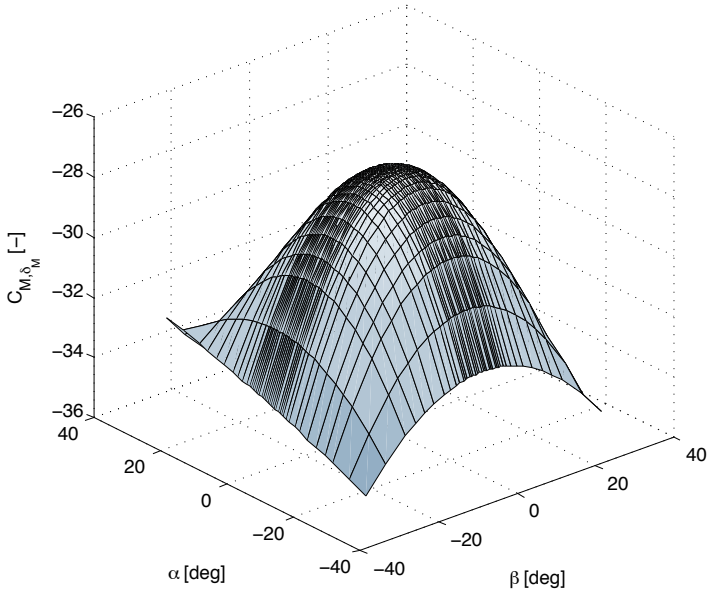

Figure C.15: $C_{M,\delta_M}\left(\alpha_K^G, \beta_K^G, M\right)$ at $(V_{K,Abs}^G)_B^I = 600\,[m/s]$ and $\left(z^G\right)_I = 10000\,[m]$

Yaw moment derivatives

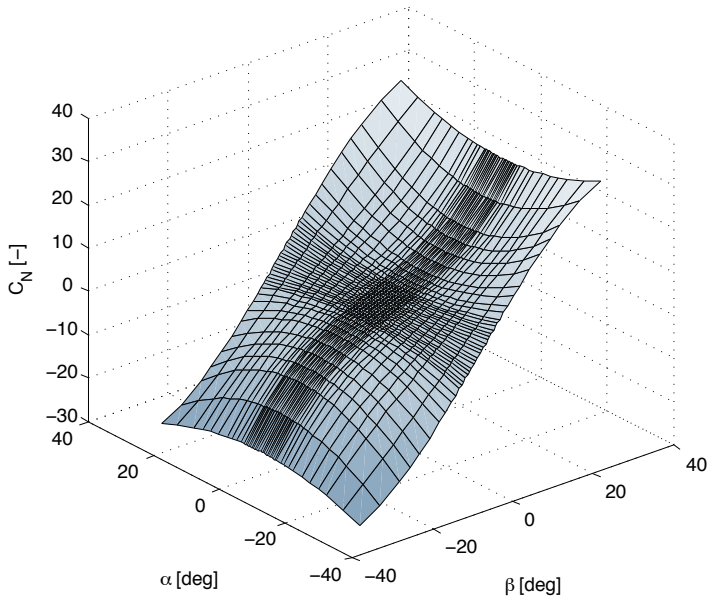

Figure C.16: $C_{N,0}\left(\alpha_K^G, \beta_K^G, M\right)$ at $(V_{K,Abs}^G)_B^I = 600\,[m/s]$ and $\left(z^G\right)_I = 10000\,[m]$

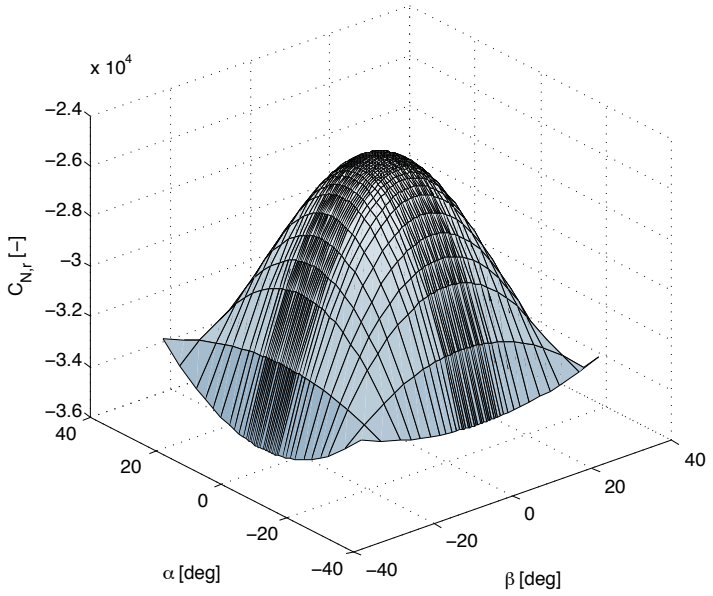

Figure C.17: $C_{N,r}\left(\alpha_K^G, \beta_K^G, M\right)$ at $(V_{K,Abs}^G)_B^I = 600\,[m/s]$ and $\left(z^G\right)_I = 10000\,[m]$

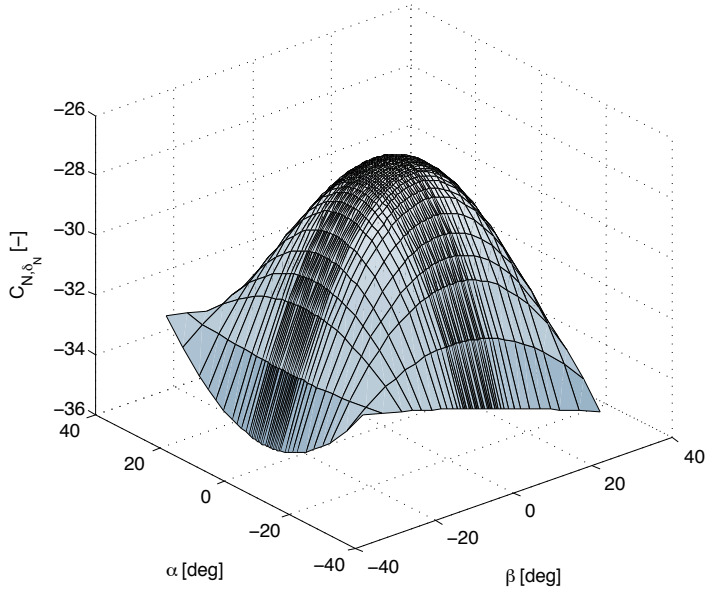

Figure C.18: $C_{N,\delta_N}\left(\alpha_K^G, \beta_K^G, M\right)$ at $(V_{K,Abs}^G)_B^I = 600\,[m/s]$ and $\left(z^G\right)_I = 10000\,[m]$

Bibliography

[1] Eric J. Abney and Melissa A. McDaniel, editors. *High Angle of Attack Aerodynamic Predictions Using Missile Datcom*, Toronto, 2005. AIAA Applied Aerodynamics Conference, American Institute of Aeronautics and Astronautics.

[2] R. Adams, J. Buffington, and S. Banda. Design of nonlinear control laws for high-angle-of-attack flight. *Journal of Guidance, Control and Dynamics*, 17(4):737–746, 1994.

[3] M. Arcak. Observer-based backstepping with weak nonlinear damping. *Proceedings of the 2002 IEEE American Control Conference*, 5:3478–3483, 2002.

[4] G. Bastin and G. Campion, editors. *Indirect adaptive control of linearly parametrized nonlinear systems*, Glasgow, 1989. Proceedings of the 3^{rd} IFAC Symposium on Adaptive Systems in Control, and Signal Processing.

[5] G. Bastin and G. Campion. Indirect adaptive state-feedback control of linearly parametrized nonlinear systems. *International Journal of Adaptive Control and Signal Processing*, 4:345–358, 1990.

[6] R. Beck. *Application of control allocation methods to linear systems with four or more objectives*. Dissertation, Virginia Polytechnic Institute and State University, 2002.

[7] D. J. Biezad. *Integrated Navigation and Guidance Systems*. American Institute of Aeronautics and Astronautics, Reston, 1999.

[8] W. B. Blake. *Missile DATCOM User's Manual - 1997 Fortran 90 Revision*. Air Force Research Laboratory, 1997.

[9] J. H. Blakelock. *Automatic Control of Aircraft and Missiles*. John Wiley & Sons, Inc., Hoboken, 2^{nd} edition, 1991.

[10] M. Bodson. Evaluation of optimization methods for control allocation. *Journal of Guidance, Control and Dynamics*, 25(4):703–711, 2001.

[11] J.-L. Boiffier. *The Dynamics of Flight - The Equations*. John Wiley & Sons, Inc., Baffins Lane, 1998.

[12] M. A. Bolender and D. B. Doman. Non-linear control allocation using piecewise linear functions. *Journal of Guidance, Control and Dynamics*, 27(6):1017–1027, 2004.

[13] K. Bordignon. *Constrained Control Allocation for Systems with Redundant Control Effectors*. Dissertation, Virginia Polytechnic Institute and State University, 1996.

[14] J. Brandeis and J. Gill. Experimental investigation of side-jet steering for supersonic and hypersonic missiles. *Journal of Spacecraft and Rockets*, 33(3):346–352, 1996.

[15] K. R. Britting. *Inertial Navigation Systems Analysis*. Wiley-Interscience, New York, 1971.

[16] R. Brockhaus. *Flugregelung*. Springer-Verlag, Berlin, 2^{nd} edition, 2001.

[17] G. Brüning, X. Hafer, and G. Sachs. *Flugleistungen*. Springer-Verlag, Berlin, 3^{rd} edition, 2006.

[18] J. Buffington and D. Enns. Lyapunov stability analysis of daisy chain control allocation. *Journal of Guidance, Control and Dynamics*, 19(6):1226–1230, 1996.

[19] J. Burken, P. Lu, Z. Wu, and C. Bahm. Two reconfigurable flight-control design methods: Robust servomechanism and control allocation. *Journal of Guidance, Control and Dynamics*, 24(3):482–493, 2001.

[20] C. I. Byrnes and A. Isidori. New results and examples in nonlinear feedback stabilization. *Systems & Control Letters*, 12:437–442, 1989.

[21] P. Champigny and Lacau R. G., editors. *Lateral Jet Control for Tactical Missiles*. NATO AGARD R-804, Special Course on Missile Aerodynamics, 1994.

[22] A. C. Chatfield. *Fundamentals of High Accuracy Inertial Navigation*, volume 174 of *Progress in Astronautics and Aeronautics*. American Institute of Aeronautics and Astronautics, Reston, 1997.

[23] J. J. Craig. *Adaptive Control of Mechanical Manipulators*. Addison-Wesley, Reading, 1988.

[24] W. Dayawansa, W. M. Boothby, and D. L. Elliott. Global state and feedback equivalence of nonlinear systems. *Systems & Control Letters*, 6:229–234, 1985.

[25] D. A. Dickmann and F. K. Lu, editors. *Jet in Supersonic Crossflow on a Flat Plate*, San Francisco, 2006. 25^{th} AIAA Aerodynamic Measurement Technology and Ground Testing Conference, American Institute of Aeronautics and Astronautics.

[26] D. A. Dickmann and F. K. Lu, editors. *Shock/Boundary Layer Interaction Effects on Transverse Jets in Crossflow Over a Flat Plat*, Seattle, 2008. 38^{th} Fluid Dynamics Conference and Exhibit, American Institute of Aeronautics and Astronautics.

[27] D. B. Doman, B. J. Gamble, and A. D. Ngo. Quantized control allocation of reaction control jets and aerodynamic control surfaces. *Journal of Guidance, Control and Dynamics*, 32(1):13–24, 2009.

[28] R. B. Dow. *Fundamentals of Advanced Missiles*. John Wiley & Sons, Inc., New York, 1958.

[29] W. Durham. Constrained control allocation. *Journal of Guidance, Control and Dynamics*, 16(4):717–725, 1993.

[30] W. Durham. Attainable moments for the constrained control allocation problem. *Journal of Guidance, Control and Dynamics*, 17(6):1371–1373, 1994.

[31] W. Durham, editor. *Computationally Efficient Control Allocation*. AIAA Guidance, Navigation and Control Conference, 1999.

[32] W. Durham and K. Bordignon. Multiple control effector rate limiting. *Journal of Guidance, Control and Dynamics*, 19(1):30–37, 1996.

[33] H.-D. Ebbinghaus, editor. *Zahlen*. Springer-Verlag, Berlin, 3^{rd} edition, 1992.

[34] R. Eberhard and D. Ward, editors. *Indirect adaptive flight control of a tailless fighter aircraft*. AIAA Guidance, Navigation and Control Conference and Exhibit, 1994.

[35] D. Enns, editor. *Control Allocation Approaches*, Boston, 1998. AIAA Guidance, Navigation and Control Conference and Exhibit.

[36] B. Etkin. *Dynamics of Atmospheric Flight*. Wiley, New York, 1972.

[37] A. Feuer and A. S. Morse, editors. *Local stability of parameter adaptive control systems*, John Hopkins, 1978. Proceedings of the 1978 Conference on Information Sciences and Systems.

[38] R. Fletcher and M. J. D. Powell. A rapidly convergent descent method for minimization. *The Computer Journal*, 6:163, 1963.

[39] O. Föllinger. *Regelungstechnik - Einführung in die Methoden und ihre Anwendung*. Hüthig, Heidelberg, 8^{th} edition, 1994.

[40] P. Gnemmi and F. Seiler, editors. *Interaction of lateral jet with the projectile external flow*, Denver, 2000. AIAA Atmospheric Flight Mechanics Conference, American Institute of Aeronautics and Astronautics.

[41] W. Hahn. *Stability of Motion*. Springer, Berlin, 1967.

[42] O. Härkegård, editor. *Efficient active set algorithms for solving constrained least squares problems in aircraft control allocation*. Proceedings of the 41^{st} IEEE Conference on Decision and Control, 2002.

[43] O. Härkegård. *Backstepping and Control Allocation with Applications to Flight Control*. Ph. D. Dissertation, Linköping University, Linköping, 2003.

[44] O. Härkegård and T. Glad, editors. *Vector backstepping design for flight control*, Hilton Head, 2007. AIAA Guidance, Navigation and Control Conference and Exhibit, American Institute of Aeronautics and Astronautics.

[45] F. Holzapfel. *Linearisierung des Flugzeugverhaltens für grosse seitliche Schwerpunktverschiebung*. Seminararbeit, Technische Universität München, Garching, 1999.

[46] F. Holzapfel. *Nichtlineare adaptive Regelung eines unbemannten Fluggerätes*. Verlag Dr. Hut, München, 2004.

[47] F. Holzapfel. Flugregelung I. Lecture notes, Garching, 2008.

[48] F. Holzapfel. Flugsystemdynamik II. Lecture notes, Garching, 2008.

[49] F. Holzapfel, M. Heller, C. Zähringer, and G. Sachs, editors. *Flight Dynamics Modeling Environment for Controller Design and Analysis of Hypersonic Vehicles*, Kyoto, 2001. AIAA International Space Planes and Hypersonic Systems and Technologies Conference, American Institute of Aeronautics and Astronautics.

[50] F. Holzapfel, C. Zähringer, and G. Sachs, editors. *Computergestützte Entwicklungsumgebung zur Automatisierung flugdynamischer Analyse- und Regelungsaufgaben*, Hamburg, 2001. Deutscher Luft- und Raumfahrtkongress 2001, Deutsche Gesellschaft für Luft- und Raumfahrt e. V.

[51] F. Holzapfel, C. Zähringer, and G. Sachs, editors. *PC Based Configurable Aircraft Simulation Environment for Dynamics and Control Analysis*, Montreal, 2001. AIAA Modeling and Simulation Technologies Conference and Exhibit, American Institute of Aeronautics and Astronautics.

[52] L. R. Hunt, R. Su, and G. Meyer. Global transformations of nonlinear systems. *IEEE Transactions on Automatic Control*, 28:24–31, 1983.

[53] A. Isidori. *Nonlinear Control Systems*. Springer-Verlag, Berlin, 3^{rd} edition, 1995.

[54] A. Isidori. *Nonlinear Control Systems II*. Springer-Verlag, London, 1999.

[55] ISO 1151-1:1988. *Flight Dynamics – Concepts, quantities and symbols – Part 1: Aircraft motion relative to the air*, 1988.

[56] ISO 1151-3:1989. *Flight dynamics – Concepts, quantities, and symbols – Part 3: Derivatives of forces, moments and their coefficients*, 1989.

[57] S. L. S. Jacoby, J. S. Kowalik, and J. T. Pizzo. *Iterative Methods for Nonlinear Optimization Problems*. Prentice-Hall, Englewood Cliffs, 1972.

[58] B. Jakubczyk and W. Respondek. On linearization of systems. *Bulletin of the Polish Academy of Science, Series on Mathematical Science*, 28:517–522, 1980.

[59] J. J. Jerger. *Systems Preliminary Design*. Principles of Guided Missile Design. D. van Nostrand Company, Inc., Princeton, 1960.

[60] Z. P. Jiang and L. Praly, editors. *Iterative designs of adaptive controllers for systems with nonlinear integrators*, Brighton, 1991. Proceedings of the 30th IEEE Conference on Decision and Control.

[61] T. Kailath. *Linear Systems*. Prentice Hall, Inc., Englewood Cliffs, 1980.

[62] T. Kailath. *Linear least-squares estimation*. Hutchinson & Ross, 2001.

[63] I. Kanellakopoulos. *Adaptive control of Nonlinear Systems*. Ph. D. Dissertation, University of Illinois, Urbana, 1991.

[64] I. Kanellakopoulos, P. Kokotović, and R. Marino. An extended direct scheme for robust adaptive nonlinear control. *Automatica*, 27:247–255, 1991.

[65] I. Kanellakopoulos, P. Kokotović, and A. S. Morse. Systematic design of adaptive controllers for feedback linearizable systems. *IEEE Transactions on Automatic Control*, 36:1241–1253, 1990.

[66] H. K. Khalil. *Nonlinear Systems*. Prentice-Hall, Upper Saddle River, 3^{rd} edition, 2002.

[67] P. Kokotović. *Foundations of Adaptive Control*. Springer-Verlag, Berlin, 1991.

[68] P. Kokotović and H. J. Sussmann. A positive real condition for global stabilization of nonlinear systems. *Systems & Control Letters*, 13:125–133, 1989.

[69] M. Krstić. *Adaptive Nonlinear Control*. Ph. D. Dissertation, University of California, Santa Barbara, 1994.

[70] M. Krstić, I. Kanellakopoulos, and P. Kokotović. Adaptive nonlinear control without overparametrization. *Systems & Control Letters*, 19:177–185, 1992.

[71] M. Krstić, I. Kanellakopoulos, and P. Kokotović. *Nonlinear and Adaptive Control Design*. John Wiley & Sons, Inc., New York, 1995.

[72] M. Krstić and P. Kokotović. Lean backstepping design for a jet engine compressor model. *Proceedings of the* 4^{th} *IEEE Conference on Control Applications*, pages 1047–1052, 1995.

[73] J. La Salle and S. Lefschetz. *Die Stabilitätstheorie von Ljapunow*. Bibliographisches Institut, Mannheim, 1967.

[74] J. P. La Salle. Stability theory for ordinary differential equations. *Journal of Differential Equations*, 4:57–65, 1968.

[75] L. Laine and J. Andreasson, editors. *Control Allocation based Electronic Stability Control System for a Convetional Road Vehicle*, Seattle, 2007. Proceedings of the 2007 IEEE Intelligent Transportation Systems Conference.

[76] H. Leipholz. *Stabilitätstheorie*. B. G. Teubner, Stuttgart, 1968.

[77] B. Lian, H. Bang, and J. Hurtado, editors. *Adaptive Backstepping Control Based Autopilot Design for Reentry Vehicle*, Rhode Island, 2004. AIAA Guidance, Navigation and Control Conference and Exhibit, American Institute of Aeronautics and Astronautics.

[78] F. K. Lu and D. A. Dickmann, editors. *Topology of Supersonic Jet Interaction Flowfields at High Pressure Ratios*, Nice, 2008. 13^{th} International Symposium on Flow Visualization.

[79] P. Lu. Constrained tracking control of nonlinear systems. *Systems & Control Letters*, 27:305–314, 1996.

[80] J. Lunze. *Regelungstechnik 2*. Springer-Verlag, Berlin, 4^{th} edition, 2006.

[81] J. Lunze. *Regelungstechnik 1*. Springer-Verlag, Berlin, 6^{th} edition, 2007.

[82] R. Marino. On the largest feedback linearizable subsystem. *Systems & Control Letters*, 6:345–351, 1986.

[83] R. Marino, W. M. Boothby, and D. L. Elliott. Geometric properties of linearizable control systems. *Mathematical Systems Theory*, 18:97–123, 1985.

[84] R. Marino and P. Tomei. Dynamic output-feedback linearization and global stabilization. *Systems & Control Letters*, 17:115–121, 1991.

[85] R. Marino and P. Tomei. Global adaptive observers for nonlinear systems via filtered transformations. *IEEE Transactions on Automatic Control*, 37:1239–1245, 1992.

[86] R. Marino and P. Tomei. Global adaptive output-feedback control of nonlinear systems, part i: linear parametrization. *IEEE Transactions on Automatic Control*, 38:17–32, 1993.

[87] R. Marino and P. Tomei. Global adaptive output-feedback control of nonlinear systems, part ii: nonlinear parametrization. *IEEE Transactions on Automatic Control*, 38:33–49, 1993.

[88] R. Marino and P. Tomei. *Nonlinear Control Design: Geometric, Adaptive & Robust*. Prentice-Hall, London, 1995.

[89] P. S. Maybeck. *Stochastic Models, Estimation, and Control*, volume 1. Academic Press, New York, 1979.

[90] D. Mc Ruer, I. Ashkenas, and D. Graham. *Aircraft Dynamics and Automatic Control*. Princton University Press, Princeton, 1990.

[91] P. Menon, G. Sweriduk, S. Vaddi, and E. Ohlmeyer, editors. *Nonlinear Discrete-time Design Methods for Missile Flight Control Systems*, Providence, 2004. AIAA Guidance, Navigation and Control Conference and Exhibit, American Institute of Aeronautics and Astronautics.

[92] P. K. Menon, V. R. Iragavarapu, G. Sweriduk, and E. Ohlmeyer, editors. *Software Tools for Nonlinear Missile Autopilot Design*, Portland, 1999. AIAA Guidance, Navigation and Control Conference and Exhibit, American Institute of Aeronautics and Astronautics.

[93] R. H. Middleton and Goodwin G. C. Adaptive computed torque control for rigid link manipulators. *Systems & Control Letters*, 10:9–16, 1988.

[94] K. W. Naumann, H. Ende, A. George, and G. Mathieu, editors. *The Near Interaction of Lateral Control Jets and Hypervelocity Cross Flow*, Sorrento, 1998. RTO Meeting Proceedings 5, NATO Research and Technology Organization.

[95] J. A. Nelder and R. Mead. A simplex method for function minimization. *The Computer Journal*, 7:308–313, 1965.

[96] J. Nocedal and S. Wright. *Numerical Optimization*. Springer, New York, 1999.

[97] M. W. Oppenheimer, D. B. Doman, and M. A. Bolender, editors. *Control Allocation for Overactuated Systems*. 14^{th} Mediterranean Conference on Control and Automation, 2006.

[98] R. Ortega and M. W. Spong. Adaptive motion control of rigid robots: a tutorial. *Automatica*, 25:877–888, 1989.

[99] M. Papageorgiou and O. Stryk. *Optimierung: Statistische, dynamische, stochastische Verfahren*. Springer, 2^{nd} edition, 1996.

[100] J. A. Paradiso. Adaptable method of managing jets and aerosurfaces for aerospace vehicle control. *Journal of Guidance, Control and Dynamics*, 14(1):44–50, 1991.

[101] M. Philippi. *Control Allocation*. Semesterarbeit, Technische Universität München, München, 2008.

[102] M. J. D. Powell. An iterative method for finding stationary value of a function of several variables. *The Computer Journal*, 5:147, 1962.

[103] M. J. D. Powell. An efficient method for finding of a function of several variables without calculating derivatives. *The Computer Journal*, 7:155, 1964.

[104] W. H. Press, S. A. Teukolsky, W. T. Vetterling, and B. P. Flannery. *Numerical Recipes*. Cambridge University Press, Cambridge, 3^{rd} edition, 2007.

[105] A. E. Puckett and S. Ramo. *Guided Missile Engineering*. McGraw-Hill Book Company, Inc., New York, 1959.

[106] Z. Qu. *Robust Control of Nonlinear Uncertain Systems*. Wiley-Interscience, New York, 1998.

[107] D. B. Ridgely, Y. Lee, and T. Fanciullo, editors. *Dual Aero/Propulsive Missile Control - Optimal Control and Control Allocation*, Keystone, 2006. AIAA Guidance, Navigation and Control Conference and Exhibit.

[108] J. M. Rolfe and K. J. Staples. *Flight Simulation*. Cambridge University Press, Cambridge, 1986.

[109] H. Rosenbrock. An automatic method for finding the greatest or least value of a function. *The Computer Journal*, 3:175, 1960.

[110] J. Roskam. *Airplane Flight Dynamics and Automatic Flight Controls - Part I*. DARCorporation, Lawrence, 2^{nd} edition, 1998.

[111] A. Saberi, P. Kokotović, and H. J. Sussmann. Global stabilization of partially linear composite systems. *SIAM Journal Control & Optimization*, 28:1491–1503, 1990.

[112] S. Sastry. *Nonlinear Systems: Analysis, Stability and Control*. Springer-Verlag, New York, 1985.

[113] H. Schäfer, E. Augenstein, H. Esch, and H. Emunds. Experimental investigation of transverse jet interaction on a missile body using laser velocimetry and flow visualization. 2001.

[114] H. Schlichting and E. Truckenbrodt. *Aerodynamik des Flugzeuges, Aerodynamik des Tragflügels, des Rumpfes, der Flügel-Rumpf-Anordnungen und der Leitwerke, Zweiter Band*. Springer-Verlag, Berlin, 3^{rd} edition, 2001.

[115] H. Schlichting and E. Truckenbrodt. *Aerodynamik des Flugzeuges, Grundlagen aus der Strömungsmechanik: Aerodynamik des Tragflügels, Erster Band*. Springer-Verlag, Berlin, 3^{rd} edition, 2001.

[116] F. Seiler, P. Gnemmi, H. Ende, M. Schwenzer, and R. Meuer. Jet interaction at supersonic cross flow conditions. *Shock Waves*, 13:13–23, 2003.

[117] R. Sepulchre, M. Jankovic, and P. Kokotović. *Constructive Nonlinear Control*. Springer-Verlag, London, 1997.

[118] M. Sharma and N. Richards, editors. *Adaptive, Integrated Guidance and Control for Missile Interceptors*, Providence, 2004. AIAA Guidance, Navigation and Control Conference and Exhibit, American Institute of Aeronautics and Astronautics.

[119] S. Skogestad and I. Postlethwaite. *Multivariable Feedback Control - Analysis and Design*. John Wiley & Sons, Inc., Chichester, 1996.

[120] J.-J. E. Slotine and W. Li. On adaptive control of robot manipulators. *International Journal of Robotics Research*, 6:49–59, 1987.

[121] J.-J. E. Slotine and W. Li. Adaptive manipulator control: a case study. *IEEE Transactions on Automatic Control*, 33:995–1003, 1988.

[122] J.-J. E. Slotine and L. Weiping. *Applied Nonlinear Control*. Prentice-Hall, Englewood Cliffs, 1991.

[123] L. Sonneveldt, Q. P. Chu, and J. A. Mulder, editors. *Constrained Adaptive Backstepping Flight Control: Application to a Nonlinear F-16/MATV Model*, Keystone, 2006. AIAA Guidance, Navigation and Control Conference and Exhibit, American Institute of Aeronautics and Astronautics.

[124] L. Sonneveldt, Q. P. Chu, and J. A. Mulder. Nonlinear flight control design using constrained adaptive backstepping. *Journal of Guidance, Control and Dynamics*, 30(2):322–336, 2007.

[125] E. D. Sontag. *Mathematical Control Theory.* Springer-Verlag, New York, 2^{nd} edition, 1998.

[126] E. D. Sontag and H. J. Sussmann. Further comments on the stabilizability of the angular velocity of a rigid body. *Systems & Control Letters*, 12:437–442, 1988.

[127] W. Spendley, G. R. Hext, and Himsworth F. R. Sequential application of simplex designs in optimization and evolutionary operation. *Technometrics*, 4:441, 1962.

[128] A. Steinicke and G. Michalka, editors. *Improving Transient Performance of Dynamic Inversion Missile Autopilot by Use of Backstepping*, Monterey, 2002. AIAA Guidance, Navigation and Control Conference and Exhibit, American Institute of Aeronautics and Astronautics.

[129] R. F. Stengel. *Stochastic Optimal Control.* Wiley, New York, 1986.

[130] B. L. Stevens and F. L. Lewis. *Aircraft Control and Simulation.* John Wiley & Sons, Inc., New York, 1992.

[131] M. Stölzle. *Untersuchung zur Robustheit der nichtlinearen Regelungsmethode "Exact Backstepping" - Anwendung in der Flugzustandsregelung von Lenkflugkörpern.* Diplomarbeit, Technische Universität München, München, 2002.

[132] D. Taylor, P. Kokotović, and R. Marino. Adaptive regulation of nonlinear systems with unmodeled dynamics. *IEEE Transactions on Automatic Control*, 34:405–412, 1989.

[133] J. Thunberg and J. Robinson, editors. *Block Backstepping, NDI and Related Cascade Designs for Efficient Development of Nonlinear Flight Control Laws*, Honolulu, 2008. AIAA Guidance, Navigation and Control Conference and Exhibit, American Institute of Aeronautics and Astronautics.

[134] J. Tsinias. Sufficient lyapunov-like conditions for stabilization. *Mathematics of Control, Signals and Systems*, 2:343–357, 1989.

[135] H. Unbehauen. *Regelungstechnik I.* Vieweg, Braunschweig, 9^{th} edition, 1997.

[136] R. Unbehauen. *Systemtheorie 1.* R. Oldenbourg, München, 7^{th} edition, 1997.

[137] E. R. van Oort, L. Sonneveldt, Q. P. Chu, and J. A. Mulder, editors. *Comparison of Inverse Optimal and Tuning Functions Designs for Adaptive Missile Control*, Hilton Head, 2007. AIAA Guidance, Navigation and Control Conference and Exhibit, American Institute of Aeronautics and Astronautics.

[138] E. R. van Oort, L. Sonneveldt, Q. P. Chu, and J. A. Mulder, editors. *Modular Adaptive Input-to-State Stable Backstepping of a Nonlinear Missile Model*, Hilton Head, 2007. AIAA Guidance, Navigation and Control Conference and Exhibit, American Institute of Aeronautics and Astronautics.

[139] E. R. van Oort, L. Sonneveldt, Q. P. Chu, and J. A. Mulder, editors. *A Comparison of Adaptive Nonlinear Control Designs for an Over-Actuated Fighter Aircraft Model*, Honolulu, 2008. AIAA Guidance, Navigation and Control Conference and Exhibit, American Institute of Aeronautics and Astronautics.

[140] J. Virnig and D. Bodden, editors. *Multivariable control allocation and control law conditioning when control effectors limit*. AIAA Guidance, Navigation and Control Conference and Exhibit, 1994.

[141] W. S. Widnall and P. A. Grundy, editors. *Inertial Navigation System Error Models*, number TR-03-73, Alexandria, 1973.

[142] J. L. Willems. *Stabilität dynamischer Systeme*. R. Oldenbourg, München, 1973.

[143] L. A. Yarbro and S. N. Deming. Selection and preprocessing of factors for simplex optimization. *Analytica Chimica Acta*, 73:391–398, 1974.

[144] S. Yoon, Y. Kim, and S. Kim, editors. *Pursuit Guidance Law and Adaptive Backstepping Controller Design for Vision-Based Net-Recovery UAV*, Honolulu, 2008. AIAA Guidance, Navigation and Control Conference and Exhibit, American Institute of Aeronautics and Astronautics.

[145] T. Yoshizawa. *Stability Theory by Lyapunov's Second Method*. The Mathematical Society of Japan, 1966.

[146] K. Youdan, editor. *Backstepping control of rigid spacecraft slew maneuver*, Montreal, 2001. AIAA Guidance, Navigation and Control Conference and Exhibit, American Institute of Aeronautics and Astronautics.

[147] C. T. K. Young and B. F. Barfield. Viscous interaction of sonic transverse jets with supersonic external flows. *AIAA Journal*, 10:853–854, 1972.

[148] P. H. Zipfel. *Modeling and Simulation of Aerospace Vehicle Dynamics*. American Institute of Aeronautics and Astronautics, Reston, 2^{nd} edition, 2007.